STABLE NITROGEN AND SULFUR ISOTOPES IN ATMOSPHERIC CHEMISTRY

by

Jianghanyang Li

A Dissertation

Submitted to the Faculty of Purdue University

In Partial Fulfillment of the Requirements for the degree of

Doctor of Philosophy

Department of Earth, Atmospheric, and Planetary Sciences

West Lafayette, Indiana

May 2021

THE PURDUE UNIVERSITY GRADUATE SCHOOL
STATEMENT OF COMMITTEE APPROVAL

Dr. Greg Michalski, Chair

Department of Earth, Atmospheric, and Planetary Sciences

Dr. Lisa Welp

Department of Earth, Atmospheric, and Planetary Sciences

Dr. Alexander Laskin

Department of Chemistry

Dr. Amisha Shah

Lyles School of Civil Engineering

Approved by:

Dr. Daniel J. Cziczo

To My Family

For their unconditional love and support

ACKNOWLEDGMENTS

I would like to express my deepest appreciation and gratitude to my advisor, Dr. Greg Michalski for his guidance, mentorship and support in the past five years. Since I came to Purdue in 2016, Greg has been an excellent mentor, an inspiring scientist, and a good workmate. His immerse knowledge, patience, and enthusiasm to science, have shaped my intellectual development and made me into the researcher I am today.

I would also like to thank my committee members, Dr. Lisa Welp, Dr. Alexander Laskin and Dr. Amisha Shah, for their friendly guidance and help during my Ph.D. study. Learning from them have broadened my vision and greatly benefited my research. I thank my lab mates, Benjamin Wilkins, Huan Fang, Elizabeth Olson, Illyda Kelley, our lab manager Jani Sparks, and many undergraduate students that I have had the privilege to work with. Their hard work and assist helped me completing numerous projects.

I would like to thank my collaborators: Dr. Xuan Zhang, Dr. John Orland and Dr. Geoff Tyndall at the National Center for Atmospheric Research, Dr. Yan-Lin Zhang at Nanjing University of Information Science and Technology, Dr. Fan Wang at Sun Yat-sen University, Dr. Perry Davy at National Isotope Center of New Zealand and Dr. Mike Harvey at National Institute of Water and Atmospheric Research of New Zealand. Our collaborations have been more than pleasant, and I have learned a lot of each of them. I would also like to thank the National Center for Atmospheric Research, Purdue Climate Change Research Center, Purdue Graduate Student Government, Purdue College of Science, and Department of Earth, Atmospheric and Planetary Sciences for their funding support in the past five years.

I would like to give special thanks to my family. Even though I am 7,211 miles away from home, my parents have been more than supportive in the past five years. Their love, support and education in the past 29 years have made me into what I am today, and I am proud of my parents. My parents, and my late grandparents, always tell me education is the most important thing for one's career and I am glad I did my best to meet their expectations.

I met and married my best friend and the love of my life, Dr. Xinyue Wang, at West Lafayette. She has made my life at Purdue University much more vivid. I would like to express my thanks to her for her love, encouragement and sacrifices in the past five years.

TABLE OF CONTENTS

LIST OF TABLES

LIST OF FIGURES

ABSTRACT

SO_2 and NO_x ($NO+NO_2$) are important trace gases in the atmosphere as they adversely affect air quality and are precursors to sulfate and nitrate aerosols in the atmosphere. However, there are significant uncertainties in the emission inventories and the atmospheric chemistry processes of both gases. Addressing these uncertainties will help us to 1) better regulate their emissions from anthropogenic activities, 2) understand the formation mechanism of aerosol pollution events, during which rapid accumulation of nitrate and sulfate aerosols are commonly observed, and 3) better constrain the impact of SO_2, NO_x, sulfate aerosols and nitrate aerosols to the global radiation balance. Stable isotopes of nitrogen and sulfur are useful tools in understanding both the origins and chemistry of SO_2 and NO_x since different emission sources usually display distinct sulfur and nitrogen isotopic compositions, and different SO_2 and NO_x oxidation pathways fractionate sulfur and nitrogen isotopes differently. In this dissertation, five studies are conducted to 1) use sulfur isotopes to investigate the sources and chemistry of atmospheric sulfur, and 2) improve our understanding of the isotopic fractionation processes associated with the atmospheric chemistry of reactive nitrogen.

Using stable sulfur isotopes, we first analyzed the sources of sulfate aerosols collected at Baring Head, New Zealand and atmospheric deposition at the Atacama Desert. At Baring Head, we found that the secondary sulfate, i.e., sulfate formed from atmospheric oxidation of SO_2, is mainly observed in fine aerosols (<1 μm) while the sulfate in coarse aerosols (>1 μm) is mostly sea salt sulfate. 73-77% of the secondary sulfate is sourced from biogenic emissions by ocean phytoplankton, and the rest is originated from anthropogenic activities. The sulfate deposition across the Atacama Desert, on the other hand, is a mixture of sea salt sulfate (only near the coast), anthropogenic SO_2 emissions, local soil, and lake salts. Then, sulfur isotopes were used to investigate the formation chemistry of sulfate aerosols collected during a strong winter haze episode in Nanjing, China, where the sources of SO_2 were well-understood. We found that, although the sources of sulfur remain unchanged during the haze episode, the sulfur isotopic compositions of sulfate vary significantly, suggesting isotopic fractionation occurred during the formation of sulfate aerosols. We interpreted the variation using a Rayleigh distillation model to evaluate the contribution of sulfate formation pathways. The model suggested that the Transition

Metal Ion catalyzed O_2 oxidation pathway contributed 49±10% of the total sulfate production, while the O_3/H_2O_2 oxidations accounted for the rest.

Next, we conducted experiments in an atmospheric simulation chamber to determine the isotopic fractionations between NO and NO_2. This isotopic fractionation is controlled by a combination of two factors: 1) the equilibrium isotopic exchange between NO and NO_2 molecules, and 2) the kinetic isotope effects of the NO_x photochemical cycle, namely the Leighton Cycle Isotope Effect (LCIE). Our experiments showed that the fractionation factor during the isotopic exchange is 1.0289±0.0019, and the fractionation factor of LCIE is 0.990±0.005. A model was constructed to assess the relative importance of the two factors, showing the isotopic exchange should be the dominant factor when NO_x >20 ppb, while LCIE should be more important at low NO_x concentrations (<1 ppb) and high rates of NO_2 photolysis. Last, we quantified the overall nitrogen isotopic fractionation during the formation of nitrate aerosols collected at Baring Head, New Zealand. Our results showed that significant and variable (0-15‰) isotopic fractionations occurred during the formation of nitrate aerosols. The isotopic fractionation factors are lower in the summer and higher in the winter, which is mainly caused by seasonal variations in nitrate formation pathways.

Overall, this dissertation first applied stable sulfur isotopes in aerosol samples collected in different environments, demonstrating that isotopes are excellent tools in identifying the origins and chemistry of atmospheric sulfur. Then, we investigated the isotopic fractionation processes during the atmospheric nitrogen chemistry, which can be useful for future studies aimed at understanding the origins and chemistry of atmospheric nitrogen using stable nitrogen isotopes.

CHAPTER 1. INTRODUCTION

1.1 Origins and atmospheric chemistry of NO_x and SO_2

SO_2 and NO_x (NO and NO_2) are two of the most important trace gases in the troposphere. Both gases have long been recognized as air pollutants and precursors to secondary aerosols, i.e., aerosols formed from atmospheric oxidation of gases. In urban regions with high NO_x and SO_2 emissions, they adversely impact air quality and human health; in remote environments, they play important roles in the formation of aerosols, which affect global radiation balance and the climate (IPCC, 2007). NO_x is also a key driver to the tropospheric chemistry since it regulates the concentrations of atmospheric oxidants such as ozone (O_3), an air pollutant, and hydroxyl radicals, which is commonly referred to as "atmospheric detergent" due to its role in removing many atmospheric pollutants (Crutzen, 1979). Both SO_2 and NO_x are originated from multiple natural and anthropogenic sources: SO_2 is emitted by volcanoes, biomass burning, fossil fuel combustion, and marine biological emissions (Dentener et al., 2006; Lamarque et al., 2010), and NO_x is originated from lightning, biomass burning, microbial nitrification, and denitrification, fossil fuel combustions, and transportation activities (Galloway et al., 2008; Reis et al., 2009). In the troposphere, most SO_2 and NO_x are finally oxidized into sulfuric acid and nitric acid via multiple pathways (Seinfeld & Pandis, 2016), then these molecules are either dissolved into droplets creating acid rain or forming secondary aerosols. The atmospheric deposition of sulfate and nitrate also has many harmful ecological effects on soil acidification (Fenn et al., 1998), eutrophication in aquatic systems (Jensen & Andersen, 1992), poor vegetation health (Aber et al., 1989), and biodiversity (Tilman, 1996). However, there are still significant uncertainties in the emission inventories and atmospheric chemistry of SO_2 and NO_x. Constraining these uncertainties can help us better understand their impact on human health, global climate, and ecosystems.

While it is clear that anthropogenic activities, especially fossil fuel combustions, are the main source of SO_2, there still remain some uncertainties in its emission inventory due to the rapid changes in fuel consumption worldwide (Smith et al., 2011). Anthropogenic SO_2 emissions are usually estimated using a bottom-up approach: the amount of SO_2 emitted from a source equals the amount of sulfur contained in the fuel that has been combusted minus the sulfur that is either removed or retained in combustion residuals or products (Smith et al., 2011). This estimation,

although shows a good agreement with observations globally, displays high uncertainties (up to 65% compared to satellite observations) at the regional scale (Liu et al., 2018). Especially, the origins of SO_2 and sulfate in the marine boundary layer are of particular interest due to their essential role in the formation of aerosols and cloud condensation nucleus, which impact the climate (Charlson et al., 1987). The origins of sulfate in the marine boundary layer are a combination of three main sources: sea-salt aerosols, marine biogenic sulfur (mainly oxidation product of marine phytoplankton emitted dimethylsulfide or DMS) and anthropogenic sulfur, which mainly comprise terrestrial sulfur outflow and emissions from international shipping activities (Barnes et al., 2006; Norman et al., 1999). Currently, the emission inventory of international shipping activities and their distributions between northern and southern hemispheres are still poorly quantified (Capaldo et al., 1999; McCoy et al., 2015; Smith et al., 2011). Thus, a better understanding of the sources of atmospheric sulfur in the marine boundary layer is urgently needed.

Similarly, there are significant uncertainties in the sources of NO_x. NO_x emission inventories are also calculated using a bottom-up approach with several assumptions, such as the efficiency of catalytic NO_x reduction technologies and the emission factors of different sources. However, these assumptions sometimes bring significant uncertainties (Zhao et al., 2017), due to the natural degradation of catalytic reduction devices (Fang & DaCosta, 2003), or the uncertainties in the energy statistics (Hong et al., 2017). In addition, NO_x emission from soil microbial activities, i.e., nitrification and denitrification, is even more difficult to quantify. This is mainly because microbial activities are highly sensitive to environmental conditions, including temperature, soil moisture, soil redox condition, pH, and soil nitrogen concentration (Groffman et al., 2009). For example, a recent study (Almaraz et al., 2018) suggested that farmland NO_x emission in the central valley of California is underestimated by a factor of 6-8, which accounts for over 30% of total NO_x emissions in California. Addressing these uncertainties in emission inventories is extremely important not only for the scientific community but also for policy makers as well as the general public.

The oxidations of SO_2 and NO_x into sulfate and nitrate aerosols are complex processes that are still not well-understood. In the troposphere, SO_2 is oxidized into sulfate by two general pathways: 1) gas phase oxidation by hydroxyl radicals (Stockwell & Calvert, 1983), 2) heterogeneous oxidation in cloud droplets (Schwartz, 1986) or on the surface of deliquescent

aerosols (Chameides & Stelson, 1992; Sievering et al., 1991; Song & Carmichael, 1999). However, the latter pathway has many uncertainties because of the numerous possible oxidants and catalysts. In clouds, SO_2 oxidation occurs mainly via H_2O_2 (McArdle & Hoffmann, 1983) but O_3 becomes important at pH>6 (Calvert et al., 1985; Chameides, 1984). Recent research debated on the importance of O_2 oxidation catalyzed by transition metal ions (TMI pathway, Alexander et al., 2009; Brandt & Van Eldik, 1995; Harris et al., 2013; Jacob & Hoffmann, 1983): some studies suggested TMI pathway contributed 9-17% of global secondary sulfate formation, while other studies suggest this pathway may contribute to over half of sulfate production in some regions (Amiri et al., 2018; Harris et al., 2013). NO_2 was also proposed to be an important oxidant during haze events in some Chinese cities (Cheng et al., 2016; Wang et al., 2016) but its importance was still uncertain (Shao et al., 2019; Zhao et al., 2018). Also, oxidations by photochemically important compounds such as NO_3, HNO_4, HOBr, and HOCl need to be better quantified in some environments (Dentener et al., 2002; Feingold et al., 2002; von Glasow et al., 2002; Lee & Schwartz, 1983; Vogt et al., 1996; Warneck, 1999). Addressing these uncertainties is particularly important to improve our understanding of the fast sulfate formation during air pollution events that are currently occurring in many megacities in developing countries with less strict emission control (Huang et al., 2014; Zheng et al., 2015).

Atmospheric chemistry of NO_x is also complicated. In the daytime, photochemical cycling between NO and NO_2 (namely Leighton Cycle) is the key factor regulating the formation of tropospheric O_3 (Leighton, 1961; Seinfeld & Pandis, 2016):

$NO+O_3 \rightarrow NO_2+O_2$

$NO_2+h\nu \rightarrow NO+O(^3P)$

$O+O_2+M \rightarrow O_3+M$

These reactions reach steady state within minutes, producing O_3, then further drive the formation of other radicals such as OH, HO_2, and RO_2, which are important oxidants in the troposphere (Seinfeld & Pandis, 2016). In the daytime, nitric acid (HNO_3) is formed from the oxidation of NO_2 by OH radical (Calvert et al., 1985):

$NO_2+OH \rightarrow HNO_3$

In the nighttime, HNO_3 is formed via:

$NO_2+O_3 \rightarrow NO_3$

$NO_3+\text{hydrocarbon} \rightarrow HNO_3$

$NO_3+NO_2 \rightarrow N_2O_5$

$N_2O_5+H_2O \rightarrow HNO_3$

These reactions produce gas phase HNO_3 (except for $N_2O_5+H_2O$, which occurs on the aerosol surface), then the gas phase HNO_3 can either react with NH_3 to form particulate NH_4NO_3 or directly condense onto existing particles. To date, there are still uncertainties in 1) the relative importance of each pathway to nitrate formation (Wang et al., 2017), and 2) the distribution of nitrogen between nitrate and other organic nitrogen species (Galloway et al., 2008). These uncertainties are at least partially due to the strong spatial and temporal variations of NO_x chemistry. Therefore, to better understand the formation of nitrate aerosols and to better address the impact of anthropogenic activities to air quality and global climate, more work is needed to study the sources and formation chemistry of sulfate and nitrate aerosols.

1.2 Stable isotopes of Nitrogen and Sulfur

The stable isotopic compositions of reactive nitrogen and sulfur in the atmosphere imprinted the information about their sources and atmospheric chemistry, therefore isotopic studies are becoming an important tool in understanding the fate of these molecules (Michalski et al., 2005; Morin et al., 2009; Patris et al., 2007; Walters et al., 2015). The nitrogen and sulfur isotopic compositions of nitrogen and sulfur in samples are normally expressed in delta notation:

$$\delta^{15}N_{sample}\ (‰) = (R_{N,sample}/R_{N,referece}-1)*1000‰$$

$$\delta^{34}S_{sample}\ (‰) = (R_{S,sample}/R_{S,referece}-1)*1000‰$$

In which R_N values represent the $^{15}N/^{14}N$ ratios in sample and reference material, respectively, and R_S values are the $^{34}S/^{32}S$ ratios. The reference materials are air N_2 for $\delta^{15}N$ and Canyon Diablo Troilite for $\delta^{34}S$.

$\delta^{34}S$ values of atmospheric sulfate aerosols can be used to investigate the sources of sulfur as well as the oxidation pathway of SO_2. The $\delta^{34}S$ value of sulfate in sea-salt aerosols is a constant 21.0‰ (Rees et al., 1978), and the $\delta^{34}S$ value of sulfate from atmospheric oxidation of DMS is approximately 18‰ (Amrani et al., 2013; Oduro et al., 2012). Anthropogenic sulfur usually displays much lower $\delta^{34}S$ values ranging from -5‰ to +10‰ (Calhoun & Bates, 1989; Krouse & Grinenko, 1991; Zhu et al., 2016) with an average value of 3‰ (Ghahremaninezhad et al., 2016; Rempillo et al., 2011). This significant difference in $\delta^{34}S$ values between marine and

anthropogenic sulfur can distinguish the sources of sulfate aerosols in marine or coastal environments. In addition, isotopic fractionations occur during atmospheric oxidation of SO_2, which could potentially alter the $\delta^{34}S$ of sulfate, especially when the oxidation is incomplete (Harris et al., 2013; Saltzman et al., 1983). Since the isotopic fractionation factors of most sulfate formation pathways are well-understood (Harris et al., 2012; Harris et al., 2013), this isotopic fractionation could be used to assess the formation pathways of sulfate aerosols.

Different NO_x sources display distinctive $\delta^{15}N$ values but there are still many uncertainties in the isotopic fractionations during the atmospheric oxidation of NO_x. The NO_x originated from coal-fired power plants without selective catalytic reduction technology has $\delta^{15}N$ values of 10±1‰ and can be as high as 20‰ (Felix et al., 2012); other fossil fuel sources, such as gasoline and diesel, emit NO_x with $\delta^{15}N$ values ranging from -20‰ to +5‰ (Walters et al., 2015; Walters et al., 2015); while NO_x originated from biological activities, especially bacterial nitrification and denitrification, show low (-50‰ to -20‰) $\delta^{15}N$ values (Felix & Elliott, 2014; Li & Wang, 2008). These $\delta^{15}N$ values are then imprinted into nitrate in aerosols and precipitations, therefore isotopic analysis is widely used in field observation studies to investigate the sources of NO_x and nitrate (Chang et al., 2018; Geng et al., 2015; Gobel et al., 2013; Hastings et al., 2004; Miller et al., 2017; Morin et al., 2009; Park et al., 2018; Savard et al., 2017; Savarino et al., 2013; Zong et al., 2017). However, the isotopic fractionations during the chemistry of NO_x are highly uncertain (Chang et al., 2018; Walters et al., 2016). The uncertainties are mainly originated from the complex and variable chemistry of atmospheric reactive nitrogen, and the unknown isotopic fractionation factors of each reaction. Significant isotopic fractionations exist in most, if not all, atmospheric nitrogen reactions. The fractionation processes include: 1) the kinetic isotope effect (KIE), which occurs during unidirectional reactions due to the differences in the rate constants between isotopes (Bigeleisen & Wolfsberg, 1957); 2) the equilibrium isotope effect (EIE), which is the isotopic exchange between co-existing molecules (Walters et al., 2016); and 3) photochemistry-induced isotopic fractionation effect (PHIFE), the isotopic fractionation during molecular photolysis (Miller and Yung, 2000). Although previous studies have investigated some of the fractionation factors (Begun & Melton, 1956; Walters et al., 2016; Walters & Michalski, 2015), many of them are still unknown. Therefore, a better quantification of the isotopic fractionation during NO_x oxidation is essential for future field observations to use nitrogen isotopes to investigate the sources and chemistry of NO_x.

1.3 Research objectives

To address the numerous uncertainties in the origins of SO_2 and NO_x, their atmospheric oxidation chemistry, and the formation process of sulfate and nitrate aerosols, this dissertation has the following research objectives:

1. Investigating the sources and size distributions of sulfate aerosols in the Southern Ocean, by analyzing the stable sulfur isotopic composition of sulfate aerosols collected at Baring Head, New Zealand.

2. Characterizing the geochemical characteristics and origins of atmospheric dry deposition across the Atacama Desert, with an emphasis on its soluble inorganic salts, and examine the interannual variations of atmospheric deposition and its linkage to the climate.

3. Evaluating the contributions of SO_2 oxidation pathways to the rapid sulfate formation during a strong haze episode occurred in Nanjing, China in winter 2015 using stable sulfur isotopes.

4. Measuring the nitrogen isotopic fractionation factors of the photochemical reactions between NO and NO_2 by conduction experiments in an atmospheric simulation chamber; then constructing a numerical model for quantifying this isotopic fractionation process.

5. Studying the seasonal variations of nitrate formation processes and quantify its overall isotopic fractionations by analyzing the isotopic compositions of nitrate aerosols collected at Baring Head, New Zealand.

1.4 Outline

This dissertation is composed of 7 chapters, including this introduction and is organized as the following:

Chapter 2: Investigating source contributions of size-aggregated aerosols collected in Southern Ocean and Baring Head, New Zealand using sulfur isotopes. (Published by Li, J., Michalski, G., Davy, P., Harvey, M., Katzman, T., and Wilkins, B. in *Geophysical Research Letters*, **2018**, 45(8), 3717-3727)

Chapter 3: Atmospheric deposition across the Atacama Desert, Chile: compositions, source distributions, and interannual comparisons. (Published by Li, J., Wang, F., Michalski, G., and Wilkins, B. in *Chemical Geology*, **2019**, 525, 435-446)

Chapter 4: Stable sulfur isotopes revealed a major role of transition-metal-ion catalyzed SO_2 oxidation in haze episodes. (Published by Li, J., Zhang, Y., Cao, F., Zhang, W., Fan, M., Lee, X., and Michalski, G. in *Environmental Science & Technology*, **2020**, 54, 2626−2634)

Chapter 5: Quantifying the nitrogen isotope effects during photochemical equilibrium between NO and NO_2: implications for $\delta^{15}N$ in tropospheric reactive nitrogen. (Published by Li, J., Zhang, X., Orlando, J., Tyndall, G., and Michalski, G., in *Atmospheric Chemistry and Physics,* **2020**, 20 (16), 9805-9819)

Chapter 6: Nitrogen isotopes in nitrate aerosols collected at remote boundary layer: implications for nitrogen isotopic fractionations among atmospheric reactive nitrogen species. (Published by Li, J., Davy, P., Harvey, M., Katzman, T., Mitchell, T., & Michalski, G., in *Atmospheric Environment*, **2021**, 245, 118028)

Chapter 7: Conclusions and outlooks

1.5 References

Aber, J. D., Nadelhoffer, K. J., Steudler, P., & Melillo, J. M. (1989). Nitrogen saturation in northern forest ecosystems. *BioScience*, *39*(6), 286–378.

Alexander, B., Park, R. J., Jacob, D. J., & Gong, S. (2009). Transition metal-catalyzed oxidation of atmospheric sulfur: Global implications for the sulfur budget. *Journal of Geophysical Research*, *114*(D2), D02309. https://doi.org/10.1029/2008JD010486

Almaraz, M., Bai, E., Wang, C., Trousdell, J., Conley, S., Faloona, I., & Houlton, B. Z. (2018). Agriculture is a major source of NOx pollution in California. *Science Advances*, *4*(1), eaao3477.

Amiri, N., Ghahremaninezhad, R., Rempillo, O., Tokarek, T. W., Odame-Ankrah, C. A., Osthoff, H. D., & Norman, A.-L. (2018). Stable sulfur isotope measurements to trace the fate of SO 2 in the Athabasca oil sands region. *Atmospheric Chemistry and Physics*, *18*(11), 7757–7780.

Amrani, A., Said-Ahmad, W., Shaked, Y., & Kiene, R. P. (2013). Sulfur isotope homogeneity of oceanic DMSP and DMS. *Proceedings of the National Academy of Sciences of the United States of America*, *110*(46), 18413–8. https://doi.org/10.1073/pnas.1312956110

Barnes, I., Hjorth, J., Mihalapoulos, N., & Mihalopoulos, N. Dimethyl sulfide and dimethyl sulfoxide and their oxidation in the atmosphere, 106 Chemical Reviews § (2006). https://doi.org/10.1021/cr020529+

Begun, G. M., & Melton, C. E. (1956). Nitrogen isotopic fractionation between NO and NO2 and mass discrimination in mass analysis of NO2. *The Journal of Chemical Physics*, *25*(6), 1292–1293.

Bigeleisen, J., & Wolfsberg, M. (1957). Theoretical and experimental aspects of isotope effects in chemical kinetics. *Advances in Chemical Physics*, 15–76.

Brandt, C., & Van Eldik, R. (1995). Transition metal-catalyzed oxidation of sulfur (IV) oxides. Atmospheric-relevant processes and mechanisms. *Chemical Reviews*, *95*(1), 119–190.

Calhoun, J. A., & Bates, T. S. (1989). Sulfur isotope ratios: Tracers of non-sea salt sulfate in the remote atmosphere. ACS Publications.

Calvert, J. G., Lazrus, A., Kok, G. L., Heikes, B. G., Walega, J. G., Lind, J., & Cantrell, C. A. (1985). Chemical mechanisms of acid generation in the troposphere. *Nature*, *317*(6032), 27–35.

Capaldo, K., Corbett, J. J., Kasibhatla, P., Fischbeck, P., & Pandis, S. N. (1999). Effects of ship emissions on sulphur cycling and radiative climate forcing over the ocean. *Nature*, *400*(6746), 743–746. https://doi.org/10.1038/23438

Chameides, W L, & Stelson, A. W. (1992). Aqueous-phase chemical processes in deliquescent sea-salt aerosols: A mechanism that couples the atmospheric cycles of S and sea salt. *Journal of Geophysical Research: Atmospheres*, *97*(D18), 20565–20580.

Chameides, William L. (1984). The photochemistry of a remote marine stratiform cloud. *Journal of Geophysical Research: Atmospheres*, *89*(D3), 4739–4755.

Chang, Y., Zhang, Y., Tian, C., Zhang, S., Ma, X., Cao, F., et al. (2018). Nitrogen isotope fractionation during gas-to-particle conversion of NO x to NO 3− in the atmosphere–implications for isotope-based NO x source apportionment. *Atmospheric Chemistry and Physics*, *18*(16), 11647–11661.

Charlson, R. J., Lovelock, J. E., Andreae, M. O., & Warren, S. G. (1987). Oceanic phytoplankton, atmospheric sulphur, cloud albedo and climate. *Nature*, *326*(6114), 655–661. https://doi.org/10.1038/326655a0

Cheng, Y., Zheng, G., Wei, C., Mu, Q., Zheng, B., Wang, Z., et al. (2016). Reactive nitrogen chemistry in aerosol water as a source of sulfate during haze events in China. *Science Advances*, *2*(12), e1601530.

Crutzen, P. J. (1979). The role of NO and NO2 in the chemistry of the troposphere and stratosphere. *Annual Review of Earth and Planetary Sciences*, *7*(1), 443–472.

Dentener, F, Kinne, S., Bond, T., Boucher, O., Cofala, J., Generoso, S., et al. (2006). Emissions of primary aerosol and precursor gases in the years 2000 and 1750, prescribed data-sets for AeroCom.

Dentener, Frank, Williams, J., & Metzger, S. (2002). Aqueous phase reaction of HNO 4: The impact on tropospheric chemistry. *Journal of Atmospheric Chemistry*, *41*(2), 109–133.

Fang, H. L., & DaCosta, H. F. M. (2003). Urea thermolysis and NOx reduction with and without SCR catalysts. *Applied Catalysis B: Environmental*, *46*(1), 17–34.

Feingold, G., Frost, G. J., & Ravishankara, A. R. (2002). Role of NO3 in sulfate production in the wintertime northern latitudes. *Journal of Geophysical Research: Atmospheres*, *107*(D22).

Felix, J. D., & Elliott, E. M. (2014). Isotopic composition of passively collected nitrogen dioxide emissions: Vehicle, soil and livestock source signatures. *Atmospheric Environment*, *92*, 359–366.

Felix, J. D., Elliott, E. M., & Shaw, S. L. (2012). Nitrogen isotopic composition of coal-fired power plant NO x: influence of emission controls and implications for global emission inventories. *Environmental Science & Technology*, *46*(6), 3528–3535.

Fenn, M. E., Poth, M. A., Aber, J. D., Baron, J. S., Bormann, B. T., Johnson, D. W., et al. (1998). Nitrogen excess in North American ecosystems: predisposing factors, ecosystem responses, and management strategies. *Ecological Applications*, *8*(3), 706–733.

Galloway, J. N., Townsend, A. R., Erisman, J. W., Bekunda, M., Cai, Z., Freney, J. R., et al. (2008). Transformation of the nitrogen cycle: recent trends, questions, and potential solutions. *Science*, *320*(5878), 889–892.

Geng, L., Zatko, M. C., Alexander, B., Fudge, T. J., Schauer, A. J., Murray, L. T., & Mickley, L. J. (2015). Effects of postdepositional processing on nitrogen isotopes of nitrate in the Greenland Ice Sheet Project 2 ice core. *Geophysical Research Letters*, *42*(13), 5346–5354.

Ghahremaninezhad, R., Norman, A.-L., Abbatt, J. P. D., Levasseur, M., & Thomas, J. L. (2016). Biogenic, anthropogenic and sea salt sulfate size-segregated aerosols in the Arctic summer. *Atmos. Chem. Phys*, *16*, 5191–5202. https://doi.org/10.5194/acp-16-5191-2016

von Glasow, R., Sander, R., Bott, A., & Crutzen, P. J. (2002). Modeling halogen chemistry in the marine boundary layer 1. Cloud-free MBL. *Journal of Geophysical Research: Atmospheres*, *107*(D17).

Gobel, A. R., Altieri, K. E., Peters, A. J., Hastings, M. G., & Sigman, D. M. (2013). Insights into anthropogenic nitrogen deposition to the North Atlantic investigated using the isotopic composition of aerosol and rainwater nitrate. *Geophysical Research Letters*, *40*(22), 5977–5982. https://doi.org/10.1002/2013GL058167

Groffman, P. M., Williams, C. O., Pouyat, R. V, Band, L. E., & Yesilonis, I. D. (2009). Nitrate leaching and nitrous oxide flux in urban forests and grasslands. *Journal of Environmental Quality*, *38*(5), 1848–1860.

Harris, E, Sinha, B., Hoppe, P., Crowley, J. N., Ono, S., & Foley, S. (2012). Sulfur isotope fractionation during oxidation of sulfur dioxide: gas-phase oxidation by OH radicals and aqueous oxidation by H 2 O 2 , O 3 and iron catalysis. *Atmos. Chem. Phys. Atmospheric Chemistry and Physics*, *12*, 407–424. https://doi.org/10.5194/acp-12-407-2012

Harris, Eliza, Sinha, B., Van Pinxteren, D., Tilgner, A., Fomba, K. W., Schneider, J., et al. (2013). Enhanced role of transition metal ion catalysis during in-cloud oxidation of SO2. *Science*, *340*(6133), 727–730. https://doi.org/10.1126/science.1230911

Harris, Eliza, Sinha, B., Hoppe, P., & Ono, S. (2013). High-precision measurements of 33S and 34S fractionation during SO2 oxidation reveal causes of seasonality in SO2 and sulfate isotopic composition. *Environmental Science & Technology*, *47*(21), 12174–12183.

Hastings, M. G., Steig, E. J., & Sigman, D. M. (2004). Seasonal variations in N and O isotopes of nitrate in snow at Summit, Greenland: Implications for the study of nitrate in snow and ice cores. *Journal of Geophysical Research: Atmospheres*, *109*(D20).

Hong, C., Zhang, Q., He, K., Guan, D., Li, M., Liu, F., & Zheng, B. (2017). Variations of China's emission estimates: response to uncertainties in energy statistics. *Atmospheric Chemistry and Physics*, *17*(2), 1227–1239.

Huang, R.-J., Zhang, Y., Bozzetti, C., Ho, K.-F., Cao, J.-J., Han, Y., et al. (2014). High secondary aerosol contribution to particulate pollution during haze events in China. *Nature*, *514*(7521), 218.

IPCC, C. (2007). The Fourth Assessment Report of the Intergovernmental Panel on Climate Change. *Geneva, Switzerland*.

Jacob, D. J., & Hoffmann, M. R. (1983). A dynamic model for the production of H+ NO3−, and SO4 2− in urban fog. *Journal of Geophysical Research: Oceans*, *88*(C11), 6611–6621.

Jensen, H. S., & Andersen, F. O. (1992). Importance of temperature, nitrate, and pH for phosphate release from aerobic sediments of four shallow, eutrophic lakes. *Limnology and Oceanography*, *37*(3), 577–589.

Krouse, H. R., & Grinenko, V. A. (1991). Stable isotopes: natural and anthropogenic sulphur in the environment.

Lamarque, J.-F., Bond, T. C., Eyring, V., Granier, C., Heil, A., Klimont, Z., et al. (2010). Historical (1850–2000) gridded anthropogenic and biomass burning emissions of reactive gases and aerosols: methodology and application.

Lee, Y. N., & Schwartz, S. E. (1983). Kinetics of oxidation of aqueous sulfur (IV) by nitrogen dioxide, in precipitation Scavenging, Dry Deposition and Resuspension, Vol. 1, HR Pruppacher, RG Semonin, and W. GN Slinn, eds. Elsevier, New York.

Leighton, P. (1961). *Photochemistry of air pollution*. Elsevier.

Li, D., & Wang, X. (2008). Nitrogen isotopic signature of soil-released nitric oxide (NO) after fertilizer application. *Atmospheric Environment*, *42*(19), 4747–4754.

Liu, F., Choi, S., Li, C., Fioletov, V. E., McLinden, C. A., Joiner, J., et al. (2018). A new global anthropogenic SO2 emission inventory for the last decade: a mosaic of satellite-derived and bottom-up emissions.

McArdle, J. V, & Hoffmann, M. R. (1983). Kinetics and mechanism of the oxidation of aquated sulfur dioxide by hydrogen peroxide at low pH. *The Journal of Physical Chemistry*, *87*(26), 5425–5429.

McCoy, D. T., Burrows, S. M., Wood, R., Grosvenor, D. P., Elliott, S. M., Ma, P.-L., et al. (2015). Natural aerosols explain seasonal and spatial patterns of Southern Ocean cloud albedo. *Science Advances*, *1*(6), e1500157.

Michalski, G., Bockheim, J. G., Kendall, C., & Thiemens, M. (2005). Isotopic composition of Antarctic Dry Valley nitrate: Implications for NOy sources and cycling in Antarctica. *Geophysical Research Letters*, *32*(13).

Miller, D. J., Wojtal, P. K., Clark, S. C., & Hastings, M. G. (2017). Vehicle NOx emission plume isotopic signatures: Spatial variability across the eastern United States. *Journal of Geophysical Research: Atmospheres*, *122*(8), 4698–4717.

Morin, S., Savarino, J., Frey, M. M., Domine, F., Jacobi, H.-W., Kaleschke, L., & Martins, J. M. F. (2009). Comprehensive isotopic composition of atmospheric nitrate in the Atlantic Ocean boundary layer from 65°S to 79°N. *J. Geophys. Res*, *114*. https://doi.org/10.1029/2008JD010696

Norman, A. L., Barrie, L. A., Toom-Sauntry, D., Sirois, A., Krouse, H. R., Li, S. M., & Sharma, S. (1999). Sources of aerosol sulphate at Alert: Apportionment using stable isotopes. *Journal of Geophysical Research: Atmospheres*, *104*(D9), 11619–11631. https://doi.org/10.1029/1999JD900078

Oduro, H., Van Alstyne, K. L., & Farquhar, J. (2012). Sulfur isotope variability of oceanic DMSP generation and its contributions to marine biogenic sulfur emissions. *Proceedings of the National Academy of Sciences of the United States of America*, *109*(23), 9012–6. https://doi.org/10.1073/pnas.1117691109

Park, Y.-M., Park, K.-S., Kim, H., Yu, S.-M., Noh, S., Kim, M.-S., et al. (2018). Characterizing isotopic compositions of TC-C, NO3--N, and NH4+-N in PM2.5 in South Korea: Impact of China's winter heating. https://doi.org/10.1016/j.envpol.2017.10.072

Patris, N., Cliff, S. S., Quinn, P. K., Kasem, M., & Thiemens, M. H. (2007). Isotopic analysis of aerosol sulfate and nitrate during ITCT-2k2: Determination of different formation pathways as a function of particle size. *Journal of Geophysical Research*, *112*(D23), D23301. https://doi.org/10.1029/2005JD006214

Rees, C. E., Jenkins, W. J., & Monster, J. (1978). The sulphur isotopic composition of ocean water sulphate. *Geochimica et Cosmochimica Acta*, *42*(4), 377–381.

Reis, S., Pinder, R. W., Zhang, M., Lijie, G., & Sutton, M. A. (2009). Reactive nitrogen in atmospheric emission inventories. *Atmospheric Chemistry and Physics*, *9*(19), 7657–7677.

Rempillo, O., Seguin, A. M., Norman, A.-L., Scarratt, M., Michaud, S., Chang, R., et al. (2011). Dimethyl sulfide air-sea fluxes and biogenic sulfur as a source of new aerosols in the Arctic fall. *Journal of Geophysical Research*, *116*(D17), D00S04. https://doi.org/10.1029/2011JD016336

Saltzman, E. S., Brass, G. W., & Price, D. A. (1983). The mechanism of sulfate aerosol formation: Chemical and sulfur isotopic evidence. *Geophysical Research Letters*, *10*(7), 513–516. https://doi.org/10.1029/GL010i007p00513

Savard, M. M., Cole, A., Smirnoff, A., & Vet, R. (2017). δ15N values of atmospheric N species simultaneously collected using sector-based samplers distant from sources–Isotopic inheritance and fractionation. *Atmospheric Environment*, *162*, 11–22.

Savarino, J., Morin, S., Erbland, J., Grannec, F., Patey, M. D., Vicars, W., et al. (2013). Isotopic composition of atmospheric nitrate in a tropical marine boundary layer. *Proceedings of the National Academy of Sciences*, *110*(44), 17668–17673. https://doi.org/10.1073/pnas.1216639110

Schwartz, S. E. (1986). Aqueous-phase reactions in clouds. ACS Publications.

Seinfeld, J. H., & Pandis, S. N. (2016). *Atmospheric chemistry and physics: from air pollution to climate change*. John Wiley & Sons.

Shao, J., Chen, Q., Wang, Y., Lu, X., He, P., Sun, Y., et al. (2019). Heterogeneous sulfate aerosol formation mechanisms during wintertime Chinese haze events: air quality model assessment using observations of sulfate oxygen isotopes in Beijing. *Atmospheric Chemistry and Physics*, *19*(9), 6107–6123.

Sievering, H., Boatman, J., Galloway, J., Keene, W., Kim, Y., Luria, M., & Ray, J. (1991). Heterogeneous sulfur conversion in sea-salt aerosol particles: the role of aerosol water content and size distribution. *Atmospheric Environment. Part A. General Topics*, *25*(8), 1479–1487.

Smith, S. J., van Aardenne, J., Klimont, Z., Andres, R. J., Volke, A., & Delgado Arias, S. (2011). Anthropogenic sulfur dioxide emissions: 1850-2005. *Atmospheric Chemistry and Physics*, *11*(3), 1101–1116.

Song, C. H., & Carmichael, G. R. (1999). The aging process of naturally emitted aerosol (sea-salt and mineral aerosol) during long range transport. *Atmospheric Environment*, *33*(14), 2203–2218.

Stockwell, W. R., & Calvert, J. G. (1983). The mechanism of the HO-SO2 reaction. *Atmospheric Environment (1967)*, *17*(11), 2231–2235.

Tilman, D. (1996). Biodiversity: population versus ecosystem stability. *Ecology*, *77*(2), 350–363.

Vogt, R., Crutzen, P. J., & Sander, R. (1996). A mechanism for halogen release from sea-salt aerosol in the remote marine boundary layer. *Nature*, *383*(6598), 327–330.

Walters, W. W., & Michalski, G. (2015). Theoretical calculation of nitrogen isotope equilibrium exchange fractionation factors for various NOy molecules. *Geochimica et Cosmochimica Acta*, *164*, 284–297.

Walters, W. W., Tharp, B. D., Fang, H., Kozak, B. J., & Michalski, G. (2015). Nitrogen isotope composition of thermally produced NO x from various fossil-fuel combustion sources. *Environmental Science & Technology*, *49*(19), 11363–11371.

Walters, W. W., Goodwin, S. R., & Michalski, G. (2015). Nitrogen stable isotope composition (δ15N) of vehicle-emitted NO x. *Environmental Science & Technology*, *49*(4), 2278–2285.

Walters, W. W., Simonini, D. S., & Michalski, G. (2016). Nitrogen isotope exchange between NO and NO2 and its implications for δ15N variations in tropospheric NOx and atmospheric nitrate. *Geophysical Research Letters*, *43*(1), 440–448.

Wang, G., Zhang, R., Gomez, M. E., Yang, L., Levy Zamora, M., Hu, M., et al. (2016). Persistent sulfate formation from London Fog to Chinese haze. *Proceedings of the National Academy of Sciences of the United States of America*, 201616540.

Wang, H., Lu, K., Chen, X., Zhu, Q., Chen, Q., Guo, S., et al. (2017). High N2O5 concentrations observed in urban Beijing: implications of a large nitrate formation pathway. *Environmental Science & Technology Letters*, *4*(10), 416–420.

Warneck, P. (1999). The relative importance of various pathways for the oxidation of sulfur dioxide and nitrogen dioxide in sunlit continental fair weather clouds. *Physical Chemistry Chemical Physics*, *1*(24), 5471–5483.

Zhao, D., Song, X., Zhu, T., Zhang, Z., Liu, Y., & Shang, J. (2018). Multiphase oxidation of SO 2 by NO 2 on CaCO 3 particles. *Atmospheric Chemistry and Physics*, *18*(4), 2481–2493.

Zhao, Y., Zhou, Y., Qiu, L., & Zhang, J. (2017). Quantifying the uncertainties of China's emission inventory for industrial sources: From national to provincial and city scales. *Atmospheric Environment*, *165*, 207–221.

Zheng, B., Zhang, Q., Zhang, Y., He, K. B., Wang, K., Zheng, G. J., et al. (2015). Heterogeneous chemistry: a mechanism missing in current models to explain secondary inorganic aerosol formation during the January 2013 haze episode in North China. *Atmospheric Chemistry and Physics (Online)*, *15*(4).

Zhu, G., Guo, Q., Chen, T., Lang, Y., Peters, M., Tian, L., et al. (2016). Chemical and sulfur isotopic composition of precipitation in Beijing, China. *Environmental Science and Pollution Research*, *23*(6), 5507–5515. https://doi.org/10.1007/s11356-015-5746-2

Zong, Z., Wang, X., Tian, C., Chen, Y., Fang, Y., Zhang, F., et al. (2017). First assessment of NO x sources at a regional background site in North China using isotopic analysis linked with modeling. *Environmental Science & Technology*, *51*(11), 5923–5931

CHAPTER 2. INVESTIGATING SOURCE CONTRIBUTIONS OF SIZE-AGGREGATED AEROSOLS COLLECTED IN SOUTHERN OCEAN AND BARING HEAD, NEW ZEALAND USING SULFUR ISOTOPES

This chapter is a reprint from a published article (Li, J., Michalski, G., Davy, P., Harvey, M., Katzman, T., & Wilkins, B. (2018). Investigating Source Contributions of Size-Aggregated Aerosols Collected in Southern Ocean and Baring Head, New Zealand Using Sulfur Isotopes. *Geophysical Research Letters*, *45*(8), 3717-3727).

Abstract

Marine sulfate aerosols in the Southern Ocean are critical to the global radiation balance, yet the sources of sulfate and their seasonal variations are unclear. We separately sampled marine and ambient aerosols at Baring Head, New Zealand for one year using two collectors, and evaluated the sources of sulfate in coarse (1-10 μm) and fine (0.05-1 μm) aerosols using sulfur isotopes ($\delta^{34}S$). In both collectors, sea-salt sulfate ($SO_4^{2-}{}_{SS}$) mainly existed in coarse aerosols and non-sea-salt sulfate ($SO_4^{2-}{}_{NSS}$) dominated the sulfate in fine aerosols, although some summer $SO_4^{2-}{}_{NSS}$ appeared in coarse particles due to aerosol coagulation. $SO_4^{2-}{}_{NSS}$ in the marine aerosols was mainly (88-100%) from marine biogenic dimethylsulfide (DMS) emission, while the $SO_4^{2-}{}_{NSS}$ in the ambient aerosols was a combination of DMS (73-79%) and SO_2 emissions from shipping activities (~21-27%). The seasonal variations of $SO_4^{2-}{}_{NSS}$ concentrations inferred from the $\delta^{34}S$ values in both collectors were mainly controlled by the DMS flux.

2.1 Introduction

Sulfate is one of the major inorganic components in aerosols and is essential to aerosol nucleation and accumulation processes (Andronache et al., 1997; Kulmala et al., 2000), which greatly affect Earth's radiation budget. However, the impact of sulfate aerosols to the radiation budget is still poorly quantified (IPCC, 2007), partly because the sources and fluxes of sulfate show strong spatial and seasonal variations. In the marine boundary layer, sulfate aerosols consist of primary and secondary sulfate. Primary sulfate, i.e., sea-salt sulfate ($SO_4^{2-}{}_{SS}$) is formed via sea-spray and air bubble bursting at the ocean surface (Lewis and Schwartz, 2004; O'Dowd et al., 2007); its size distribution and flux are controlled by wind speed, wave height and other

meteorological conditions (Gong, 2003; Lewis and Schwartz, 2004; Van Eijk et al., 2011). Non-sea-salt sulfate ($SO_4^{2-}{}_{NSS}$), also called secondary sulfate, is formed via atmospheric oxidation of S, the sources of which are 1) dimethylsulfide ($SO_4^{2-}{}_{DMS}$) emitted by marine phytoplankton (Barnes et al., 2006); 2) natural terrestrial S emission ($SO_4^{2-}{}_{nat}$), including sulfate from SO_2 emitted by volcanic and terrestrial biological activities; or 3) anthropogenic S emissions ($SO_4^{2-}{}_{anth}$). In the mid-latitudes of the Southern Ocean (~35-45°S), $SO_4^{2-}{}_{DMS}$ is thought to play a critical role in the cloud physics and climate by controlling the number of cloud condensation nuclei (CCN), resulting in strong reflection of solar radiation in the summer when the DMS flux is high (Ayers and Gras, 1991, Boers et al., 1994, Korhonen et al., 2008, McCoy et al., 2015). However, the sources, size distributions and seasonal variations of the Southern Ocean sulfate are not well understood, which limits our ability to predict its response to the changing climate.

Previous studies have investigated the sources and size distributions of marine sulfate aerosols in several locations (Calhoun and Bates, 1989; Calhoun et al., 1991; Norman et al., 1999; Novák et al., 2001; Faloona, 2009; Rempillo et al., 2011; Seguin et al., 2011; Ghahremaninezhad et al., 2016), however, several questions remain unanswered. First, substantial amounts of $SO_4^{2-}{}_{NSS}$ had been observed in the coarse aerosols (1-16 μm) sampled at Baring Head originating from the biologically productive sub-tropical frontal region of the Chatham Rise (Sievering et al., 2004), suggesting $SO_4^{2-}{}_{NSS}$ was mainly formed on coarse sea-salt particles. This is in contrast with observations in the Northern Hemisphere (Norman et al., 1999; Rempillo et al., 2011; Seguin et al., 2011; Ghahremaninezhad et al., 2016) and modelling results (Alexander et al., 2005), all of which suggested $SO_4^{2-}{}_{NSS}$ should mainly distributed in the fine particles (<1 μm). Second, the contribution of anthropogenic emission to the Southern Ocean sulfate is uncertain. Capaldo et al., (1999) suggested that international shipping emission, which is the main anthropogenic sulfur source in mid-latitude Southern Ocean (~40°S) contributes to ~5% to 20% of total sulfate, while McCoy et al. (2015) showed a higher anthropogenic contribution of 20%-35% at 40°S. Third, the observed seasonal variations of Southern Ocean sulfate (e.g., Udisti et al., 2012; McCoy et al., 2015) were unexplained and difficult to predict because the variation of each sulfate source was unknown.

Geochemical and sulfur isotopic analysis are useful tools in determining the sources of sulfate. Cation and anion analyses are useful in partitioning between $SO_4^{2-}{}_{SS}$ and $SO_4^{2-}{}_{NSS}$ and changes in the sulfur isotopic composition ($\delta^{34}S$) can help in differentiate SO_4^{2-} sources: $\delta^{34}S$ of

$SO_4^{2-}{}_{SS}$ ($\delta^{34}S_{SS}$) is a constant +21‰ (Rees et al., 1978), $\delta^{34}S$ values of DMS range between +15‰ - +19‰ (Krouse and Grinenko, 1991; Oduro et al., 2012; Amrani et al., 2013), while most anthropogenic and terrestrial sulfate display much lower $\delta^{34}S$ values between -5‰ to +10‰ (Sakai et al., 1982; Calhoun et al., 1991; Krouse and Grinenko, 1991; McCardle et al., 1998; Zhu et al., 2016). In this work, a full-year sampling campaign was conducted to collect size-segregated aerosols derived from the marine sector (sub-tropical frontal region and the Southern Ocean) and all-sector (ambient environment) at Baring Head, New Zealand (41.4°S, 174.9°E, Figure 2.1). Geochemical and sulfur isotopic analysis were used to investigate S sources and their seasonal variations.

2.2 Methods

The aerosol sampling campaign spanned from 6/30/2015 to 8/11/2016 and sampled both marine and ambient air. Two high-volume samplers equipped with Cascade Impactors were set up on a 15-meter tower at Baring Head, New Zealand (Figure 2.1),where the metrological conditions were measured, to collect coarse (1-10 μm) and fine aerosols (0.05-1.0 μm) at a flow rate of ~1 m^3/min. Cellulose filters were used to minimize ion contamination (especially Na^+ and SO_4^{2-}), which were tested using eight blanks and resulted in $[Na^+] < 0.6\%$ of average the $[Na^+]$ in the field samples (e.g. <0.05 nmol/m^3). One of the collectors (marine collector, set on top of the tower) was configured to sample oceanic air masses by only collecting when the average southerly (onshore) wind speed was above 5 m/s for at least 30 minutes. Filters on this collector were replaced after 100 to 150 hours of collection to acquire enough sample (every two to six weeks). The ambient collector sampled air mass regardless of the wind direction, and filters were replaced every 7 days (154 hours). Previous studies (Dorling et al., 1992; Steinkamp et al., 2017) confirmed the origins of the collected aerosols using cluster analysis (Figure 2.1) showing aerosols in the marine collector originated from the oceanic sector of the sub-tropical front/Chatham Rise (red shaded area), while the aerosols in the ambient collector were from both the ocean and the New Zealand mainland (blue lines). Meantime, a wave buoy off the coast was used to measure the wave peak height. The filters were carefully sealed and shipped to Purdue Stable Isotope (PSI) Laboratory. All the exposed cellulose filters were weighted to calculate the aerosol mass before further portioning and analysis. The filters were then sealed into Ziploc bags, labelled and shipped to Purdue University. Each filter was soaked into 100 mL deionized water and well-shook to

completely dissolve all inorganic salts. The solutions were then filtered by 0.2 um filter to remove any microbes and filter paper fibers.

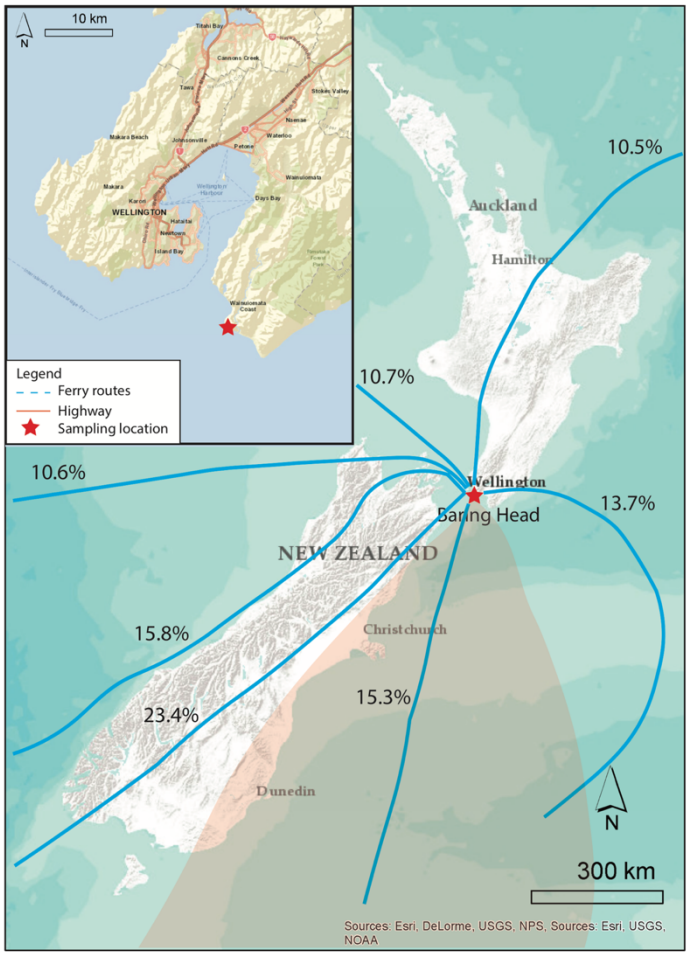

Figure 2.1 Sampling location and result of air parcel 4-day back trajectory of air mass arriving at Baring Head. Blue lines and the numbers above indicate the mean path and percentage of air mass from each cluster; red shaded area indicates the envelope of all trajectories during southerly wind, modified from Steinkamp et al., (2017).

Standard methods were used to analyse cations (ICP-OES), anions (IC) and sulfur isotopic compositions of sulfate (IRMS). Cation (Na^+, K^+, Ca^{2+}, Mg^{2+}) analysis was accomplished in the Purdue Rare Isotope Measurement (PRIME) Laboratory at Purdue University. A 5-mL aliquot of each solution was mixed with 5-mL 10% AR HNO_3, then analyzed by ICP-OES (Thermo Scientific, Pittsburgh, PA, USA). The Standard Error is ±2%. Another aliquot of each solution was used to carry out the anion (Cl^-, NO_3^-, SO_4^{2-}) analysis in the Purdue Stable Isotope (PSI) Laboratory by a Dionex DX-500 Ion Chromatography (Dionex Corp., Sunnyvale, CA, USA). The Standard Error is ±5%. Sulfur isotopic analysis of the sulfate is accomplished at the Purdue Stable Isotope (PSI) Laboratory. 0.5 mL of 5% acidified $BaCl_2$ is added into 5 ml of each solution to completely precipitate sulfate. $BaSO_4$ is then extracted, dried, weighted, mixed with V_2O_5, and combusted at 980 °C in a Costech Elemental Analyzer. The product SO_2 was then directed to an IRMS equipped with a Conflow for isotopic analysis. The sulfur isotopic compositions are reported in delta notation: $\delta^{34}S = (({}^{34}S/{}^{32}S)_{sample}/({}^{34}S/{}^{32}S)_{reference}-1)*1000‰$, in which the reference material is Vienna-Canyon Diablo Troillite (VCDT). The Standard Deviation of sulfur isotopic analysis is ±0.1‰.

The concentrations of $SO_4^{2-}{}_{SS}$ were calculated using the seawater $[SO_4^{2-}]/[Na^+]$ molar ratio (0.058) and the measured Na concentrations: $[SO_4^{2-}{}_{SS}] = 0.058*[Na^+]$ (Keene et al., 2007). The residual sulfate was considered $SO_4^{2-}{}_{NSS}$. This assumes sodium is a conservative element, seawater is its sole source, and it is insensitive to chemical or biological loss (Keene et al., 1986).

2.3 Results and discussion

2.3.1 Distribution of sea-salt and non-sea-salt sulfate in coarse and fine aerosols

Sulfate in coarse aerosols was mainly $SO_4^{2-}{}_{SS}$ and $SO_4^{2-}{}_{NSS}$ was found primarily in the fine aerosol fraction, which was in contrast with a previous study at Baring Head (Sievering et al., 2004). Coarse aerosol sulfate concentrations in the two collectors were similar (8.8 ± 1.9 nmol/m^3 in marine collector and 8.1 ± 3.8 nmol/m^3 in ambient collector), which is remarkably close to a previous study at Baring Head that averaged 8.3 nmol/m^3 (Sievering et al., 2004). $SO_4^{2-}{}_{SS}$ accounted for 88±5% of the coarse aerosol sulfate (Figure 2.2 A, B), but the contribution of $SO_4^{2-}{}_{NSS}$ in the course mode slightly increased during the summer (discussed below). In contrast, fine particle sulfate concentrations were lower, (averaging 1.7 nmol/m^3 in marine collector and 2.7 nmol/m^3 in ambient collector), and $SO_4^{2-}{}_{SS}$ accounted for only ~16±1% of total sulfate, the remaining 84±1% was $SO_4^{2-}{}_{NSS}$. This general $SO_4^{2-}{}_{SS}$ distribution pattern was similar to the distribution previously observed at Baring Head by Sievering et al. (2004), but in that study only 53% of coarse aerosol sulfate was attributed to $SO_4^{2-}{}_{SS}$ compared to this study's 88%. They also suggested coarse aerosol sulfate accounted for 81% of total $SO_4^{2-}{}_{NSS}$ while our results showed a much lower contribution of ~24-36%.

The discrepancy in $SO_4^{2-}{}_{NSS}$ distribution could be attributed to either 1) differences in sampling conditions or 2) differences in $SO_4^{2-}{}_{SS}$ estimation. Sievering et al. (2004) suggested that under clear sky conditions, pH buffering by excess calcium provided from coccolithophores fragments could enhance the effectiveness of ozone mediated oxidation in sea-salt aerosol droplets, leading to greater coarse mode $SO_4^{2-}{}_{NSS}$. In this work, aerosols from both clear and cloudy conditions were sampled therefore this mechanism was likely less important and results in lower coarse mode $SO_4^{2-}{}_{NSS}$. Alternatively, the discrepancy may be due to our use of aerosol $[Na^+]$ to estimate $SO_4^{2-}{}_{SS}$ rather than $[Mg^{2+}]$ used by Sievering et al. (2004). Sodium is the most widely used conservative tracer of sea-salt (Norman et al., 1999; Udisti et al., 2016; Lin et al., 2017)

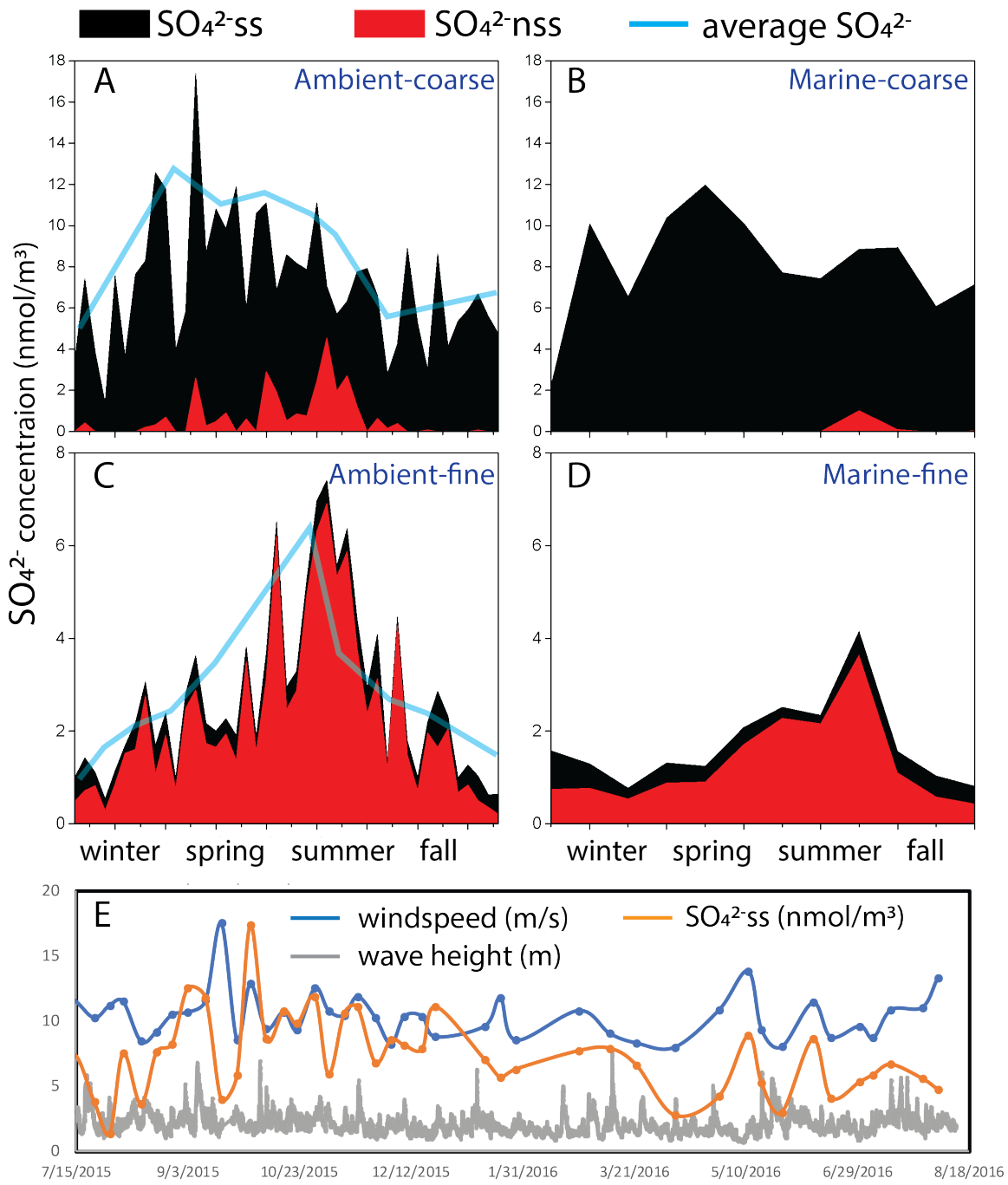

Figure 2.2 A, B, C, D: $SO_4^{2-}{}_{SS}$ (black), $SO_4^{2-}{}_{NSS}$ (red) concentrations in coarse and fine aerosols from ambient and marine collectors; blue lines in panels A and C are averaged (to fit the marine collector sampling window) total sulfate concentrations. E: wind speed, wave height and coarse $SO_4^{2-}{}_{SS}$ concentrations in ambient collector.

because 1) it has a high concentration in the seawater, 2) non-marine sodium inputs are trivial in most places (McInnes et al., 1994) and 3) it is insensitive to secondary alterations. Sievering et al.

(2004) used $[Mg^{2+}]$ to calculate $SO_4^{2-}{}_{SS}$ fraction because of abnormally high $[Na^+]/[Cl^-]$ and $[Na^+]/[Mg^{2+}]$ ratios in their aerosols that they attributed to either contamination by filter blanks or possible contributions of sodium in soil. Likewise, $[Mg^{2+}]$ has been used to estimate $SO_4^{2-}{}_{SS}$ in aerosols collected at Cape Grim, Tasmania and La Jolla, California because sodium from either filter blanks or soil was believed to be significant (Cainey et al., 1999; Hill-Falkenthal et al., 2012; Priyadarshi et al., 2012). The cellulose filters used in this study had a very low Na^+ blank relative to typical glass fiber filters (Dams et al., 1972) and Southern Ocean derived air masses should have minimal terrestrial influence Baring Head. Further, the coarse aerosol $[Mg^{2+}]/[Na^+]$ in both of our collectors averaged at 0.111±0.005, much higher than the 0.05 ratio determined by Sievering et al. (2004) and very close to the seawater ratio of 0.11 (Keene et al., 2007), indicating minimal contribution of sodium from either soil or filter blank. Furthermore, the low $[Mg^{2+}]/[Na^+]$ ratio observed by Sievering et al., (2004) may be a consequence of biased $[Mg^{2+}]$ measurements. A recent study has observed that sea-spray Mg^{2+} and Ca^{2+} forms complexes with lipids, fatty acids and saccharides (Jayarathne et al., 2016) during sea-salt aerosol formation, potentially biasing $[Mg^{2+}]$ analyzed by ion chromatography (Sievering et al., 2004). Using ICP-OES to analyze $[Mg^{2+}]$ does not require it to be in ionic form, so could be a more accurate measure of $[Mg^{2+}]/[Na^+]$ in the sea-salt aerosols given the possibility of complexation and provides confidence in the accuracy of the $SO_4^{2-}{}_{SS}$ presented here.

The size distribution patterns of $SO_4^{2-}{}_{SS}$ and $SO_4^{2-}{}_{NSS}$ agrees with other field observations and atmospheric modeling results, indicating $SO_4^{2-}{}_{NSS}$ is the main sulfur source in CCN. Observations in the North Atlantic, Arctic, and Pacific Ocean have suggested similar distribution patterns, of which >90% of $SO_4^{2-}{}_{SS}$ was distributed in coarse aerosols and >60% of $SO_4^{2-}{}_{NSS}$ was in fine aerosols (Murphy et al., 1998; Norman et al., 1999; Rempillo et al., 2011; Seguin et al., 2011; Ghahremaninezhad et al., 2016). Therefore, we suggest in the Southern Ocean $SO_4^{2-}{}_{NSS}$ was also the main sulfate source of CCN, since CCN are usually < 0.2 μm (Hudson and Noble, 2006). Additionally, we noticed coarse aerosol $SO_4^{2-}{}_{NSS}$ was observed when the total $SO_4^{2-}{}_{NSS}$ concentrations ($SO_4^{2-}{}_{NSS\text{-}coarse}$+$SO_4^{2-}{}_{NSS\text{-}fine}$) exceeded 2.0 nmol/m^3. This indicates higher $SO_4^{2-}{}_{NSS}$ concentrations helped coagulation form larger $SO_4^{2-}{}_{NSS}$ particles. Further experiments and field sample analysis should take place to quantify the relationship between $SO_4^{2-}{}_{NSS}$ concentration and their size distribution.

The variations in $SO_4^{2-}{}_{SS}$ concentrations were attributed to variations in wind speed and wave heights at Baring Head. Early studies have suggested the mass concentration of sea-salt aerosols is positively correlated to wind speed (O'Dowd and Smith, 1993; O'Dowd et al., 1997), however recent studies had suggested other physical conditions, such as whitecap coverage and wave peak height on the coast are also important (Mårtensson et al., 2003; Lewis and Schwartz, 2004; Clarke et al., 2006; O 'Dowd et al., 2007). Our observed $SO_4^{2-}{}_{SS}$ concentrations only showed a weak correlation with the average wind speed ($P>0.05$, $R^2=0.03$, Figure 2.2e) similar to other field studies (Lewis and Schwartz, 2004; Jaeglé et al., 2011; Rempillo et al., 2011; Seguin et al., 2011; Ghahremaninezhad et al., 2016). In contrast, maximums in wave peak heights usually corresponded to high $SO_4^{2-}{}_{SS}$ concentrations at Baring Head (Figure 2.2e) supporting the hypothesis that breaking waves increase sea-salt aerosol formation near the coast (Van Eijk et al., 2011; Monahan et al., 1986; Jensen et al., 1997). Therefore, we suggest wave height was a more important than wind speed, under low median wind speeds (9.9 ± 3.9 m/s), in generating sea-salt aerosols at Baring Head during the study period.

2.3.2 Sources and seasonal variations of $SO_4^{2-}{}_{NSS}$ in the marine collector

The sulfur isotopic compositions of sulfate also indicated a mixture of $SO_4^{2-}{}_{SS}$ and $SO_4^{2-}{}_{NSS}$. The $\delta^{34}S$ values of total sulfate ($SO_4^{2-}{}_{SS}$+ $SO_4^{2-}{}_{NSS}$) were interpreted using a two-endmember isotope mixing model (Figure 2.3a): $SO_4^{2-}{}_{SS}$ with $\delta^{34}S$ value that is the same (+21‰) as seawater (Rees et al., 1978) and $SO_4^{2-}{}_{NSS}$ with lower $\delta^{34}S$ value(s). Most coarse aerosol sulfate had $\delta^{34}S$ values near the seawater endmember, indicating the coarse aerosol sulfate was predominately composed of $SO_4^{2-}{}_{SS}$, which supports our $SO_4^{2-}{}_{SS}$ estimates using $[Na^+]$. In contrast, the fine aerosol had lower $\delta^{34}S$ values (+11‰ - +21‰), suggesting a higher proportion of $SO_4^{2-}{}_{NSS}$ relative to the coarse aerosols.

The $\delta^{34}S$ values of $SO_4^{2-}{}_{NSS}$ ($\delta^{34}S_{NSS}$) can give insight into the origin of $SO_4^{2-}{}_{NSS}$ sources. The $\delta^{34}S_{NSS}$ values were calculated using $\delta^{34}S_{NSS} = (\delta^{34}S_{bulk}-(1-SO_4^{2-}{}_{NSS}\%)*+21‰)/SO_4^{2-}{}_{NSS}\%$, where $SO_4^{2-}{}_{NSS}\%$ is the fraction of $SO_4^{2-}{}_{NSS}$ (using $[Na^+]$), the +21‰ is the $\delta^{34}S$ value of seawater sulfate, and $\delta^{34}S_{bulk}$ is the $\delta^{34}S$ value of the total aerosol sulfate. The calculated $\delta^{34}S_{NSS}$ values ranged from +6‰ to +19‰ (Figure 2.3). $\delta^{34}S_{NSS}$ values in the marine collector range from +15‰ - +19‰ (Figure 2.3b), which is the same range previously observed in $\delta^{34}S_{DMS}$ (Krouse and

Grinenko, 1991; Patris et al., 2002; Wadleigh, 2004; Sanusi et al., 2006). This indicates that $SO_4^{2-}{}_{DMS}$ was the dominant source of $SO_4^{2-}{}_{NSS}$ in the marine collector. The ambient aerosol $\delta^{34}S_{NSS}$ values were as low as +6‰, which cannot be explained by oxidation of DMS, and points to non-marine sulfur sources. The main anthropogenic S sources in the region are international and local shipping activity (Capaldo et al., 1999; McCoy et al., 2015) and the $\delta^{34}S$ value of sulfur derived from ships has been estimated to be +3‰ (Patris et al., 2000; Rempillo et al., 2011). Likewise, the $\delta^{34}S$ values of sulfate derived from terrestrial sulfur sources near Baring Head also has been estimated to be +3‰ (discussed below). Thus, the range of Baring Head $SO_4^{2-}{}_{NSS}$ values are interpreted as a second mixture of $SO_4^{2-}{}_{DMS}$ (Calhoun et al., 1991; Krouse and Grinenko, 1991; Patris et al., 2002; Sanusi et al., 2006) and $SO_4^{2-}{}_{anth}$ whose fractions (f_{DMS}, f_{anth}) can be quantified using a simple two endmember isotope mixing model: $\delta^{34}S_{NSS} = f_{DMS}*\delta^{34}S_{DMS} + f_{anth}*\delta^{34}S_{anth}$. Using this mixing model, we can first estimate the f_{DMS} and f_{anth} (given in %) in the marine collector.

The high $\delta^{34}S_{NSS}$ values (Figure 2.2b) of marine $SO_4^{2-}{}_{NSS}$ indicates that it was primarily (88-100%) $SO_4^{2-}{}_{DMS}$ and only 0-12% was $SO_4^{2-}{}_{anth}$. To estimate the upper limit of f_{anth}, we assume a constant $\delta^{34}S_{DMS}$ endmember of +19‰ (Wadleigh, 2004), and the $\delta^{34}S_{anth}$ endmember was from ship emissions with $\delta^{34}S$ =+3‰. The variation of $\delta^{34}S_{NSS}$ can be solely attributed to changing in f_{anth} and the calculated upper limit of f_{anth} is ~12%. This $SO_4^{2-}{}_{anth}$ contribution to $SO_4^{2-}{}_{NSS}$ is much lower than the 20-35% estimated by (McCoy et al., 2015), but in agreement with the 5-20% estimated by (Capaldo et al., 1999). However, this calculation assumed the $\delta^{34}S_{DMS}$ was a constant +19‰ and ignored the observed +15‰ - +19‰ range in other studies (Krouse and Grinenko, 1991; Patris et al., 2002; Wadleigh, 2004; Sanusi et al., 2006). This 4‰ variation in $\delta^{34}S_{DMS}$ values is thought to be caused by a combination of 1) variation of isotopic fractionation during SO_2 oxidized to sulfate ($\delta^{34}S_{sulfate}$-$\delta^{34}S_{SO2}$, Harris et al., 2012, 2013) and 2) the $\delta^{34}S$ of DMS gas could slightly vary (Amrani et al., 2013). If we consider the $\delta^{34}S_{DMS}$ variation, then the contribution of anthropogenic S in marine aerosols could be as low as zero at Baring Head. This 0-12% anthropogenic S contribution to the $SO_4^{2-}{}_{NSS}$ budget is significantly lower than the estimates of 30-70% in the Northern Atlantic Ocean and other Pacific Ocean sites (Capaldo et al., 1999; Patris et al., 2000; Yang et al., 2017). We suggest this lower anthropogenic sulfate fraction in $SO_4^{2-}{}_{NSS}$ at Baring Head is due to significantly lower sulfur emission in the Southern Hemisphere (IEA, 2014),

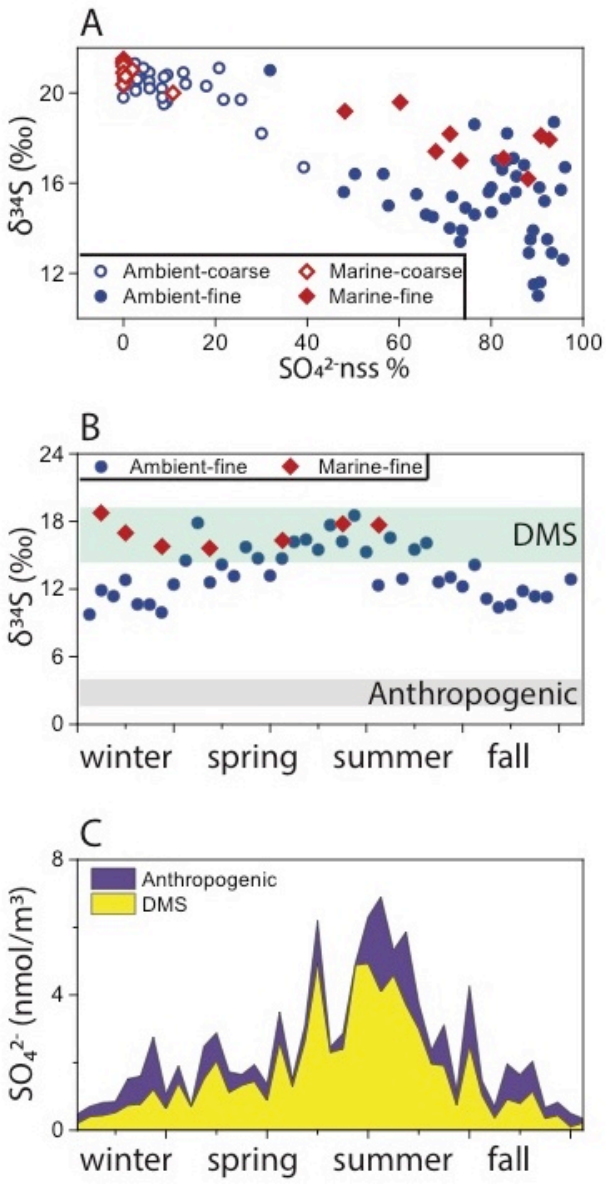

Figure 2.3 A) $\delta^{34}S$ distribution of all samples, showing a mixing of $SO_4^{2-}{}_{SS}$ and $SO_4^{2-}{}_{NSS}$; B) the $\delta^{34}S_{NSS}$ values of ambient and marine fine sulfate; horizontal bars indicate the $\delta^{34}S$ values of each endmember; C) estimated anthropogenic and DMS contribution to $SO_4^{2-}{}_{NSS}$ in ambient fine sulfate.

fewer shipping routes in the Southern Hemisphere, thus minimal influence of ship sulfur emissions (Paxian et al., 2010), and poor inter-hemispheric mixing of sulfate that minimizes the influence of the Northern Hemisphere sulfur emissions at Baring Head (Capaldo et al., 1999).

The observed seasonal variation of $SO_4^{2-}{}_{NSS}$ in the marine collector (Figure 2.2d), which was primarily from DMS emissions, must be controlled by seasonal changes in the DMS flux. Baring Head's average summer $SO_4^{2-}{}_{DMS}$ concentration was ~2.7 nmol/m^3, while winter concentrations averaged at 0.6 nmol/m^3 (Figure 2.2d), similar to the $SO_4^{2-}{}_{DMS}$ concentrations observed in Arctic, Southern Pacific and Northern Atlantic Ocean (Allen et al., 1997; Quinn et al., 2009; Rempillo et al., 2011; Seguin et al., 2011; Ghahremaninezhad et al., 2016; Huang et al., 2017). The observed average summer $SO_4^{2-}{}_{DMS}$ concentration was ~4.5 times higher than the winter $SO_4^{2-}{}_{DMS}$, which agrees with the recent observation of dissolved seawater DMS concentration by Lana et al. (2011) who showed at least a 4-fold higher concentration of dissolved DMS in the austral summer compared to winter. In addition, Law et al. (2017) discussed evidence suggesting this seasonal variation presented by Lana et al. (2011) also occurred in the waters offshore of New Zealand. Therefore, since $SO_4^{2-}{}_{DMS}$ was the main source of fine sulfate particles,

the seasonal variation of $SO_4^{2-}{}_{DMS}$ could explain the 300% increase of CCN in the summer observed by Ayers et al. (1991).

2.3.3 Sources and seasonal variations of $SO_4^{2-}{}_{NSS}$ in the ambient collector

The ambient aerosol $\delta^{34}S_{NSS}$ values were lower than the marine aerosol $\delta^{34}S_{NSS}$ and displayed a distinct seasonal trend, indicating changing contribution of anthropogenic sulfur over the year (Figure 2.3b). The ambient aerosol $\delta^{34}S_{NSS}$ values (+6‰ - +18‰) were close to those of marine aerosols during the summer suggesting the $SO_4^{2-}{}_{NSS}$ was also dominated by DMS during the summer months. In contrast, the $\delta^{34}S_{NSS}$ values in the winter were significantly lower (Figure 2.3b) than in the marine aerosols, suggesting $SO_4^{2-}{}_{nat}$ and/or $SO_4^{2-}{}_{anth}$ input (e.g., Calhoun et al., 1991; Patris et al., 2000; Rempillo et al., 2011; Ghahremaninezhad et al., 2016). Potential terrestrial sulfur sources include terrestrial biogenic emissions, volcanic emissions and anthropogenic emissions. Terrestrial biogenic sulfur should be a minor contributor because the estimated biogenic sulfur flux ($<1x10^5$ mol/day) in New Zealand (Bates et al., 1992) is small compared to $1x10^6$ mol/day anthropogenic emission from Wellington, which is adjacent to the Baring Head site (Ministry of the Environment, 2004). The volcanic activity should also be minor at Baring Head since the nearest volcano and geothermally active regions with H_2S emission are ~300 km away, and there was no significant volcanic activity during our sampling period (GeoNet volcanic emission database). Therefore, $SO_4^{2-}{}_{nat}$ is likely small, and $SO_4^{2-}{}_{anth}$ were likely the main non-marine sulfur sources (Wilton et al., 2008) of $SO_4^{2-}{}_{NSS}$ in the ambient collector. 82% of anthropogenic sulfur emissions in the Wellington region were from commercial shipping (Ministry of the Environment, 2004) that uses low-grade fuel oil. Early study showed that the $\delta^{34}S$ values of fuel oil center around 5‰ (Nielsen, 1974), recent measurements of ship emissions also have $\delta^{34}S$ value of +3‰±3‰ (Patris et al., 2000; Rempillo et al., 2011). Other anthropogenic sources, such as coal burning and industrial fossil fuel combustions, also showed $\delta^{34}S$ values of +3‰±3‰ (e.g., Proemise and Mayer, 2012, Gorka et al., 2017). Rainwater sulfate collected at Gracefield, a semi-industrial district ~25 km inland from Baring Head and Wellington, had $\delta^{34}S$ values of ~+3±5‰ (Mizutani and Rafter, 1969), which was consistent with the endmembers. Thus, the ambient aerosol $\delta^{34}S_{anth}$ endmember was estimated to be ~+3‰ and the $\delta^{34}S_{NSS}$ in the ambient collector

can be again interpreted as a mixing between $SO_4^{2-}{}_{anth}$ and $SO_4^{2-}{}_{DMS}$ using same isotope mixing model (above).

The f_{anth} values varied within and by season: ~40-60% in the winter, ~20-40% in the spring and fall, and 0-20% in the summer. The $SO_4^{2-}{}_{anth}$ concentrations (f_{anth}*[$SO_4^{2-}{}_{NSS}$]) range from 0-2.5 nmol/m^3, with an annual average of 0.6 nmol/m^3, accounted for 27% of total $SO_4^{2-}{}_{NSS}$. Then, assuming the $SO_4^{2-}{}_{NSS}$ in the marine collector was purely derived from DMS, the $\delta^{34}S_{NSS}$ in the marine collector can be used as the $\delta^{34}S_{DMS}$ in the equation. Under this situation, the f_{anth} values were ~40-50% in the winter, ~5-20% in the spring and fall, and 0-15% in the summer (Figure 2.3c). The annual average f_{anth} was 21%. Therefore, we suggest the $SO_4^{2-}{}_{anth}$ accounted for 21-27% of total $SO_4^{2-}{}_{NSS}$ at Baring Head. Davy (2007) and Davy et al. (2008, 2012) had also observed similar $SO_4^{2-}{}_{NSS}$ concentrations and seasonal variations at Lower Hutt, a coastal town ~20 km from Baring Head, but the contribution of $SO_4^{2-}{}_{DMS}$ were unexamined. We suggest their $SO_4^{2-}{}_{NSS}$ sources were similar to our results: $SO_4^{2-}{}_{DMS}$ contributed >70% of total $SO_4^{2-}{}_{NSS}$, and $SO_4^{2-}{}_{anth}$ accounted for the rest.

The anthropogenic sulfate contributions at Baring Head were significantly lower than the Northern Hemisphere marine boundary layer. The 21-27% anthropogenic contribution was much lower than most studies in the Northern Hemisphere coastal areas where 30% to >90% $SO_4^{2-}{}_{NSS}$ was anthropogenic (Seguin et al., 2011; Xu and Gao, 2015; Ghahremaninezhad et al., 2016), but only slightly higher than remote Midway Island (20%) in the Northern Pacific Ocean (Savoie and Prospero, 1989). Local sulfur emission at Midway Island are minor (IEA, 2014), thus $SO_4^{2-}{}_{anth}$ should represent the sulfate background in the Northern Hemisphere. In contrast, Baring Head is ~20 km from Wellington that has significant SO_2 emission, and our data suggests this is the major, if not sole, $SO_4^{2-}{}_{anth}$ source at Baring Head. This means the background $SO_4^{2-}{}_{anth}$ level near the Southern Ocean must be very low, in agreement with our observation from the marine collector and the modeled results in (Capaldo et al., 1999). Future atmospheric modeling work incorporated with sulfur isotopic module could potentially distinguish the Southern Hemisphere background $SO_4^{2-}{}_{anth}$ from $SO_4^{2-}{}_{anth}$ emissions from Wellington.

$SO_4^{2-}{}_{DMS}$ collected in the ambient aerosols showed similar seasonal trend as the marine collector, while the anthropogenic sulfate displayed little seasonal variation (Figure 2.3c). Sulfate source apportionment determined using sulfur isotopes allow us to examine the seasonal variations of both DMS and anthropogenic derived sulfate. Similar to the SO_4^{2-} from the marine collector,

the ambient $SO_4^{2-}{}_{DMS}$ show lower flux in the winter and higher flux in the summer, but with a more significant variation (0.5 to 4 nmol/m^3) throughout the year. This is because the samples were collected weekly, so they would better capture the variation of DMS oxidation at a finer time scale. If we average the $SO_4^{2-}{}_{NSS}$ concentration in the ambient collector to the same sampling window as the marine collector, a similar seasonal trend was observed. Meantime, the anthropogenic flux ranged from near zero to ~2.5 nmol/m^3, with little variation throughout the year and no clear seasonal trend. Overall, because of the low contribution of $SO_4^{2-}{}_{anth}$, the seasonal variation of sulfate concentration at Baring Head is mainly controlled by the variation of $SO_4^{2-}{}_{DMS}$.

However, uncertainties exist in our source appointment because 1) the sampling intervals were ~one month for the marine collector and one week for the ambient collector, thus the marine collector could not record the accurate $\delta^{34}S_{DMS}$ endmember; 2) the atmospheric chemistry of sulfate formation in the urban areas and the open ocean were different because of the differences in NO_x, VOC and O_3 concentrations, hence the isotopic fractionation between SO_2 and sulfate may be different (Harris et al., 2012); and 3) the $\delta^{34}S$ of anthropogenic sulfate could display a wider range (Calhoun et al., 1991; Norman et al., 1999; Wadleigh, 2004). Nevertheless, these uncertainties would not significantly impact our calculation.

2.4 Conclusions

We investigated the source distribution and seasonal variations of size-aggregated sulfate aerosols on a coastal site at Baring Head, New Zealand from marine and ambient collectors. We suggested using total [Na^+] or [Mg^{2+}] instead of purely ionic [Mg^{2+}] to estimate the sea-salt sulfate concentration could exclude the error caused by high Na in filter blanks and Mg complexes in sea salt aerosols. In our samples, coarse aerosol sulfate was dominated by $SO_4^{2-}{}_{SS}$, the variation of which was mainly determined by a combination of wind speed and wave height; fine aerosol sulfate was dominated by $SO_4^{2-}{}_{NSS}$. Therefore, the sulfate in the oceanic CCN was mainly controlled by $SO_4^{2-}{}_{NSS}$.

$\delta^{34}S_{NSS}$ in both collectors provided a direct observation of the relative importance of $SO_4^{2-}{}_{DMS}$ and $SO_4^{2-}{}_{anth}$ in the mid-latitude Southern Ocean. The $SO_4^{2-}{}_{NSS}$ in marine collector was primarily (88-100%) of DMS origin. The concentrations of $SO_4^{2-}{}_{DMS}$ showed significant seasonal variation, which allow us to attribute the observed high summer CCN level in the Southern Ocean troposphere to the elevated DMS emission. The ambient $SO_4^{2-}{}_{NSS}$ displayed a lower and wider

range of $\delta^{34}S$ values, indicating a mixture between $SO_4^{2-}{}_{DMS}$ and $SO_4^{2-}{}_{anth}$ with the average anthropogenic contribution range between 21-27%. Our observations suggested a much lower $SO_4^{2-}{}_{anth}$ background in the Southern Hemisphere than the Northern Hemisphere.

2.5 References

Alexander, B., R. J. Park, D. J. Jacob, Q. B. Li, R. M. Yantosca, J. Savarino, C. C. W. Lee, and M. H. Thiemens (2005), Sulfate formation in sea-salt aerosols: Constraints from oxygen isotopes, J. Geophys. Res., 110(D10), D10307, doi:10.1029/2004JD005659.

Allen, A. G., A. L. Dick, and B. M. Davison (1997), Sources of atmospheric methanesulphonate, non-sea-salt sulphate, nitrate and related species over the temperate South Pacific, Atmos. Environ., 31(2), 191–205.

Amrani, A., W. Said-Ahmad, Y. Shaked, and R. P. Kiene (2013), Sulfur isotope homogeneity of oceanic DMSP and DMS., Proc. Natl. Acad. Sci. U. S. A., 110(46), 18413–8, doi:10.1073/pnas.1312956110.

Andronache, C., W. L. Chameides, D. D. Davis, B. E. Anderson, R. F. Pueschel, A. R. Bandy, D. C. Thornton, R. W. Talbot, P. Kasibhatla, and C. S. Kiang (1997), Gas-to-particle conversion of tropospheric sulfur as estimated from observations in the western North Pacific during PEM-West B, J. Geophys. Res. Atmos., 102(D23), 28511–28538.

Sanusi, A., A., Norman, C., Burridge, M., Wadleigh, and W., Tang (2006), Determination of the S Isotope Composition of Methanesulfonic Acid, doi:10.1021/AC0600048.

Ayers, G. P., and J. L. Gras (1991), Seasonal relationship between cloud condensation nuclei and aerosol methanesulphonate in marine air, Nature, 353(6347), 834–835.

Barnes, I., J. Hjorth, N. Mihalapoulos, and N. Mihalopoulos (2006), Dimethyl sulfide and dimethyl sulfoxide and their oxidation in the atmosphere.

Bates, T. S., B. K. Lamb, A. Guenther, J. Dignon, and R. E. Stoiber (1992), Sulfur emissions to the atmosphere from natural sources, J. Atmos. Chem., 14(1–4), 315–337.

Boers, R., Ayers, G. P., and Gras, J. L.: Coherence between seasonal variation in satellite-derived cloud optical depth and boundary layer CCN concentrations at a mid-latitude Southern Hemisphere station, Tellus, 46B, 123-131, 1994.

Cainey, J. M., G. P. Ayers, H. Sievering, R. W. Gillett, and M. A. Hooper (1999), The use of magnesium as a marker for sea salt at Cape Grim, Baseline Atmos. Program—1996, 7–14.

Calhoun, J. A., and T. S. Bates (1989), Sulfur isotope ratios: Tracers of non-sea salt sulfate in the remote atmosphere, ACS Publications.

Calhoun, J. A., T. S. Bates, and R. J. Charlson (1991), Sulfur isotope measurements of submicrometer sulfate aerosol particles over the Pacific Ocean, Geophys. Res. Lett., 18(10), 1877–1880, doi:10.1029/91GL02304.

Campbell, J. E., J. A. Berry, U. Seibt, S. J. Smith, S. A. Montzka, T. Launois, S. Belviso, L. Bopp, and M. Laine (2017), Large historical growth in global terrestrial gross primary production, Nature, 544(7648), 84–87, doi:10.1038/nature22030.

Capaldo, K., J. J. Corbett, P. Kasibhatla, P. Fischbeck, and S. N. Pandis (1999), Effects of ship emissions on sulphur cycling and radiative climate forcing over the ocean, Nature, 400(6746), 743–746, doi:10.1038/23438.

Clarke, A. D., S. R. Owens, and J. Zhou (2006), An ultrafine sea-salt flux from breaking waves: Implications for cloud condensation nuclei in the remote marine atmosphere, J. Geophys. Res. Atmos., 111(D6).

Dams, R., K. A. Rahn, and J. W. Winchester (1972), Evaluation of filter materials and impaction surfaces for nondestructive neutron activation analysis of aerosols, Environ. Sci. Technol., 6(5), 441–448.

Davy, P. K. (2007), Composition and sources of aerosol in the Wellington Region of New Zealand. PhD Thesis. School of Chemical and Physical Sciences. Wellington, Victoria University of Wellington.

Davy, P. K., A. Markwitz, W. J. Trompetter, and D. C. Weatherburn (2008), Source apportionment of airborne particles at Seaview, Lower Hutt. GNS Science consultancy report, Institute of Geological and Nuclear Sciences**:** v, 92 p.

Davy, P. K., T. Ancelet, W. J. Trompetter, A. Markwitz and D. C. Weatherburn (2012). Composition and source contributions of air particulate matter pollution in a New Zealand suburban town." Atmospheric Pollution Research **3**(1): 143-147.

Dorling, S. R., T. D. Davies, and C. E. Pierce (1992), Cluster analysis: a technique for estimating the synoptic meteorological controls on air and precipitation chemistry—method and applications, Atmos. Environ. Part A. Gen. Top., 26(14), 2575–2581.

Faloona, I. (2009), Sulfur processing in the marine atmospheric boundary layer: A review and critical assessment of modeling uncertainties, Atmos. Environ., 43(18), 2841–2854, doi:10.1016/j.atmosenv.2009.02.043.

Ghahremaninezhad, R., A.-L. Norman, J. P. D. Abbatt, M. Levasseur, and J. L. Thomas (2016), Biogenic, anthropogenic and sea salt sulfate size-segregated aerosols in the Arctic summer, Atmos. Chem. Phys, 16, 5191–5202, doi:10.5194/acp-16-5191-2016.

Gong, S. L. (2003), A parameterization of sea-salt aerosol source function for sub- and super-micron particles, Global Biogeochem. Cycles, 17(4), doi:10.1029/2003GB002079.

Górka, M., Skrzypek, G., Hałas, S., Jędrysek, M. O., & Strąpoć, D. (2017). Multi-seasonal pattern in 5-year record of stable H, O and S isotope compositions of precipitation (Wrocław, SW Poland). Atmospheric environment, *158*, 197-210.

Harris, E., B. Sinha, P. Hoppe, S. Foley, and S. Borrmann (2012), Fractionation of sulfur isotopes during heterogeneous oxidation of SO_2 on sea salt aerosol: a new tool to investigate non-sea salt sulfate production in the marine boundary layer, Atmos. Chem. Phys. Atmos. Chem. Phys., 12, 4619–4631, doi:10.5194/acp-12-4619-2012.

Harris, E., B. Sinha, P. Hoppe, and S. Ono (2013), High-precision measurements of ^{33}S and ^{34}S fractionation during SO_2 oxidation reveal causes of seasonality in SO_2 and sulfate isotopic composition, Environ. Sci. Technol., 47(21), 12174–12183.

Hill-Falkenthal, J., A. Priyadarshi, and M. Thiemens (2012), Differentiating sulfate aerosol oxidation pathways for varying source altitudes using ^{35}S and $\Delta^{17}O$ tracers, J. Geophys. Res. Atmos., 117(D18), doi:10.1029/2012JD018242.

Huang, S., L. Poulain, D. van Pinxteren, M. van Pinxteren, Z. Wu, H. Herrmann, and A. Wiedensohler (2017), Latitudinal and Seasonal Distribution of Particulate MSA over the Atlantic using a Validated Quantification Method with HR-ToF-AMS, Environ. Sci. Technol., 51(1), 418–426, doi:10.1021/acs.est.6b03186.

Hudson, J. G., and S. Noble (2006), Cloud Condensation Nuclei Sizes, in AGU Fall Meeting Abstracts.

I. E. A. (2014), CO_2 Emissions from Fuel Combustion 2014.

I. P. C. C. (2007), The Fourth Assessment Report of the Intergovernmental Panel on Climate Change, Geneva, Switz.

Jaeglé, L., P. K. Quinn, T. S. Bates, B. Alexander, and J.-T. Lin (2011), Global distribution of sea salt aerosols: new constraints from in situ and remote sensing observations, Atmos. Chem. Phys., 11(7), 3137–3157.

Jayarathne, T., C. M. Sultana, C. Lee, F. Malfatti, J. L. Cox, M. A. Pendergraft, K. A. Moore, F. Azam, A. V Tivanski, and C. D. Cappa (2016), Enrichment of saccharides and divalent cations in sea spray aerosol during two phytoplankton blooms, Environ. Sci. Technol, 50(21), 11511–11520.

Jensen, D. R., C. R. Zeisse, K. M. Littfin, and S. G. Gathman (1997), EOPACE (electro-optical propagation assessment in coastal environments): overview and initial accomplishments, in Propagation and Imaging through the Atmosphere, vol. 3125, pp. 98–109, International Society for Optics and Photonics.

Johnson, J. E. (1981), The lifetime of carbonyl sulfide in the troposphere, Geophys. Res. Lett., 8(8), 938–940, doi:10.1029/GL008i008p00938.

Keene, W. C., A. A. P. Pszenny, J. N. Galloway, and M. E. Hawley (1986), Sea-salt corrections and interpretation of constituent ratios in marine precipitation, J. Geophys. Res., 91(D6), 6647, doi:10.1029/JD091iD06p06647.

Keene, W. C., H. Maring, J. R. Maben, D. J. Kieber, A. A. P. Pszenny, E. E. Dahl, M. A. Izaguirre, A. J. Davis, M. S. Long, and X. Zhou (2007), Chemical and physical characteristics of nascent aerosols produced by bursting bubbles at a model air-sea interface, J. Geophys. Res. Atmos., 112(D21).

Korhonen, H., K. S. Carslaw, D. V Spracklen, G. W. Mann, and M. T. Woodhouse (2008), Influence of oceanic dimethyl sulfide emissions on cloud condensation nuclei concentrations and seasonality over the remote Southern Hemisphere oceans: A global model study, J. Geophys. Res. Atmos., 113(D15).

Krouse, H. R., and V. A. Grinenko (1991), Stable isotopes: natural and anthropogenic sulphur in the environment,

Kulmala, M., L. Pirjola, and J. M. Makela (2000), Stable sulphate clusters as a source of new atmospheric particles, Nature, 404(6773), 66.

Lana, A., Bell, T. G., Simó, R., Vallina, S. M., Ballabrera-Poy, J., Kettle, A. J., Dachs, J., Bopp, L., Saltzman, E. S., Stefels, J., Johnson, J. E., and Liss, P. S.: An updated climatology of surface dimethlysulfide concentrations and emission fluxes in the global ocean, Global Biogeochem. Cycles, 25, GB1004, doi:10.1029/2010gb003850, 2011.

Law, C. S., Smith, M. J., Harvey, M. J., Bell, T. G., Cravigan, L. T., Elliott, F. C., Lawson, S. J., Lizotte, M., Marriner, A., McGregor, J., Ristovski, Z., Safi, K. A., Saltzman, E. S., Vaattovaara, P., and Walker, C. F.: Overview and preliminary results of the Surface Ocean Aerosol Production (SOAP) campaign, Atmos. Chem. Phys., 17, 13645-13667, doi:10.5194/acp-17-13645-2017, 2017.

Lewis, E. R., and S. E. Schwartz (2004), Sea salt aerosol production: mechanisms, methods, measurements, and models-A critical review, American geophysical union.

Lin, M., S. Biglari, Z. Zhang, D. Crocker, J. Tao, B. Su, L. Liu, and M. H. Thiemens (2017), Vertically uniform formation pathways of tropospheric sulfate aerosols in East China detected from triple stable oxygen and radiogenic sulfur isotopes, Geophys. Res. Lett., 44(10), 5187–5196, doi:10.1002/2017GL073637.

Mårtensson, M., E. D. Nilsson, G. De Leeuw, L. H. Cohen, and H. C. Hansson (2003), Laboratory simulations of the primary marine aerosol generated by bubble bursting, JGR-Atmospheres, 108(10.1029).

McArdle, N., Liss, P., and Dennis, P.: An isotopic study of atmospheric sulphur at three sites in Wales and at Mace Head, Eire, Journal of Geophysical Research: Atmospheres, 103, 31079-31094, doi:10.1029/98JD01664, 1998.

McCoy, D. T., S. M. Burrows, R. Wood, D. P. Grosvenor, S. M. Elliott, P.-L. Ma, P. J. Rasch, and D. L. Hartmann (2015), Natural aerosols explain seasonal and spatial patterns of Southern Ocean cloud albedo, Sci. Adv., 1(6), e1500157.

McInnes, L. M., D. S. Covert, P. K. Quinn, and M. S. Germani (1994), Measurements of chloride depletion and sulfur enrichment in individual sea-salt particles collected from the remote marine boundary layer, J. Geophys. Res. Atmos., 99(D4), 8257–8268.

Ministry of the Environment (2004), New Zealand, Emission inventories for CO, NO_x, SO_2, ozone, benzene and benzo(a)pyrene in New Zealand. Air Quality Technical Report 44.

Mizutani, Y., and T. A. Rafter (1969), Oxygen isotopic composition of sulfates. Part 5. Isotopic composition of sulfate in rain water, Gracefield, New Zealand., Inst. of Nuclear Sciences, Lower Hutt, NZ.

Monahan, E. C., D. E. Spiel, and K. L. Davidson (1986), A model of marine aerosol generation via whitecaps and wave disruption, in Oceanic whitecaps, pp. 167–174, Springer.

Murphy, D. M., J. R. Anderson, P. K. Quinn, L. M. McInnes, F. J. Brechtel, S. M. Kreidenweis, A. M. Middlebrook, M. Pósfai, D. S. Thomson, and P. R. Buseck (1998), Influence of sea-salt on aerosol radiative properties in the Southern Ocean marine boundary layer, Nature, 392(6671), 62–65.

Nielsen, H. (1974). Isotopic composition of the major contributors to atmospheric sulfur. *Tellus*, *26*(1-2), 213-221.

Norman, A. L., L. A. Barrie, D. Toom-Sauntry, A. Sirois, H. R. Krouse, S. M. Li, and S. Sharma (1999), Sources of aerosol sulphate at Alert: Apportionment using stable isotopes, J. Geophys. Res. Atmos., 104(D9), 11619–11631, doi:10.1029/1999JD900078.

Novák, M., I. Jacková, and E. Prechová (2001), Temporal trends in the isotope signature of air-borne sulfur in Central Europe., Environ. Sci. Technol., 35(2), 255–60.

O'Dowd, C. D., and M. H. Smith (1993), Physicochemical properties of aerosols over the northeast Atlantic: Evidence for windspeed-related submicron sea-salt aerosol production, J. Geophys. Res. Atmos., 98(D1), 1137–1149.

O'Dowd, C. D., M. H. Smith, I. E. Consterdine, and J. A. Lowe (1997), Marine aerosol, sea-salt, and the marine sulphur cycle: A short review, Atmos. Environ., 31(1), 73–80.

O'Dowd, C. D., G. De Leeuw, C. D. O'Dowd, and G. De Leeuw (2007), Marine aerosol production: a review of the current knowledge, Philos. Trans. R. Soc. London A Math. Phys. Eng. Sci., 365(1856), doi:10.1098/rsta.2007.2043.

Oduro, H., K. L. Van Alstyne, and J. Farquhar (2012), Sulfur isotope variability of oceanic DMSP generation and its contributions to marine biogenic sulfur emissions., Proc. Natl. Acad. Sci. U. S. A., 109(23), 9012–6, doi:10.1073/pnas.1117691109.

Patris, N., N. Mihalopoulos, E. D. Baboukas, and J. Jouzel (2000), Isotopic composition of sulfur in size-resolved marine aerosols above the Atlantic Ocean, J. Geophys. Res. Atmos., 105(D11), 14449–14457, doi:10.1029/1999JD901101.

Patris, N., R. Delmas, M. Legrand, M. De Angelis, F. A. Ferron, M. Stiévenard, and J. Jouzel (2002), First sulfur isotope measurements in central Greenland ice cores along the preindustrial and industrial periods, J. Geophys. Res. Atmos., 107(D11), ACH 6-1-ACH 6-11, doi:10.1029/2001JD000672.

Paxian, A., V. Eyring, W. Beer, R. Sausen, and C. Wright (2010), Present-Day and Future Global Bottom-Up Ship Emission Inventories Including Polar Routes, Environ. Sci. Technol., 44(4), 1333–1339, doi:10.1021/es9022859.

Priyadarshi, A., J. Hill-Falkenthal, E. Coupal, G. Dominguez, and M. H. Thiemens (2012), Measurements of ^{35}S in the marine boundary layer at La Jolla, California: A new technique for tracing air mass mixing during Santa Ana events, J. Geophys. Res. Atmos., 117(D8).

Proemse, B. C., and B. Mayer, Tracing industrial nitrogen and sulfur emissions in the Athabasca oil sands region using stable isotopes. Developments in Environmental Science. Vol. 11. Elsevier, 2012. 243-266.

Pszenny, A. A. P., A. J. Castelle, J. N. Galloway, and R. A. Duce (1989), A study of the sulfur cycle in the Antarctic marine boundary layer, J. Geophys. Res., 94(D7), 9818, doi:10.1029/JD094iD07p09818.

Quinn, P. K., T. S. Bates, K. Schulz, and G. E. Shaw (2009), Decadal trends in aerosol chemical composition at Barrow, Alaska: 1976–2008, Atmos. Chem. Phys., 9(22), 8883–8888.

Rees, C. E., W. J. Jenkins, and J. Monster (1978), The sulphur isotopic composition of ocean water sulphate, Geochim. Cosmochim. Acta, 42(4), 377–381.

Rempillo, O. et al. (2011), Dimethyl sulfide air-sea fluxes and biogenic sulfur as a source of new aerosols in the Arctic fall, J. Geophys. Res., 116(D17), D00S04, doi:10.1029/2011JD016336.

Sakai, H., T. J. Casadevall, and J. G. Moore (1982), Chemistry and isotope ratios of sulfur in basalts and volcanic gases at Kilauea Volcano, Hawaii, Geochim. Cosmochim. Acta, 46(5), 729–738.

Savoie, D. L., and J. M. Prospero (1989), Comparison of oceanic and continental sources of non-sea-salt sulphate over the Pacific Ocean, Nature, 339(6227), 685–687.

Seguin, A. M., A.-L. Norman, S. Eaton, and M. Wadleigh (2011), Seasonality in size segregated biogenic, anthropogenic and sea salt sulfate aerosols over the North Atlantic, Atmos. Environ., 45(38), 6947–6954, doi:10.1016/j.atmosenv.2011.09.033.

Sievering, H., J. Cainey, M. Harvey, J. McGregor, S. Nichol, and P. Quinn (2004), Aerosol non-sea-salt sulfate in the remote marine boundary layer under clear-sky and normal cloudiness conditions: Ocean-derived biogenic alkalinity enhances sea-salt sulfate production by ozone oxidation, J. Geophys. Res., 109(D19), D19317, doi:10.1029/2003JD004315.

Simpson, R., S. G. Howell, B. W. Blomquist, A. D. Clarke, and B. J. Huebert (2014), Dimethyl sulfide: Less important than long-range transport as a source of sulfate to the remote tropical Pacific marine boundary layer, J. Geophys. Res. Atmos., 119(14), 9142–9167.

Steinkamp, K., S. E. Mikaloff Fletcher, G. Brailsford, D. Smale, S. Moore, E. D. Keller, W. T. Baisden, H. Mukai, and B. B. Stephens (2017), Atmospheric CO_2 observations and models suggest strong carbon uptake by forests in New Zealand, Atmos. Chem. Phys., 17(1), 47–76, doi:10.5194/acp-17-47-2017.

Udisti, R. et al. (2012), Sea spray aerosol in central Antarctica. Present atmospheric behaviour and implications for paleoclimatic reconstructions, Atmos. Environ., 52, 109–120, doi:10.1016/j.atmosenv.2011.10.018.

Udisti, R. et al. (2016), Sulfate source apportionment in the Ny-Ålesund (Svalbard Islands) Arctic aerosol, Rend. Lincei, 27(S1), 85–94, doi:10.1007/s12210-016-0517-7.

Van Eijk, A. M. J., J. T. Kusmierczyk-Michulec, M. J. Francius, G. Tedeschi, J. Piazzola, D. L. Merritt, and J. D. Fontana (2011), Sea-spray aerosol particles generated in the surf zone, J. Geophys. Res. Atmos., 116(D19).

Wadleigh, M. A. (2004), Sulphur isotopic composition of aerosols over the western North Atlantic Ocean, Can. J. Fish. Aquat. Sci., 61(5), 817–825, doi:10.1139/f04-073.

Xu, G., and Y. Gao (2015), Characterization of marine aerosols and precipitation through shipboard observations on the transect between 31° N–32° S in the West Pacific, Atmos. Pollut. Res., 6(1), 154–161.

Yang, Y., H. Wang, S. J. Smith, R. Easter, P.-L. Ma, Y. Qian, H. Yu, C. Li, and P. J. Rasch (2017), Global source attribution of sulfate concentration and direct and indirect radiative forcing, Atmos. Chem. Phys., 17(14), 8903.

Zhu, G., Q. Guo, T. Chen, Y. Lang, M. Peters, L. Tian, H. Zhang, and C. Wang (2016), Chemical and sulfur isotopic composition of precipitation in Beijing, China, Environ. Sci. Pollut. Res., 23(6), 5507–5515, doi:10.1007/s11356-015-5746-2.

CHAPTER 3. ATMOSPHERIC DEPOSITION ACROSS THE ATACAMA DESERT, CHILE: COMPOSITIONS, SOURCE DISTRIBUTIONS, AND INTERANNUAL COMPARISONS

This chapter is a reprint from a published article (Li, J., Wang, F., Michalski, G., & Wilkins, B. (2019). Atmospheric deposition across the Atacama Desert, Chile: Compositions, source distributions, and interannual comparisons. *Chemical Geology*, *525*, 435-446).

Abstract

Hyper-arid areas such as the Atacama Desert accumulated significant amounts of insoluble dust and soluble salts from the atmosphere, providing minable salt deposits as well as mimicking the surface processes on Mars. The deposition rates, compositions and sources, however, were poorly constrained. Especially, the variabilities of atmospheric deposition in the Atacama Desert corresponding to a changing climate were unassessed. In this work, the atmospheric depositions collected using dust traps across a west-east elevation gradient in the Atacama (~23°S) from 1/2/2010 to 12/31/2011 were analyzed and compared to previous results in 2007-2009. The insoluble dust deposition rates in our sampling period were significantly higher than those of 2007-2009 in most dust traps, which was attributed to the changes in wind, highlighting the importance of long-term monitoring of insoluble dust fluxes. Soluble salts, instead, showed less distinct interannual variations in deposition rates, geochemical compositions or source contributions. At the coastal site (T1), soluble salts were originated from both primary sea-salt (SS) aerosols and non-sea-salt (NSS) sources such as anthropogenic emission, marine biogenic emission and biomass burning; the deposition rates of these salts largely depended on the wind speed and the amount of anthropogenic emissions. Sulfur isotopic evidence further showed that NSS sulfate at T1 was mainly originated from local SO_2 emission from local power plants. The inland sites (T2-T8) displayed much lower soluble salts deposition rates, and the salts were primarily sourced from entrainment of local surface minerals, including Na(Cl, NO_3), $CaSO_4$, and nitrate formed via atmospheric oxidation of anthropogenic NO_x. Sulfur isotopic compositions of sulfate deposited at T2-T8 were similar to those in local surface soil; however, three sites near the Chuquicamata mine showed slightly lower $\delta^{34}S_{sulfate}$ values, indicating the presence of secondary sulfate originated from mining activities. The soluble salts deposited at the Andean site (T10) were dominantly from

wet deposition that incorporated local lake salts, and therefore, the deposition rates were mainly controlled by the amount of precipitation.

3.1 Introduction

As one of the driest places on Earth, the Atacama Desert has a hyperarid climate with mean annual precipitation (MAP) less than 10 mm (Ericksen, 1981). The surface soil in the Atacama Desert is characterized by 1) very little organic matter content (Ericksen, 1981; Navarro-Gonzalez, 2003), 2) little to no microbial activity (Navarro-Gonzalez, 2003), 3) slow weathering, leaching, and water erosion rates (Ericksen, 1981; Ewing et al., 2008, 2006), and 4) a surface layer of desert pavement (Cooke and Warren, 1973; McFadden et al., 1987). In addition, high concentrations of soluble salts, such as nitrate, sulfate, chloride, and perchlorate, have been found within Atacama soils (e.g., Rech et al., 2003, Bao et al., 2004). This is similar to the occurrences of nitrate salts (Kounaves et al., 2014; Stern et al., 2015), subsurface gypsum ($CaSO_4{\cdot}2H_2O$) crusts (Edwards et al., 2005; Fishbaugh et al., 2007), massive chloride deposits (Osterloo et al., 2008), and abundant perchlorate (Hecht et al., 2009) on Mars (e.g., Catling et al., 2010; Navarro-Gonzalez, 2003; Vítek et al., 2012). Given the similar climatic conditions and soil chemical composition between the Atacama and Mars, the processes that led to the formation of these two unique planetary surfaces are possibly similar. Therefore, the Atacama Desert is considered as an ideal analog for studying the pedogenesis on Mars (e.g., Catling et al., 2010; Navarro-Gonzalez, 2003; Vítek et al., 2012).

The origins of the Atacama soil salts have long been debated (e.g., Darwin, 1906; Ericksen, 1983 and refererences therein). While several studies have suggested that groundwater (~43-88 meters below surface) played a significant role in the formation of some salt deposits in the Atacama Desert (Cameron and Leybourne, 2005, Perez-Fodich et al., 2014, Alvarez et al., 2015), stable isotopic evidences have suggested that the majority of nitrate, sulfate and perchlorate ions in the Atacama top soil were produced photochemically in the atmosphere and then dry deposited as gases or dust (Bao et al., 2004; Böhlke et al., 1997; Michalski et al., 2004; Rech et al., 2003). Additionally, Wang et al. (2015) proposed a mechanism of soil accumulation via atmospheric deposition based on the meteoric ^{10}Be record of a 225 cm soil profile from the hyperarid core of the Atacama Desert, further suggesting atmospheric deposition is an important, even the dominant, process controlling soil development in the Atacama. Therefore, characterizing the rates, chemical compositions and sources of atmospheric deposition across the Atacama will help understand the

soil development processes in the Atacama, with potential implications for a surface evolution mechanism on Mars.

Due to the lack of standard deposition monitoring stations, only a few studies have attempted to collect and analyze the atmospheric depositions in the Atacama. Ewing et al. (2006) first quantified the deposition rates of major ions (Na^+, Ca^{2+}, NO_3^-, Cl^- and SO_4^{2-}) at three sites along a 300 km north-south transect and observed significant spatial variations in ion depositions. However, since these sites were all located the hyperarid core of the Atacama, whether they can represent the atmospheric deposition over the entire Atacama region was unclear. To fill this knowledge gap, Wang et al. (2014) set up a series of dust traps along a west-east transect from the Pacific coast to the Andean plateau and reported the chemical, mineral, and nitrate isotopic compositions of atmospheric deposition collected during 7/10/2007 - 12/31/2009 to characterize the atmospheric deposition along this transect.

However, a few questions still remain after this one-time recovery of atmospheric deposition over a 2.5-year sampling period. First, it is unclear whether the atmospheric depositions in the Atacama show interannual variations, which were observed in some other arid areas such as Southern California, U.S., Nevada, U.S., and Gansu, China (e.g., Reheis, 1997; Reheis and Kihl, 1995; Ta et al., 2004). Second, it is unknown how shifted climate conditions would affect the deposition in the Atacama. Last, there is little knowledge on the impact of anthropogenic activities (mainly mining and transportation) to the atmospheric deposition in the Atacama Desert. Thus, a follow-up comparison study to (Wang et al., 2014) was necessary to examine and interpret the interannual variabilities of atmospheric deposition in the Atacama.

In this study, atmospheric depositions were collected during 1/2/2010 - 12/31/2011 by the same nine dust traps set up by (Wang et al., 2014). The deposition rates as well as the chemical and isotopic compositions were analyzed and compared with the 2007-2009 results to investigate their interannual variations. These interannual comparisons can help understand the impact of climate, weather conditions and anthropogenic activities on the atmospheric deposition in the Atacama and assess the credibility of using annual average deposition to estimate the deposition over a longer period.

3.2 Sampling and analytical methods

The Atacama Desert, bordered on the west and by the Pacific Ocean on the east by the Andes , is divided into three physiographic provinces (Figure 3.1A, from west to east): Coastal Range consisting of Mesozoic igneous and sedimentary rocks (Clarke, 2005), which runs in a general north-south direction adjacent to the Pacific Ocean with altitude less than 2000 m; the Central Valley that is filled with Oligocene to Pliocene clastic sedimentary rocks (Sernageomin, 1982; Sillitoe et al., 1968) with altitude between 900 to 2500 m; and the Andes consisting of an altiplano about 4000 m in altitude and several intertwined pre-Andean ranges and basins (e.g. the Atacama Basin, Clarke, 2005) that abut the Andean Cordillera.

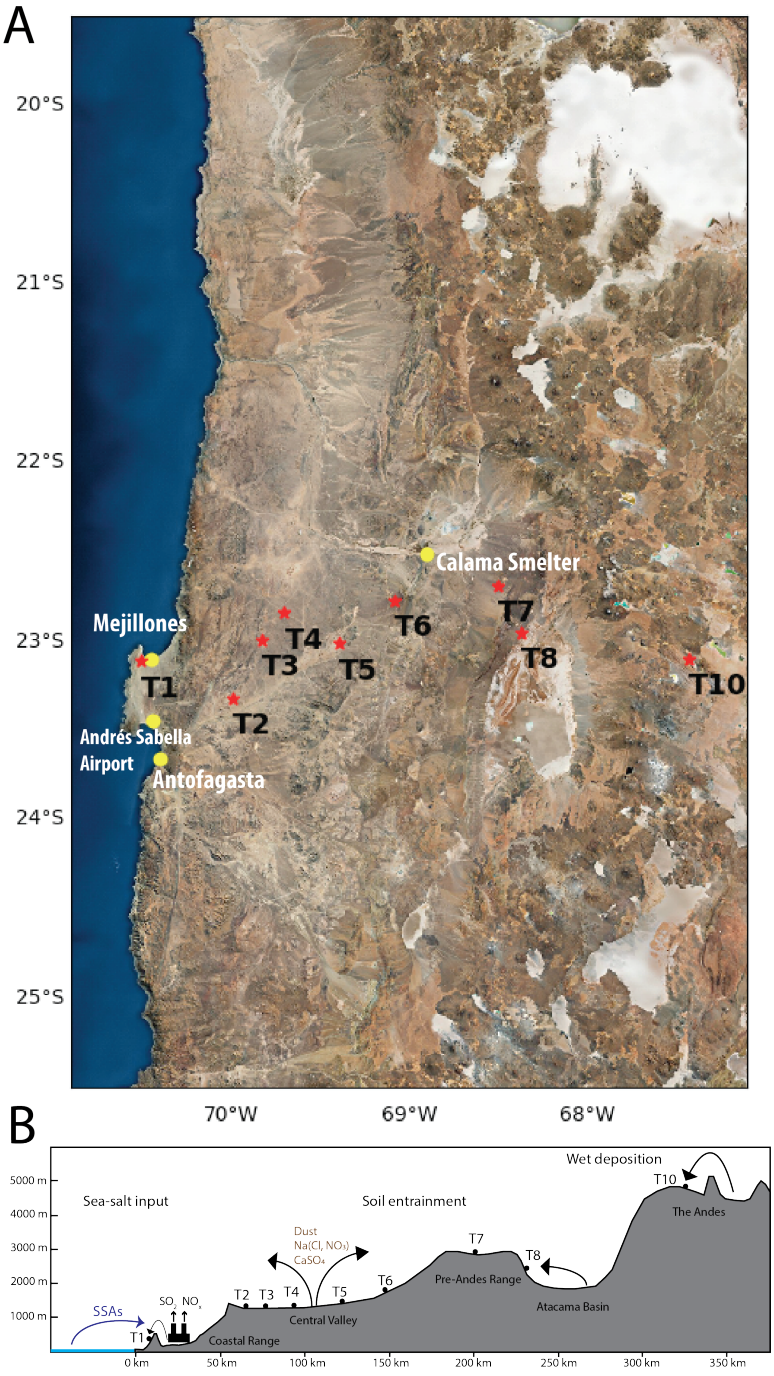

Figure 3.1 Geological map (A) of the Atacama Desert showing the locations of dust traps, and the sketch of the transect (B) modified from Wang et al., (2014).

A series of nine dust traps were previously set up as shown in Figure 3.1 (Wang et al., 2014) along a west-east transect in the Atacama: T1 on the Costal Range, T2-T6 in the Central Valley, T7 on the pre-Andean range, T8 in the Atacama Basin and T10 on the Andes. Locations of dust traps were carefully selected to minimize the influence of anthropogenic activities, particularly open-pit

mining activities that were widespread in the region. Each dust trap was made of a single-piece Bundt pan with the outer ring diameter of 25 cm and surface area of 477 cm^2. One piece of 0.25-inch-galvanized mesh was fixed on top of each pan, and a layer of glass marbles were spread on the mesh to simulate the effect of surface gravels in preventing wind erosion (Reheis and Kihl, 1995). The dust traps were all mounted ~1 m above ground to avoid the contamination from surface dust. Sample collection spanned from 1/2/2010 to 12/31/2011.

The sample collection and processing procedures were identical to those used for the 2007-2009 depositions in Wang et al. (2014). At the end of the exposure period, atmospheric deposition in each trap was carefully washed multiple times with Millipore water (18.2 MΩ·cm) into a 1 L plastic bottle, to ensure complete transferring of both insoluble and soluble material into the bottle. The solutions were then kept frozen, shipped to Purdue University, and freeze-dried to evaporate all the water. The residual solid materials were weighed, dissolved in ~100 mL Millipore water, and then filtered to separate the soluble salts from insoluble dust. The insoluble dust was subsequently freeze-dried to ensure minimum volatilization and weighed to calculate the mass of soluble salts. The soluble material mainly included (Na, K)(Cl, NO_3), (Na, K)$_2SO_4$, (Mg, Ca)SO_4^{2-}, (Mg, Ca)(Cl, NO_3)$_2$ and some organic salts. Since the major inorganic salts were undersaturated (see results section) in these solutions, we suggest all the major ions have been completely dissolved. However, some trace elements (*e.g.* Mn, Fe, Cu, Zn) forming low-solubility salts might not have been completely dissolved (Pan and Wang, 2015), but their fluxes were 3-4 orders of magnitude lower than those of the major ions (Pan and Wang, 2015). Therefore, their contributions to the total soluble material deposition was less than 0.1%, and the incomplete dissolution of trace elements would not introduce significant uncertainties to the calculation of the soluble material deposition rates here.

For cation (Na^+, K^+, Ca^{2+}, Mg^{2+}) analysis, 5 mL of each solution was mixed with 5 mL 10% HNO_3, then analyzed by ICP-OES (Thermo Scientific, Pittsburgh, PA, USA) in the Purdue Rare Isotope Measurement (PRIME) Laboratory at Purdue University. Another aliquot of each solution was used for anion (Cl^-, NO_3^-, SO_4^{2-}) analysis using a Dionex DX-500 Ion Chromatography (Dionex Corp., Sunnyvale, CA, USA) in the Purdue Stable Isotope Laboratory at Purdue University. For all ions at the T1 site, we calculated the enrichment factors (EF) relative to seawater by assuming all the Na^+ deposition in T1 was originated from seawater (Table 2, see discussion):

$$EF_X=(X/Na^+)_{T1}/(X/Na^+)_{seawater}$$

in which $(X/Na^+)_{T1}$ represented the molar ratio of any ion (X) to Na^+ at T1 and $(X/Na^+)_{seawater}$ was the molar ratio of ion X to Na^+ in seawater (Pilson, 2012). EF values less than 1 suggested biologic, chemical, or physical losses of ion X, and the loss of X was defined as X deficit: X deficit = $[Na^+]_{T1}\times(X/Na^+)_{seawater} - [X]_{T1}$. EF values greater than 1 indicated extra source(s) other than seawater for ion X, and the ion X was divided into sea-salt ion (SS-X) and non-sea-salt ion (NSS-X): SS-X= $[Na^+]_{T1}\times(X/Na^+)_{seawater}$; NSS-X = $[X]_{T1} - [Na^+]_{T1}\times(X/Na^+)_{seawater}$.

Sulfur isotopic analysis of soluble sulfate was performed at the Purdue Stable Isotope Laboratory. A 0.5 mL of 5% acidified $BaCl_2$ was added into 5 ml of each solution to completely precipitate sulfate as $BaSO_4$ that was then extracted, weighed, mixed with V_2O_5 powder, and combusted at 980 °C in a Costech Elemental Analyzer. The produced SO_2 was then directed to an isotope ratio mass spectrometer (IRMS-Thermo Delta V Plus) equipped with a ConFlo interface for isotopic analysis. The sulfur isotopic compositions were reported in delta notation: $\delta^{34}S = (({}^{34}S/{}^{32}S)_{sample}/({}^{34}S/{}^{32}S)_{reference}-1)*1000‰$, in which the reference material is Vienna-Canyon Diablo Troillite (VCDT), the standard deviation (1σ) of our sulfur isotopic analysis was ±0.2‰.

3.3 Results

Bulk mass (insoluble dust and soluble salts) atmospheric deposition rates varied significantly along the west-east transect, with the lowest deposition rate of 4.3 g/m^2/yr at T8 and the highest of 149.2 g/m^2/yr at T10 (Figure 3.2). The spatial variations in the bulk mass deposition rates were mainly controlled by the insoluble dust deposition rates that spanned from 3.8 g/m^2/yr to 149.0 g/m^2/yr (Figure 3.2). Dust traps in mountainous regions showed higher insoluble dust deposition rates: 18.5 g/m^2/yr at T1, 80.9

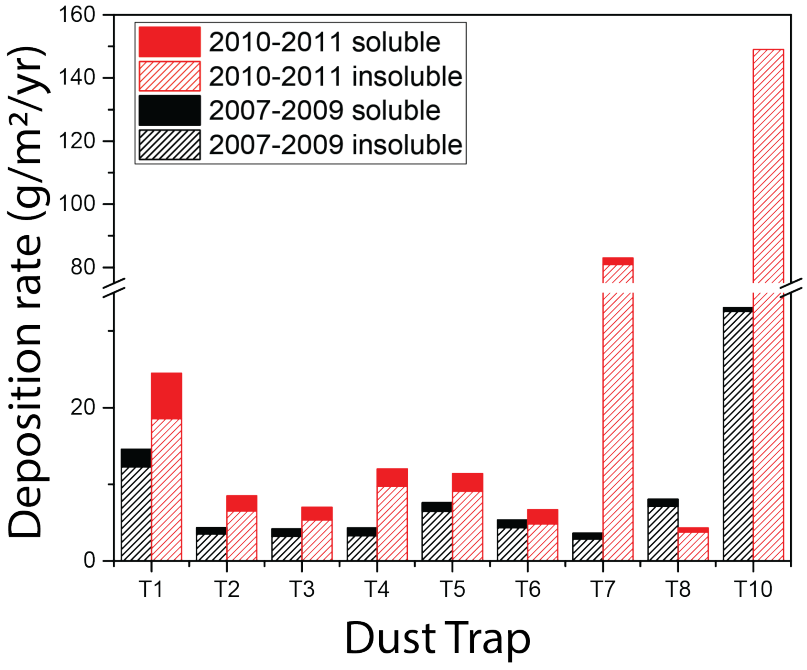

Figure 3.2 Insoluble dust and soluble salts depositions of T1-T10 during both sampling periods.

g/m^2/yr at T7 and 149.0 g/m^2/yr at T10, while T2-T6 (Central Valley) and T8 (Atacama Basin) displayed lower insoluble dust deposition rates ranging from 3.8 g/m^2/yr to 9.8 g/m^2/yr. Comparing to the 2007-2009 period, the insoluble dust deposition rates in 2010-2011 increased by 11% to 2723%. The exception was T8, the insoluble dust deposition of which decreased by 47% from 7.1 g/m^2/yr to 3.8 g/m^2/yr (Figure 3.2).

The deposition rates of soluble salts ranged from 0.2 to 6.0 g/m^2/yr and displayed a general decreasing trend from T1 to T10 (Figures 3.2 and 3.3). The coastal site (T1) had the highest soluble salts deposition rate (6.0 g/m^2/yr) and the central depression (T2-T7) showed lower but consistent deposition rates ranging from 1.7 to 2.3 g/m^2/yr. The lowest soluble salts deposition rates were at T8 and T10 (<0.5 g/m^2/yr). The soluble salts deposition rates also showed interannual variabilities. The 2010-2011 soluble salts deposition rates at T1 to T7 increased by 67% - 176% relative to 2007-2009, while the rates in T8 and T10 decreased by 46% and 57%, respectively.

Major cations (Na^+, Ca^{2+}, K^+, Mg^{2+}) and anions (Cl^-, NO_3^-, SO_4^{2-}) accounted for 47±11% of total soluble salts in the dust traps (Table 3.1 and Figure 3.3). Ion concentrations in sample solutions suggested that all the solutions were undersaturated, indicating complete dissolving of the major ions. Their deposition rates showed a similar spatial variation pattern as the soluble salts deposition rates. Among all the sites, T1 displayed the highest ion deposition rates, with the depositions of Na^+, K^+, NO_3^-, Cl^- and SO_4^{2-} were 3 to 20 times higher than the other sites. T2-T7 sites had consistently lower ion deposition rates than T1, and the deposition rates of all ions were lowest at T8 and T10. Compared to 2007-2009, the 2010-2011 total ion deposition (sum of Na^+, Ca^{2+}, K^+, Mg^{2+}, Cl^-, NO_3^-, SO_4^{2-}, Figure 3.3) was 98% higher at T1, 20%-85% lower at T3, T4, T6 and T8, and not significantly different at T2, T5 and T7.

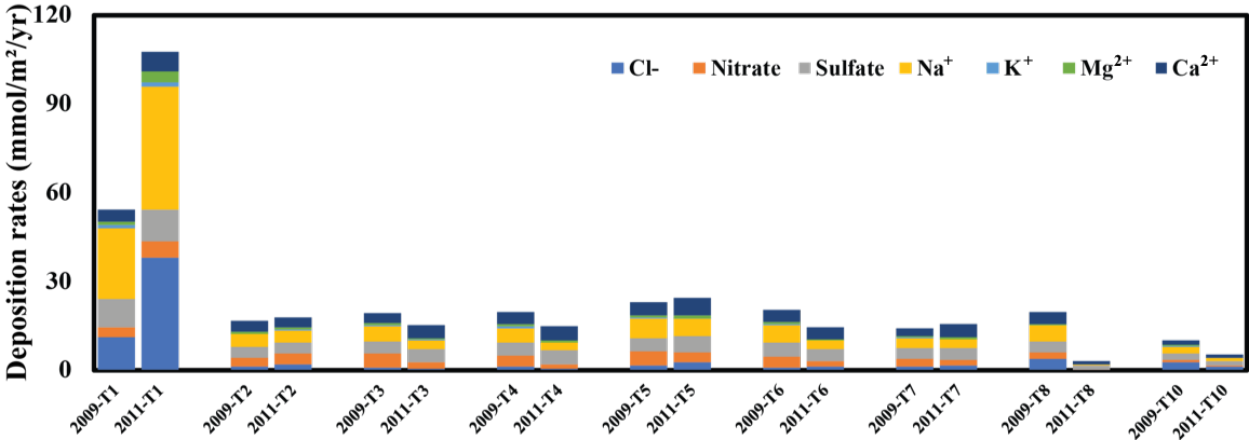

Figure 3.3 Soluble ion deposition rates at T1-T10 sites during both sampling periods

The sulfur isotopic composition of soluble sulfate ($\delta^{34}S_{sulfate}$) in the nine dust traps ranged from 4.0‰ to 8.3‰ (Table 3.1, Figure 3.5). The lowest $\delta^{34}S_{sulfate}$ value (4.0‰) occurred at T1 while T8 had the highest $\delta^{34}S_{sulfate}$ value of 8.3‰. The $\delta^{34}S_{sulfate}$ at T2-T4 were similar (7.1‰ to 7.6‰), and then showed a decreasing trend from 7.5‰ to 4.7‰ from T4 to T7. The Andean dust trap (T10) had the $\delta^{34}S_{sulfate}$ of 5.8‰.

Table 3.1 Deposition rates of soluble cations and anions (in mmol/m^2/yr) and insoluble dust (in g/m^2/yr) during 2010-2011, and their changes (in %) comparing to during 2007-2009.

Trap	Cl^-	NO_3^-	SO_4^{2-}	Na^+	K^+	Mg^{2+}	Ca^{2+}	Dust	$Na^+/(Cl^-+NO3^-)$	$Ca^{2+}/SO4^{2-}$	Negative/positive	$\delta^{34}S$ (‰)
T1	**38.0**	**5.6**	**10.4**	**41.9**	**1.2**	**3.8**	**6.7**	**18.5**	0.96	0.64	1.01	4.0
change(%)	244.1	62.3	9.2	75.1	23.9	208.4	62.2	50.8				
T2	**2.1**	**3.6**	**3.6**	**4.2**	**0.2**	**0.9**	**3.2**	**6.5**	0.75	0.88	1.02	7.6
	49.3	24.4	-1.7	2.7	10.9	9.4	-9.7	85.6				
T3	**0.6**	**1.9**	**4.5**	**3.0**	**0.3**	**0.6**	**4.4**	**5.3**	1.2	0.97	0.88	7.1
	-36.3	-58.4	13.0	-42.1	-28.6	-21.3	37.6	66.5				
T4	**0.6**	**1.4**	**4.8**	**2.4**	**0.3**	**0.6**	**4.9**	**9.8**	1.14	1.03	0.85	7.5
	-50.3	-59.8	5.1	-51.6	-50.2	-29.4	25.7	195.6				
T5	**2.6**	**3.6**	**5.5**	**5.6**	**0.3**	**0.9**	**6.1**	**9.1**	0.9	1.1	0.87	6.1
	48.5	-25.5	30.1	-17.8	16.5	21.3	37.5	40.2				
T6	**1.4**	**1.6**	**4.2**	**2.8**	**0.2**	**0.4**	**3.8**	**4.8**	0.95	0.91	0.99	5.6
	64.1	-57.9	-14.0	-51.4	-46.8	-38.2	-4.7	11.8				
T7	**1.7**	**1.8**	**4.2**	**2.8**	**0.2**	**0.5**	**4.4**	**81.0**	0.81	1.05	0.92	4.7
	48.6	-34.7	18.7	-20.1	26.3	47.0	50.7	2723.1				
T8	**0.2**	**0.1**	**1.2**	**0.4**	**0.1**	**0.1**	**1.1**	**3.8**	1.41	0.87	1.01	8.3
	-95.3	-94.0	-67.3	-92.2	-76.4	-86.1	-74.1	-46.7				
T10	**1.3**	**0.4**	**1.5**	**1.0**	**0.1**	**0.2**	**1.0**	**149.0**	0.59	0.69	1.3	5.8
	-56.4	-32.0	-37.8	-56.9	-34.6	-34.3	-34.5	357.7				

3.4 Discussion

3.4.1 Coastal site T1

The deposition rate of insoluble dust at T1 had significant interannual variations, which could be attributed to variations in wind speed, precipitation, and/or anthropogenic activities. T1 was located on the west side of a hill slope, ~6 km away from the ocean. During 2010-2011, the deposition rate of insoluble dust (18.5 g/m^2/yr) was 50% higher relative to that of 2007-2009 (12.3 g/m^2/yr, Figures 3.2 and 3.3). The insoluble dust at T1 had been hypothesized to be primarily from 1) entrainment of down slope dust, which was mainly weathered silicates, and 2) nearby surface

and subsurface soil due to nearby open-pit mining activities (Wang et al., 2014). However, no significant geomorphology alteration was observed near the city of Mejillones during 2007-2011 (Sargent et al., 2010), therefore, dust from nearby open-pit mining activities should be minimal. Fluctuations in weather conditions, such as increased wind speed, would greatly increase the insoluble dust deposition by increasing the entrainment of particles from the surface (Goudie and Middleton, 1992; Reheis and Kihl, 1995; Shao et al., 1993). The wave height data off the coast supported a higher wind speed during 2010-2011 than 2007-2009. A buoy ~1500 km off the coast of Chile in Southern Pacific Ocean (Station 32ST0, National Data Buoy Center, 2018) measured hourly wave heights during both sampling periods. The average wave heights during 2010-2011 (2.42 ± 0.65 m) were higher than those of 2007-2009 (2.21 ± 0.60 m), corresponding to a ~0.5 m/s increase in average wind speed using the statistical wave forecasting equation (Group, 1988). Besides, the changes in wind speed was likely tied to the occurrence of El Niño since El Niño was suggested to reduce the average wind speeds and precipitation in northern and central Chile (Watts et al., 2017). 2007, 2008, 2010 and 2011 were all moderate to strong La Niña years, but 2009 was a moderate El Niño year (National Weather Service, 2015). Therefore, the average wind speed during 2010-2011 could be higher than during 2007-2009, possibly resulting in a higher dust deposition rate.

The soluble salts deposition rates at T1 had increased by 159% in 2010-2011 (6.0 $g/m^2/yr$, Figure 3.2) relative to 2007-2009 (2.6 $g/m^2/yr$), and all the inorganic ion deposition rates increased, but to different extents (Table 1). The contributions of local soil to the soluble salt depositions were estimated using the ion concentrations in the nearby Morro Mejillones surface soil (Wang et al., 2014). For most ions, less than 4% of ion deposition could be attributed to the local soil deposition, and ~10% K^+ was originated from local soil. Therefore, the 159% increase in the soluble salts deposition rate cannot be explained by the increased soil flux during 2010-2011 (Wang et al. 2014). In the following discussion we have subtracted the amount of salts attributed to local soil to assess the interannual variations of other ion sources at T1.

The 2010-2011 deposition rates of major cations (Na^+, K^+, Mg^{2+} and Ca^{2+}) at T1 were significantly higher than those during 2007-2009, which could, in part, be attributed to the interannual variabilities in sea-salt aerosols (SSA) deposition. SSAs were formed by entraining the seawater droplets into the atmosphere that were generated by bursting air bubbles or tearing off of wave crests. The SSA deposition rates were commonly estimated using the Na^+ deposition rate

(e.g., Li et al., 2018, Norman et al., 1999) for three reasons. First, it is the most abundant cation in seawater (1.08 wt.%, Rees et al., 1978) thus a major component in the SSAs. Second, Na^+ is biologically inactive and is not likely subject to post-depositional chemical losses in arid regions. Third, it has low concentrations in local surface soil (discussed above) and lack any major anthropogenic sources. Using Na^+ concentrations, we suggest the SSA concentration had increased by 75% during 2010-2011 relative to during 2007-2009.

The deposition of SSA at T1 consist of both wet (precipitation and fog) and dry depositions. For any ion, the annual ion deposition rate is quantified by:

$$\text{Ion deposition rate} = p_d C_p + f_d v_f C_f + 365 * v_d C_a \qquad \text{Eq. 1}$$

The first two terms in Eq. 1 are the wet deposition rate and the latter is the dry deposition rate. In Eq.1, p_d is the annual precipitation depth (m), C_p is the molar concentration of a SSA ion in rain (mmol*m^{-3}), f_d is the number of fog days per year, v_f is the fog deposition velocity (m/day), C_f is the concentration of a SSA ion in fog water (mmol/m^3), v_d is the dry deposition velocity (m/day) and C_a is the concentration of a SSA ion in the atmosphere (mmol/m^3). An increase in precipitation, fog deposition velocities, and/or SSA concentrations would result in an increase in annual ion deposition rates, therefore we evaluated any potential increase in these terms during 2010-2011 relative to 2007-2009.

Changes in the annual precipitation depth (p_d) was determined using archived data from ASA (Andres Sabella Airport, NOAA Climate Data Online Database, 2018) station, located ~30 km south of the T1 site (Figure 3.1). Annual precipitation depth at ASA was 1.0 mm/yr during 2007-2009 and 4.3 mm/yr during 2010-2011. The contribution of precipitation to total deposition, however, was small. Assuming the precipitation contains 20 ppm Na^+, an upper limit for Na^+ concentrations in coastal rain (Brecciaroli et al., 2012), the precipitation only contributed 3.3 mmol/m^2/yr of Na^+ during 2010-2011 (8% of total Na^+ deposition) and 0.5 mmol/m^2/yr of Na^+ during 2007-2009 (2% of total Na^+ deposition). This was a net increase in Na^+ deposition of only 2.8 mmol/m^2/yr, which could only account for 15% of the observed increase (75%) in the Na^+ deposition rate.

Changes in annual fog water deposition depth ($f_d v_f$) was also determined using archived meteorology data collected at ASA. Fog deposition was estimated by assuming fog would form when the minimum daily temperature was lower than the daily dew point and v_f was the same in

both study periods. Daily temperature minimums at T1 (T_{min}) were estimated using the minimum temperatures at ASA (T_0), the altitude difference between T1 and ASA (h=0.454 km), and the dry adiabatic lapse rate (L=-9.8 K/km): $T_{min}=T_0+h*L$. By comparing T_{min} and the daily dew point, fog events likely occurred 186 days/yr during 2007-2009 and 176 days/yr during 2010-2011. Using an estimated fog deposition of 0.1 mm per event (Merriam, 1973), and measured fog water Na^+ concentration of 5 ppm (Schemenauer et al., 1992), we estimated that the Na^+ flux from fog deposition was 4.2 mmol/m^2/yr during 2007-2009 and 3.8 mmol/m^2/yr during 2010-2011. This resulted in a 5% decrease, also cannot explain the observed 75% increase in SSA deposition in 2010-2011.

The higher SSA deposition at T1 may be due to an increased SSA dry deposition flux (v_d*C_a). The dry deposition velocity (v_d) of SSA deposition was often treated as a constant (Seinfeld et al., 1998, Tedeschi et al., 2017) since most SSA masses are in the large particle fraction (Liang et al., 2016; McDonald et al., 1982). Therefore, the changes in SSA should be mainly due to changes in SSA concentrations (C_a), which were strongly affected by wind speed (Jaeglé et al., 2011; Kishcha et al., 2011; Lewis and Schwartz, 2004; Li et al., 2018; Mårtensson et al., 2003; McDonald et al., 1982; O 'dowd et al., 2007; Zakey et al., 2008). In the open ocean, SSA concentration is positively correlated to the wind speed. For example, Dror et al. (2018) observed a linear relationship between annual average wind speed and SSA concentration at South Pacific Ocean, showing a 0.4 m/s increase in wind speed would increase SSA concentration by ~10%. Using the wave height data (discussed above), which corresponding to an average wind speed increase of ~0.5 m/s in the 2010-2011 relative to 2007-2009, we suggested that the average SSA concentration in the open ocean during 2010-2011 should be 10% - 20% higher than during 2007-2009. While significant, this predicted increase was still significantly lower than our observed 75% increase at T1.

Unlike open ocean, the SSA production at coastal regions was also affected by the depth and topography of the sea floor (Lewis and Schwartz, 2004). As a result, the effect of wind speed on the concentrations of SSAs was no longer a simple linear relationship (Lewandowska and Falkowska, 2013). Exponential relationships between the wind speed and SSA concentrations had been observed along coastal areas (McDonald et al., 1982; Lewandowska and Falkowska, 2013). McDonald et al. (1982) suggested that an increase in wind speed from 3.4 m/s to 10 m/s could increase the SSA concentration by 6.7 times along the coast. Using the data in McDonald et al.

(1982) and assuming SSA concentration increases exponentially with increasing wind speed, we estimated that 0.5 m/s increase in coastal wind speed could increase the SSA concentration by 15.2%. Lewandowska and Falkowska (2013) also noted an exponential increase of SSA concentration (i.e., Na^+ concentration) with increased wind speed (v) along coastal zones in southern Baltic Sea: $[Na^+] = 0.3*e^{0.55*v}$ when v>7 m/s and $[Na^+] = 4.3*e^{0.30*v}$ when v<7 m/s and v>5 m/s. Using these equations, we calculated that an increase in wind speed of 0.5 m/s would result in 16-32% increase of SSA flux. The combination of above factors (15% increase of SSA from wet deposition, 10%-20% increase of SSA produced in the open ocean and 16-32% increase of SSA produced on the coast) still cannot fully account for the observed 75% increase in our sampling period, indicating other factors, i.e., strong wind events from the ocean, were important but unaccounted. Future study should use more sophisticated models to better quantify the emission of SSAs in the coastal areas (e.g., Callaghan, 2013; Demoisson et al., 2013) but it is beyond the scope of our work.

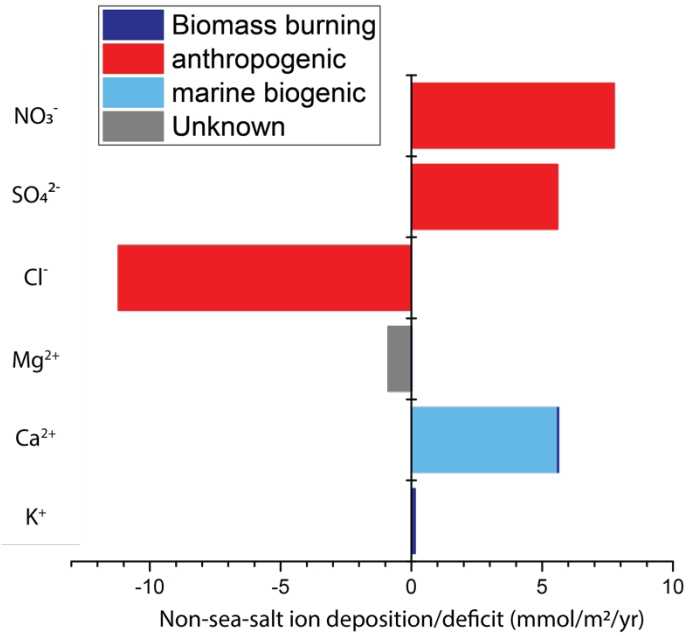

Figure 3.4 NSS ions depositions (or SSA deficit) at T1. Positive values indicate non-sea-salt ion input (EF>1) and negative values indicate deficit from sea salt composition. Different colors represent different processes that might lead to SSA deficit or serve as non-sea-salt sources.

Non-sea-salt (NSS) soluble salts also contributed to the deposition of some inorganic ions at T1. The EFs of SO_4^{2-}, K^+ and Ca^{2+} were higher than 1, indicating extra sources of these ions other than SSAs at T1 (Table 3.2 and Figure 3.4). Additionally, since SSAs contain little NO_3^- (Rees et al., 1978), the observed NO_3^- at T1 was also originated from NSS sources. While NSS-SO_4^{2-} and NO_3^- were mainly produced by atmospheric oxidation of NO_x and SO_2 gases (see detailed discussions below), NSS-K^+ and

Table 3.2 Enrichment Factors of each ion at T1

Ion	EF
Na^+	1.00
K^+	1.17
Mg^{2+}	0.81
Ca^{2+}	7.26
Cl^-	0.76
SO_4^{2-}	4.14

NSS-Ca^{2+} were likely directly emitted during several processes, including biomass burning, anthropogenic emissions and marine biogenic activities.

The NSS-K^+ deposition rate was calculated (NSS-K^+=$[K^+]_{T1}$ – $[Na^+]_{T1}$×$(K^+/Na^+)_{seawater}$, where $(K^+/Na^+)_{seawater}$ = 0.0218, Rees et al., 1978) to be 0.15 mmol/m^2/yr during 2010-2011, decreased by ~63% compared to during 2007-2009 (0.41 mmol/m^2/yr). The origins of NSS-K^+ at T1 were possibly forest biomass burning in central Chile and anthropogenic emissions (Figure 3.4). Forest biomass burning in central Chile could be a major source of NSS-K^+ deposition (Bańales-Seguel et al., 2018; Pachon et al., 2013). The NSS-K^+ in aerosols (~40 ng/m^3) at Paposo, a small coastal town ~150 km away from Antofagasta, was suggested to be mainly originated from biomass burning (Chand et al., 2010). Meantime, anthropogenic emissions, especially coal burning, could be a potential NSS-K^+ source. Coal burning ash was suggested to contain 0.19% wt. to 0.71% wt. K^+ (Zhang et al., 2018), which could account for some of the K^+ deposition at T1 but was difficult to quantify. The number of forest fires in Chile had decreased from 6092 events per year during 2007-2009 to 4511 events per year during 2010-2011 (National Forest Corporation in Chile, 2018, in Spanish), and the energy production rate at Edelnor Power Plant located ~10 km from T1 the had decreased by 12% from 2007-2009 to 2010-2011 (Global Energy Observatory, 2011). These suggested a decreased NSS-K^+ emissions during 2010-2011, in agreement with the observed lower NSS-K^+ deposition rate.

The NSS-Ca^{2+} increased by 58% from 3.6 mmol/m^2/yr during 2007-2009 to 5.6 mmol/m^2/yr during 2010-2011. Using the emission factors of K^+ (0.29 g/kg) and Ca^{2+} (0.085 g/kg) during biomass burning (Akagi et al., 2011) and assuming all NSS-K^+ at T1 was originated from biomass burning, the maximum contribution of biomass burning NSS-Ca^{2+} was calculated to be 0.044 mmol/m^2/yr. This small contribution was corresponding to 1.2% of total NSS-Ca^{2+}, suggesting biomass burning was not an important NSS-Ca^{2+} source (Figure 3.4). Also, the NSS-Ca^{2+} was not likely derived from the entrainment of gypsum minerals because the nearest gypsum-rich salt playas existed >80 km away from T1 and on the east side of the Costal Range (Rech et al., 2003; Stoertz and Ericksen, 2009; Wang et al., 2014) from which the gypsum transportation should be substantially blocked. Therefore, we suggest marine $CaCO_3$ input from the microorganisms with calcified shells on the surface layer of the ocean might be the major source of NSS-Ca^{2+} (Fitzgerald, 1991; Hardy, 1982; MacIntyre, 1974; Wang et al., 2014). Although $CaCO_3$ aerosols were less soluble in water, they could form $Ca(NO_3)_2$ or $CaSO_4$ with soluble Ca^{2+}

ions via acid displacement reactions in the atmosphere (see discussion below). Additionally, since marine biogenic $CaCO_3$ particles would be entrained into the atmosphere similar to SSAs, their variation in deposition rates should also be similar: the observed 58% increase in NSS-Ca^{2+} was in general agreement with the 75% increase in SSAs, again supporting our hypothesis that NSS-Ca^{2+} was probably marine biogenically originated.

The Mg^{2+} deposition rate was 3.8 mmol/m^2/yr during 2010-2011, slightly depleted relative to seawater (EF_{Mg} =0.8), and the Mg^{2+} deficit (0.9 mmol/m^2/yr) decreased by 41% compared to during 2007-2009 (1.5 mmol/m^2/yr, EF_{Mg}=0.5, Figure 3.4). Biomass burning could be a potential NSS-Mg^{2+} source and was calculated (similar to biomass burning Ca^{2+}) to be ~0.02 mmol/m^2/yr. However, a depletion of Mg^{2+} relative to SSAs was observed, which was also previously observed during 2007-2009 and attributed to the formation of $MgCO_3$ and $Mg(OH)_2$ inside the dust collection pan during fog events (Wang et al., 2014). Alternatively, the formation of Mg complexes with lipids, fatty acids and saccharides during the formation of SSAs (Jayarathne et al., 2016) might also resulted in the observed Mg^{2+} depletion. These Mg complexes were less soluble (or insoluble) due to their high molecular weight, thus some Mg might not be dissolved and were removed during the filtration, resulting in a lower dissolved Mg concentration relative to seawater.

The Cl^- deposition rate during 2010-2011 also increased relative to during 2007-2009 because of a higher SSA flux, but Cl^- was very depleted relative to seawater (EF_{Cl} =0.76, Figure 3.4). This chloride deficit was commonly observed in marine aerosols (Kerminen et al., 1998; Laskin et al., 2012; McInnes et al., 1994; Wang et al., 2014) and was due to the loss of Cl^- (and CO_3^{2-}) in aerosols via acid displacement reactions (Ayers et al., 1999; Metzger et al., 2006; Newberg et al., 2005):

$$HNO_{3(g)} + NaCl_{(p)} \rightarrow NaNO_{3(p)} + HCl_{(g)} \quad (R1)$$

$$H_2SO_{4(g)} + 2NaCl_{(p)} \rightarrow Na_2SO_{4(p)} + 2HCl_{(g)} \quad (R2)$$

$$2HNO_{3(g)} + CaCO_{3(p)} \rightarrow Ca(NO_3)_{2(p)} + H_2O + CO_{2(g)} \quad (R3)$$

$$H_2SO_{4(g)} + CaCO_{3(p)} \rightarrow CaSO_{4(p)} + H_2O + CO_{2(g)} \quad (R4)$$

Assuming SSA was the sole source of Cl^- at T1, the Cl^- deficit was calculated to be 11.2 mmol/m^2/yr, significantly less than the 17.9 mmol/m^2/yr deficit during 2007-2009. This may be because CO_3^{2-} is kinetically and thermodynamically favorable to be displaced by HNO_3 or H_2SO_4 relative to Cl^- (Clarke and Karani, 1992). Assuming that CO_3^{2-} is present as $CaCO_3$ then the amount of CO_3^{2-} displaced should be equal to the amount of NSS-Ca^{2+}, i.e. 5.6 mmol/m^2/yr. The total

negative charge deficit from Cl^- (11.2 mmol/m^2/yr) and CO_3^{2-} (5.6 mmol/m^2/yr) in milliequivents (meq) was 11.2+5.6*2=22.4 meq/m^2/yr. This is close to the total amount of NO_3^- (5.6 meq/m^2/yr) and NSS-SO_4^{2-} (7.8*2=15.6 meq/m^2/yr) measured at T1.

The deposition of NO_3^- at T1 must be largely originated from anthropogenic N emissions and any interannual variation must be due to a change in N emissions (Alexander et al., 2009; Fitzgerald, 1991). The deposition rate of NO_3^- at T1 during 2010-2011 was 5.6 mmol/m^2/yr, a ~61% increase compared to during 2007-2009 (Wang et al., 2014), which should be attribute to an increased local NO_x emission (Galloway, 1985; Galloway et al., 1996). In November 2010 a new nitric acid plant was built near the city of Mejillones (Panna 4, Enaex S.A., Figure 3.1), which was only 10 to 15 km away from T1 (Enaex Memoria Annual, 2011). Nitric acid plants emitted NO_x, N_2O and trace amounts of HNO_3 mist (Wood and Cowie, 2004), which could significantly increase local deposition rate of NO_3^- (Kumar et al., 2005; Schindler et al., 2006). This extra emission occurred in 14 of our 24-month sampling period (Nov. 2010 to Dec. 2011). Assuming the NO_3^- deposition rate in the first 10 months was the same as the 2007-2009 value, then the NO_3^- deposition rate due to the nitric acid plant could be as high as 7.1 mmol/m^2/yr, twice the NO_3^- deposition rate of 2007-2009. This increase was supported by the calculated HNO_3 emission from the plant that was calculated from the annual yield (800,000 tons/yr, Panna 4, Enaex S.A.; Enaex Memoria Annual, 2011, in Spanish) and the estimated NO_x emission factors ranging from 0.5-3 kg/ton (Cheremisinoff, 2016) by assuming the emitted HNO_3 were evenly spread within a 50 km radius. The HNO_3 deposition due to the plant ranged from 0.81 to 4.85 mmol/m^2/yr, consistent with the observed increase of 3.6 mmol/m^2/yr.

Both SS-SO_4^{2-} and NSS-SO_4^{2-} were important sulfate sources at T1. The SS-SO_4^{2-} deposition rate was 2.5 mmol/m^2/yr, and the NSS-SO_4^{2-} deposition rate (7.9 mmol/m^2/yr) accounted for 76% of total SO_4^{2-} deposition rate at T1 during 2010-2011, similar to that of 8.1 mmol/m^2/yr in 2007-2009. The NSS-SO_4^{2-} at T1, accounting for 74% of total Cl^- and CO_3^{2-} deficit, was also suggested to directly impact the number of cloud condensation nuclei (Lana et al., 2011; Li et al., 2018), and therefore, was important to understand its sources. Volcanic sources were ignored because of there was no nearby volcanic eruptions during the sampling period. Therefore, NSS-SO_4^{2-} were mainly sourced from oxidation of SO_2, which was either directly emitted from anthropogenic activities, or formed from oxidation of dimethyl sulfide (DMS) produced during marine biological processes (Li et al., 2018).

$\delta^{34}S_{sulfate}$ values were used to evaluate the relative contribution of anthropogenic and biogenic emissions to the NSS-SO_4^{2-} deposition rate. A two-component isotope mixing model was first used to evaluate the $\delta^{34}S$ of NSS-SO_4^{2-} ($\delta^{34}S_{NSS}$):

$$f_{SS}\,\delta^{34}S_{SS} + f_{NSS}\,\delta^{34}S_{NSS} = \delta^{34}S_{T1} \quad \text{Eq. 2}$$

$$f_{SS} + f_{NSS} = 1 \quad \text{Eq. 3}$$

where f_{SS} and f_{NSS} are the mole fractions of SS-SO_4^{2-} (0.24) and NSS-SO_4^{2-} (0.76), respectively; the $\delta^{34}S$ value of SS-SO_4^{2-} ($\delta^{34}S_{SS}$) is 21.0±0.1‰ (Rees et al., 1978), and the measured $\delta^{34}S_{sulfate}$ value at T1 ($\delta^{34}S_{T1}$) is 4.0‰. This resulted in the $\delta^{34}S_{NSS}$ of -1.4‰. Sulfate derived from anthropogenic coal burning had $\delta^{34}S$ values ranging from -3‰ to +3‰ (Norman et al., 1999), while biogenic DMS-derived SO_4^{2-} had the $\delta^{34}S$ values of ~+18‰ (Sanusi et al., 2006; Patris et al., 2007). The calculated $\delta^{34}S_{NSS}$ of -1.4‰ suggested that regional anthropogenic SO_2 emissions (mostly coal burning at Edelnor Power Plant located ~10 km from T1) should be the dominant NSS-SO_4^{2-} source at T1: the contribution of anthropogenic emission was at least 92% (~7.3 mmol/m^2/yr) using the lower limit of anthropogenic $\delta^{34}S$ value (-3‰) and could be as high as 100% (~7.9 mmol/m^2/yr). Anthropogenic sulfate deposition rate at T1 were previously estimated by Wang et al. (2014) using the inventory calculations, which suggested a range of 3.1 mmol/m^2/yr to 5.8 mmol/m^2/yr, lower than our estimation. This discrepancy could be attributed to two possibilities. The first possibility was that the anthropogenic emissions during our sampling period had increased since the 2007-2009 period, possibly due to significantly higher SO_2 emissions at the Edelnor power plant. However, the energy production rate of the Edelnor power plant had decreased by 12% from 2007-2009 to 2010-2011 (Global Energy Observatory, 2011), and the SO_2 emission was unlikely to increase considering the anthropogenic S emission was usually proportional to the energy production in power plants. Alternatively, we suggest the flux calculation using emission inventory may underestimate the NSS-SO_4^{2-} deposition. Wang et al. (2014) calculated the SO_2 flux at T1 by assuming the emitted SO_2 was evenly distributed in a circle area with radius of 180-216 km, which was likely to underestimate the SO_4^{2-} deposition rate at T1 since T1 was only 10 km from the power plant.

The $\delta^{34}S_{T1}$ was significantly lower than the $\delta^{34}S$ of sulfate extracted from surface soil samples (Figure 3.5) along a 50 km long west-east transect starting near Antofagasta by Rech et

al. (2003). Sulfate in soils located ~30 km to the south of T1 site had $\delta^{34}S_{sulfate}$ values of +15‰ - +18‰, which were attributed to SS-SO_4^{2-} being the main source of soil sulfate near the coast. Our data suggested that anthropogenic sulfate depositions have recently dwarfed natural SO_4^{2-} deposition along the coast and is a further evidence of the Anthropocene (Capaldo et al., 1999; Crutzen, 2002; Li et al., 2018; Wadleigh, 2004).

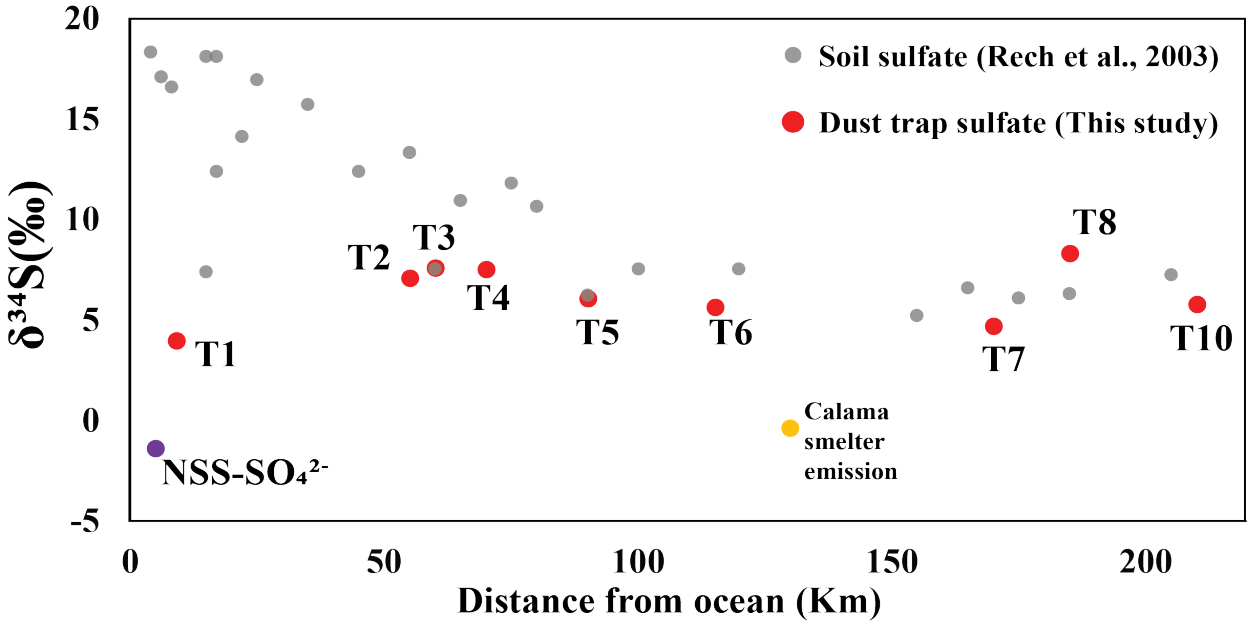

Figure 3.5 $\delta^{34}S_{sulfate}$ values of atmospheric depositions at T1-T10 (red dots) comparing with $\delta^{34}S_{sulfate}$ values of nearby soil gypsum in Rech et al. (2003).

3.4.2 Inland sites T2-T8

The 2010-2011 deposition data confirmed that the atmospheric depositions at T2 to T8 sites were likely controlled by local entrainment of insoluble dust and soluble salts as suggested by (Wang et al., 2014). Oceanic inputs at our inland sites were small because of fast settlement of large particles and efficient blocking by the Coastal Range (Wang et al., 2014, Rech et al., 2003), evidenced by the fact that the deposition rate of Na^+ at T2 was 90% lower than T1. Similarly, the material from the Andes was also unlikely to be transported to the inland sites for several reasons. First, the deposition rates of salts at the Andean site (T10, see discussion in 4.3) were much lower than the inland site traps, indicating very limited input from the Andean to the Atacama. Secondly, due to the daytime upslope air flow caused by the fast heating of the Andean west slopes, namely

the “Andean pump effect” (Rutllant et al., 2013), the seaward air mass movement should be low and not conducive to the inland transportation of Andean inputs. Instead, the depositions at these inland sites were more likely derived from local entrainments of surface soil and anthropogenic emissions.

Insoluble dust deposition at the inland sites showed significant variations between the two sampling periods (50%-100% increase at T2-T6 sites, 46% decrease at T8 site, and 27 times increase at T7), which was caused by a combination of increased wind speed and anthropogenic activities. Significant spatial variations among different sites (3.8-80.9 $g/m^2/yr$) were again observed. Since all the traps were set in the open field with small geomorphological variations among the locations of traps (Wang et al., 2014), these spatial variations were unlikely caused by biased sampling but reflected the average atmospheric depositions of the region. However, all the sites except for T8 (discussed below) displayed significant increases in insoluble dust deposition rates during 2010-2011, which can be attributed to a combination of higher average wind speed (Watt et al., 2017) and enhanced anthropogenic activities. The archived wind speed data at Calama site (Figure 3.1, NOAA Climate Data Online Database, 2018) showed that the average wind speed during 2010-2011 (14.9±2.0 m/s, n=630) was statistically significantly higher ($p<0.05$) than those of 2007-2009 (14.6±2.0 m/s, n=811). This increased wind speed can at least partially explain the general increasing trend in insoluble dust deposition at T2-T6, similar to the increased insoluble dust deposition at the coastal site (T1). Similar interannual variations have also been observed at several desert sites in California (Reheis, 1997; Reheis and Kihl, 1995), probably owing to the susceptibility of surface soil to local entrainment in arid environments. Meanwhile, the huge increase in insoluble dust deposition at T7 (27 times increase) was possibly caused by nearby anthropogenic activities. The satellite images near T7 (Figures 3.6A, B) suggested that a major new mine located ~ 60 km SW from T7 came into operation between 2007 and 2011. Meantime, the size of another open-pit gravel mine located 10 km from T7 expanded significantly from 2007 to 2011 (Figures 3.6C, D). These mining activities could significantly increase local soil entrainment and insoluble dust deposition rate at T7.

The soluble salts at T2-T8 were mainly in the forms of Na(Cl, NO_3) and $CaSO_4$ with the molar ratios of both $Na^+/(Cl^-+NO_3^-)$ and Ca^{2+}/SO_4^{2-} close to 1 (except for T8, see discussion below). The Ca^{2+}/SO_4^{2-} molar ratios in these traps of ~1 (i.e. 0.87 to 1.10) suggested that $CaSO_4$ was

mostly sourced from the widespread gypsum minerals in local surface soil (Ericksen, 1981, Rech et al., 2003). Na^+ and Cl^- were likely originated from chloride deposits in the nearby salt playas.

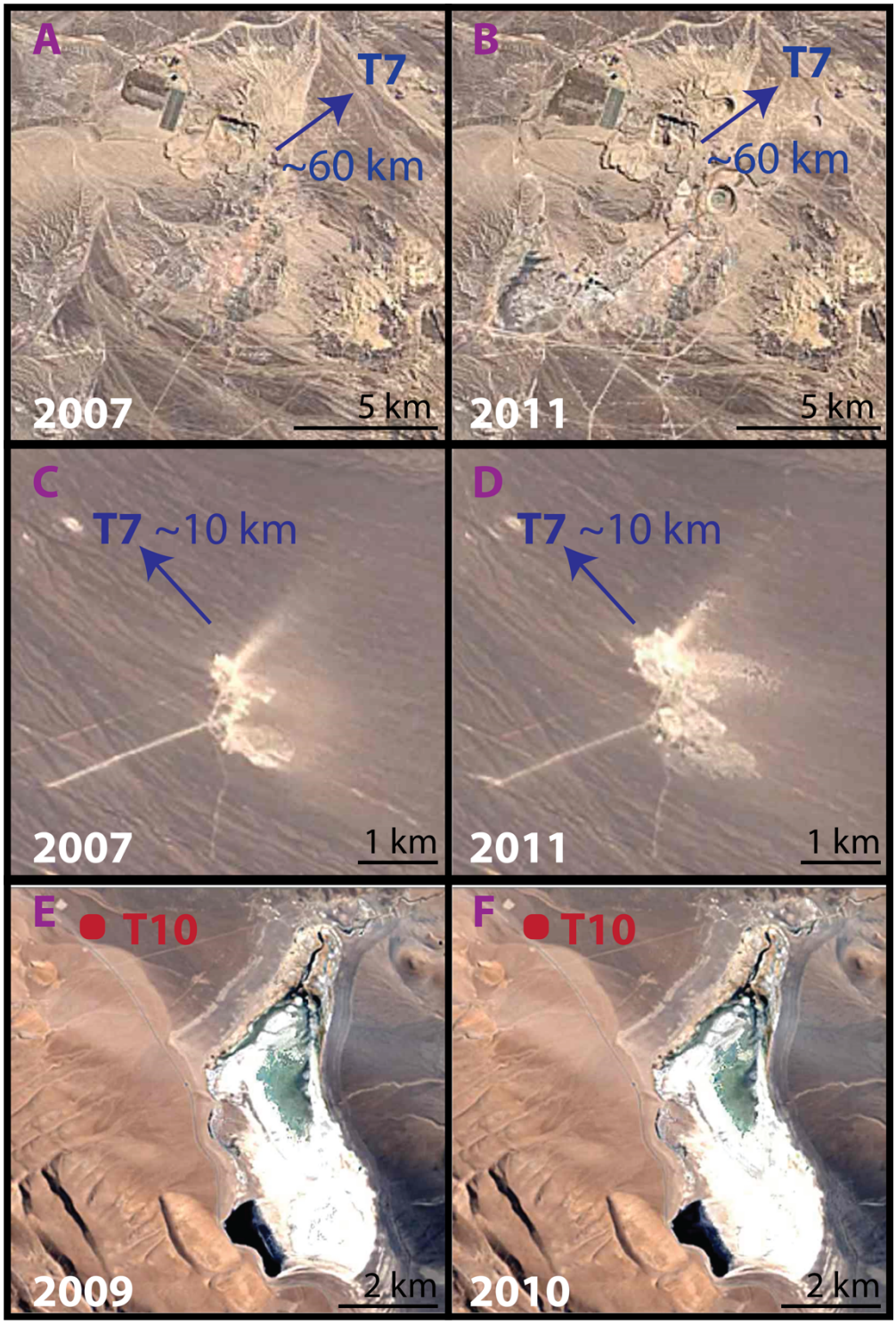

Figure 3.6 Google Time Lapse images for 3 locations near sampling sites: A, B: a mine site located ~ 60 km SW from T7; C, D: an open-pit mine located 10 km from T7; E, F: the lake next to T10.

For example, the Salar de Pampa Blanca located only 7.5 km from T5 (Stoertz and Ericksen, 2009) likely contributed to the highest deposition rates of Na^+ and Cl^- at T5 among the seven inland sites. The NO_3^- deposition at T2-T7 (1.4 to 3.6 mmol/m^2/yr) can originate from both anthropogenic NO_x emissions and local soil entrainment (Michalski et al., 2003). The Cl^-/Na^+ ratio at T2-T7 averaged at 0.42±0.15, close to the average Cl^-/Na^+ ratio (0.43) in the Atacama soil (Grossling and Ericksen, 1971; Michalski et al., 2004), supporting that most Na^+ and Cl^- should be originated from local soil and salt playas. In 2010-2011, the deposition rates of $CaSO_4$ at T2 and T6 slightly decreased by 5.7%-9.4% while other traps showed increases of 15.4%-34.7%; the Na^+ deposition rate at T2 increased by 2.7% and other traps showed decreased depositions by 17.8%-51.6%. This overall increased $CaSO_4$ deposition and decreased $Na(Cl,NO_3)$ deposition can also be explained by the increased wind during 2010-2011. Most Atacama soil had a well-developed gypsum crust on the surface, while the nitrate and chloride were usually observed beneath the surface layer (Wang et al., 2014). As a result, stronger wind would result in more entrainment from the surface layer and less entrainment from the deeper soil layers. However, these ratios were significantly higher than the Cl^-/Na^+ ratios observed in 2007-2009 (0.25±0.07), where (Wang et al., 2014) suggested that significant acidic displacement reaction had occurred. This higher ratio, along with lower NO_3^- deposition rate in 2010-2011 (38% lower than 2007-2009), suggested weaker acidic displacement during our sampling period. This may at least partially be attributed to a drier climate during 2010-2011 since the acidic displacement reaction will be greatly inhibited at a lower relative humidity (RH, Laskin et al., 2012): at the Calama site (near T6 & T7): the average RH during 2007-2009 was 33.5% while the average RH during 2010-2011 was 27.6%.

The $\delta^{34}S_{sulfate}$ at T2-T4 ranged from 7.1‰ to 7.6‰, similar to those of gypsum minerals from nearby surface soil observed in Rech et al. (2003, Figure 3.5), corroborating the major source of sulfate in these inland dust traps was local soil entrainment. A decrease in $\delta^{34}S_{sulfate}$ from 7.1‰ to 4.7‰ was observed at T5-T7, possibly due to the mixing of gypsum mineral and secondary sulfate oxidized from SO_2 emitted from Chuquicamata smelter near T7, where the $\delta^{34}S$ of sulfide minerals at this mine sites ranged from -4.7‰ to +4.0‰ (U.S. Geological Survey, 2005). If we assume the $\delta^{34}S$ value of sulfate in local soil was 7.4‰ (average value of T2-T4), and the secondary sulfate from Chuquicamata smelters had a $\delta^{34}S$ value of -0.4‰, the contribution of sulfate from anthropogenic SO_2 at T5, T6, T7 would be 17%, 23% and 35%, respectively.

The decrease in both insoluble dust and soluble salts depositions at T8 during 2010-2011 may be attributed to a combination of lower atmospheric deposition and the loss of deposition sample during the sampling period. The insoluble dust flux at T8 had decreased by 47% in 2010-2011 while the soluble salts deposition had a much higher decrease of 80%, from 0.92 $g/m^2/yr$ (highest among T2-T8) during 2007-2009 to 0.18 $g/m^2/yr$ (lowest among T2-T8). We suggest these low values should at least partially be attributed to the loss of some insoluble dust and soluble salts by leaching during the sampling period. Two facts could support this hypothesis. First, Na^+, Cl^-, and NO_3^- depositions had decreased by ~92-95% while Ca^{2+} and SO_4^{2-} decreased by only 67% and 74% (Figure 3.3), and this discrepancy was likely resulted from leaching since Na(Cl, NO_3) was more soluble and subject to leaching losses than $CaSO_4$. Second, the $\delta^{34}S_{sulfate}$ at T8 showed the highest value of 8.3‰ among the inland sites (Figure 3.5), significantly higher than at T7 (4.7‰) and adjacent surface soil (5.4‰, Rech et al., 2003). This is likely caused by the enrichment in $\delta^{34}S_{sulfate}$ during dissolution of gypsum minerals, with the equilibrium fractionation factor between solid and dissolved $CaSO_4$ of ~2‰ at 273K (Van Driessche et al., 2016).

3.4.3 Andean site T10

The insoluble dust deposition rate (149.0 $g/m^2/yr$) at T10 during 2010-2011 was the highest among all sites and increased by 3.6 times compared to that of 2007-2009 (Figure 3.2), probably due to the interannual variations in precipitation. T10 was located at a valley on the Andean altiplano receiving significant amount of precipitation (MAP ~150 mm). The insoluble dust was likely from local soil entrainment by winds; hence its deposition rate would be strongly affected by both wind speed and precipitation. However, there was no wind speed or precipitation observation available near T10. We used the ERA-interim reanalysis data (Dee et al., 2011) to investigate the variations in wind speed. The modelled average wind speeds were 1.59 m/s during 2007-2009 and 1.61 m/s during 2010-2011, therefore it might not be able to account for the 3.6 times increase in insoluble dust flux. The precipitation during 2010-2011 likely decreased comparing to 2007-2009, since the size of local lakes located near T10 was observed to have deceased in December of 2010 (Figure 3.6E, F) compared to that in January of 2009. This observation agreed with the occurrence of El Niño in 2009: El Niño has been linked to increased precipitation in the Andean area (Bozkurt et al., 2016; Mason and Goddard, 2001; Ropelewski and Halpert, 1989; Valdés-Pineda et al., 2016), and therefore the average precipitation during 2007-

2009 (2 years of La Niña and 1 year of El Niño) was likely higher than that of 2010-2011 (2 years of La Niña). The decreased precipitation at T10 could increase wind erosion and thus significantly increase the insoluble dust flux (Reheis and Kihl, 1995).

In contrast with T1-T8, the soluble salts depositions at T10 had decreased. This is because the soluble salts at T10 were mostly from wet deposition, mainly snow, as suggested by (Ginot et al., 2001; Houston, 2007; Wang et al., 2014). The dry deposition had little contribution to the total salt deposition at T10 because 1) concentrations of soluble ions in dust (local soil) near T10 were extremely low (0.0005 mmol/g Cl^-, 0.0004 mmol/g SO_4^{2-} and undetectable NO_3^-, Wang et al., 2014) thus the salt from dust only accounted for <6% of total Cl^- and <5% of total SO_4^{2-}; 2) T10 was distant from both the ocean and anthropogenic activities, thus lacking SSAs or anthropogenic secondary aerosols. Meantime, wet deposition, especially snow deposition, played an important role in the salt deposition at T10 because snow could incorporate ions from a few reservoirs, such as NaCl and $CaSO_4$ from the salt lakes (e.g., Tara Lake, Wang et al., 2014) on the Andean plateau. In 2010-2011, the deposition rates of Na^+, Cl^-, Ca^{2+}, SO_4^{2-} decreased by 34% to 57% relative to 2007-2009, which should be attributed to the decreased precipitation at T10 during 2010-2011.

The $\delta^{34}S_{sulfate}$ at T10 was 5.8‰, close to the $\delta^{34}S$ value of gypsum at Tara Lake (5.2‰, Risacher et al., 2011), again supporting that the origin of sulfate deposition was local gypsum. Precipitations could incorporate some gypsum from nearby salt lakes and deposit back to the surface (Wang et al., 2014), the $\delta^{34}S$ value of which was also similar to the $\delta^{34}S$ values of soil gypsum (5.2-7.5‰) in the Atacama (Rech et al., 2003), further evidencing that the surface soil gypsum in the Atacama Desert was probably originated from local salt lakes. The salt-rich soil was either formed via subsurface chemical weathering processes (Rech et al., 2003), or other deeper soil development processes, such as groundwater flow (Camron and Leybourne, 2005). The salts were then transported either directly by wind as insoluble dust across the Atacama Desert (T2-T8) or incorporated into precipitation (at T10) and transported within the Andes, then deposited onto the surface.

The NO_3^- deposition rate at T10 were 0.37 mmol/m^2/yr during 2010-2011, slightly lower than 0.54 mmol/m^2/yr during 2007-2009, which also could be due to the decrease in precipitation. These values are close to the NO_3^- deposition rate at the Torres del Paine National Park in southern Chile (0.36 mmol/m^2/yr, Galloway et al., 1996), which is a remote coastal site with minor anthropogenic activities, suggesting minimal anthropogenic N emission at T10 (Wang et al.,

2014). In remote areas, N could generally derive from soil emissions (nitrification and denitrification), lightning, lower stratosphere mixing and long-distance transportation of peroxyacetyl nitrate (PAN) at the top of troposphere (Crutzen, 1979; Galloway et al., 2004; Holland et al., 1999; Singh et al., 1985; Singh and Hanst, 1981). The 31% decrease of NO_3^- in 2010-2011 is similar to the decrease of Na^+, Cl^-, Ca^{2+}, SO_4^{2-} depositions, indicating that these deposition rates were likely controlled by wet deposition.

3.5 Conclusions

In this work we investigated the sources, compositions and interannual variabilities of atmospheric depositions across the Atacama Desert. The nine dust trap sites across the Atacama Desert displayed significant spatial variations in atmospheric deposition because of their different geomorphological features and the characteristics sources at each site. The atmospheric deposition at coastal site T1 mainly consisted of local soil (as insoluble dust) and sea-salt aerosols (as soluble salts). NSS-SO_4^{2-} and NO_3^- at T1 were mainly originated from anthropogenic emissions, then entered particle phase via acidic displacement reaction. At inland sites T2-T8, the insoluble dust was from local soil entrainment and the soluble salts were likely originated from nearby salars and salt lakes. The insoluble dust deposition at the Andean site (T10) was also dominated by local soil but the soluble salts were mainly from wet depositions. The rate of atmospheric deposition (both insoluble dust and soluble salts) display strong variations between the two sampling periods. At the coastal site T1, the deposition rates of both insoluble dust and salts during 2010-2011 had increased significantly comparing to during 2007-2009, due to higher wind speeds. Anthropogenic NO_3^- also had increased as a result of higher NO_x emissions from a newly built nitric acid plant near T1. At the inland sites T2-T8, the increased insoluble dust and gypsum depositions resulted from a windier and drier climate in the Atacama during 2010-2011. In the meantime, a drier climate at the Andean site (T10) likely had resulted in a higher insoluble dust deposition rate and a lower soluble salts deposition rate.

Our observation confirmed that the insoluble dust at all the sampling sites was mainly originated from local surface soil and weathered material. The salt depositions were strongly impacted by the ocean input in the coastal region, but in inland areas the erosions of local salars and salt lakes were more important. Shifted climate conditions (such as wind speed and

precipitations) can impact the flux of both insoluble dust and soluble salts, and the dust fluxes were more easily to be influenced than salt fluxes.

Anthropogenic activities impacted the atmospheric depositions across the Atacama in two ways. First, the open-pit mining activities greatly increased the dust flux at nearby areas, as suggested by the observed high dust flux at T7 during our sampling period. Second, anthropogenic SO_2 and NO_x formed sulfate and nitrate aerosols, which increased SO_4^{2-} and NO_3^- deposited in the Atacama Desert. Our isotopic evidence suggested that the SO_4^{2-} originated from smelters contributed up to 35% of total sulfate in nearby dust traps.

3.6 References

Akagi, S.K., Yokelson, R.J., Wiedinmyer, C., Alvarado, M.J., Reid, J.S., Karl, T., Crounse, J.D., Wennberg, P.O., 2011. Emission factors for open and domestic biomass burning for use in atmospheric models. Atmos. Chem. Phys. 11, 4039–4072

Alexander, B., Hastings, M.G., Allman, D.J., Dachs, J., Thornton, J.A., Kunasek, S.A., 2009. Quantifying atmospheric nitrate formation pathways based on a global model of the oxygen isotopic composition ($\Delta^{17}O$) of atmospheric nitrate. Atmos. Chem. Phys. 9, 5043–5056.

Álvarez, F., Reich, M., Snyder, G., Pérez-Fodich, A., Muramatsu, Y., Daniele, L., Fehn, U., 2016. Iodine budget in surface waters from Atacama: Natural and anthropogenic iodine sources revealed by halogen geochemistry and iodine-129 isotopes. Appl. geochemistry 68, 53–63.

Astrid A. Sanusi, Ann-Lise Norman, Carolyn Burridge, Moire Wadleigh, and, Tang, W.-W., 2006. Determination of the S Isotope Composition of Methanesulfonic Acid. doi:10.1021/AC0600048

Ayers, G.P., Gillett, R.W., Cainey, J.M., Dick, A.L., 1999. Chloride and Bromide Loss from Sea-Salt Particles in Southern Ocean Air. J. Atmos. Chem. 33, 299–319. doi:10.1023/A:1006120205159

Bańales-Seguel, C., De La Barrera, F., Salazar, A., 2018. An analysis of wildfire risk and historical occurrence for a mediterranean biosphere reserve, Central Chile. J. Environ. Eng. Landsc. Manag. 26, 128–140.

Bao, H., Jenkins, K.A., Khachaturyan, M., Díaz, G.C., 2004. Different sulfate sources and their post-depositional migration in Atacama soils. Earth Planet. Sci. Lett. 224, 577–587. doi:10.1016/j.epsl.2004.05.006

Böhlke, J.K., Ericksen, G.E., Revesz, K., 1997. Stable isotope evidence for an atmospheric origin of desert nitrate deposits in northern Chile and southern California, U.S.A. Chem. Geol. 136, 135–152. doi:10.1016/S0009-2541(96)00124-6

Bozkurt, D., Rondanelli, R., Garreaud, R., Arriagada, A., 2016. Impact of warmer eastern tropical Pacific SST on the March 2015 Atacama floods. Mon. Weather Rev. 144, 4441–4460.

Brecciaroli, G., Cocco, S., Agnelli, A., Courchesne, F., Corti, G., 2012. From rainfall to throughfall in a maritime vineyard. Sci. Total Environ. 438, 174–188.

Callaghan, A.H., 2013. An improved whitecap timescale for sea spray aerosol production flux modeling using the discrete whitecap method. J. Geophys. Res. Atmos. 118, 9910–9997.

Cameron, E.M., Leybourne, M.I., 2005. Relationship between groundwater chemistry and soil geochemical anomalies at the Spence copper porphyry deposit, Chile. Geochemistry Explor. Environ. Anal. 5, 135–145.

Capaldo, K., Corbett, J.J., Kasibhatla, P., Fischbeck, P., Pandis, S.N., 1999. Effects of ship emissions on sulphur cycling and radiative climate forcing over the ocean. Nature 400, 743–746. doi:10.1038/23438

Catling, D.C., Claire, M.W., Zahnle, K.J., Quinn, R.C., Clark, B.C., Hecht, M.H., Kounaves, S., 2010. Atmospheric origins of perchlorate on Mars and in the Atacama. J. Geophys. Res. 115, E00E11. doi:10.1029/2009JE003425

Chand, D., Hegg, D.A., Wood, R., Shaw, G.E., Wallace, D., Covert, D.S., 2010. Source attribution of climatically important aerosol properties measured at Paposo (Chile) during VOCALS. Atmos. Chem. Phys. 10, 10789–10801.

Cheremisinoff, N., 2016. AP-42, Compilation of Air Pollutant Emission Factors. Pollut. Control Handb. Oil Gas Eng. doi:doi:10.1002/9781119117896.ch6

Clarke, A.G., Karani, G.N., 1992. Characterisation of the Carbonate Content of Atmospheric Aerosols. J. Atmos. Chem&try 14, 119–128.

Clarke, J.D.A., 2005. Antiquity of aridity in the Chilean Atacama Desert. doi:10.1016/j.geomorph.2005.06.008

Cooke, R.U., Warren, A., 1973. Geomorphology in deserts. Univ of California Press.

Crutzen, P.J., 2002. The “anthropocene,” in: Journal de Physique IV (Proceedings). EDP sciences, pp. 1–5.

Crutzen, P.J., 1979. The role of NO and NO_2 in the chemistry of the troposphere and stratosphere. Annu. Rev. Earth Planet. Sci. 7, 443–472.

Darwin, C., 1906. The voyage of the Beagle. JM Dent & sons.

Dee, D.P., Uppala, S.M., Simmons, A.J., Berrisford, P., Poli, P., Kobayashi, S., Andrae, U., Balmaseda, M.A., Balsamo, G., Bauer, d P., 2011. The ERA-Interim reanalysis: Configuration and performance of the data assimilation system. Q. J. R. Meteorol. Soc. 137, 553–597.

Demoisson, A., Tedeschi, G., Piazzola, J., 2013. A model for the atmospheric transport of sea-salt particles in coastal areas. Atmos. Res. 132, 144–153.

Dror, T., Lehahn, Y., Altaratz, O., Koren, I., 2018. Temporal-Scale Analysis of Environmental Controls on Sea Spray Aerosol Production Over the South Pacific Gyre. Geophys. Res. Lett. 45, 8637–8646.

Edwards, H.G.M., Villar, S.E.J., Parnell, J., Cockell, C.S., Lee, P., 2005. Raman spectroscopic analysis of cyanobacterial gypsum halotrophs and relevance for sulfate deposits on Mars. Analyst 130, 917–923.

Enaex Memoria Annual, 2011. http://www.enaex.com/wp-content/uploads/2015/07/Memoria_2011.pdf.

Ericksen, G.E., 1983. The Chilean nitrate deposits: the origin of the Chilean nitrate deposits, which contain a unique group of saline minerals, has provoked lively discussion for more than 100 years. Am. Sci. 71, 366–374.

Ericksen, G.E., 1981. Geology and origin of the Chilean nitrate deposits. USGPO.

Ewing, S.A., Sutter, B., Owen, J., Nishiizumi, K., Sharp, W., Cliff, S.S., Perry, K., Dietrich, W., McKay, C.P., Amundson, R., 2006. A threshold in soil formation at Earth's arid–hyperarid transition. Geochim. Cosmochim. Acta 70, 5293–5322. doi:10.1016/j.gca.2006.08.020

Ewing, S.A., Yang, W., DePaolo, D.J., Michalski, G., Kendall, C., Stewart, B.W., Thiemens, M., Amundson, R., 2008. Non-biological fractionation of stable Ca isotopes in soils of the Atacama Desert, Chile. Geochim. Cosmochim. Acta 72, 1096–1110. doi:10.1016/j.gca.2007.10.029

Fishbaugh, K.E., Poulet, F., Chevrier, V., Langevin, Y., Bibring, J., 2007. On the origin of gypsum in the Mars north polar region. J. Geophys. Res. Planets 112.

Fitzgerald, J.W., 1991. Marine aerosols: A review. Atmos. Environ. Part A. Gen. Top. 25, 533–545. doi:10.1016/0960-1686(91)90050-H

Galloway, J.N., 1985. The Deposition of Sulfur and Nitrogen from the Remote Atmosphere Background Paper, in: The Biogeochemical Cycling of Sulfur and Nitrogen in the Remote Atmosphere. Springer, pp. 143–175.

Galloway, J.N., Dentener, F.J., Capone, D.G., Boyer, E.W., Howarth, R.W., Seitzinger, S.P., Asner, G.P., Cleveland, C.C., Green, P.A., Holland, E.A., Karl, D.M., Michaels, A.F., Porter, J.H., Townsend, A.R., Vosmarty, C.J., 2004. Nitrogen Cycles: Past, Present, and Future. Biogeochemistry 70, 153–226. doi:10.1007/s10533-004-0370-0

Galloway, J.N., Keene, W.C., Likens, G.E., 1996. Processes controlling the composition of precipitation at a remote southern hemispheric location: Torres del Paine National Park, Chile. J. Geophys. Res. Atmos. 101, 6883–6897. doi:10.1029/95JD03229

Giardina, M., Buffa, P., 2018. A new approach for modeling dry deposition velocity of particles. Atmos. Environ. 180, 11–22.

Ginot, P., Kull, C., Schwikowski, M., Schotterer, U., Gäggeler, H.W., 2001. Effects of postdepositional processes on snow composition of a subtropical glacier (Cerro Tapado, Chilean Andes). J. Geophys. Res. Atmos. 106, 32375–32386. doi:10.1029/2000JD000071

Goudie, A.S., Middleton, N.J., 1992. The changing frequency of dust storms through time. Clim. Change 20, 197–225.

Grossling, B.F., Ericksen, G.E., 1971. Computer studies of the composition of Chilean Nitrate ores: data reduction, basic statistics and correlation analysis. US Geological Survey,.

Group, T.W., 1988. The WAM model—A third generation ocean wave prediction model. J. Phys. Oceanogr. 18, 1775–1810.

Hardy, J.T., 1982. The sea surface microlayer: biology, chemistry and anthropogenic enrichment. Prog. Oceanogr. 11, 307–328.

Hecht, M.H., Kounaves, S.P., Quinn, R.C., West, S.J., Young, S.M.M., Ming, D.W., Catling, D.C., Clark, B.C., Boynton, W. V, Hoffman, J., 2009. Detection of perchlorate and the soluble chemistry of martian soil at the Phoenix lander site. Science (80-.). 325, 64–67.

Holland, E.A., Dentener, F.J., Braswell, B.H., Sulzman, J.M., 1999. Contemporary and pre-industrial global reactive nitrogen budgets, in: New Perspectives on Nitrogen Cycling in the Temperate and Tropical Americas. Springer, pp. 7–43.

Houston, J., 2007. Recharge to groundwater in the Turi Basin, northern Chile: An evaluation based on tritium and chloride mass balance techniques. J. Hydrol. 334, 534–544. doi:10.1016/j.jhydrol.2006.10.030

Jaeglé, L., Quinn, P.K., Bates, T.S., Alexander, B., Lin, J.-T., 2011. Global distribution of sea salt aerosols: new constraints from in situ and remote sensing observations. Atmos. Chem. Phys. 11, 3137–3157.

Jayarathne, T., Sultana, C.M., Lee, C., Malfatti, F., Cox, J.L., Pendergraft, M.A., Moore, K.A., Azam, F., Tivanski, A. V, Cappa, C.D., 2016. Enrichment of saccharides and divalent cations in sea spray aerosol during two phytoplankton blooms. Environ. Sci. Technol 50, 11511–11520.

Kerminen, V.-M., Teinilä, K., Hillamo, R., Pakkanen, T., 1998. Substitution of chloride in sea-salt particles by inorganic and organic anions. J. Aerosol Sci. 29, 929–942.

Kishcha, P., Starobinets, B., Bozzano, R., Pensieri, S., Canepa, E., Nickovic, S., di Sarra, A., Udisti, R., Becagli, S., Alpert, P., 2011. Sea-salt aerosol forecasts compared with wave height and sea-salt measurements in the open sea, in: Air Pollution Modeling and Its Application XXI. Springer, pp. 299–303.

Kounaves, S.P., Carrier, B.L., O'Neil, G.D., Stroble, S.T., Claire, M.W., 2014. Evidence of martian perchlorate, chlorate, and nitrate in Mars meteorite EETA79001: Implications for oxidants and organics. Icarus 229, 206–213.

Kumar, R., Rani, A., Kumari, K.M., Srivastava, S.S., 2005. Atmospheric dry deposition to marble and red stone. J. Atmos. Chem. 50, 243–261.

Lana, A., Bell, T.G., Simó, R., Vallina, S.M., Ballabrera-Poy, J., Kettle, A.J., Dachs, J., Bopp, L., Saltzman, E.S., Stefels, J., Johnson, J.E., Liss, P.S., 2011. An updated climatology of surface dimethlysulfide concentrations and emission fluxes in the global ocean. Global Biogeochem. Cycles. doi:10.1029/2010GB003850

Laskin, A., Moffet, R.C., Gilles, M.K., Fast, J.D., Zaveri, R.A., Wang, B., Nigge, P., Shutthanandan, J., 2012. Tropospheric chemistry of internally mixed sea salt and organic particles: Surprising reactivity of NaCl with weak organic acids. J. Geophys. Res. Atmos. 117.

Lewandowska, A.U., Falkowska, L.M., 2013. Sea salt in aerosols over the southern Baltic. Part 1. The generation and transportation of marine particles. Oceanologia 55, 279–298.

Lewis, E.R., Schwartz, S.E., 2004. Sea salt aerosol production: mechanisms, methods, measurements, and models-A critical review. American geophysical union.

Li, J., Michalski, G., Davy, P., Harvey, M., Katzman, T., Wilkins, B., 2018. Investigating Source Contributions of Size-Aggregated Aerosols Collected in Southern Ocean and Baring Head, New Zealand using Sulfur Isotopes. Geophys. Res. Lett.

Liang, T., Chamecki, M., Yu, X., 2016. Sea salt aerosol deposition in the coastal zone: A large eddy simulation study. Atmos. Res. 180, 119–127.

MacIntyre, F., 1974. Chemical fractionation and sea-surface microlayer processes. sea 5, 245–299.

Mårtensson, M., Nilsson, E.D., De Leeuw, G., Cohen, L.H., Hansson, H.C., 2003. Laboratory simulations of the primary marine aerosol generated by bubble bursting. JGR-Atmospheres 108.

Mason, S.J., Goddard, L., 2001. Probabilistic precipitation anomalies associated with ENSO. Bull. Am. Meteorol. Soc. 82, 619–638.

McDonald, R.L., Unni, C.K., Duce, R.A., 1982. Estimation of atmospheric sea salt dry deposition: wind speed and particle size dependence. J. Geophys. Res. Ocean. 87, 1246–1250.

McFadden, L.D., Wells, S.G., Jercinovich, M.J., 1987. Influences of eolian and pedogenic processes on the origin and evolution of desert pavements. Geology 15, 504–508.

McInnes, L.M., Covert, D.S., Quinn, P.K., Germani, M.S., 1994. Measurements of chloride depletion and sulfur enrichment in individual sea-salt particles collected from the remote marine boundary layer. J. Geophys. Res. Atmos. 99, 8257–8268.

Merriam, R.A., 1973. Fog drip from artificial leaves in a fog wind tunnel. Water Resour. Res. 9, 1591–1598.

Metzger, S., Mihalopoulos, N., Lelieveld, J., 2006. Importance of mineral cations and organics in gas-aerosol partitioning of reactive nitrogen compounds: case study based on MINOS results. Atmos. Chem. Phys. Atmos. Chem. Phys. 6, 2549–2567.

Michalski, G., Böhlke, J.K.K., Thiemens, M., 2004. Long term atmospheric deposition as the source of nitrate and other salts in the Atacama Desert, Chile: New evidence from mass-independent oxygen isotopic compositions. Geochim. Cosmochim. Acta 68, 4023–4038. doi:10.1016/j.gca.2004.04.009

Michalski, G., Scott, Z., Kabiling, M., Thiemens, M.H., 2003. First measurements and modeling of $\Delta^{17}O$ in atmospheric nitrate. Geophys. Res. Lett. 30. doi:10.1029/2003GL017015

Navarro-Gonzalez, R., 2003. Mars-Like Soils in the Atacama Desert, Chile, and the Dry Limit of Microbial Life. Science 302, 1018–1021. doi:10.1126/science.1089143

Newberg, J.T., Matthew, B.M., Anastasio, C., 2005. Chloride and bromide depletions in sea-salt particles over the northeastern Pacific Ocean. J. Geophys. Res. Atmos. 110, n/a-n/a. doi:10.1029/2004JD005446

Norman, A.L., Barrie, L.A., Toom-Sauntry, D., Sirois, A., Krouse, H.R., Li, S.M., Sharma, S., 1999. Sources of aerosol sulphate at Alert: Apportionment using stable isotopes. J. Geophys. Res. Atmos. 104, 11619–11631. doi:10.1029/1999JD900078

O 'dowd, C.D., De Leeuw, G., O'Dowd, C.D., De Leeuw, G., 2007. Marine aerosol production: a review of the current knowledge. Philos. Trans. R. Soc. London A Math. Phys. Eng. Sci. 365. doi:10.1098/rsta.2007.2043

Osterloo, M.M., Hamilton, V.E., Bandfield, J.L., Glotch, T.D., Baldridge, A.M., Christensen, P.R., Tornabene, L.L., Anderson, F.S., 2008. Chloride-bearing materials in the southern highlands of Mars. Science (80-.). 319, 1651–1654.

Pachon, J.E., Weber, R.J., Zhang, X., Mulholland, J.A., Russell, A.G., 2013. Revising the use of potassium (K) in the source apportionment of PM2. 5. Atmos. Pollut. Res. 4, 14–21.

Pan, Y. P., & Wang, Y. S., 2015. Atmospheric wet and dry deposition of trace elements at 10 sites in Northern China. Atmospheric Chemistry and Physics, 15(2), 951-972.

Patris, N., Cliff, S.S., Quinn, P.K., Kasem, M., Thiemens, M.H., 2007. Isotopic analysis of aerosol sulfate and nitrate during ITCT-2k2: Determination of different formation pathways as a function of particle size. J. Geophys. Res. 112, D23301. doi:10.1029/2005JD006214

Pérez-Fodich, A., Reich, M., Álvarez, F., Snyder, G.T., Schoenberg, R., Vargas, G., Muramatsu, Y., Fehn, U., 2014. Climate change and tectonic uplift triggered the formation of the Atacama Desert's giant nitrate deposits. Geology 42, 251–254.

Pilson, M.E.Q., 2012. An Introduction to the Chemistry of the Sea. Cambridge University Press.

Rech, J.A., Quade, J., Hart, W.S., 2003. Isotopic evidence for the source of Ca and S in soil gypsum, anhydrite and calcite in the Atacama Desert, Chile. Geochim. Cosmochim. Acta 67, 575–586. doi:10.1016/S0016-7037(02)01175-4

Rees, C.E., Jenkins, W.J., Monster, J., 1978. The sulphur isotopic composition of ocean water sulphate. Geochim. Cosmochim. Acta 42, 377–381.

Reheis, M.C., 1997. Dust deposition downwind of Owens (dry) Lake, 1991–1994: Preliminary findings. J. Geophys. Res. Atmos. 102, 25999–26008.

Reheis, M.C., Kihl, R., 1995. Dust deposition in southern Nevada and California, 1984–1989: Relations to climate, source area, and source lithology. J. Geophys. Res. Atmos. 100, 8893–8918. doi:10.1029/94JD03245

Risacher, F., Fritz, B., Hauser, A., 2011. Origin of components in Chilean thermal waters. J. South Am. Earth Sci. 31, 153–170.

Ropelewski, C.F., Halpert, M.S., 1989. Precipitation patterns associated with the high index phase of the Southern Oscillation. J. Clim. 2, 268–284.

Rutllant, J.A., Muñoz, R.C., Garreaud, R.D., 2013. Meteorological observations on the northern Chilean coast during VOCALS-REx. Atmos. Chem. Phys. 13, 3409–3422.

Sargent, R., Bartley, C., Dille, P., Keller, J., Nourbakhsh, I., LeGrand, R., 2010. Timelapse GigaPan: Capturing, sharing, and exploring timelapse gigapixel imagery, in: Fine International Conference on Gigapixel Imaging for Science.

Schemenauer, R.S., Cereceda, P., Schemenauer, R.S., Cereceda, P., 1992. The Quality of Fog Water Collected for Domestic and Agricultural Use in Chile. J. Appl. Meteorol. 31, 275–290.

Schindler, D.W., Dillon, P.J., Schreier, H., 2006. A review of anthropogenic sources of nitrogen and their effects on Canadian aquatic ecosystems, in: Nitrogen Cycling in the Americas: Natural and Anthropogenic Influences and Controls. Springer, pp. 25–44.

Seinfeld, J.H., Pandis, S.N., Noone, K., 1998. Atmospheric chemistry and physics: from air pollution to climate change.

Sernageomin, 1982. Mapa Geológico de Chile.

Shao, Y., Raupach, M.R., Findlater, P.A., 1993. Effect of saltation bombardment on the entrainment of dust by wind. J. Geophys. Res. 98, 12719. doi:10.1029/93JD00396

Sillitoe, R.H., Mortimer, C., Clark, A.H., 1968. A chronology of landform evolution and supergene mineral alteration, southern Atacama Desert, Chile. Inst. Min. Metall. Trans. (Section B) 27, 166–169.

Singh, H.B., Hanst, P.L., 1981. Peroxyacetyl nitrate (PAN) in the unpolluted atmosphere: An important reservoir for nitrogen oxides. Geophys. Res. Lett. 8, 941–944.

Singh, H.B., Salas, L.J., Ridley, B.A., Shetter, J.D., Donahue, N.M., Fehsenfeld, F.C., Fahey, D.W., Parrish, D.D., Williams, E.J., Liu, S.C., 1985. Relationship between peroxyacetyl nitrate and nitrogen oxides in the clean troposphere.

Stern, J.C., Sutter, B., Freissinet, C., Navarro-González, R., McKay, C.P., Archer, P.D., Buch, A., Brunner, A.E., Coll, P., Eigenbrode, J.L., 2015. Evidence for indigenous nitrogen in sedimentary and aeolian deposits from the Curiosity rover investigations at Gale crater, Mars. Proc. Natl. Acad. Sci. 201420932.

Stoertz, G.E., Ericksen, G.E., 2009. Geology of salars in northern Chile.

Ta, W., Xiao, H., Qu, J., Xiao, Z., Yang, G., Wang, T., Zhang, X., 2004. Measurements of dust deposition in Gansu Province, China, 1986–2000. Geomorphology 57, 41–51. doi:10.1016/S0169-555X(03)00082-5

Tedeschi, G., Van Eijk, A.M.J., Piazzola, J., Kusmierczyk-Michulec, J.T., 2017. Influence of the Surf Zone on the Marine Aerosol Concentration in a Coastal Area. Boundary-layer Meteorol. 163, 327–350.

Valdés-Pineda, R., Valdés, J.B., Diaz, H.F., Pizarro-Tapia, R., 2016. Analysis of spatio-temporal changes in annual and seasonal precipitation variability in South America-Chile and related ocean–atmosphere circulation patterns. Int. J. Climatol. 36, 2979–3001.

Van Driessche, A.E.S., Canals, A., Ossorio, M., Reyes, R.C., García-Ruiz, J.M., 2016. Unraveling the Sulfate Sources of (Giant) Gypsum Crystals Using Gypsum Isotope Fractionation Factors. J. Geol. 124, 235–245. doi:10.1086/684832

Vance, T.R., van Ommen, T.D., Curran, M.A.J., Plummer, C.T., Moy, A.D., 2013. A millennial proxy record of ENSO and eastern Australian rainfall from the Law Dome ice core, East Antarctica. J. Clim. 26, 710–725.

Vítek, P., Jehlička, J., Edwards, H.G.M., Hutchinson, I., Ascaso, C., Wierzchos, J., 2012. The Miniaturized Raman System and Detection of Traces of Life in Halite from the Atacama Desert: Some Considerations for the Search for Life Signatures on Mars. Astrobiology 12, 1095–1099. doi:10.1089/ast.2012.0879

Wadleigh, M.A., 2004. Sulphur isotopic composition of aerosols over the western North Atlantic Ocean. Can. J. Fish. Aquat. Sci. 61, 817–825. doi:10.1139/f04-073

Wang, F., Michalski, G., Seo, J.-H., Granger, D.E., Lifton, N., Caffee, M., 2015. Beryllium-10 concentrations in the hyper-arid soils in the Atacama Desert, Chile: Implications for arid soil formation rates and El Niño driven changes in Pliocene precipitation. Geochim. Cosmochim. Acta 160, 227–242.

Wang, F., Michalski, G., Seo, J. hye, Ge, W., 2014. Geochemical, isotopic, and mineralogical constraints on atmospheric deposition in the hyper-arid Atacama Desert, Chile. Geochim. Cosmochim. Acta 135, 29–48. doi:10.1016/j.gca.2014.03.017

Watts, D., Durán, P., Flores, Y., 2017. How does El Niño Southern Oscillation impact the wind resource in Chile? A techno-economical assessment of the influence of El Niño and La Niña on the wind power. Renew. Energy 103, 128–142. doi:10.1016/j.renene.2016.10.031

Wood, S., Cowie, A., 2004. A review of greenhouse gas emission factors for fertiliser production, in: IEA Bioenergy Task. pp. 1–20.

Yang, Y., Russell, L.M., Lou, S., Lamjiri, M.A., Liu, Y., Singh, B., Ghan, S.J., 2016. Changes in sea salt emissions enhance ENSO variability. J. Clim. 29, 8575–8588.

Zakey, A.S., Giorgi, F., Bi, X., 2008. Modeling of sea salt in a regional climate model: Fluxes and radiative forcing. J. Geophys. Res. Atmos. 113.

Zhang, B., Zhong, Z., Xue, Z., Xue, J., Xu, Y., 2018. Release and transformation of potassium in co-combustion of coal and wheat straw in a BFB reactor. Appl. Therm. Eng. 144, 1010–1016.

National Weather Service, 2015, http://origin.cpc.ncep.noaa.gov/products/analysis_monitoring/ensostuff/ONI_v4.shtml

U.S. Geological Survey, 2005, Mineral Resources Data System: U.S. Geological Survey, Reston, Virginia. https://mrdata.usgs.gov/mrds/show-mrds.php?dep_id=10079698

National Data Buoy Center, 2018, https://www.ndbc.noaa.gov/station_page.php?station=32012

Global Energy Observatory, 2011, http://globalenergyobservatory.org/geoid/44595

NOAA Climate Data Online Database, 2018, https://www7.ncdc.noaa.gov/CDO

National Forest Corporation in Chile, 2018, http://www.conaf.cl/incendios-forestales/incendios-forestales-en-chile/estadisticas-historicas/

CHAPTER 4. STABLE SULFUR ISOTOPES REVEALED A MAJOR ROLE OF TRANSITION-METAL ION-CATALYZED SO_2 OXIDATION IN HAZE EPISODES

This chapter is a reprint from a published article (Li, J., Zhang, Y., Cao, F., Zhang, W., Fan, M., Lee, X., & Michalski, G. (2020). Stable Sulfur Isotopes Revealed a Major Role of Transition-Metal-Ion Catalyzed SO_2 Oxidation in Haze Episodes. Environmental Science & Technology. 2020, 54, 2626−2634).

Abstract

Secondary sulfate aerosols played an important role in aerosol formation and aging processes, especially during haze episodes in China. Secondary sulfate was formed via atmospheric oxidation of SO_2 by OH, O_3, H_2O_2 and transition metal catalyzed (TMI) O_2. However, the relative importance of these oxidants in haze episodes was strongly debated. Here we use stable sulfur isotopes ($\delta^{34}S$) of sulfate aerosols and a Rayleigh distillation model to quantify the contributions of each oxidant during a haze episode in Nanjing, a megacity in China. The observed $\delta^{34}S$ values of sulfate aerosols showed a negative correlation with sulfur oxidation ratios, which was attributed to the sulfur isotopic fractionations during the sulfate formation processes. Using the average fractionation factor calculated from our observations and 0-D atmospheric chemistry modeling estimations, we suggest that OH oxidation was trivial during the haze episode, while the TMI pathway contributed 49±10% of the total sulfate production and O_3/H_2O_2 oxidations accounted for the rest. Our results displayed good agreement with several atmospheric chemistry models that carry aqueous and heterogeneous TMI oxidation pathways, suggesting the role of the TMI pathway was significant during haze episodes.

4.1 Introduction

Haze episodes in Chinese cities are adversely affecting the environment and the health of millions of residents. Most haze episodes are characterized by high concentrations and fast accumulation of aerosol sulfate[1–4], which could contribute to as much as 45% of total aerosol mass. Over 90% sulfate in haze episodes is secondary sulfate, i.e., sulfate produced from SO_2 oxidation in the atmosphere via 1) gas phase oxidation by OH radical[5]; 2) aqueous oxidation by H_2O_2, O_3,

and Transition Metal Ions (TMI) catalyzed O_2[6–12]; and 3) heterogeneous oxidation on the surface of aerosols, cloud droplets and mineral dusts by the same oxidants as aqueous oxidation[1,13–16]. Some studies[11,12,14,17,18] also suggested the NO_2 might played an important role during the formation of aerosol sulfate, probably by facilitating TMI oxidation[19], which is based on an experimental study[20] that demonstrated the direct oxidation of SO_2 by NO_2 was several orders of magnitude slower than gas phase OH oxidation. However, aerosol collected from several Chinese urban areas (e.g., Nanjing) were acidic[21], suggesting NO_2 oxidation might not be important in these regions. Furthermore, a recent GEOS-Chem modeling study[22] has suggested NO_2 oxidation contributed less than 2% of total sulfate production during haze episodes. While the gas phase oxidation rate of SO_2+OH is well-constrained, there are many uncertainties in quantifying the rates of aqueous and heterogeneous SO_2 oxidation. One of the ongoing debates is the relative contribution of each SO_2 oxidation pathway during haze episodes. Some[8,12,13] have suggested that O_3 and H_2O_2 oxidation of SO_2 in aqueous phase contributed to the majority of total sulfate production, while the TMI pathway played a minor role. Others[17,23] have countered that the TMI pathway is likely also very important in highly polluted regions. Therefore, addressing this debate is essential to unravel the complex atmospheric sulfur chemistry in haze episodes.

Atmospheric chemistry models are often used to study the sulfate chemistry, but many models have uncertainties in parameterizing aqueous and heterogeneous SO_2 oxidation chemistry under haze conditions, resulting in underestimation of sulfate formation rates during haze episodes[1,24–26]. One of the biggest uncertainties is the pH of aerosol water: several studies had attempted to calculate the aerosol water pH in Beijing[12,17,27–29] using the same model (ISORROPIA II). Depending on assumptions about whether the aqueous phase is at thermodynamic stable state[17,30], the calculated pH was either 3-5 or >5.5. This uncertainty greatly impacts the quantification of aqueous SO_2 oxidation rate[31]. A pH increase of 1 unit will increase the O_3 oxidation rate by two orders of magnitude but decrease the TMI oxidation rate by 2-3 orders of magnitude. Conversely, the rate of SO_2 oxidation by H_2O_2 is insensitive to changing pH. Additionally, atmospheric models usually quantify the rate of TMI oxidation pathway using modeled aerosol Fe and Mn concentrations[10]. However, studies[9,32] have suggested that aerosol surface type, temperature, irradiation, and the existence of other transition metals in aerosol water, could alter the rate of TMI oxidation by as much as two orders of magnitude, adding more complexity to this question. Therefore, in order to 1) reduce the uncertainties in atmospheric

models and 2) verify the performance in models during haze episodes, an alternative approach is needed to assess the relative importance of each oxidation pathway.

The isotopic composition of sulfate aerosols has been used to determine the formation processes of sulfate aerosols. The mass-independent fractionation signals (non-zero $\Delta^{17}O$, where $\Delta^{17}O = \delta^{18}O-0.52*\delta^{17}O$) of oxygen isotopes in sulfate are often used to estimate the contributions of $SO_2 + O_3$ and H_2O_2 to the formation of sulfate aerosols[10,17,33], since $SO_2 + O_3$ and $SO_2 + H_2O_2$ are the only known two pathways that produce non-zero $\Delta^{17}O$ values in sulfate[34]. Sulfate formed via $SO_2 + O_3$ yields $\Delta^{17}O$=6.5‰ and sulfate formed via $SO_2 + H_2O_2$ shows $\Delta^{17}O$ = 0.7‰. This method can easily identify the significant contribution of SO_2+O_3 pathway when high $\Delta^{17}O$ (>3‰) are measured in sulfate samples. There is significant uncertainty, however, when interpreting sulfate aerosols with low $\Delta^{17}O$ values (<1‰). Unfortunately, most sulfate aerosols in haze episodes show $\Delta^{17}O$ < 1‰[17,22], suggesting limited contribution from SO_2+O_3 pathway, but the relative importance of the $SO_2 + H_2O_2$ pathway and the TMI pathway is still unclear. Therefore, solely using $\Delta^{17}O$ probably cannot precisely distinguish the contributions from the $SO_2 + H_2O_2$ and the TMI pathways in haze episodes.

Stable sulfur isotopes ($\delta^{34}S$) have the potential to indicate the formation pathways of sulfate aerosols. The fractionation factors for sulfur isotopes during multiple oxidation pathways (SO_2+OH, SO_2+H_2O_2/O_3, TMI) have been determined experimentally[35–37]. Yet to date there are few studies using sulfate $\delta^{34}S$ values to interpret the oxidation pathways of SO_2[35,38,39]. This is because the $\delta^{34}S$ values of sulfate aerosols ($\delta^{34}S_{sulfate}$) are simultaneously controlled by the $\delta^{34}S$ value of SO_2 sources[40,41] ($\delta^{34}S_{emisssion}$) and the kinetic and equilibrium isotope effects occurring during the oxidation process. The $\delta^{34}S_{emisssion}$ strongly depends on the origin of SO_2 therefore can be difficult to constrain. However, during haze episodes, SO_2 generally originates from local sources because air stagnation limits long range transport, and the $\delta^{34}S_{emission}$ can be well-constrained using local SO_2 emission inventory and observations. Thus, the differences between $\delta^{34}S_{emission}$ and $\delta^{34}S_{sulfate}$ can be attributed to the isotopic fractionations during the oxidation processes, which are controlled by the oxidation pathways. This isotopic fractionation during SO_2 oxidation should be treated as a Rayleigh distillation process[42] since isotopic exchange between the product sulfate and the reactant SO_2 is minimal[35]. Currently, many studies have measured the $\delta^{34}S_{sulfate}$ in Chinese megacities[38,39,43–47] in order to understand the sources of atmospheric SO_2 and

the secondary sulfate aerosols. Some works also have measured $\delta^{33}S$ and $\delta^{36}S$[47–51] to further constrain the origins of atmospheric SO_2. However, the differences between $\delta^{34}S_{emission}$ and $\delta^{34}S_{sulfate}$, as well as the isotopic fractionation process during the formation of sulfate, were rarely discussed and poorly understood. Here, we used the Rayleigh distillation model to investigate the sulfur isotopic fractionations of sulfate aerosols collected during a haze episode in winter 2015 at Nanjing, China, to understand the relative contribution of each SO_2 oxidation pathway.

4.2 Materials and methods

Sulfate aerosols were sampled during a severe haze episode in winter 2015, in Nanjing, Peoples Republic of China. The sampling site was located at the Agrometeorological station in Nanjing University of Information Science and Technology (NUIST). Two large industrial areas are located ~10 km northeast and ~5 km southwest of the sampling site, and downtown Nanjing is 20 km to the southeast (Figure 4.1). A high-volume aerosol sampler equipped with a pre-combusted quartz filter was used to collect ambient aerosol samples (<2.5 μm in diameter, $PM_{2.5}$) from January 22th to 28th at a flow rate of 1 m^3/min, and the filter was replaced every 3 hours. Once the aerosol samples were collected, the filters were wrapped in aluminum foil, sealed in air-tight polyethylene bags and stored in freezer to minimize sample loss or evaporation. To determine the anion, cation concentrations of filter

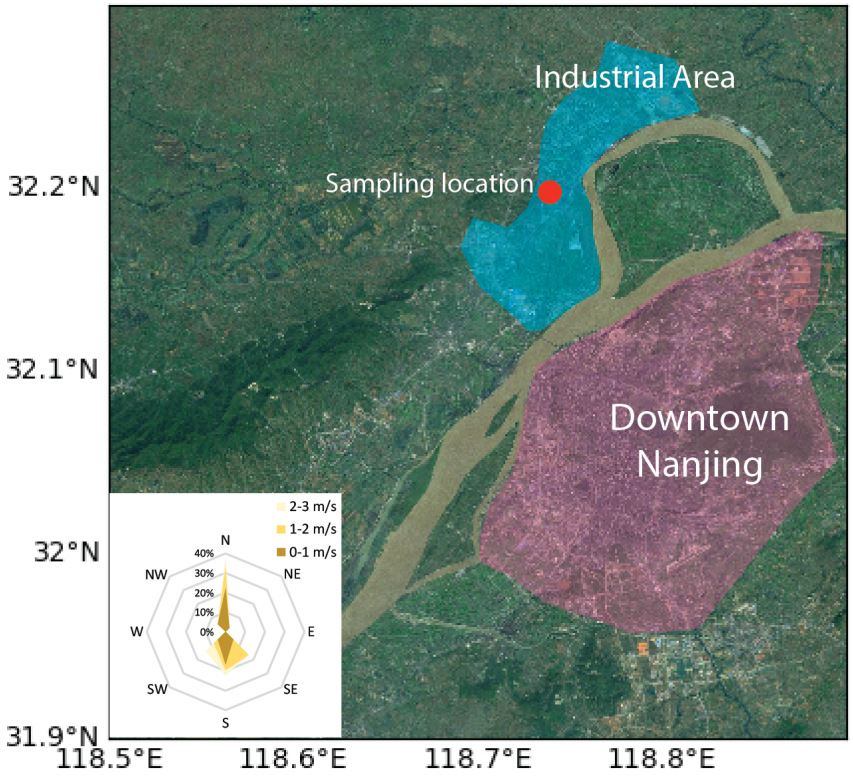

Figure 4.1 The sampling location was in between two large industrial areas (blue) and downtown Nanjing (red) is 20 km to the southeast. Wind rose during the sampling period (lower left corner) suggests the highest 3-hr wind speed was < 3m/s.

samples, a quarter of each filter was cut and the soluble components on the filter were dissolved into 50 mL of Millipore water (18.2 MΩ). Then the solution was sonicated for at least 30 min to ensure all the soluble ions were completely dissolved. Subsequently the solutions were filtered through 0.45 μm filters to remove insoluble material. An aliquot of each solution was taken and used to measure the anion and cation concentrations using a Dionex ICS 5000+ at NUIST following standard ion chromatography (IC) procedure[52] while the rest solutions were kept frozen. The analytical uncertainty for the IC analysis was ±5%. Meteorological data (wind speed and direction, temperature, RH) were obtained from an automatic meteorological station next to the sampling site. Concentrations of pollutants ($PM_{2.5}$, NO, NO_2, O_3, CO and SO_2) were obtained from the Environmental Supervising Station at Pukou district, Nanjing, ~15 km away from the sampling site.

Sulfur isotopic analysis was conducted at the Purdue Stable Isotope Laboratory at Purdue University. The sulfur isotopic analysis follows the procedure in Li et al. (2018)[40]. Another quarter of each sample was again dissolved into 10 mL of Millipore water (18.2 MΩ), and each solution was sonicated for 30 min to completely dissolve all the sulfate on the filter. To completely precipitate $BaSO_4$, 1 mL of 5% $BaCl_2$ solution and subsequently 0.5 mL of 37% HCl were added into each sample solution. Between 0.1 to 0.5 mg of $BaSO_4$ precipitate was then weighed into tin boats and combusted at 980 °C in an elemental analyzer (Costec), then the product SO_2 was directed into an Isotope Ratio Mass Spectrometer (ThermoDeltaV) to measure the $\delta^{34}S$ values. The analytical uncertainty of the sulfur isotopic analysis was ±0.1‰ inferred from IAEA-SO5 and IAEA-SO6 external standards.

4.3 Results and discussion

The haze episode occurred in Nanjing during winter 2015 and was characterized by high $PM_{2.5}$, high sulfate concentrations, and air stagnation. Prior to the haze episode (between Jan. 18 and Jan. 21, 2015) the $PM_{2.5}$ concentrations averaged 83.1 $\mu g/m^3$. The haze episode began between Jan. 22 00:00 and Jan. 23 12:00 when $PM_{2.5}$ became elevated, with concentrations of 109.3±16.0 $\mu g/m^3$. $PM_{2.5}$ continued increased to an average of 159.4 $\mu g/m^3$ between the 22nd and 26th of Jan. during which two significant $PM_{2.5}$ accumulation events were observed. The first accumulation (Event I, Figure 4.2A) started on Jan. 23 13:30 and lasted for 33 hours, during which the $PM_{2.5}$

concentration more than doubled, from 104.0 μg/m^3 to 268.3 μg/m^3. This was followed by a 2-hour light precipitation (~1 mm), which rinsed out some of the $PM_{2.5}$, decreasing its concentration

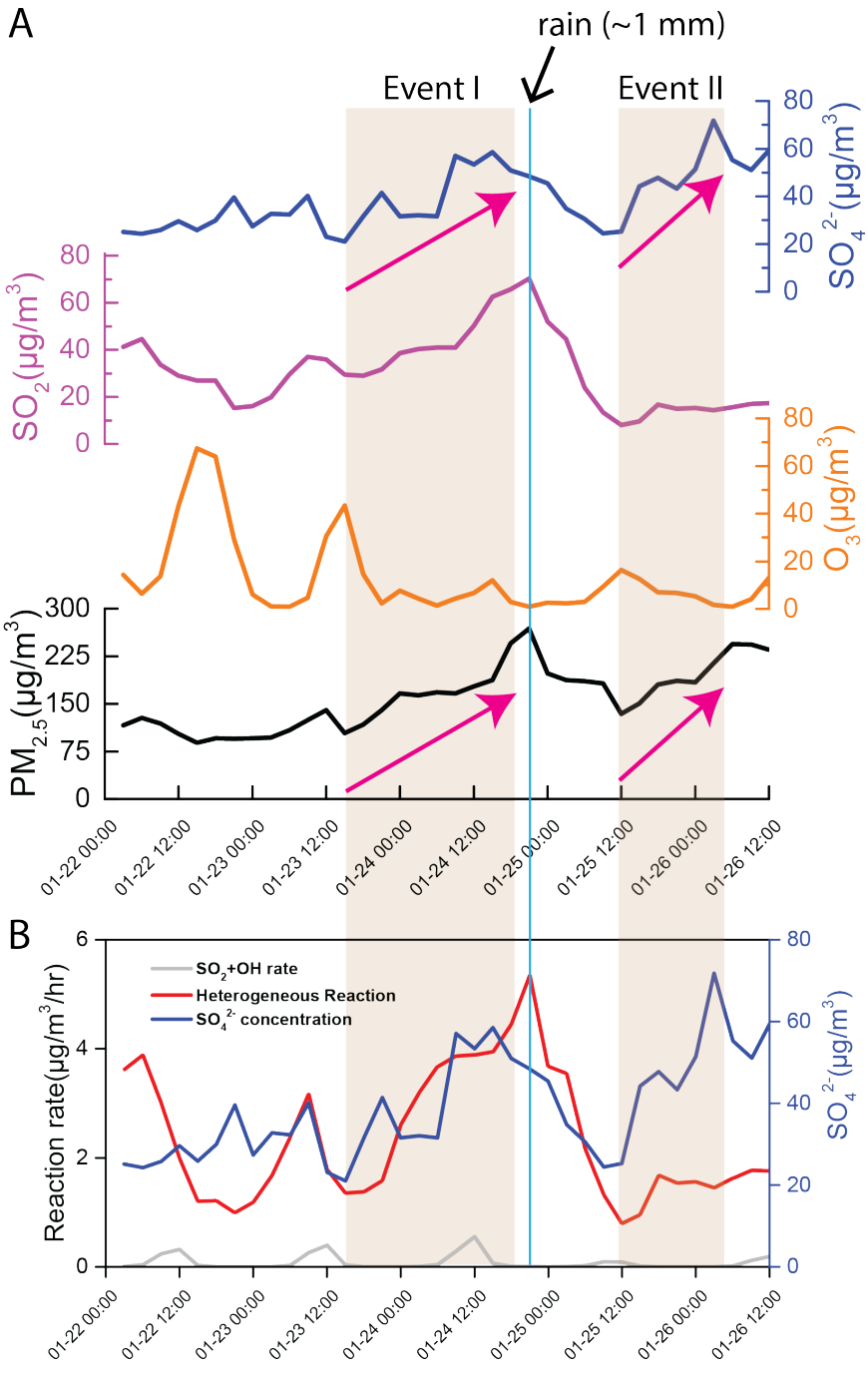

Figure 4.2 A) Concentrations of sulfate, SO_2, O_3 and $PM_{2.5}$ during the haze episode. Shaded areas indicated two rapid $PM_{2.5}$ and sulfate accumulation events, blue line indicated a small rain event during the sampling period; B) calculated reaction rates of SO_2+OH (grey) and heterogeneous reaction (red) plotted with sulfate concentrations (blue).

to 134.0 μg/m^3 within 15 hours. A subsequent $PM_{2.5}$ accumulation period (Event II) occurred within 24 hours, when the $PM_{2.5}$ concentration increased from 134.0 to 243.7 μg/m^3. Sulfate aerosol concentrations followed trends similar to $PM_{2.5}$ concentrations and mirrored the two rapid accumulation events. During Event I, sulfate have increased from 21.0 μg/m^3 to 58.5 μg/m^3 in 27 hours (accumulation rate of 1.39 μg/m^3/h) and during Event II sulfate increased from 24.4 μg/m^3 to 71.8 μg/m^3 within 21 hours (accumulation rate of 2.26 μg/m^3/h). Primary sulfate (includes soil sulfate, sea-salt sulfate, and sulfate directly emitted with SO_2) was determined to be trivial during these events. Low concentrations of Ca^{2+} (1.88±1.09 μg/m^3) and Na^+ (0.97±0.86 μg/m^3) in the aerosols indicated contribution of sulfate from soil entrainment[53] (SO_4^{2-}/Ca^{2+}=0.18) and sea-salt aerosols[54] (SO_4^{2-}/Na^+=0.25) should be less than 0.58 μg/m^3, corresponding to <2% of total sulfate observed. Primary sulfate emitted with SO_2 during coal burning has been estimated to be only <4% of SO_2 emission[10,55], which based on observed SO_2 concentrations, would average at 1.66 ± 0.6 μg/m^3 during the sampling period (Figure 4.2A). Thus, total primary sulfate only contributed for <6% of total sulfate, indicating most was secondary sulfate (i.e. SO_2 oxidation). Additionally, the wind speed during the entire haze episode averaged at 1.03±0.71 m/s with a maximum 3-h wind speed of 2.58 m/s (wind rose in Figure 4.1), indicating air stagnation. Considering the short lifetime[31] of atmospheric SO_2 (~12 h) and aerosols (~5 days) and the relatively low sulfur emissions outside of Nanjing within 200 km inferred from SO_2 emission inventory[56], long-range transportation of $SO_{2(g)}$ and sulfate should be minor, thus local SO_2 emissions and oxidation within Nanjing should be the dominant source of aerosol sulfate.

The measured $\delta^{34}S_{sulfate}$ values were significantly higher than the estimated $\delta^{34}S_{emission}$ value in Nanjing[38,39,44], showing a ~5‰ variation throughout the sampling period, and displayed a negative correlation with SO_2 Oxidation Ratio (SOR = $SO_4^{2-}/(SO_4^{2-}+SO_2)$). $\delta^{34}S_{sulfate}$ values (Figure 4.3A) in our samples ranged from +4.3‰ to +9.4‰ with an average of 6.2‰, similar to the values observed in a number of other Chinese megacities[23,44–46]. Because of the air stagnation, the SO_2 likely originated from local emissions, the majority of which in Nanjing was coal combustion with a $\delta^{34}S$ value of 3.0±0.9‰[43]. Several studies have measured the $\delta^{34}S$ values of both SO_2 and sulfate simultaneously at Nanjing, showing that the $\delta^{34}S_{emission}$ ($\delta^{34}S_{emission}=\delta^{34}S_{SO2}*(1-SOR)+\delta^{34}S_{SO42-}*SOR$) was +4.0±0.1‰[44] in 1997 and 2.4±0.6‰[38] in fall 2014. Chen et al. (2017)[39] have analyzed the $\delta^{34}S_{emission}$ in Nanjing prior to our sampling period (daily SO_2 and sulfate samples from Jan. 1 to Jan. 23 while this work sampled 3-hour sulfate

samples from Jan. 22 to Jan. 26) and found a constant $\delta^{34}S_{emission}$ value of 2.7±1.0‰[39]. Therefore, we suggest that the $\delta^{34}S_{emission}$ value during our sampling period should also be 2.7±1.0‰ (Figure 4.3A). These values are in good agreement with the SO_2 emission inventory[56] which suggested that over 96% SO_2 emission in winter in the Nanjing area was from industrial and coal burning power plants, which had $\delta^{34}S$ values of 3±3‰[44,57]. The measured $\delta^{34}S_{sulfate}$ values were significantly higher than the $\delta^{34}S_{emission}$, suggesting enrichment of ^{34}S in the sulfate and hence a depletion of ^{34}S in the remaining SO_2. This phenomenon has been observed in other studies, where the $\delta^{34}S$ values of aerosol sulfate were usually 0-8‰ higher than the coexisting SO_2[38,39,41,44,58,59] but this phenomenon was not quantitatively explained. Also, the $\delta^{34}S_{sulfate}$ values showed a ~5.1‰ variation throughout the sampling period. If the $\delta^{34}S_{emission}$ remain constant during our sampling period, this variation could be explained as a result of sulfur isotopic fractionation during the oxidation process. Furthermore, we observed a negative correlation (slope=-6.2, r=0.6, Fig 3A, B) between SOR and $\delta^{34}S$ value of sulfate in our samples, indicating that as oxidation of SO_2 progressed the $\delta^{34}S$ values of sulfate decreased, making them approach $\delta^{34}S_{emission}$ (by isotope mass balance). This negative correlation supported our hypothesis that the elevated and variable $\delta^{34}S_{sulfate}$ values should be attribute to the isotopic fractionation during SO_2 oxidation processes.

The discrepancies between $\delta^{34}S_{sulfate}$ and $\delta^{34}S_{emission}$ (therefore, $\delta^{34}S_{SO2}$) values have been observed, especially at low SOR levels. Forrest and Newman (1973)[59] measured $\delta^{34}S$ values of $SO_{2(g)}$ and sulfate particles in polluted environment with very low SOR (average SOR=9.9% among 3 experiments), the $\delta^{34}S_{sulfate}$ values were ~1.5-2.5‰ higher than the $\delta^{34}S_{SO2}$ values. Saltzman (1983)[41] conducted similar experiment at Hubbard Brook Experimental Forest, New Hampshire, USA, observed ~3‰ difference between $\delta^{34}S_{sulfate}$ and $\delta^{34}S_{SO2}$ values when the SOR were <40%. Later studies by Guo et al. (2016)[38] and Chen et al. (2017)[39] have suggested the $\delta^{34}S_{sulfate}$-$\delta^{34}S_{SO2}$ values at Nanjing ranged between ~1-7‰ during fall 2014 and winter 2015. These differences have suggested that $\delta^{34}S_{sulfate}$ may deviate from the $\delta^{34}S_{emission}$ by several permil, especially when the SOR value was low. This deviation might complicate the use of $\delta^{34}S_{sulfate}$ to calculate the sources of SO_2 in urban regions, since most urban (anthropogenic) SO_2 sources have a narrow range of $\delta^{34}S$ values[45,57] (+1-+11‰), which could be potentially altered by the isotopic fractionations during the formation of sulfate when SOR was low. This uncertainty might be reduced by analyzing other minor sulfur isotopes (^{33}S, ^{35}S, ^{36}S)[47–51], but this is beyond the scope

of our work. Therefore, extra cautious must be taken when using $\delta^{34}S$ values to estimate the sources of SO_2 in urban environment with low SOR.

The observed differences in $\delta^{34}S_{sulfate}$ and $\delta^{34}S_{emission}$ values can be explained using a Rayleigh distillation model, and to the isotopic enrichment factor ($\varepsilon = (\square\text{-}1)*1000‰$) for the total oxidation processes can also be quantified. The Rayleigh distillation model[42,60] is used to calculate the kinetic isotopic fractionation of a reaction (A→B) in an open system by assuming no isotopic exchange between A and B. In aqueous solution, $SO_{2(g)}$ dissolving into aerosol water was 2-3 order of magnitude faster than the subsequent oxidation into SO_4^{2-}, thus the isotopic fractionation should be controlled by the kinetic isotopic effect occurring during any aqueous SO_2 oxidation process[35]. In this model, the $\delta^{34}S$ value of SO_2 is a function of $\delta^{34}S_{emission}$, fraction (f) of remaining SO_2 (f = 1-SOR), and observed fractionation factor of the oxidation process (ε_{obs}):

$$\delta^{34}S_{SO2} = \delta^{34}S_{emission} + \ln(f) * \varepsilon_{obs} \quad \text{Eq. 1}$$

Thus $\delta^{34}S_{sulfate}$ is:

$$\delta^{34}S_{sulfate} = \delta^{34}S_{emission} - \varepsilon_{obs} * \ln(f) * f/(1-f) \quad \text{Eq. 2}$$

Using the observed $\delta^{34}S_{sulfate}$, f, and the estimated $\delta^{34}S_{emission}$ during our sampling period (2.7‰±1.0‰), we found the ε_{obs} values ranged from 2.2‰ to 10.0‰ (Figure 4.3B) with an average value of +5.3‰±1.8‰ (1σ).

This changing ε_{obs} value suggest that multiple SO_2 oxidation pathways have contributed to the observed sulfate accumulation. At 273K (average temperature during the sampling period), OH oxidation enriches ^{34}S in the product sulfate with an enrichment factor (ε_{OH}) of +11.0‰[35], and oxidation by TMI pathway depletes ^{34}S (ε_{TMI}=-5.0‰) in the product sulfate with a ε_{TMI} value of -5.0‰[35,36]. Several laboratory experiments[35–37] measured the ε values of $SO_2 + O_3$ and $SO_2 + H_2O_2$, and these two pathways showed similar ε values ranging from +15.1‰ to +17.4‰. Therefore, here we use $\varepsilon_{O3/H2O2}$ = +15.1‰ to represent the combined isotopic effect of O_3 and/or H_2O_2 pathways. Since the variation of temperature during the entire sampling period was small (standard deviation of ±3.7 K), the variations of the fractionation factors (<1‰) was insignificant comparing to the differences between the fractionation factors (~20‰). Therefore, in the following calculation we assume the fractionation factors are constants. The ε_{obs} value does not agree with any of the

laboratory-determined ε values, suggesting none of the pathway had a dominant role in the formation of the sulfate. Instead, the ε_{obs} should be a result of mixing of multiple oxidation pathways:

$$\varepsilon_{obs} = \varepsilon_{O3/H2O2} * f_{O3/H2O2} + \varepsilon_{TMI} * f_{TMI} + \varepsilon_{OH} * f_{OH} \quad \text{Eq. 3}$$

In which ε_i and f_i are the enrichment factor and the contribution of pathway *i*, and $f_{O3/H2O2} + f_{TMI} + f_{OH} = 1$.

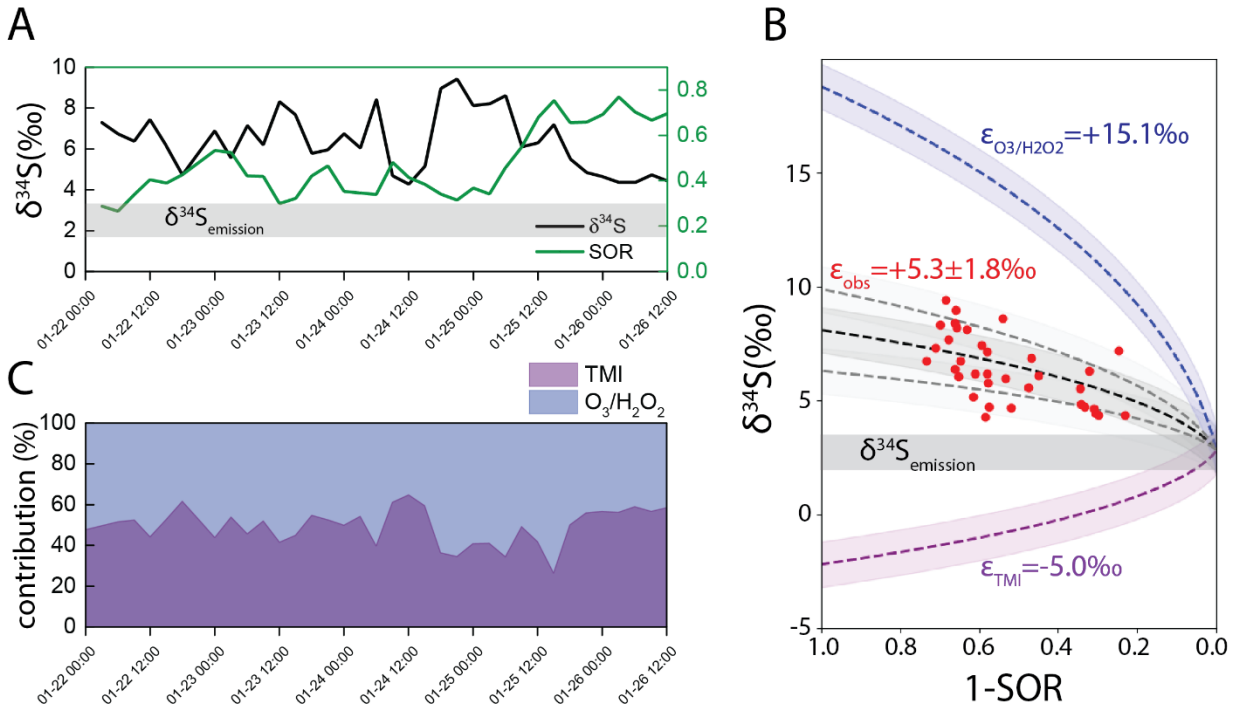

Figure 4.3 A) measured $\delta^{34}S_{sulfate}$ (black), calculated sulfur oxidation ratio (SOR, green) throughout the sampling period; and compare with estimated $\delta^{34}S_{emission}$ (grey bar); B) Rayleigh distillation model of sulfate production. Grey bar indicates the $\delta^{34}S_{emission}$ (+2.7±1.0‰) in Nanjing, red circles are the measured $\delta^{34}S_{sulfate}$ in this study. Dashed lines with shaded areas are calculated $\delta^{34}S_{sulfate}$ values based on the $\delta^{34}S_{emission}$: blue line indicates the $\delta^{34}S_{sulfate}$ when SO_2 is oxidized solely by O_3 and H_2O_2, purple line indicates the $\delta^{34}S_{sulfate}$ when SO_2 is oxidized solely by TMI oxidation, black line is the estimated ε value of +5.3‰ and two grey lines represent the upper and lower limit for the estimated ε values (+3.5‰ and +7.1‰).

The sulfate formed via the gas phase SO_2+OH pathway was calculated to be unimportant. Concentrations of OH radical were first obtained using a 0-D atmospheric chemistry model coupled with time-dependent photochemistry. The model used Tropospheric Ultraviolet and

Visible (TUV) radiation model[61] to determine the molecular photolysis frequencies (j values) for the major molecules (O_3, NO_2, NO_3, HONO, N_2O_5, H_2O_2, and other organic molecules) during the sampling period a time step of 3 hours. Subsequently calculated j values were incorporated into a 0-D atmospheric chemistry model driven by "Regional Atmospheric Chemistry Modeling" (RACM) mechanism[62]. The model then calculated time-dependent OH radical concentrations using average concentrations of trace gases (O_3, H_2O, NO_2, SO_2, CO, CH_4) during the pollution period. The OH concentrations display clear diurnal variation, with the peak concentration of $1.35*10^6$ molecules/cm^3 at noon, and a daily average value of $0.31*10^6$ molecules/cm^3, similar to the observed winter OH concentrations in other urban areas[63,64]. The reaction rates of gas phase SO_2 oxidation (SO_2+OH) were then calculated using:

$$d[SO_4^{2-}]/dt = k * [SO_2] * [OH] \quad \text{Eq. 4}$$

in which k is the reaction constant[5] at 273K ($1.5*10^{-12}$ molecule^{-1}*cm^3*s^{-1}), [SO_2] and [OH] are observed SO_2 concentrations and calculated OH concentrations. The results (grey line in Figure 4.2B) suggest that the OH oxidation rate averaged at 0.05 μg/m^3/h during the entire sampling period and the maximum oxidation rate with highest OH concentration at noon was only 0.3 μg/m^3/h. Since the measured sulfate accumulation rates were 1.3 and 2.1 μg/m^3/hr during the two accumulation events, respectively, and assuming a negligible sulfate dry deposition of 0.1 cm/s[65] and an average boundary layer height of 600 m, then the sulfate production rates during the two events were 1.55 and 2.38 μg/m^3/hr. These estimated sulfate production rates are 26-46 times faster than the average OH oxidation rate. Similar low sulfate production via gas phase oxidation was also inferred during winter haze episodes in Beijing[17]. This low contribution (2-3%) of gas phase sulfate production was probably because of a combination of weak photochemistry in winter, high aerosol concentration that scattered light, and extremely high heterogeneous and aqueous oxidation in haze episodes[11,66,67]. Therefore, O_3, H_2O_2 and TMI pathways should be the dominate contributors to the observed high sulfate production, and Eq. 3 can be simplified as:

$$\varepsilon_{obs} = \varepsilon_{O3/H2O2} * f_{O3/H2O2} + \varepsilon_{TMI} * f_{TMI} \quad \text{Eq. 5}$$

Eq. 5 can be used to estimate the role of heterogeneous and aqueous oxidations of $SO_{2(g)}$ by O_3, H_2O_2 and TMI-catalyzed O_2 that were likely to be responsible for the fast accumulation of sulfate aerosols during the haze episode. This hypothesis is further confirmed by applying a

pseudo-first-order uptake process to estimate heterogeneous and aqueous sulfate production[1]. This approach treats SO_2 oxidation on/in the aerosols as a first order uptake reaction on the surface of the aerosols:

$SO_{2(g)}$ + aerosol → sulfate

Its rate is expressed as[1,17,68]:

$$d[SO_4^{2-}]/dt_{het}=(R_a/D_g+4/\gamma\nu)^{-1}*S_a*[SO_2] \quad \text{Eq. 6}$$

in which D_g ($2*10^{-5}$) is SO_2 diffusion coefficient[68], ν (300 m^2*s^{-1}) is SO_2 mean molecular velocity[68], R_a is the effective radius of aerosols, which is estimated using the following equation that was empirically derived from two haze episodes in Beijing[2]:

$$R_a =(0.254*[PM_{2.5}]/(\mu g/m^3)+10.259)*10^{-9} \text{ m} \quad \text{Eq. 7}$$

S_a is the aerosol surface area density (cm^2/cm^3) estimated using the average aerosol effective radius and average density (ρ) of $PM_{2.5}$ (1.5 g/cm^3):

$$S_a = [PM_{2.5}] * 3 / (R_a*\rho) \quad \text{Eq. 8}$$

and γ is the SO_2 uptake coefficient. Although laboratory determined γ values of SO_2 uptake can vary by several orders of magnitude depending on the surface property, particle compositions, temperature and RH, previous modelling work have shown that setting the average γ values as a function of relative humidity[1] would best match modeled sulfate to observations:

$$\gamma = \max(2.0*10^{-5}, 6.0*10^{-7}*RH(\%)-1*10^{-5}) \quad \text{Eq. 9}$$

The calculated sulfate production rates ranged from 0.8-5.2 $\mu g/m^3/h$ with a mean value of 2.3 $\mu g/m^3/h$ during the sampling period (Figure 4.2B), similar to the observed sulfate accumulation rates (1.5 and 2.1 $\mu g/m^3/h$). Therefore, this calculation implies that heterogeneous and aqueous oxidation via O_3, H_2O_2 and TMI pathways were the main sources of sulfate during the haze episode. The overall calculated sulfate production rate agree well with the observed data, but this approach seems to be overestimating the sulfate production during Event I by ~80% (2.79 $\mu g/m^3/h$ vs. observed 1.55 $\mu g/m^3/h$) and underestimating the sulfate production in Event II by ~44% (1.32 $\mu g/m^3/h$ vs. observed 2.38 $\mu g/m^3/h$). Since the $PM_{2.5}$ mass and hence aerosol surface area were

similar between the two events (141±41 μg/m^3 in Event I vs. 171±24 μg/m^3 in Event II) but the RH in Event II (81±2%) was higher than Event I (57±17%), and that the SO_2 uptake coefficient is a function of RH, we suggest this discrepancy might be due to the over/under estimation of SO_2 uptake coefficient at low/high RH. The calculated SO_2 uptake coefficient ranged from $2*10^{-5}$ to $5*10^{-5}$, but experimental data has shown that these coefficients are a function of aerosol surface material. SO_2 uptake coefficients can be as low[69] as $0.41*10^{-5}$ on Sahara dust or as high[70] as $6.6*10^{-5}$ on iron oxides. Therefore, we suggest the pseudo-first-order uptake process estimation[1] showed general agreement with observed average production rate, although it is possible to under/overestimate the uptake coefficients (therefore oxidation rate) over a short time period at certain conditions because of the heterogeneity of aerosol compositions.

These calculations suggest that sulfate in the haze episode was primarily controlled by the heterogeneous and aqueous oxidation via O_3, H_2O_2, and TMI pathways, enabling us to use the ε_{obs} and Eq. 5 to estimate the contributions of the oxidation pathways. The overall ε_{obs} value (+5.3 ± 1.8‰) falls in between $\varepsilon_{O3/H2O2}$ and ε_{TMI} values, indicating both O_3/H_2O_2 and TMI pathways played important roles in the oxidation process. Using Eq. 5 we determined the overall contributions from TMI and O_3/H_2O_2 pathways (Figure 4.3C) were roughly equal (f_{TMI} = 49±10%, $f_{O3/H2O2}$= 51±10%) during the haze episode. Notably, however, there were two time periods (at the end of $PM_{2.5}$ accumulation events I and II) when decreases in the ε_{obs} values were observed. In the first time period (Jan. 24, 6:00 to 18:00), sulfate concentration increased by ~100%, SOR remained steady, while the $\delta^{34}S_{sulfate}$ values decreased from 8.4‰ to +4.6‰. The calculated ε_{obs} values, thus, have decreased from 7.2‰ to 2.8‰, suggesting the TMI pathway have played a more important role during this process. The second time period (Jan. 25, 12:00 to Jan. 26, 3:00) was similar, when sulfate concentration increased by ~180% and the ε_{obs} value decreased from 9.9‰ to 3.4‰. Both events were associated with high $PM_{2.5}$ and low O_3 concentrations. The decreased ε_{obs} values suggested elevated contributions of TMI pathway (accounting for 57-62% of sulfate production). The increased TMI pathway contribution likely resulted from a combination of two factors. First, the high aerosol concentrations, which likely provided high aerosol surface area and high amount of transition metal ions (e.g., Fe, Mn, Cu, Zn, Pb) from local industrial emission[71], which could enhance the rate of TMI oxidation. The second, O_3/H_2O_2 oxidation rate was likely decreased due to decreased O_3 concentrations and liquid water content. The average O_3 concentrations (6.2 and

5.0 μg/m^3) and RH (51% and 65%) during these two periods were significantly lower than the rest of the haze episode (averaging 13.0 μg/m^3 O_3 and 81% RH), which might reduce the oxidation rate of O_3/H_2O_2. However, since it is difficult to quantitatively determine the rate of TMI pathway and the accurate pH of aerosol water therefore the rate of O_3 oxidation, either factor or both factors could be the dominant cause. Future experimental work is needed to separately investigate the effects of aerosol surface area, transition metal ion concentrations, RH, O_3 concentration etc., to each oxidation pathway.

4.4 Conclusions

The significant contribution from the TMI pathway (49±10%) suggest an elevated role of the TMI pathway during the rapid formation of sulfate aerosols in the haze episode, showing general agreement with atmospheric chemistry modeling studies. Globally the TMI pathway was estimated to contributed to 9-18% of total aerosol production[8,10], in most regions in China (including Nanjing), model simulations suggested that TMI had played a more important role, contributing to ~20-50% of total sulfate production[10]. Harris et al. (2013)[35] also pointed out that at least 35% of sulfate in several Chinese cities[44] was produced via the TMI pathway. During haze episodes, the contributions of the TMI pathway among the heterogeneous and aqueous oxidations seems to increase: a recently-developed modeling study[22] suggest the TMI pathway was responsible for as much as 80% of total heterogeneous and aqueous sulfate production during haze episodes in Beijing, and oxygen isotopic evidence suggested similar contributions (66-73%)[17]. Furthermore, field observation work at another heavily polluted region (Fort McMurray, Alberta, Canada) also implied the importance of the TMI pathway during the formation of secondary sulfate[72]. Our study had pointed out that, the TMI pathway was an important but probably not sole sulfate formation pathway during the haze episodes, and its contribution was likely elevated during the haze episodes. The increased contribution of the TMI pathway during haze episodes might originate from a combination of high aerosol surface, high atmospheric liquid water content and dust flux. In the meantime, the O_3 and/or H_2O_2 also played a major role in the formation of sulfate aerosols despite their lower-than-typical concentrations. Therefore, in order to improve the simulation of sulfate aerosol formation, all the above reactions (aqueous O_3, H_2O_2, TMI oxidations and heterogeneous O_3, H_2O_2, TMI oxidations) should be carefully parameterized in atmospheric chemistry models.

4.5 References

(1) Zheng, B.; Zhang, Q.; Zhang, Y.; He, K. B.; Wang, K.; Zheng, G. J.; Duan, F. K.; Ma, Y. L.; Kimoto, T. Heterogeneous Chemistry: A Mechanism Missing in Current Models to Explain Secondary Inorganic Aerosol Formation during the January 2013 Haze Episode in North China. *Atmos. Chem. Phys.* **2015**, *15* (4), 2031-2049.

(2) Guo, S.; Hu, M.; Zamora, M. L.; Peng, J.; Shang, D.; Zheng, J.; Du, Z.; Wu, Z.; Shao, M.; Zeng, L. Elucidating Severe Urban Haze Formation in China. *Proc. Natl. Acad. Sci.* **2014**, *111* (49), 17373–17378.

(3) Zheng, G. J.; Duan, F. K.; Su, H.; Ma, Y. L.; Cheng, Y.; Zheng, B.; Zhang, Q.; Huang, T.; Kimoto, T.; Chang, D. Exploring the Severe Winter Haze in Beijing: The Impact of Synoptic Weather, Regional Transport and Heterogeneous Reactions. *Atmos. Chem. Phys.* **2015**, *15* (6), 2969–2983.

(4) Huang, R.-J.; Zhang, Y.; Bozzetti, C.; Ho, K.-F.; Cao, J.-J.; Han, Y.; Daellenbach, K. R.; Slowik, J. G.; Platt, S. M.; Canonaco, F. High Secondary Aerosol Contribution to Particulate Pollution during Haze Events in China. *Nature* **2014**, *514* (7521), 218.

(5) Atkinson, R.; Baulch, D. L.; Cox, R. A.; Crowley, J. N.; Hampson, R. F.; Hynes, R. G.; Jenkin, M. E.; Rossi, M. J.; Troe, J. Evaluated Kinetic and Photochemical Data for Atmospheric Chemistry: Volume I-Gas Phase Reactions of Ox, HOx, NOx and SOx Species. *Atmos. Chem. Phys.* **2004**, *4* (6), 1461–1738.

(6) Reid, J. S.; Jonsson, H. H.; Smith, M. H.; Smirnov, A. Evolution of the Vertical Profile and Flux of Large Sea-salt Particles in a Coastal Zone. *J. Geophys. Res. Atmos.* **2001**, *106* (D11), 12039–12053.

(7) Herrmann, H.; Ervens, B.; Jacobi, H.-W.; Wolke, R.; Nowacki, P.; Zellner, R. CAPRAM2. 3: A Chemical Aqueous Phase Radical Mechanism for Tropospheric Chemistry. *J. Atmos. Chem.* **2000**, *36* (3), 231–284.

(8) Sofen, E. D.; Alexander, B.; Kunasek, S. A. The Impact of Anthropogenic Emissions on Atmospheric Sulfate Production Pathways, Oxidants, and Ice Core $\Delta^{17}O$ (SO_4^{2-}). *Atmos. Chem. Phys.* **2011**, *11* (7), 3565–3578.

(9) Harris, E.; Sinha, B.; Pinxteren, D. Van; Tilgner, A.; Fomba, K. W.; Schneider, J.; Roth, A.; Gnauk, T.; Fahlbusch, B.; Mertes, S., Lee, T., Collett, J., Foley, S., Borrmann, S., Hoppe, P., Herrmann, H.; Enhanced Role of Transition Metal Ion Catalysis during In-Cloud Oxidation of SO_2. *Science (80-.).* **2013**, *340* (6133), 727–730. https://doi.org/10.1126/science.1230911.

(10) Alexander, B.; Park, R. J.; Jacob, D. J.; Gong, S. Transition Metal-Catalyzed Oxidation of Atmospheric Sulfur: Global Implications for the Sulfur Budget. *J. Geophys. Res.* **2009**, *114* (D2), D02309. https://doi.org/10.1029/2008JD010486.

(11) Wang, G., Zhang, R., Gomez, M., Yang, L., Levy Zamora, M., Hu, M., Lin, Y., Peng, J., Guo, S., Meng, J., Li, J., Cheng, C., Hu, T., Ren, Y., Wang, Y., Gao, J., Cao, J., An, Z., Zhou, W., Li, G., Wang, J., Tian, P., Marrero-Ortiz, W., Secrest, J., Du, Z., Zheng, J., Shang, D., Zeng, L., Shao, M., Wang, W., Huang, Y., Wang, Y., Zhu, Y., Li, Y., Hu, J., Pan, B., Cai, L., Cheng, Y., Ji, Y., Zhang, F., Rosenfeld, D., Liss, P., Duce, R., Kolb, C., Molina, M., Persistent Sulfate Formation from London Fog to Chinese Haze. *Proc. Natl. Acad. Sci. U. S. A.* **2016**, 201616540. https://doi.org/10.1073/pnas.1616540113.

(12) Cheng, Y.; Zheng, G.; Wei, C.; Mu, Q.; Zheng, B.; Wang, Z.; Gao, M.; Zhang, Q.; He, K.; Carmichael, G. Reactive Nitrogen Chemistry in Aerosol Water as a Source of Sulfate during Haze Events in China. *Sci. Adv.* **2016**, *2* (12), e1601530.

(13) Xue, J.; Yuan, Z.; Yu, J. Z.; Lau, A. K. H. An Observation-Based Model for Secondary Inorganic Aerosols. *Aerosol Air Qual. Res.* **2014**, *14*, 862–878. https://doi.org/10.4209/aaqr.2013.06.0188.

(14) Xue, J.; Yuan, Z.; Griffith, S. M.; Yu, X.; Lau, A. K. H.; Yu, J. Z. Sulfate Formation Enhanced by a Cocktail of High NO_x, SO_2 , Particulate Matter, and Droplet PH during Haze-Fog Events in Megacities in China: An Observation-Based Modeling Investigation. *Environ. Sci. Technol.* **2016**, *50* (14), 7325–7334. https://doi.org/10.1021/acs.est.6b00768.

(15) Li, G.; Bei, N.; Cao, J.; Huang, R.; Wu, J.; Feng, T.; Wang, Y.; Liu, S.; Zhang, Q.; Tie, X. A Possible Pathway for Rapid Growth of Sulfate during Haze Days in China. *Atmos. Chem. Phys.* **2017**, *17* (5), 3301–3316.

(16) Huang, X.; Song, Y.; Zhao, C.; Li, M.; Zhu, T.; Zhang, Q.; Zhang, X. Pathways of Sulfate Enhancement by Natural and Anthropogenic Mineral Aerosols in China. *J. Geophys. Res. Atmos.* **2014**, *119* (24), 14,165-14,179. https://doi.org/10.1002/2014JD022301.

(17) He, P.; Alexander, B.; Geng, L.; Chi, X.; Fan, S.; Zhan, H.; Kang, H.; Zheng, G.; Cheng, Y.; Su, H., Liu, C., Xie, Z. Isotopic Constraints on Heterogeneous Sulfate Production in Beijing Haze. *Atmos. Chem. Phys.* **2018**, *18* (8), 5515–5528. https://doi.org/10.5194/acp-18-5515-2018.

(18) Li, L.; Hoffmann, M. R.; Colussi, A. J. Role of Nitrogen Dioxide in the Production of Sulfate during Chinese Haze-Aerosol Episodes. https://doi.org/10.1021/acs.est.7b05222.

(19) Liu, C.; Ma, Q.; Liu, Y.; Ma, J.; He, H. Synergistic Reaction between SO_2 and NO_2 on Mineral Oxides: A Potential Formation Pathway of Sulfate Aerosol. *Phys. Chem. Chem. Phys.* **2012**, *14* (5), 1668–1676.

(20) Zhao, D.; Song, X.; Zhu, T.; Zhang, Z.; Liu, Y.; Shang, J. Multiphase Oxidation of SO_2 by NO_2 on $CaCO_3$ Particles. *Atmos. Chem. Phys.* **2018**, *18* (4), 2481–2493.

(21) Wang, G.; Huang, L.; Gao, S.; Gao, S.; Wang, L. Characterization of Water-Soluble Species of PM_{10} and $PM_{2.5}$ Aerosols in Urban Area in Nanjing, China. *Atmos. Environ.* **2002**, *36* (8), 1299–1307.

(22) Shao, J.; Chen, Q.; Wang, Y.; Lu, X.; He, P.; Sun, Y.; Shah, V.; Martin, R. V; Philip, S.; Song, S. Heterogeneous Sulfate Aerosol Formation Mechanisms during Wintertime Chinese Haze Events: Air Quality Model Assessment Using Observations of Sulfate Oxygen Isotopes in Beijing. *Atmos. Chem. Phys.* **2019**, *19* (9), 6107–6123.

(23) Li, X.; Bao, H.; Gan, Y.; Zhou, A.; Liu, Y. Multiple Oxygen and Sulfur Isotope Compositions of Secondary Atmospheric Sulfate in a Mega-City in Central China. *Atmos. Environ.* **2013**, *81*, 591–599.

(24) Zhang, R.; Wang, G.; Guo, S.; Zamora, M. L.; Ying, Q.; Lin, Y.; Wang, W.; Hu, M.; Wang, Y. Formation of Urban Fine Particulate Matter. *Chem. Rev.* **2015**, *115* (10), 3803–3855.

(25) Wang, J.; Wang, S.; Jiang, J.; Ding, A.; Zheng, M.; Zhao, B.; Wong, D. C.; Zhou, W.; Zheng, G.; Wang, L. Impact of Aerosol–Meteorology Interactions on Fine Particle Pollution during China's Severe Haze Episode in January 2013. *Environ. Res. Lett.* **2014**, *9* (9), 94002.

(26) Wang, Y.; Zhang, Q.; Jiang, J.; Zhou, W.; Wang, B.; He, K.; Duan, F.; Zhang, Q.; Philip, S.; Xie, Y. Enhanced Sulfate Formation during China's Severe Winter Haze Episode in January 2013 Missing from Current Models. *J. Geophys. Res. Atmos.* **2014**, *119* (17), 10–425.

(27) Liu, M.; Song, Y.; Zhou, T.; Xu, Z.; Yan, C.; Zheng, M.; Wu, Z.; Hu, M.; Wu, Y.; Zhu, T. Fine Particle PH during Severe Haze Episodes in Northern China. *Geophys. Res. Lett.* **2017**, *44* (10), 5213–5221.

(28) Shi, G.; Xu, J.; Peng, X.; Xiao, Z.; Chen, K.; Tian, Y.; Guan, X.; Feng, Y.; Yu, H.; Nenes, A. PH of Aerosols in a Polluted Atmosphere: Source Contributions to Highly Acidic Aerosol. *Environ. Sci. Technol.* **2017**, *51* (8), 4289–4296.

(29) Weber, R. J.; Guo, H.; Russell, A. G.; Nenes, A. High Aerosol Acidity despite Declining Atmospheric Sulfate Concentrations over the Past 15 Years. *Nat. Geosci.* **2016**, *9* (4), 282.

(30) Fountoukis, C.; Nenes, A. ISORROPIA II: A Computationally Efficient Thermodynamic Equilibrium Model for K^+–Ca^{2+}–Mg^{2+}–NH_4^+–Na^+–SO_4^{2-}–NO_3^-–Cl^-–H_2O Aerosols. *Atmos. Chem. Phys.* **2007**, *7* (17), 4639–4659.

(31) Seinfeld, J. H.; Pandis, S. N.; Noone, K. Atmospheric Chemistry and Physics: From Air Pollution to Climate Change. AIP 1998, pp 265-324.

(32) Gankanda, A.; Coddens, E. M.; Zhang, Y.; Cwiertny, D. M.; Grassian, V. H. Sulfate Formation Catalyzed by Coal Fly Ash, Mineral Dust and Iron (Iii) Oxide: Variable Influence of Temperature and Light. *Environ. Sci. Process. Impacts* **2016**, *18* (12), 1484–1491.

(33) Bao, H.; Thiemens, M. H.; Loope, D. B.; Yuan, X.-L. Sulfate Oxygen-17 Anomaly in an Oligocene Ash Bed in Mid-North America: Was It the Dry Fogs? *Geophys. Res. Lett.* **2003**, *30* (16). https://doi.org/10.1029/2003GL016869.

(34) Bao, H.; Reheis, M. C. Multiple Oxygen and Sulfur Isotopic Analyses on Water-Soluble Sulfate in Bulk Atmospheric Deposition from the Southwestern United States. *J. Geophys. Res. D Atmos.* **2003**, *108* (14), 4430. https://doi.org/10.1029/2002jd003022.

(35) Harris, E.; Sinha, B.; Hoppe, P.; Ono, S. High-Precision Measurements of ^{33}S and ^{34}S Fractionation during SO_2 Oxidation Reveal Causes of Seasonality in SO_2 and Sulfate Isotopic Composition. *Environ. Sci. Technol.* **2013**, *47* (21), 12174–12183. https://doi.org/10.1021/es402824c.

(36) Harris, E.; Sinha, B.; Hoppe, P.; Foley, S.; Borrmann, S. Fractionation of Sulfur Isotopes during Heterogeneous Oxidation of SO_2 on Sea Salt Aerosol: A New Tool to Investigate Non-Sea Salt Sulfate Production in the Marine Boundary Layer. *Atmos. Chem. Phys. Atmos. Chem. Phys.* **2012**, *12*, 4619–4631. https://doi.org/10.5194/acp-12-4619-2012.

(37) Harris, E.; Sinha, B.; Hoppe, P.; Crowley, J. N.; Ono, S.; Foley, S. Sulfur Isotope Fractionation during Oxidation of Sulfur Dioxide: Gas-Phase Oxidation by OH Radicals and Aqueous Oxidation by H_2O_2, O_3 and Iron Catalysis. *Atmos. Chem. Phys. Atmos. Chem. Phys.* **2012**, *12*, 407–424. https://doi.org/10.5194/acp-12-407-2012.

(38) Guo, Z.; Shi, L.; Chen, S.; Jiang, W.; Wei, Y.; Rui, M.; Zeng, G. Sulfur Isotopic Fractionation and Source Appointment of $PM_{2.5}$ in Nanjing Region around the Second Session of the Youth Olympic Games. *Atmos. Res.* **2016**, *174*, 9–17.

(39) Chen, S.; Guo, Z.; Guo, Z.; Guo, Q.; Zhang, Y.; Zhu, B.; Zhang, H. Sulfur Isotopic Fractionation and Its Implication: Sulfate Formation in $PM_{2.5}$ and Coal Combustion under Different Conditions. *Atmos. Res.* **2017**, *194*, 142–149.

(40) Li, J.; Michalski, G.; Davy, P.; Harvey, M.; Katzman, T.; Wilkins, B. Investigating Source Contributions of Size-Aggregated Aerosols Collected in Southern Ocean and Baring Head, New Zealand Using Sulfur Isotopes. *Geophys. Res. Lett.* **2018**, *45*(8), 3717-3727.

(41) Saltzman, E. S.; Brass, G. W.; Price, D. A. The Mechanism of Sulfate Aerosol Formation: Chemical and Sulfur Isotopic Evidence. *Geophys. Res. Lett.* **1983**, *10* (7), 513–516. https://doi.org/10.1029/GL010i007p00513.

(42) Rayleigh, Lord. L. Theoretical Considerations Respecting the Separation of Gases by Diffusion and Similar Processes. *London, Edinburgh, Dublin Philos. Mag. J. Sci.* **1896**, *42* (259), 493–498.

(43) Maruyama, T.; Ohizumi, T.; Taneoka, Y.; Minami, N.; Fukuzaki, N.; Mukai, H.; Murano, K.; Kusakabe, M. Sulfur Isotope Ratios of Coals and Oils Used in China and Japan. *Nippon Kagaku Kaishi* **2000**, No. 1, 45–52.

(44) Mukai, H.; Tanaka, A.; Fujii, T.; Zeng, Y.; Hong, Y.; Tang, J.; Guo, S.; Xue, H.; Sun, Z.; Zhou, J. Regional Characteristics of Sulfur and Lead Isotope Ratios in the Atmosphere at Several Chinese Urban Sites. *Environ. Sci. Technol.* **2001**, *35* (6), 1064–1071.

(45) Han, X.; Guo, Q.; Liu, C.; Fu, P.; Strauss, H.; Yang, J.; Hu, J.; Wei, L.; Ren, H.; Peters, M. Using Stable Isotopes to Trace Sources and Formation Processes of Sulfate Aerosols from Beijing, China. *Sci. Rep.* **2016**, *6*, 29958.

(46) Wei, L.; Yue, S.; Zhao, W.; Yang, W.; Zhang, Y.; Ren, L.; Han, X.; Guo, Q.; Sun, Y.; Wang, Z.; Fu, P.; Stable Sulfur Isotope Ratios and Chemical Compositions of Fine Aerosols ($PM_{2.5}$) in Beijing, China. *Science of The Total Environment*, **2018,** 633, 1156-1164. https://doi.org/10.1016/j.scitotenv.2018.03.153.

(47) Guo, Z.; Li, Z.; Farquhar, J.; Kaufman, A. J.; Wu, N.; Li, C.; Dickerson, R. R.; Wang, P. Identification of Sources and Formation Processes of Atmospheric Sulfate by Sulfur Isotope and Scanning Electron Microscope Measurements. *J. Geophys. Res.* **2010**, *115* (D7), D00K07. https://doi.org/10.1029/2009JD012893.

(48) Han, X.; Guo, Q.; Strauss, H.; Liu, C.; Hu, J.; Guo, Z.; Wei, R.; Peters, M.; Tian, L.; Kong, J. Multiple Sulfur Isotope Constraints on Sources and Formation Processes of Sulfate in Beijing PM2. 5 Aerosol. *Environ. Sci. Technol.* **2017**, *51* (14), 7794–7803.

(49) Lin, M.; Biglari, S.; Zhang, Z.; Crocker, D.; Tao, J.; Su, B.; Liu, L.; Thiemens, M. H. Vertically Uniform Formation Pathways of Tropospheric Sulfate Aerosols in East China Detected from Triple Stable Oxygen and Radiogenic Sulfur Isotopes. *Geophys. Res. Lett.* **2017**, *44* (10), 5187–5196. https://doi.org/10.1002/2017GL073637.

(50) Lin, M.; Zhang, X.; Li, M.; Xu, Y.; Zhang, Z.; Tao, J.; Su, B.; Liu, L.; Shen, Y.; Thiemens, M. H. Five-S-Isotope Evidence of Two Distinct Mass-Independent Sulfur Isotope Effects and Implications for the Modern and Archean Atmospheres. *Proc. Natl. Acad. Sci.* **2018**, *115* (34), 8541–8546.

(51) Romero, A. B.; Thiemens, M. H. Mass-independent Sulfur Isotopic Compositions in Present-day Sulfate Aerosols. *J. Geophys. Res. Atmos.* **2003**, *108* (D16), 4524.

(52) Cao, F.; Zhang, S.-C.; Kawamura, K.; Zhang, Y.-L. Inorganic Markers, Carbonaceous Components and Stable Carbon Isotope from Biomass Burning Aerosols in Northeast China. *Sci. Total Environ.* **2016**, *572*, 1244–1251.

(53) Legrand, M.; Hammer, C.; De Angelis, M.; Savarino, J.; Delmas, R.; Clausen, H.; Johnsen, S. J. Sulfur-containing Species (Methanesulfonate and SO_4) over the Last Climatic Cycle in the Greenland Ice Core Project (Central Greenland) Ice Core. *J. Geophys. Res. Ocean.* **1997**, *102* (C12), 26663–26679.

(54) Calhoun, J. A.; Bates, T. S.; Charlson, R. J. Sulfur Isotope Measurements of Submicrometer Sulfate Aerosol Particles over the Pacific Ocean. *Geophys. Res. Lett.* **1991**, *18* (10), 1877–1880. https://doi.org/10.1029/91GL02304.

(55) Faloona, I. Sulfur Processing in the Marine Atmospheric Boundary Layer: A Review and Critical Assessment of Modeling Uncertainties. *Atmos. Environ.* **2009**, *43* (18), 2841–2854. https://doi.org/10.1016/j.atmosenv.2009.02.043.

(56) Li, M.; Zhang, Q.; Kurokawa, J.; Woo, J.-H.; He, K.; Lu, Z.; Ohara, T.; Song, Y.; Streets, D. G.; Carmichael, G. R. MIX: A Mosaic Asian Anthropogenic Emission Inventory under the International Collaboration Framework of the MICS-Asia and HTAP. *Atmos. Chem. Phys.* **2017**, *17* (2), 935-963.

(57) Hong, Y.; Zhang, H.; Zhu, Y. Sulfur Isotopic Characteristics of Coal in China and Sulfur Isotopic Fractionation during Coal-Burning Process. *Chinese J. geochemistry* **1993**, *12* (1), 51–59.

(58) Novák, M.; Jacková, I.; Prechová, E. Temporal Trends in the Isotope Signature of Air-Borne Sulfur in Central Europe. *Environ. Sci. Technol.* **2001**, *35* (2), 255–260.

(59) Forrest, J.; Newman, L. Sampling and Analysis of Atmospheric Sulfur Compounds for Isotope Ratio Studies. *Atmos. Environ.* **1973**, *7* (5), 561–573.

(60) Mariotti, A.; Germon, J. C.; Hubert, P.; Kaiser, P.; Letolle, R.; Tardieux, A.; Tardieux, P. Experimental Determination of Nitrogen Kinetic Isotope Fractionation: Some Principles; Illustration for the Denitrification and Nitrification Processes. *Plant Soil* **1981**, *62* (3), 413–430.

(61) Madronich, S.; Flocke, S. The Role of Solar Radiation in Atmospheric Chemistry. In *Environmental photochemistry*; Springer, 1999; pp 1–26.

(62) Stockwell, W. R.; Kirchner, F.; Kuhn, M.; Seefeld, S. A New Mechanism for Regional Atmospheric Chemistry Modeling. *J. Geophys. Res. Atmos.* **1997**, *102* (D22), 25847–25879.

(63) Heard, D. E.; Carpenter, L. J.; Creasey, D. J.; Hopkins, J. R.; Lee, J. D.; Lewis, A. C.; Pilling, M. J.; Seakins, P. W.; Carslaw, N.; Emmerson, K. M. High Levels of the Hydroxyl Radical in the Winter Urban Troposphere. *Geophys. Res. Lett.* **2004**, *31* (18), L18112.

(64) Ren, X.; Brune, W. H.; Mao, J.; Mitchell, M. J.; Lesher, R. L.; Simpas, J. B.; Metcalf, A. R.; Schwab, J. J.; Cai, C.; Li, Y. Behavior of OH and HO_2 in the Winter Atmosphere in New York City. *Atmos. Environ.* **2006**, *40*, 252–263.

(65) Giardina, M.; Buffa, P. A New Approach for Modeling Dry Deposition Velocity of Particles. *Atmos. Environ.* **2018**, *180*, 11–22.

(66) Han, S.; Wu, J.; Zhang, Y.; Cai, Z.; Feng, Y.; Yao, Q.; Li, X.; Liu, Y.; Zhang, M. Characteristics and Formation Mechanism of a Winter Haze–Fog Episode in Tianjin, China. *Atmos. Environ.* **2014**, *98*, 323–330.

(67) Zhang, C.; Wang, L.; Qi, M.; Ma, X.; Zhao, L.; Ji, S.; Wang, Y.; Lu, X.; Wang, Q.; Xu, R. Evolution of Key Chemical Components in $PM_{2.5}$ and Potential Formation Mechanisms of Serious Haze Events in Handan, China. *Aerosol Air Qual. Res.* **2018**, *18*, 1545–1557.

(68) Jacob, D. J. Heterogeneous Chemistry and Tropospheric Ozone. *Atmos. Environ.* **2000**, *34* (12–14), 2131–2159.

(69) Fu, H.; Wang, X.; Wu, H.; Yin, Y.; Chen, J. Heterogeneous Uptake and Oxidation of SO2 on Iron Oxides. *J. Phys. Chem. C* **2007**, *111* (16), 6077–6085.

(70) Adams, J. W.; Rodriguez, D.; Cox, R. A. The Uptake of SO 2 on Saharan Dust: A Flow Tube Study. *Atmos. Chem. Phys.* **2005**, *5* (10), 2679–2689.

(71) Shanquan, L. I.; ZHANG, G.; Jinling, Y.; Nan, J. I. A. Multi-Source Characteristics of Atmospheric Deposition in Nanjing, China, as Controlled by East Asia Monsoons and Urban Activities. *Pedosphere* **2016**, *26* (3), 374–385.

(72) Amiri, N.; Ghahremaninezhad, R.; Rempillo, O.; Tokarek, T. W.; Odame-Ankrah, C. A.; Osthoff, H. D.; Norman, A.-L. Stable Sulfur Isotope Measurements to Trace the Fate of SO 2 in the Athabasca Oil Sands Region. *Atmos. Chem. Phys.* **2018**, *18* (11), 7757–7780.

CHAPTER 5. QUANTIFYING THE NITROGEN ISOTOPE EFFECTS DURING PHOTOCHEMICAL EQUILIBRIUM BETWEEN NO AND NO_2: IMPLICATIONS FOR $\delta^{15}N$ IN TROPOSPHERIC REACTIVE NITROGEN

This chapter is a reprint from a published article (Li, J., Zhang, X., Orlando, J., Tyndall, G., & Michalski, G., (2020). Quantifying the nitrogen isotope effects during photochemical equilibrium between NO and NO_2: implications for $\delta^{15}N$ in tropospheric reactive nitrogen. *Atmospheric Chemistry and Physics*).

Abstract

Nitrogen isotope fractionations between nitrogen oxides (NO and NO_2) play a significant role in determining the nitrogen isotopic compositions ($\delta^{15}N$) of atmospheric reactive nitrogen. Both the equilibrium isotopic exchange between NO and NO_2 molecules and the isotope effects occurring during the NO_x photochemical cycle are important, but both are not well constrained. The nighttime and daytime isotopic fractionations between NO and NO_2 in an atmospheric simulation chamber at atmospherically relevant NO_x levels were measured. Then, the impact of NO_x level and NO_2 photolysis rate to the combined isotopic fractionation (equilibrium isotopic exchange and photochemical cycle) between NO and NO_2 were calculated. It was found that the isotope effects occurring during the NO_x photochemical cycle can be described using a single fractionation factor, designated the Leighton Cycle Isotope Effect (LCIE). The results showed that at room temperature, the fractionation factor of nitrogen isotopic exchange is 1.0289±0.0019, and the fractionation factor of LCIE (when O_3 solely controls the oxidation from NO to NO_2) is 0.990±0.005. The measured LCIE factor showed good agreement with previous field measurements, suggesting that it could be applied in ambient environment, although future work is needed to assess the isotopic fractionation factors of NO + $RO_2/HO_2 \rightarrow NO_2$. The results were used to model the NO-NO_2 isotopic fractionations under several NO_x conditions. The model suggested that isotopic exchange was the dominate factor when NO_x >20 nmol mol^{-1}, while LCIE was more important at low NO_x concentrations (<1 nmol mol^{-1}) and high rates of NO_2 photolysis. These findings provided a useful tool to quantify the isotopic fractionations between tropospheric NO and NO_2, which can be applied in future field observations and atmospheric chemistry models.

5.1 Introduction

The nitrogen isotopic composition ($\delta^{15}N$) of reactive nitrogen compounds in the atmosphere is an important tool in understanding the sources and chemistry of atmospheric NO_x ($NO+NO_2$). It has been suggested that the $\delta^{15}N$ value of atmospheric nitrate (HNO_3, nitrate aerosols and nitrate ions in the precipitation and snow) imprints the $\delta^{15}N$ value of NO_x sources (Elliott et al., 2009; Kendall et al., 2007) thus many studies have used the $\delta^{15}N$ values of atmospheric nitrate to investigate NO_x sources (Chang et al., 2018; Felix et al., 2012; Felix & Elliott, 2014; Gobel et al., 2013; Hastings et al., 2004, 2009; Morin et al., 2009; Park et al., 2018; Walters et al., 2015, 2018). However, there remain questions about how isotopic fractionations that may occur during photochemical cycling of NO_x could alter the $\delta^{15}N$ values as it partitions into NO_y (NO_y = atmospheric nitrate, NO_3, N_2O_5, HONO, etc., Chang et al., 2018; Freyer, 1991; Hastings et al., 2004; Jarvis et al., 2008; Michalski et al., 2005; Morin et al., 2009; Zong et al., 2017). Similarily, other complex reactive nitrogen chemistry, such as nitrate photolysis and re-deposition in ice and snow (Frey et al., 2009), may impact the $\delta^{15}N$ of NO_y and atmospheric nitrate. The fractionation between NO and NO_2 via isotope exchange has been suggested to be the dominant factor in determining the $\delta^{15}N$ of NO_2 and ultimately atmospheric nitrate (Freyer, 1991; Freyer et al., 1993; Savarino et al., 2013; Walters et al., 2016). However, isotopic fractionations occur in most, if not all, NO_x and NO_y reactions, while most of these are still unknown or, if calculated (Walters and Michalski, 2015), unverified by experiments. Since the atmospheric chemistry of NO_y varies significantly in different environments (e.g., polluted vs. pristine, night vs. day), the isotopic fractionations associated with NO_y chemistry are also likely to vary in different environments. These unknowns could potentially bias conclusions about NO_x source apportionment reached when using nitrogen isotopes. Therefore, understanding the isotopic fractionations between NO and NO_2 during photochemical cycling could improve our understanding of the relative role of sources versus chemistry for controlling the $\delta^{15}N$ variations of atmospheric NO_2 and nitrate.

In general, there are three types of isotopic fractionation effects associated with NO_x chemistry (Figure 5.1A). The first type is the equilibrium isotopic effect (EIE), i.e., isotope exchange between two compounds without forming new molecules (Urey, 1947, Bigeleisen and Mayer, 1947), which for nitrogen isotopes in the NO_x system is the $^{15}NO + {}^{14}NO_2 \leftrightarrow {}^{14}NO + {}^{15}NO_2$ exchange reaction (Begun and Melton, 1956, Walters et al., 2016). The second type is the kinetic

isotopic effect (KIE) associated with difference in isotopologue rate coefficients during unidirectional reactions (Bigeleisen & Wolfsberg, 1957). In the NO_x system this KIE would manifest in the oxidation of NO into NO_2 by $O_3/HO_2/RO_2$. The third type is the photochemical isotope fractionation effect (PHIFE, Miller & Yung, 2000), which for NO_x is the isotopic fractionation associated with NO_2 photolysis. All three fractionations could impact the $\delta^{15}N$ value of NO_2, and consequently atmospheric nitrate, but the relative importance of each may vary.

The limited number of studies on the EIE in the NO_x cycle have significant uncertainties. Discrepancies in the EIE for $^{15}NO + {}^{14}NO_2 \leftrightarrow {}^{14}NO + {}^{15}NO_2$ have been noted in several studies. Theoretical calculations predicted isotope fractionation factors (α) ranging from 1.035 to 1.042 at room temperature (Begun & Fletcher, 1960; Monse et al., 1969; Walters & Michalski, 2015) due to the different approximations used to calculate harmonic frequencies in each study. Likewise, two separate experiments measured different room temperature fractionation factors of 1.028±0.002 (Begun & Melton, 1956) and 1.0356±0.0015 (Walters et al., 2016). A concern in both experiments is that they were conducted in small chambers with high NO_x concentrations (hundreds of μmol mol^{-1}), significantly higher than typical ambient atmospheric NO_x levels (usually less than 0.1 μmol mol^{-1}). Whether the isotopic fractionation factors determined by these experiments are applicable in the ambient environment is uncertain because of possible wall effects and formation of higher oxides, notably N_2O_4 and N_2O_3 at these high NO_x concentrations.

Even less research has examined the KIE and PHIFE occurring during NO_x cycling. The KIE of $NO + O_3$ has been theoretically calculated (Walters and Michalski, 2016) but has not been experimentally verified. The NO_2 PHIFE has not been experimentally determined or theoretically calculated. As a result, field observation studies often overlook the effects of PHIFE and KIE. Freyer et al. (1993) measured NO_x concentrations and the $\delta^{15}N$ values of NO_2 over a 1-year period at Julich, Germany and inferred a combined NO_x isotope fractionation factor (EIE+KIE+PHIFE) of 1.018±0.001. Freyer et al. (1993) suggested that the NO_x photochemical cycle (KIE and PHIFE) tends to diminish the equilibrium isotopic fractionation (EIE) between NO and NO_2. Even if this approach were valid, applying this single fractionation factor elsewhere, where NO_x, O_3 concentrations and actinic fluxes are different, would be tenuous given that these factors may influence the relative importance of EIE, KIE and PHIFE (Hastings et al., 2004; Walters et al., 2016). Therefore, to quantify the overall isotopic fractionations between NO and NO_2 at various

tropospheric conditions, it is crucial to know 1) isotopic fractionation factors of EIE, KIE and PHIFE individually and 2) the relative importance of each factor under various conditions.

In this work, we aim to quantify the nitrogen isotope fractionation factors between NO and NO_2 at photochemical equilibrium. First, we measure the N isotope fractionations between NO and NO_2 in an atmospheric simulation chamber at atmospherically relevant NO_x levels. Then, we provide mathematical solutions to assess the impact of NO_x level and NO_2 photolysis rate ($j(NO_2)$) to the relative importance of EIE, KIE and PHIFE. Subsequently we use the solutions and chamber measurements to calculate the isotopic fractionation factors of EIE, KIE and PHIFE. Lastly, using the calculated fractionation factors and the equations, we model the NO-NO_2 isotopic fractionations at several sites to illustrate the behavior of $\delta^{15}N$ values of NO_x in the ambient environment.

5.2 Methods

The experiments were conducted using a 10 m^3 Atmospheric Simulation Chamber at the National Center for Atmospheric Research (see descriptions in Appendix A.1 and Zhang et al. (2018)). A set of mass flow controllers was used to inject NO and O_3 into the chamber. NO was injected at 1 L min^{-1} from an in-house NO/N_2 cylinder (133.16 μmol mol^{-1} NO in ultra-pure N_2), and O_3 was generated by flowing 5 L min^{-1} zero-air through a flow tube equipped with a UV Pen-Ray lamp (UVP LLC., CA) into the chamber. NO and NO_2 concentrations were monitored in real time by chemiluminescence with a detection limit of 0.5 nmol mol^{-1} (model CLD 88Y, Eco Physics, MI) as were O_3 concentrations using an UV absorption spectroscopy with a detection limit of 0.5 nmol mol^{-1} (model 49, Thermo Scientific, CO). In each experiment, the actual amounts of NO and O_3 injected were calculated using measured NO_x and O_3 concentrations after steady state was reached (usually within 1 h). The wall loss rate of NO_2 was tested by monitoring O_3 (29 nmol mol^{-1}) and NO_x (62 nmol mol^{-1}) over a 4-hour period. After the NO and NO_2 concentrations reached steady state, no decrease in NO_2 concentrations was observed showing that chamber wall loss was negligible.

Three experiments were conducted to measure the $\delta^{15}N$ value of the tank NO (i.e., the $\delta^{15}N$ value of total NO_x). In each of these experiments, a certain amount of O_3 was first injected into the chamber, then approximately the same amount of NO was injected into the chamber to ensure 100% of the NO_x was in the form of NO_2 with little O_3 (<15 nmol mol^{-1}) remaining in the chamber, such

that the O_3+NO_2 reaction was negligible. The NO_2 in the chamber was then collected and its $\delta^{15}N$ value measured, which equates to the $\delta^{15}N$ value of the tank NO.

Two sets of experiments were conducted to separately investigate the EIE, KIE and PHIFE. The first set of experiments was conducted in the dark. In each of these dark experiments, a range of NO and O_3 ([O_3]<[NO]) was injected into the chamber to produce NO-NO_2 mixtures with [NO]/[NO_2] ratios ranging from 0.43 to 1.17. The N isotopes of these mixtures were used to investigate the EIE between NO and NO_2. The second set of experiments was conducted under irradiation of UV lights (300-500 nm, see Appendix A.1 for irradiation spectrum). Under such conditions, NO, NO_2 and O_3 reached photochemical steady state, which combined the isotopic effects of EIE, KIE and PHIFE.

In all experiments, the concentrations of NO, NO_2 and O_3 were allowed to reach steady state, and the product NO_2 was collected from the chamber using a honeycomb denuder tube. After the NO, NO_2 and O_3 concentrations reached steady-state, well-mixed chamber air was drawn out through a 40 cm long Norprene Thermoplastic tubing at 10 L min^{-1} and passed through a honeycomb denuder system (Chemcomb 3500, Thermo Scientific). Based on flow rate, the NO_2 residence time in the was less than 0.5 second, thus in the light-on experiments where NO and O_3 coexisted, the NO_2 produced inside the transfer tube through NO+O_3 reactions should be <0.03 nmol mol^{-1} (using the upper limit of NO and O_3 concentrations in our experiments). The honeycomb denuder system consisted of two honeycomb denuder tubes connected in series. Each honeycomb denuder tube is a glass cylinder of 38 mm long, 47 mm in diameter, and consist of 212 hexagonal tubes with inner diameters of 2 mm. Before collecting samples, each denuder tube was coated with a solution of 10% KOH and 25% guaiacol in methanol and then dried by flowing N_2 gas through the denuder tube for 15 seconds (Williams and Grosjean, 1990, Walters et al., 2016). The NO_2 reacted with guaiacol coating and was converted into NO_2^- that was retained on the denuder tube wall (Williams and Grosjean, 1990). NO was inert to the denuder tube coating: a control experiment sampled pure NO using the denuder tubes, which did not show any measurable NO_2^-. The NO_2 collection efficiency of a single honeycomb denuder tube was tested in another control experiment: air containing 66 nmol mol^{-1} of NO_2 was drawn out of the chamber through a denuder tube, and the NO_2 concentration at the exit of the tube holder was measured and found to be below the detection limit (<1 nmol mol^{-1}), suggesting the collection efficiency was nearly 100% when [NO_2] <66 nmol mol^{-1}. Furthermore, when the denuder system consisted of two denuder

tubes in series and NO_2^- in the second denuder was below the detection limit indicating trivial NO_2 breakthrough. Each NO_2 collection lasted for 0.5-3 hours in order to collect enough NO_2^- for isotopic analysis (at least 300 nmol). After collection, the NO_2^- was leached from each denuder tube by rinsing thoroughly with 10 ml deionized water into a clean polypropylene container and stored frozen until isotopic analysis. Isotopic analysis was conducted at Purdue Stable Isotope Laboratory. For each sample, approximately 50 nmol of the NO_2^- extract was mixed with 2 M sodium azide solution in acetic acid buffer in an air-tight glass vial, then shaken overnight to completely reduce all the NO_2^- to $N_2O_{(g)}$ (Casciotti & McIlvin, 2007; McIlvin & Altabet, 2005). The product N_2O was directed into a Thermo GasBench equipped with cryo-trap, then the $\delta^{15}N$ of the N_2O was measured using a Delta-V Isotope Ratios Mass Spectrometer. Six coated denuders tubes that did not get exposed to NO_2 were also analyzed using the same chemical procedure, which did not show any measurable signal on the IRMS, suggesting the blank from both sampling process and the chemical conversion process was negligible. The overall analytical uncertainty for $\delta^{15}N$ analysis was 0.5 ‰ (1σ) based on replicate analysis of in house NO_2^- standards.

5.3 Results and discussion

5.3.1 Equilibrium isotopic fractionation between NO and NO_2

The equilibrium isotope fractionation factor, $\alpha(NO_2\text{-}NO)$, is the ^{15}N enrichment in NO_2 relative to NO, and is expressed as the ratio of rate constants k_2 / k_1 of two reactions:

$^{15}NO_2 + {}^{14}NO \rightarrow {}^{15}NO + {}^{14}NO_2$ R1, rate constant = k_1

$^{15}NO + {}^{14}NO_2 \rightarrow {}^{15}NO_2 + {}^{14}NO$ R2, rate constant = $k_2 = k_1\ \alpha(NO_2\text{-}NO)$

where k_1 is the rate constant of the isotopic exchange, which was previously determined to be 8.14×10^{-14} cm^3 s^{-1} (Sharma et al., 1970). The reaction time required for NO-NO_2 to reach isotopic equilibrium was estimated using the exchange rate constants in a simple kinetics box model (BOXMOX, Knote et al., 2015). The model predicts that at typical NO_x concentrations used during the chamber experiments (7.7-62.4 nmol mol^{-1}), isotopic equilibrium would be reached within 15 minutes (see Appendix A.2). Since the sample collection usually started 1 hour after NO_x was well mixed in the chamber, there was sufficient time to reach full isotope equilibrium. The isotope equilibrium fractionation factor ($\alpha(NO_2\text{-}NO)$) is then calculated to be:

$$\alpha(NO_2 - NO) = \frac{[^{15}NO_2][^{14}NO]}{[^{14}NO_2][^{15}NO]} = \frac{R(NO_2)}{R(NO)} \quad \text{Eq. (1)}$$

where R(NO, NO_2) are the $^{15}N/^{14}N$ ratios of NO and NO_2. By definition, the $\delta^{15}N(NO)=(R(NO)/R(reference)-1)\times1000$ ‰ and $\delta^{15}N(NO_2)=(R(NO_2)/R(reference)-1)\times1000$ ‰, but hereafter, the $\delta^{15}N$ values of NO, NO_2 and NO_x will be referred as δ(NO), $\delta(NO_2)$ and $\delta(NO_x)$, respectively. Eq. (1) leads to:

$$\delta(NO_2) - \delta(NO) = (\alpha(NO_2 - NO) - 1)\,(1 + \delta(NO)) \quad \text{Eq. (2)}$$

Using Eq. (2) and applying NO_x isotopic mass balance ($\delta(NO_x)=f(NO_2)\delta(NO_2)+(1-f(NO_2))\delta(NO)$, $f(NO_2)=[NO_2]/([NO]+[NO_2])$ yields:

$$\frac{\delta(NO_2)-\delta(NO_x)}{1+\delta(NO_2)} = \frac{\alpha(NO_2-NO)-1}{\alpha(NO_2-NO)}\left(1 - f(NO_2)\right) \quad \text{Eq. (3)}$$

Here, $\delta(NO_x)$ equals to the $\delta^{15}N$ value of the cylinder NO and $f(NO_2)$ is the molar fraction of NO_2 with respect to total NO_x. Three experiments (Table 1) that measured $\delta(NO_x)$ showed consistent $\delta(NO_x)$ values of (-58.7±0.8) ‰ (n = 3), indicating $\delta(NO_x)$ remained unchanged throughout the experiments (as expected for isotope mass balance). Thus, the $\delta(NO_x)$ can be treated as a constant in Eq. (3), and the linear regression of $(\delta(NO_2)-\delta(NO_x))/(1+\delta(NO_2))$ versus $1-f(NO_2)$ should have an intercept of 0 and a slope of $(\alpha(NO_2\text{-}NO)-1)/\alpha(NO_2\text{-}NO)$.

The plot of $(\delta(NO_2)-\delta(NO_x))/(1+\delta(NO_2))$ as a function of $1-f(NO_2)$ values from five experiments yields an $\alpha(NO_2\text{-}NO)$ value of 1.0289±0.0019 at room temperature (Figure 5.1B and Table 5.1). This fractionation factor is comparable to previously measured values but with some differences. Our result agrees well with the $\alpha(NO_2\text{-}NO)$ value of 1.028±0.002 obtained by Begun and Melton (1956) at room temperature. However, Walters et al., (2016) determined the $\alpha(NO_2\text{-}NO)$ values of NO-NO_2 exchange in a 1-liter reaction vessel, which showed a slightly higher $\alpha(NO_2\text{-}NO)$ value of 1.035. This discrepancy might originate from rapid heterogeneous reactions on the wall of the reaction vessel at high NO_x concentrations and the small chamber size used by Walters et al. (2016). They used a reaction vessel made of Pyrex, which is known to absorb water (Do Remus et al., 1983; Takei et al., 1997) that can react with NO_2 forming HONO, HNO_3 and other N compounds. Additionally, previous studies have suggested that Pyrex walls enhance the formation rate of N_2O_4 by over an order of magnitude (Barney & Finlayson-Pitts, 2000; Saliba et

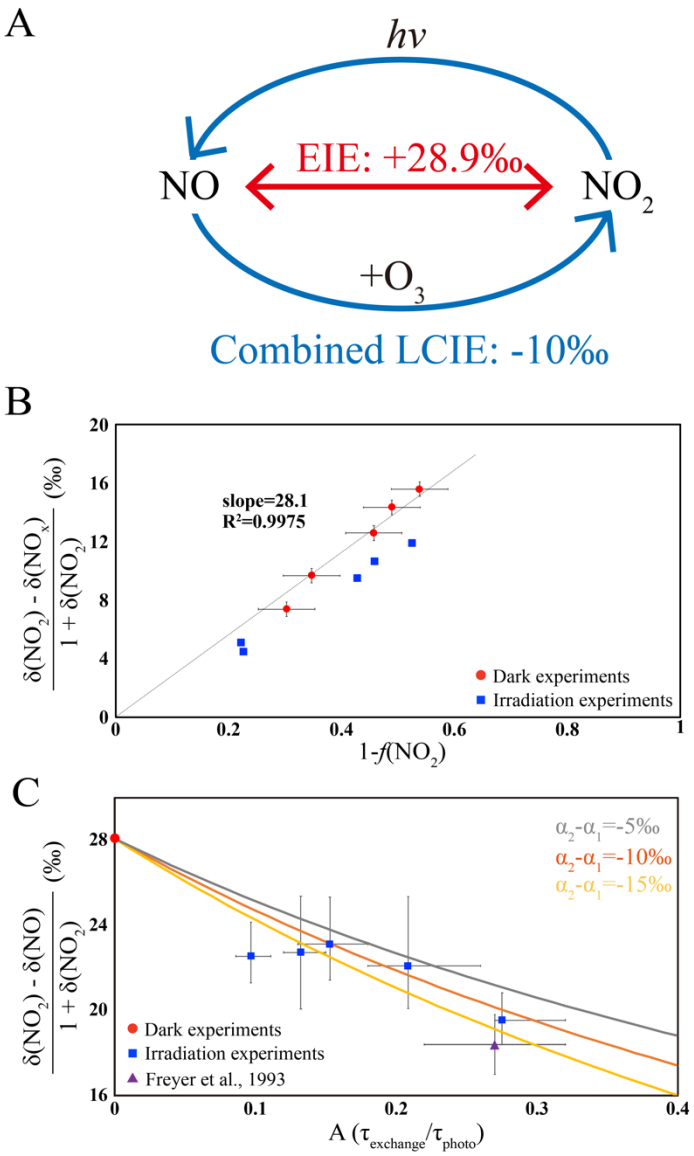

Figure 5.1 **A.** a sketch of the isotopic fractionation processes between NO and NO_2, both fractionation factors are determined in this work. **B.** Results from five dark experiments (red circles) yielded a line with slope of 28.1‰ and an α(NO_2-NO) value of 1.0289, while the results from five UV irradiation experiments (blue squares) showed a smaller slope; **C.** Results from five UV irradiation experiments (blue squares) and a previous field study (purple triangle), comparing to the dark experiments (red circle). The three lines represent different (α_2-α_1) values: the (α_2-α_1) = -10 ‰ line showed the lowest RMSE to our experimental data as well as the previous field observations. The error bars in panels B and C represented the combined uncertainties of NO_x concentration measurements and isotopic analysis.

al., 2001), which at isotopic equilibrium is enriched in ^{15}N compared to NO and NO_2 (Walters & Michalski, 2015). Therefore, their measured α(NO_2-NO) might be slightly higher than the actual α(NO_2-NO) value. In this work, the 10 m^3 chamber has a much smaller surface to volume ratio

relative to Walters et al. (2016) which minimizes wall effects, and the walls were made of Teflon that minimize NO_2 surface reactivity, which was evidenced by the NO_2 wall loss control experiment. Furthermore, the low NO_x mixing ratios in our experiments minimized N_2O_4 and N_2O_3 formation. At NO and NO_2 concentrations of 50 nmol mol^{-1} the steady state concentrations of N_2O_4 and N_2O_3 were calculated to be 0.014 and 0.001 pmol mol^{-1}, respectively (Atkinson et al., 2004). Therefore, we suggest our measured $\alpha(NO_2\text{-}NO)$ value (1.0289±0.0019) may better reflect the room temperature (298 K) NO-NO_2 EIE in the ambient environment.

Table 5.1 Experimental conditions, concentrations of NO, NO_2 and O_3 at steady state, and measured $\delta(NO_2)$ values.

Experiment	Number	NO conc. (nmol mol^{-1})	NO_2 conc. (nmol mol^{-1})	O_3 conc. (nmol mol^{-1})	$\delta(NO_2)$ (‰)	$f(NO_2)$
Determining $\delta(NO_x)$	1	0.0	17.8	13.4	-59.5	1.00
	2	0.0	61.3	0.5	-58.9	1.00
	3	0.0	18.9	10.7	-58.0	1.00
Dark experiments	1	16.0	36.8	0.0	-51.8	0.70
	2	33.6	28.8	0.0	-43.9	0.46
	3	6.7	12.6	0.0	-49.6	0.65
	4	16.2	16.9	0.0	-45.1	0.51
	5	20.4	24.2	0.0	-46.8	0.54
Irradiation experiments	1	7.1	6.4	2.8	-47.5	0.47
	2	4.5	5.3	4.5	-48.7	0.54
	3	3.3	4.4	4.2	-49.8	0.57
	4	2.5	8.5	10.7	-54.6	0.77
	5	5.2	18.1	11.0	-54.0	0.78

Unfortunately, the chamber temperature could not be controlled so we were not able to investigate the temperature dependence of the EIE. Hence, we speculate that the $\alpha(NO_2\text{-}NO)$ follows a similar temperature dependence pattern calculated in Walters et al. (2016). Walters et al. (2016) suggested that, the $\alpha(NO_2\text{-}NO)$ value would be 0.0047 higher at 273 K and 0.002 lower at 310 K, relative to room temperature (298 K). Using this pattern and our experimentally determined

data, we suggest the $\alpha(NO_2\text{-}NO)$ values at 273 K, 298 K and 310 K are 1.0336±0.0019, 1.0289±0.0019 and 1.0269±0.0019, respectively. This 0.0067 variation at least partially contribute to the daily and seasonal variations of $\delta^{15}N$ values of NO_2 and nitrate in some areas (e.g., polar regions with strong seasonal temperature variation). Thus, future investigations should be conducted to verify the EIE temperature dependence.

5.3.2 Kinetic isotopic fractionation of Leighton Cycle

The photochemical reactions of NO_x will compete with the isotope exchange fractionations between NO and NO_2. The NO-NO_2 photochemical cycle in the chamber was controlled by the Leighton cycle: NO_2 photolysis and the NO + O_3 reaction. This is because there were no VOCs in the chamber so no RO_2 was produced, which excludes the NO + RO_2 reaction. Likewise, the low water vapor content (RH<10%) and the minor flux of photons < 310 nm results in minimal OH production and hence little HO_2 formation and subsequently trivial amount of NO_2 would be formed by NO + HO_2. Applying these limiting assumptions, the EIE between NO and NO_2 (R1-R2) were only competing with the KIE (R3-R4) and the PHIFE in R5-R6:

$^{14}NO_2 \rightarrow {}^{14}NO + O$ R3, rate constant=$j(NO_2)$

$^{15}NO_2 \rightarrow {}^{15}NO + O$ R4, rate constant=$j(NO_2)$ α_1

$^{14}NO + O_3 \rightarrow {}^{14}NO_2 + O_2$ R5, rate constant=k_5

$^{15}NO + O_3 \rightarrow {}^{15}NO_2 + O_2$ R6, rate constant=k_5 α_2

In which $j(NO_2)$ is the NO_2 photolysis rate (1.4×10^{-3} s^{-1} in these experiments), k_5 is the rate constant for the NO+O_3 reaction (1.73×10^{-14} cm^3 s^{-1}, Atkinson et al., 2004), and $\alpha_{1,2}$ are isotopic fractionation factors for the two reactions. Previous studies (Freyer et al., 1993; Walters et al., 2016) have attempted to assess the competition between EIE (R1-R2), KIE and PHIFE (R3-R6), but none of them quantified the relative importance of the two processes, nor were α_1 or α_2 values experimentally determined. Here we provide the mathematical solution of EIE, KIE and PHIFE to illustrate how R1-R6 affect the isotopic fractionations between NO and NO_2.

First, the NO_2 lifetime with respect to isotopic exchange with NO ($\tau_{exchange}$) and photolysis (τ_{photo}) was determined:

$$\tau_{exchange} = \frac{1}{k_1\,[NO]} \quad \text{Eq. (4)}$$

$$\tau_{photo} = \frac{1}{j(NO_2)} \quad \text{Eq. (5)}$$

We then define an A factor:

$$A = \begin{cases} \frac{\tau_{exchange}}{\tau_{photo}} & \text{when } j(NO_2) \neq 0 \\ 0 & \text{when } j(NO_2) = 0 \end{cases} \quad \text{Eq. (6)}$$

Using R1-R6 and Eq. (1)-(6), we solved steady-state $\delta(NO_2)$ and $\delta(NO)$ values (see calculations in Appendix A.3). Our calculations show that the $\delta(NO_2)$-$\delta(NO)$ and $\delta(NO_2)$-$\delta(NO_x)$ values at steady state can be expressed as functions of α_1, α_2, $\alpha(NO_2\text{-}NO)$ and A:

$$\delta(NO_2) - \delta(NO) = \frac{(\alpha_2-\alpha_1)\,A+(\alpha(NO_2-NO)-1)}{\alpha_2 A+\alpha(NO_2-NO)}\left(1+\delta(NO_2)\right) \approx \frac{(\alpha_2-\alpha_1)\,A+(\alpha(NO_2-NO)-1)}{A+1}\left(1+\delta(NO_2)\right) \quad \text{Eq. (7)}$$

$$\delta(NO_2) - \delta(NO_x) = \frac{(\alpha_2-\alpha_1)\,A+(\alpha(NO_2-NO)-1)}{\alpha_2 A+\alpha(NO_2-NO)}\,(1+\delta(NO_2))(1-f(NO_2)) \approx \frac{(\alpha_2-\alpha_1)\,A+(\alpha(NO_2-NO)-1)}{A+1}\left(1+\delta(NO_2)\right)(1-f(NO_2)) \quad \text{Eq. (8)}$$

Equation (7) shows the isotopic fractionation between NO and NO_2 ($\delta(NO_2)$-$\delta(NO)$) is mainly determined by A, the EIE factor ($\alpha(NO_2\text{-}NO)$-1) and the (α_2-α_1) factor assuming (1+$\delta(NO_2)$) is close to 1. This (α_2-α_1) represents a combination of KIE and PHIFE, suggesting they act together as one factor; therefore, we name the (α_2-α_1) factor Leighton Cycle Isotopic Effect, i.e., LCIE. Using measured $\delta(NO_2)$, $\delta(NO_x)$ values, A values (Table 1), and the previously determined $\alpha(NO_2\text{-}NO)$ value, We plot $\frac{\delta(NO_2)-\delta(NO_x)}{(1+\delta(NO_2))(1-f(NO_2))}$ (equals to $\frac{\delta(NO_2)-\delta(NO)}{(1+\delta(NO_2))}$) against A value and use Equations (7) and (8) to estimate the (α_2-α_1) value (Figure 5.1C). The plot shows that the best fit for the LCIE factor is (-10±5) ‰ (Rooted Mean Square Error, RMSE, was lowest when α_2-α_1 =-10‰). The uncertainties in the LCIE factor are relatively higher than that of the EIE factor, mainly because of the accumulated analytical uncertainties at low NO_x and O_3 concentrations, and low A values (0.10-0.28) due to the relatively low $j(NO_2)$ value (1.4×10^{-3} s^{-1}) under the chamber irradiation conditions.

This LCIE factor determined in our experiments is in good agreement with theoretical calculations. Walters and Michalski (2016) previously used an *ab initio* approach to determine an

α_2 value of 0.9933 at room temperature, 0.9943 at 237 K and 0.9929 at 310 K. The total variation of α_2 values from 273 K to 310 K is only 1.4 ‰, significantly smaller than our experimental uncertainty (±5 ‰). The α_1 value was calculated using a ZPE shift model (Miller & Yung, 2000) to calculate the isotopic fractionation of NO_2 by photolysis. Briefly, this model assumes both isotopologues have the same quantum yield function and the PHIFE was only caused by the differences in the $^{15}NO_2$ and $^{14}NO_2$ absorption cross-section as a function of wavelength, thus α_1 values do not vary by temperature. The $^{15}NO_2$ absorption cross-section was calculated by shifting the $^{14}NO_2$ absorption cross-section by the $^{15}NO_2$ zero-point energy (Michalski et al., 2004). When the ZPE shift model was used with the irradiation spectrum of the chamber lights, the resulting α_1 value was 1.0023. Therefore, the theoretically predicted α_2-α_1 value should be -0.0090, i.e., (-9.0±0.7) ‰ when temperature ranges from 273 K to 310 K. This result shows excellent agreement with our experimentally determined room temperature α_2-α_1 value of (-10±5) ‰.

This model was then used to evaluate the variations of α_1 value to different lighting conditions. The TUV model (TUV5.3.2, Madronich & Flocke, 1999) was used to calculate the solar wavelength spectrum at three different conditions: early morning/late afternoon (solar zenith angle=85 degree), mid-morning/afternoon (solar zenith angle=45 degree), noon (solar zenith angle=0 degree). These spectrums were used in the ZPE shift model to calculate the α_1 values, which are 1.0025, 1.0028, and 1.0029 at solar zenith angles of 85, 45 and 0 degree, respectively. These values, along with the predicted α_1 value in the chamber, showed a total span of 0.6‰ (1.0026±0.0003), which is again significantly smaller than our measured uncertainty. Therefore, we suggest that our experimentally determined LCIE factor ((-10±5) ‰) can be used in most tropospheric solar irradiation spectrums.

The equations can also be applied in tropospheric environments to calculate the combined isotopic fractionations of EIE and LCIE for NO and NO_2. First, the NO_2 sink reactions (mainly NO_2+OH in the daytime) are at least 2-3 orders of magnitude slower than the Leighton cycle and the NO-NO_2 isotope exchange reactions (Walters et al., 2016), therefore their effects on the $\delta(NO_2)$ should be minor. Second, although the conversion of NO into NO_2 in the ambient environment is also controlled by NO + RO_2 and HO_2 in addition to NO+O_3 (e.g., King et al., 2001), Eq. (7) still showed good agreement with field observations in previous studies. Freyer et al. (1993) determined the annual average daytime $\delta(NO_2)$-$\delta(NO)$ at Julich, Germany along with average daytime NO concentration (9 nmol mol^{-1}, similar to our experimental conditions) to be

(+18.03±0.98) ‰. Using Eq. (7), assuming the daytime average $j(NO_2)$ value throughout the year was (5.0±1.0)×10^{-3}, and a calculated A value from measured NO_x concentration ranged from 0.22-

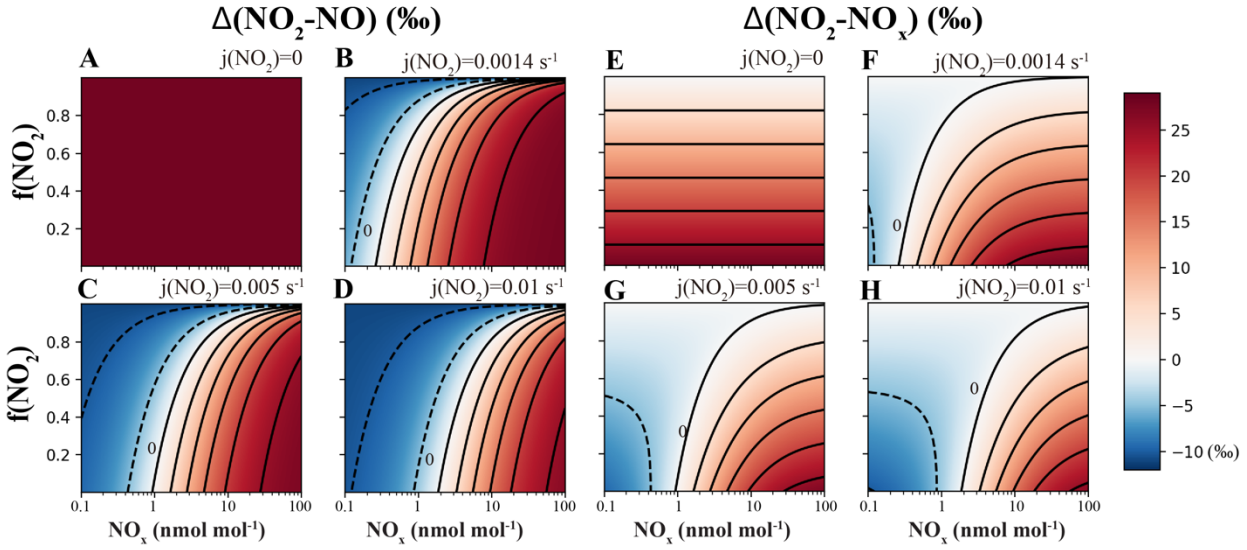

Figure 5.2 Calculating isotopic fractionation values between NO-NO_2 (Δ(NO_2-NO), **A-D**) and NO_x-NO_2 (Δ(NO_2-NO_x), **E-H**) at various $j(NO_2)$, NO_x level and $f(NO_2)$ using Eq. (7) and (8). Each panel represents a fixed $j(NO_2)$ value (showing on the upper right side of each panel), and the fractionation values are shown by color. Lines are contours with the same fractionation values, at an interval of 5‰, the contour line representing 0‰ was marked on each panel except for A and E.

0.33, the average NO-NO_2 fractionation factor was calculated to be (+19.8±1.4) ‰ (Figure 5.1C), in excellent agreement with the measurements in the present study. This agreement suggests the NO+RO_2/HO_2 reactions might have similar fractionation factors as NO+O_3. Therefore, we suggest Eq. (7) and (8) can be used to estimate the isotopic fractionations between NO and NO_2 in the troposphere.

5.3.3 Calculating nitrogen isotopic fractionations between NO and NO_2

First, Eq. (7) was used to calculate the Δ(NO_2-NO) = δ(NO_2)-δ(NO) at a wide range of NO_x concentrations, $f(NO_2)$ and $j(NO_2)$ values (Figure 5.2A-D), assuming (1+δ(NO_2)) ≈1. $j(NO_2)$ values of 0 s^{-1} (Figure 5.2A), 1.4×10^{-3} s^{-1} (Figure 5.2B), 5×10^{-3} s^{-1} (Figure 5.2C) and 1×10^{-2} s^{-1} (Figure 5.2D) were selected to represent nighttime, dawn (as well as the laboratory conditions of our experiments), daytime average and noon, respectively. Each panel represented a fixed $j(NO_2)$ value, and the Δ(NO_2-NO) values were calculated as a function of the A value, which was derived

from NO_x concentration and $f(NO_2)$. The A values have a large span, from 0 to 500, depending on the $j(NO_2)$ value and the NO concentration. When A=0 ($j(NO_2)$=0) and $f(NO_2)$<1 (meaning NO-NO_2 coexist and $[O_3]$=0), Eq. (7) and (8) become Eq. (2) and (3), showing the EIE was the sole factor, the $\Delta(NO_2\text{-}NO)$ values were solely controlled by EIE which has a constant value of +28.9 ‰ at 298K (Figure 5.2A). When $j(NO_2)$>0, the calculated $\Delta(NO_2\text{-}NO)$ values showed a wide range from -10.0 ‰ (controlled by LCIE factor: $\alpha_2\text{-}\alpha_1$=-10 ‰) to +28.9 ‰ (controlled by EIE factor: $\alpha(NO_2\text{-}NO)$-1 = +28.9 ‰). Figure 5.2B-D display the transition from a LCIE-dominated regime to an EIE-dominated regime. The LCIE-dominated regime is characterized by low $[NO_x]$ (<50 pmol mol^{-1}), representing remote ocean areas and polar regions (Beine et al., 2002; Custard et al., 2015). At this range the A value can be greater than 200, thus Eq. (7) can be simplified as: $\Delta(NO_2\text{-}NO) = \alpha_2\text{-}\alpha_1$, suggesting the LCIE almost exclusively controls the NO-NO_2 isotopic fractionation. The $\Delta(NO_2\text{-}NO)$ values of these regions are predicted to be <0 ‰ during most time of the day and < -5 ‰ at noon. On the other hand, the EIE-dominated regime was characterized by high $[NO_x]$ (>20 nmol mol^{-1}) and low $f(NO_2)$ (< 0.6), representative of regions with intensive NO emissions, e.g., near roadside or stack plumes (Clapp & Jenkin, 2001; Kimbrough et al., 2017). In this case, the $\tau_{exchange}$ are relatively short (10-50 s) compared to the τ_{photo} (approximately 100 s at noon and 1000 s at dawn), therefore the A values are small (0.01-0.5). The EIE factor in this regime thus is much more important than the LCIE factor, resulting in high $\Delta(NO_2\text{-}NO)$ values (>20 ‰). Between the two regimes, both EIE and LCIE are competitive and therefore it is necessary to use Eq. (7) to quantify the $\Delta(NO_2\text{-}NO)$ values.

Figure 5.2 also implies that changes in the $j(NO_2)$ value can cause the diurnal variations in $\Delta(NO_2\text{-}NO)$ values. Changing $j(NO_2)$ would affect the value of A and consequently the NO-NO_2 isotopic fractionations in two ways: 1) changes in $j(NO_2)$ value would change the photolysis intensity, therefore the τ_{photo} value; 2) in addition, changes in $j(NO_2)$ value would also alter the steady state NO concentration, therefore changing the $\tau_{exchange}$ (Figure 5.2C). The combined effect of these two factors on the A value varies along with the atmospheric conditions, and thus needs to be carefully calculated using NO_x concentration data and atmospheric chemistry models.

We then calculated the differences of $\delta^{15}N$ values between NO_2 and total NO_x, e.g. $\Delta(NO_2\text{-}NO_x) = \delta(NO_2)\text{-}\delta(NO_x)$ in Figure 5.2E-H. Since $\Delta(NO_2\text{-}NO_x)$ are connected through the observed $\delta^{15}N$ of NO_2 (or nitrate) to the $\delta^{15}N$ of NO_x sources, this term might be useful in field studies (e.g.,

Chang et al., 2018; Zong et al., 2017). The calculated $\Delta(NO_2\text{-}NO_x)$ values (Figure 5.2E-H) also showed a LCIE-dominated regime at low $[NO_x]$ and an EIE-dominated regime at high $[NO_x]$. The $\Delta(NO_2\text{-}NO_x)$ values were dampened by the $1\text{-}f(NO_2)$ factor comparing to $\Delta(NO_2\text{-}NO)$, as shown in Eq. (3) and (8): $\Delta(NO_2\text{-}NO_x) = \Delta(NO_2\text{-}NO)\ (1\text{-}f(NO_2))$. At high $f(NO_2)$ values (>0.8), the differences between $\delta(NO_2)$ and $\delta(NO_x)$ were less than 5 ‰, thus the measured $\delta(NO_2)$ values were similar to $\delta(NO_x)$, although the isotopic fractionation between NO and NO_2 could be noteworthy. Some ambient environments with significant NO emissions or high NO_2 photolysis rates usually have $f(NO_2)$ values between 0.4-0.8 (Mazzeo et al., 2005; Vicars et al., 2013). In this scenario, the $\Delta(NO_2\text{-}NO_x)$ values in Figure 5.2F-H showed wide ranges of -4.8 ‰ to +15.6 ‰, -6.0 ‰ to +15.0 ‰, and -6.3 ‰ to +14.2 ‰ at $j(NO_2)=1.4\times10^{-3}$ s^{-1}, 5×10^{-3} s^{-1}, 1×10^{-2} s^{-1}, respectively. These significant differences again highlighted the importance of both LCIE and EIE (Eq. (7) and (8)) in calculating the $\Delta(NO_2\text{-}NO_x)$. In the following discussion, we assume 1) the α_1 value remain constant (see discussion above), 2) the $NO+RO_2/HO_2$ reactions have the same fractionation factors (α_2) as $NO+O_3$, and 3) both EIE and LCIE do not display significant temperature dependence, then use Equations (7) and (8) and this laboratory determined LCIE factor (-10 ‰) to calculate the nitrogen isotopic fractionation between NO and NO_2 at various tropospheric atmospheric conditions.

5.4 Implications

The daily variations of $\Delta(NO_2\text{-}NO_x)$ values at two roadside NO_x monitoring sites were predicted to demonstrate the effects of NO_x concentrations to the $NO\text{-}NO_2$ isotopic fractionations. Hourly NO and NO_2 concentrations were acquired from a roadside site at Anaheim, CA (https://www.arb.ca.gov) and an urban site at Evansville, IN (http://idem.tx.sutron.com) on July 25, 2018. The hourly $j(NO_2)$ values output from the TUV model (Madronich & Flocke, 1999) at these locations was used to calculate the daily variations of $\Delta(NO_2\text{-}NO_x)$ values (Figure 5.3A, B) by applying Eq. (8) and assuming $(1+\delta(NO_2)) \approx 1$. Hourly NO_x concentrations were 12-51 nmol mol^{-1} at Anaheim and 9-38 nmol mol^{-1} at Evansville and the $f(NO_2)$ values at both sites did not show significant daily variations (0.45±0.07 at Anaheim and 0.65±0.08 at Evansville), likely because the NO_x concentrations were controlled by the high NO emissions from the road (Gao, 2007). The calculated $\Delta(NO_2\text{-}NO_x)$ values using Eq. (8) showed significant diurnal variations.

During the nighttime, the isotopic fractionations were solely controlled by the EIE, the predicted $\Delta(NO_2\text{-}NO_x)$ values were (+14.5±2.0) ‰ and (+8.7±2.1) ‰ at Anaheim and Evansville, respectively. During the daytime, the existence of LCIE lowered the predicted $\Delta(NO_2\text{-}NO_x)$ values to (+9.8±1.7) ‰ at Anaheim and (+3.1±1.5) ‰ at Evansville while the $f(NO_2)$ values at both sites remained similar. The lowest $\Delta(NO_2\text{-}NO_x)$ values for both sites (+7.0 ‰ and +1.7 ‰) occurred

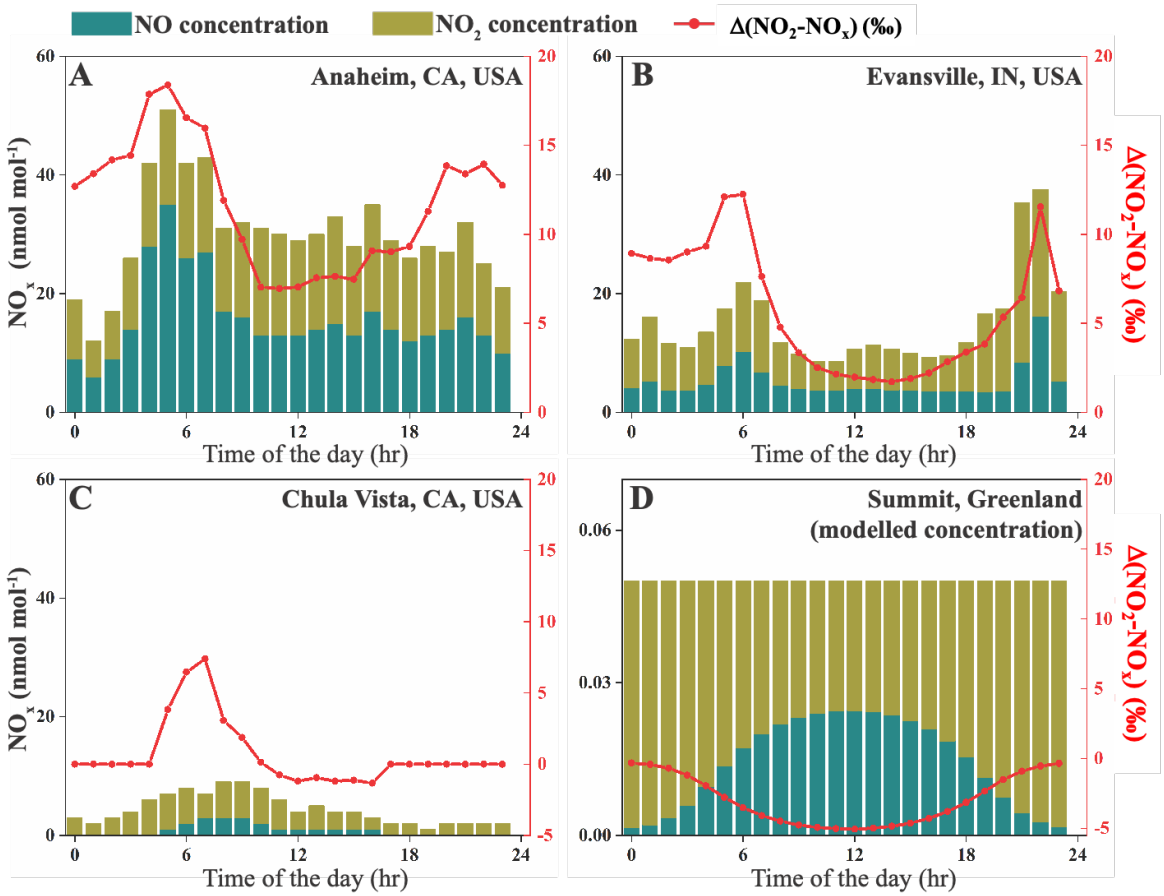

Figure 5.3 NO_x concentrations and calculated $\Delta(NO_2\text{-}NO_x)$ values at four sites. Stacked bars show the NO and NO_2 concentrations extracted from monitoring sites (A-C) or calculated using 0-D box model (D); the red lines are $\Delta(NO_2\text{-}NO_x)$ values at each site. Note that the NO_x concentration (left-y) axis on panel D is different from the rest.

around noon when the NO_x photolysis was the most intense. In contrast, if one neglects the LCIE factor in the daytime, the $\Delta(NO_2\text{-}NO_x)$ values would be (+12.9±1.5) ‰ and (+10.0±1.6) ‰ respectively, an overestimation of 3.1 ‰ and 6.9 ‰. These discrepancies suggested that the LCIE played an important role in the NO-NO_2 isotopic fractionations and neglecting it could bias the NO_x source apportionment using $\delta^{15}N$ of NO_2 or nitrate.

The role of LCIE was more important in less polluted sites. The $\Delta(NO_2\text{-}NO_x)$ values calculated for a suburban site near San Diego, CA, USA, again using the hourly NO_x concentrations (https://www.arb.ca.gov, Figure 5.3C) and $j(NO_2)$ values calculated from the TUV model. NO_x concentrations at this site varied from 1 to 9 nmol mol^{-1} and assuming $(1+\delta(NO_2)) \approx 1$. During the nighttime, NO_x was in the form of NO_2 ($f(NO_2) = 1$) because O_3 concentrations were higher than NO_x, thus the $\delta(NO_2)$ values should be identical to $\delta(NO_x)$ ($\Delta(NO_2\text{-}NO_x) = 0$). In the daytime a certain amount of NO was produced by direct NO emission and NO_2 photolysis but the $f(NO_2)$ was still high (0.73±0.08). Our calculation suggested the daytime $\Delta(NO_2\text{-}NO_x)$ values should be only (+1.3±3.2) ‰ with a lowest value of -1.3 ‰. These $\Delta(NO_2\text{-}NO_x)$ values were similar to the observed and modeled summer daytime $\delta(NO_2)$ values in West Lafayette, IN (Walters et al., 2018), which suggest the average daytime $\Delta(NO_2\text{-}NO_x)$ values at $NO_x = (3.9\pm1.2)$ nmol mol^{-1} should range from +0.1 ‰ to +2.4 ‰. In this regime, we suggest the $\Delta(NO_2\text{-}NO_x)$ values were generally small due to the significant contribution of LCIE and high $f(NO_2)$.

The LCIE should be the dominant factor controlling the NO-NO_2 isotopic fractionation at remote regions, resulting in a completely different diurnal pattern of $\Delta(NO_2\text{-}NO_x)$ compared with the urban-suburban area. Direct hourly measurements of NO_x at remote sites are rare, thus we used total NO_x concentration of 50 pmol mol^{-1}, daily O_3 concentration of 20 nmol mol^{-1} at Summit, Greenland (Dibb et al., 2002; Hastings et al., 2004; Honrath et al., 1999; Yang et al., 2002), and assumed $(1+\delta(NO_2)) \approx 1$ and the conversion of NO to NO_2 was completely controlled by O_3 to calculate the NO/NO_2 ratios. Here the isotopes of NO_x were almost exclusively controlled by the LCIE due to the high A values (>110). The $\Delta(NO_2\text{-}NO_x)$ values displayed a clear diurnal pattern (Figure 5.3D) with highest value of -0.3 ‰ in the "nighttime" (solar zenith angle >85 degree) and lowest value of -5.0 ‰ in the mid-day. This suggest that the isotopic fractionations between NO and NO_2 were almost completely controlled by LCIE at remote regions, when NO_x concentrations were <0.1 nmol mol^{-1}. However, since the isotopic fractionation factors of nitrate-formation reactions (NO_2+OH, NO_3+HC, N_2O_5+H_2O) are still unknown, more studies are needed to fully explain the daily and seasonal variations of $\delta(NO_3^-)$ at remote regions.

Nevertheless, our results have a few limitations. First, currently there are very few field observations that can be used to evaluate our model, therefore, future field observations that measure the $\delta^{15}N$ values of ambient NO and NO_2 should be carried out to test our model. Second,

more work, including theoretical and experimental studies, is needed to investigate the isotope fractionation factors occurring during the conversion from NO_x to NO_y and nitrate: in the NO_y cycle, EIE (isotopic exchange between NO_2, NO_3 and N_2O_5), KIE (formation of NO_3, N_2O_5 and nitrate) and PHIFE (photolysis of NO_3, N_2O_5, HONO and sometimes nitrate) may also exist and be relevant for the $\delta^{15}N$ of HNO_3 and HONO. In particular, the N isotope fractionation occurring during the $NO_2 + OH \rightarrow HNO_3$ reaction needs investigation. Such studies could help us modeling the isotopic fractionation between NO_x emission and nitrate, and eventually enable us to analyze the $\delta^{15}N$ value of NO_x emission by measuring the $\delta^{15}N$ values of nitrate aerosols and nitrate in wet depositions. Third, our discussion only focuses on the reactive nitrogen chemistry in the troposphere, however, the nitrogen chemistry in the stratosphere is drastically different from the tropospheric chemistry, thus future studies are also needed to investigate the isotopic fractionations in the stratospheric nitrogen chemistry. Last, the temperature dependence of both EIE and LCIE needs to be carefully investigated, because of the wide range of temperature in both troposphere and stratosphere. Changes in temperature could alter the isotopic fractionation factors of both EIE and LCIE, as well as contribute to the seasonality of isotopic fractionations between NO_x and NO_y molecules.

5.5 Conclusions

The effect of NO_x photochemistry on the nitrogen isotopic fractionations between NO and NO_2 was investigated. We first measured the isotopic fractionations between NO and NO_2 and provided mathematical solutions to assess the impact of NO_x level and NO_2 photolysis rate ($j(NO_2)$) to the relative importance of EIE and LCIE. The EIE and LCIE isotope fractionation factors, at room temperature, were determined to be 1.0289±0.0019 and 0.990±0.005, respectively. These calculations and measurements can be used to determine the steady state $\Delta(NO_2\text{-}NO)$ and $\Delta(NO_2\text{-}NO_x)$ values at room temperature. Subsequently we applied our equations to polluted, clean and remote sites to model the daily variations of $\Delta(NO_2\text{-}NO_x)$ values. We found that the $\Delta(NO_2\text{-}NO_x)$ values could vary from over +20 ‰ to less than -5 ‰ depending on the environment: in general, the role of LCIE becoming more important at low NO_x concentrations, which tend to decrease the $\Delta(NO_2\text{-}NO_x)$ values. Our work provided a mathematical approach to quantify the nitrogen isotopic

fractionations between NO and NO_2 that can be applied to many tropospheric environments, which could help interpret the measured $\delta^{15}N$ values of NO_2 and nitrate in field observation studies.

5.6 References

Atkinson, R., Baulch, D. L., Cox, R. A., Crowley, J. N., Hampson, R. F., Hynes, R. G., Jenkin, M. E., Rossi, M. J., and Troe, J. (2004). Evaluated kinetic and photochemical data for atmospheric chemistry: Volume I-gas phase reactions of O_x, HO_x, NO_x and SO_x. Atmospheric chemistry and physics, 4(6), 1461-1738. https://doi.org/10.5194/acp-4-1461-2004, 2004.

Barney, W. S., & Finlayson-Pitts, B. J. (2000). Enhancement of N_2O_4 on porous glass at room temperature: A key intermediate in the heterogeneous hydrolysis of NO_2? The Journal of Physical Chemistry A, 104(2), 171–175. https://doi.org/10.1021/jp993169b

Begun, G. M., & Fletcher, W. H. (1960). Partition function ratios for molecules containing nitrogen isotopes. The Journal of Chemical Physics, 33(4), 1083–1085. https://doi.org/10.1063/1.1731338

Begun, G. M., & Melton, C. E. (1956). Nitrogen isotopic fractionation between NO and NO_2 and mass discrimination in mass analysis of NO_2. The Journal of Chemical Physics, 25(6), 1292–1293. https://doi.org/10.1063/1.1743215

Beine, H. J., Honrath, R. E., Dominé, F., Simpson, W. R., & Fuentes, J. D. (2002). NO_x during background and ozone depletion periods at Alert: Fluxes above the snow surface. Journal of Geophysical Research: Atmospheres, 107(D21), ACH-7. https://doi.org/10.1029/2002JD002082

Bigeleisen, J., & Mayer, M. G. (1947). Calculation of equilibrium constants for isotopic exchange reactions. The Journal of Chemical Physics, 15(5), 261-267. https://doi.org/10.1063/1.1746492

Bigeleisen, J., & Wolfsberg, M. (1957). Theoretical and experimental aspects of isotope effects in chemical kinetics. Advances in Chemical Physics, 15–76. https://doi.org/10.1002/9780470143476.ch2

Casciotti, K. L., & McIlvin, M. R. (2007). Isotopic analyses of nitrate and nitrite from reference mixtures and application to Eastern Tropical North Pacific waters. Marine Chemistry, 107(2), 184–201. https://doi.org/10.1016/j.marchem.2007.06.021

Chang, Y., Zhang, Y., Tian, C., Zhang, S., Ma, X., Cao, F., et al. (2018). Nitrogen isotope fractionation during gas-to-particle conversion of NO_x to NO_3^- in the atmosphere–implications for isotope-based NO_x source apportionment. Atmospheric Chemistry and Physics, 18(16), 11647–11661. https://doi.org/10.5194/acp-18-11647-2018, 2018.

Clapp, L. J., & Jenkin, M. E. (2001). Analysis of the relationship between ambient levels of O_3, NO_2 and NO as a function of NO_x in the UK. Atmospheric Environment, 35(36), 6391–6405. https://doi.org/10.1016/S1352-2310(01)00378-8

Custard, K. D., Thompson, C. R., Pratt, K. A., Shepson, P. B., Liao, J., Huey, L. G., Orlando, J. J., Weinheimer, A. J., Apel, E., Hall, S. R., Flocke, F., Mauldin, L., Hornbrook, R. S., Pöhler, D., General, S., Zielcke, J., Simpson, W. R., Platt, U., Fried, A., Weibring, P., Sive, B. C., Ullmann, K., Cantrell, C., Knapp, D. J., and Montzka, D. D.: The NOx dependence of bromine chemistry in the Arctic atmospheric boundary layer, Atmos. Chem. Phys., 15, 10799–10809, https://doi.org/10.5194/acp-15-10799-2015, 2015.

Dibb, J. E., Arsenault, M., Peterson, M. C., & Honrath, R. E. (2002). Fast nitrogen oxide photochemistry in Summit, Greenland snow. Atmospheric Environment, 36(15–16), 2501–2511. https://doi.org/10.1016/S1352-2310(02)00130-9

Do Remus, R. H., Mehrotra, Y., Lanford, W. A., & Burman, C. (1983). Reaction of water with glass: influence of a transformed surface layer. Journal of Materials Science, 18(2), 612–622. https://doi.org/10.1007/BF00560651

Elliott, E. M., Kendall, C., Boyer, E. W., Burns, D. A., Lear, G. G., Golden, H. E., Harlin, K., Bytnerowicz, A., Butler, T. J., and Glatz, R. (2009). Dual nitrate isotopes in dry deposition: Utility for partitioning NO_x source contributions to landscape nitrogen deposition. Journal of Geophysical Research: Biogeosciences, 114(G4), G04020. https://doi.org/10.1029/2008JG000889

Felix, J. D., & Elliott, E. M. (2014). Isotopic composition of passively collected nitrogen dioxide emissions: Vehicle, soil and livestock source signatures. Atmospheric Environment, 92, 359–366. https://doi.org/10.1016/j.atmosenv.2014.04.005

Felix, J. D., Elliott, E. M., & Shaw, S. L. (2012). Nitrogen isotopic composition of coal-fired power plant NO_x: influence of emission controls and implications for global emission inventories. Environmental Science & Technology, 46(6), 3528–3535. https://doi.org/10.1021/es203355v

Frey, M. M., Savarino, J., Morin, S., Erbland, J., & Martins, J. M. F. (2009). Photolysis imprint in the nitrate stable isotope signal in snow and atmosphere of East Antarctica and implications for reactive nitrogen cycling. Atmos. Chem. Phys, 9, 8681-8696. https://doi.org/10.5194/acp-9-8681-2009, 2009.

Freyer, H. D. (1991). Seasonal variation of $^{15}N/^{14}N$ ratios in atmospheric nitrate species. Tellus B, 43(1), 30–44. https://doi.org/10.1034/j.1600-0889.1991.00003.x

Freyer, H. D., Kley, D., Volz-Thomas, A., & Kobel, K. (1993). On the interaction of isotopic exchange processes with photochemical reactions in atmospheric oxides of nitrogen. Journal of Geophysical Research: Atmospheres, 98(D8), 14791–14796. https://doi.org/10.1029/93JD00874

Gao, H. O. (2007). Day of week effects on diurnal ozone/NO_x cycles and transportation emissions in Southern California. Transportation Research Part D: Transport and Environment, 12(4), 292–305. https://doi.org/10.1016/j.trd.2007.03.004

Gobel, A. R., Altieri, K. E., Peters, A. J., Hastings, M. G., & Sigman, D. M. (2013). Insights into anthropogenic nitrogen deposition to the North Atlantic investigated using the isotopic composition of aerosol and rainwater nitrate. Geophysical Research Letters, 40(22), 5977–5982. https://doi.org/10.1002/2013GL058167

Hastings, M G, Jarvis, J. C., & Steig, E. J. (2009). Anthropogenic impacts on nitrogen isotopes of ice-core nitrate. Science, 324(5932), 1288. DOI: 10.1126/science.1170510

Hastings, M G, Steig, E. J., & Sigman, D. M. (2004). Seasonal variations in N and O isotopes of nitrate in snow at Summit, Greenland: Implications for the study of nitrate in snow and ice cores. Journal of Geophysical Research: Atmospheres, 109(D20). https://doi.org/10.1029/2004JD004991

Honrath, R. E., Peterson, M. C., Guo, S., Dibb, J. E., Shepson, P. B., & Campbell, B. (1999). Evidence of NO_x production within or upon ice particles in the Greenland snowpack. Geophysical Research Letters, 26(6), 695–698. https://doi.org/10.1029/1999GL900077

Jarvis, J. C., Steig, E. J., Hastings, M. G., & Kunasek, S. A. (2008). Influence of local photochemistry on isotopes of nitrate in Greenland snow. Geophysical Research Letters, 35(21). https://doi.org/10.1029/2008GL035551

Kendall, C., Elliott, E. M., & Wankel, S. D. (2007). Tracing anthropogenic inputs of nitrogen to ecosystems. Stable Isotopes in Ecology and Environmental Science, 2, 375–449. https://doi.org/10.1002/9780470691854.ch12

Kimbrough, S., Owen, R. C., Snyder, M., & Richmond-Bryant, J. (2017). NO to NO_2 conversion rate analysis and implications for dispersion model chemistry methods using Las Vegas, Nevada near-road field measurements. Atmospheric Environment, 165, 23–34. https://doi.org/10.1016/j.atmosenv.2017.06.027

King, M. D., Canosa-Mas, C. E. and Wayne R. P. (2001). Gas-phase reactions between RO_2 and NO, HO_2 or CH_3O_2: correlations between rate constants and the SOMO energy of the peroxy (RO_2) radical. Atmospheric Environment 35.12 (2001): 2081-2088. https://doi.org/10.1016/S1352-2310(00)00501-X

Knote, C., Tuccella, P., Curci, G., Emmons, L., Orlando, J. J. Madronich, S., Baró, R., Jiménez-Guerrero, P., Luecken, D., Hogrefe, C., Forkel, R., Werhahn, J., Hirtl, M., Pérez, J. L., San José, R., Giordano, L., Brunner, D., Yahya, K., Zhang, Y., Influence of the choice of gas-phase mechanism on predictions of key gaseous pollutants during the AQMEII phase-2 intercomparison. Atmospheric Environment 115 (2015): 553-568. https://doi.org/10.1016/j.atmosenv.2014.11.066.

Li, J. (2019). Quantifying the nitrogen equilibrium and photochemistry-induced kinetic isotopic effects between NO and NO_2. Retrieved from osf.io/jw8hu

Madronich, S., & Flocke, S. (1999). The role of solar radiation in atmospheric chemistry. In Environmental photochemistry (pp. 1–26). The Handbook of Environmental Chemistry (Reactions and Processes), vol 2 / 2L. Springer, Berlin, Heidelberg. https://doi.org/10.1007/978-3-540-69044-3_1

Mazzeo, N. A., Venegas, L. E., & Choren, H. (2005). Analysis of NO, NO_2, O_3 and NO_x concentrations measured at a green area of Buenos Aires City during wintertime. Atmospheric Environment, 39(17), 3055–3068. https://doi.org/10.1016/j.atmosenv.2005.01.029

McIlvin, M. R., & Altabet, M. A. (2005). Chemical conversion of nitrate and nitrite to nitrous oxide for nitrogen and oxygen isotopic analysis in freshwater and seawater. Analytical Chemistry, 77(17), 5589–5595. https://doi.org/10.1021/ac050528s

Michalski, G., Jost, R., Sugny, D., Joyeux, M., & Thiemens, M. (2004). Dissociation energies of six NO_2 isotopologues by laser induced fluorescence spectroscopy and zero-point energy of some triatomic molecules. The Journal of Chemical Physics, 121(15), 7153–7161. https://doi.org/10.1063/1.1792233

Michalski, G., Bockheim, J. G., Kendall, C., & Thiemens, M. (2005). Isotopic composition of Antarctic Dry Valley nitrate: Implications for NO_y sources and cycling in Antarctica. Geophysical Research Letters, 32(13). https://doi.org/10.1029/2004GL022121

Miller, C. E., & Yung, Y. L. (2000). Photo-induced isotopic fractionation. Journal of Geophysical Research: Atmospheres, 105(D23), 29039–29051. https://doi.org/10.1029/2000JD900388

Monse, E. U., Spindel, W., & Stern, M. J. (1969). Analysis of isotope-effect calculations illustrated with exchange equilibria among oxynitrogen compounds. Rutgers-The State Univ., Newark, NJ. DOI: 10.1021/ba-1969-0089.ch009

Morin, S., Savarino, J., Frey, M. M., Domine, F., Jacobi, H.-W., Kaleschke, L., & Martins, J. M. F. (2009). Comprehensive isotopic composition of atmospheric nitrate in the Atlantic Ocean boundary layer from 65°S to 79°N. J. Geophys. Res, 114. https://doi.org/10.1029/2008JD010696

Park, Y.-M., Park, K.-S., Kim, H., Yu, S.-M., Noh, S., Kim, M.-S., Kim, J.-Y., Ahn, J.-Y., Lee, M.-D., Seok, K.-S., Kin, Y.-H., (2018). Characterizing isotopic compositions of TC-C, NO_3^--N, and NH_4^+-N in PM2.5 in South Korea: Impact of China's winter heating. https://doi.org/10.1016/j.envpol.2017.10.072

Saliba, N. A., Yang, H., & Finlayson-Pitts, B. J. (2001). Reaction of gaseous nitric oxide with nitric acid on silica surfaces in the presence of water at room temperature. The Journal of Physical Chemistry A, 105(45), 10339–10346. https://doi.org/10.1021/jp012330r

Savarino, J., Morin, S., Erbland, J., Grannec, F., Patey, M. D., Vicars, W., Alexander, B., Achterberg, E. P., (2013). Isotopic composition of atmospheric nitrate in a tropical marine boundary layer. Proceedings of the National Academy of Sciences, 110(44), 17668–17673. https://doi.org/10.1073/pnas.1216639110

Sharma, H. D., Jervis, R. E., & Wong, K. Y. (1970). Isotopic exchange reactions in nitrogen oxides. The Journal of Physical Chemistry, 74(4), 923–933. https://doi.org/10.1021/j100699a044

Takei, T., Yamazaki, A., Watanabe, T., & Chikazawa, M. (1997). Water adsorption properties on porous silica glass surface modified by trimethylsilyl groups. Journal of Colloid and Interface Science, 188(2), 409–414. https://doi.org/10.1006/jcis.1997.4777

Urey, H. C. (1947). The thermodynamic properties of isotopic substances. Journal of the Chemical Society (Resumed), 562-581. https://doi.org/10.1039/JR9470000562

Vicars, W. C., Morin, S., Savarino, J., Wagner, N. L., Erbland, J., Vince, E., Martins, J. M. F., Lerner, B. M., Quinn, P. K., Coffman, D. J., Williams, E. J., Brown, S. S., (2013). Spatial and diurnal variability in reactive nitrogen oxide chemistry as reflected in the isotopic composition of atmospheric nitrate: Results from the CalNex 2010 field study. Journal of Geophysical Research: Atmospheres, 118(18), 10–567. https://doi.org/10.1002/jgrd.50680

Walters, W. W., & Michalski, G. (2015). Theoretical calculation of nitrogen isotope equilibrium exchange fractionation factors for various NO_y molecules. Geochimica et Cosmochimica Acta, 164, 284–297. https://doi.org/10.1016/j.gca.2015.05.029

Walters, W. W., Goodwin, S. R., & Michalski, G. (2015). Nitrogen stable isotope composition ($\delta^{15}N$) of vehicle-emitted NO_x. Environmental Science & Technology, 49(4), 2278–2285. https://doi.org/10.1021/es505580v

Walters, W. W., & Michalski, G. (2016). Ab initio study of nitrogen and position-specific oxygen kinetic isotope effects in the $NO+O_3$ reaction. The Journal of chemical physics, 145(22), 224311. https://doi.org/10.1063/1.4968562

Walters, W. W., Simonini, D. S., & Michalski, G. (2016). Nitrogen isotope exchange between NO and NO_2 and its implications for $\delta^{15}N$ variations in tropospheric NO_x and atmospheric nitrate. Geophysical Research Letters, 43(1), 440–448. https://doi.org/10.1002/2015GL066438

Walters, W. W., Fang, H., & Michalski, G. (2018). Summertime diurnal variations in the isotopic composition of atmospheric nitrogen dioxide at a small midwestern United States city. Atmospheric Environment, 179, 1–11. https://doi.org/10.1016/j.atmosenv.2018.01.047

Williams, E. L., & Grosjean, D. (1990). Removal of atmospheric oxidants with annular denuders. Environmental Science & Technology, 24(6), 811–814. https://doi.org/10.1021/es00076a002

Yang, J., Honrath, R. E., Peterson, M. C., Dibb, J. E., Sumner, A. L., Shepson, P. B., Frey, M., Jacobi, H.-W., Swanson, A., Blake, N., (2002). Impacts of snowpack emissions on deduced levels of OH and peroxy radicals at Summit, Greenland. Atmospheric Environment, 36(15–16), 2523–2534. https://doi.org/10.1016/S1352-2310(02)00128-0

Zhang, X., Ortega, J., Huang, Y., Shertz, S., Tyndall, G. S., & Orlando, J. J. (2018). A steady-state continuous flow chamber for the study of daytime and nighttime chemistry under atmospherically relevant NO levels. Atmospheric Measurement Techniques, 11(5), 2537–2551. https://doi.org/10.5194/amt-11-2537-2018

Zong, Z., Wang, X., Tian, C., Chen, Y., Fang, Y., Zhang, F., Li, C., Sun, J., Li, J., Zhang, G., (2017). First assessment of NO_x sources at a regional background site in North China using isotopic analysis linked with modeling. Environmental Science & Technology, 51(11), 5923–5931. https://doi.org/10.1021/acs.est.6b06316

CHAPTER 6. NITROGEN ISOTOPIC FRACTIONATIONS OF ATMOSPHERIC REACTIVE NITROGEN AT REMOTE BOUNDARY LAYER: IMPLICATIONS FOR NITROGEN ISOTOPES IN NITRATE AEROSOLS

This chapter is a reprint from a published article (Li, J., Davy, P., Harvey, M., Katzman, T., Mitchell, T., & Michalski, G. (2021). Nitrogen isotopes in nitrate aerosols collected in the remote marine boundary layer: Implications for nitrogen isotopic fractionations among atmospheric reactive nitrogen species. *Atmospheric Environment*, 245, 118028.).

Abstract

The nitrogen isotopic composition ($\delta^{15}N$) of atmospheric nitrate aerosols is determined by both the $\delta^{15}N$ of its precursor, NO_x emissions, and the isotopic fractionations during the atmospheric oxidation of NO_x. However, the latter has not been well-understood nor quantified by field observations. In addition, the seasonal variations of this isotopic fractionation have not been determined. To better understand this isotopic fractionation process, in this study, we analyzed the $\delta^{15}N$ of nitrate aerosols collected from 30 June 2015 to 6 August 2016 at Baring Head, New Zealand, where the sources of NO_x are well-studied. Our results showed that the $\delta^{15}N$ values in nitrate aerosols display a clear seasonal variation, with lower $\delta^{15}N$ values (-12‰ to ~-9‰) in the summer (January to March) and higher $\delta^{15}N$ values (0‰ to 3‰) in the winter (June-August), while the $\delta^{15}N$ values of NO_x sources exhibit a narrow range of variation from -10.7±1.4‰ to -9.8±1.4‰. We attribute this discrepancy to the significant and variable isotopic fractionations during the oxidation processes of NO_x. We then quantified the isotopic fractionation during 1) the equilibrium and kinetic isotopic fractionations between NO and NO_2; and 2) the oxidation of NO_2 to nitrate. Our calculations suggest that at Baring Head, the seasonal variations in the oxidation pathways of NO_2 are the main driver of the seasonal variations of nitrate $\delta^{15}N$ values. Furthermore, the overall isotopic fractionation factors of the oxidation process determined by two models (Kinetic fractionation model and Equilibrium fractionation model) are generally lower in the summer (from +6.3±1.7‰ to +9.5±5.2‰) and higher in the winter (from +15.8±1.9‰ to +17.0±2.4‰).

6.1 Introduction

Nitrate is one of the most important inorganic compounds in tropospheric aerosols and is predicted to become more prevalent in the coming decades based on assumptions about future NO_x ($NO+NO_2$) emission rates (Bauer et al., 2007, Fiore et al., 2015). Nitrate aerosols can affect regional air quality (Chang et al., 2018; Fan et al., 2020; Luo et al., 2019) and the global radiation balance (Khodayari et al., 2014; Paulot et al., 2017). Most atmospheric nitrate originates from the oxidation of NO_x (NO and NO_2), the major sources of which include fossil fuel combustion, biomass burning, soil emissions and lightning (Seinfeld and Pandis, 2016). Emissions of NO_x, a vital catalyst in tropospheric O_3 production, were estimated to be 124 Tg per year globally in 2015 (Crippa et al., 2019). The source appointment of NO_x, and therefore the production of nitrate aerosols, remains a difficult and sometimes controversial topic (Silvern et al., 2019; Zhao et al., 2017), because of its short lifetime (usually less than 24 hours, Browne and Cohen, 2012) and regionally different NO_x emission rates. These result in strong spatial and temporal heterogeneities in NO_x mixing ratios and nitrate aerosol concentrations. Additionally, the NO_x emissions are evolving rapidly in many regions worldwide due to economic development (e.g., fast urbanization), in particular the rapid rise of NO_x emissions in East Asia from 1995 to 2011 (Liu et al., 2017; Zhang et al., 2007). Changes in environmental regulations and advancements in NO_x emission control technologies introduce more uncertainties to the existing emission inventories, further complicating accurate NO_x source appointment (Srivastava et al., 2005). There is also uncertainty in the amount of NO_x emitted by soils via nitrification and denitrification. For example, a recent study by Almaraz et al. (2018) claimed that soil emissions accounted for 50 % of total NO_x emissions in the central valley of California, suggesting that previous agricultural NO_x emission factors have been underestimated by a factor of 6-8. Likewise, NO_x emissions derived from satellite observations over China displayed some discrepancies with local emission inventories, further suggesting significant uncertainties in either NO_x emission inventories (Liu et al., 2017) or transformation rates of NO_x into atmospheric nitrate. Therefore, it is important to improve our understanding in the sources of NO_x emission sources in various environments and its transformation into nitrate aerosols.

The nitrogen isotopic composition ($\delta^{15}N$) of nitrate has been proposed as a powerful tool in studying the sources of atmospheric NO_x. NO_x produced by different sources display distinctive $\delta^{15}N$ values (Walters et al., 2015a). For example, biogenic emitted NO_x shows low $\delta^{15}N$ values <

-26‰, (Felix and Elliott, 2014, 2013) NO_x emitted from vehicles displays higher and a wide range of $\delta^{15}N$ values ranging from -19‰ to +20‰ (Walters et al., 2015a, Fibiger and Hastings, 2016) depending on the type of fuel and the emission mitigation technology, and NO_x originated from coal-fired power plants shows higher $\delta^{15}N$ values ranging from +5‰ to +25‰ (Felix et al., 2012, Fibiger and Hastings, 2016). These unique NO_x $\delta^{15}N$ values are then imprinted into the nitrate aerosols during its atmospheric oxidation (Kendall et al., 2007), and many studies have attempted to use $\delta^{15}N$ values of nitrate aerosols to budget regional sources of NO_x (Chang et al., 2018; Felix et al., 2012; Felix and Elliott, 2014; Gobel et al., 2013; Hastings et al., 2004; Morin et al., 2009; Savarino et al., 2007, Liu et al., 2018, Zong et al., 2020).

There are, however, a number of uncertainties that could potentially bias the use of $\delta^{15}N$ as a NO_x source appointment proxy. In particular the assumption the NO_x $\delta^{15}N$ value is preserved during the oxidation of NO_x into atmospheric nitrate is questionable. This is because there are likely isotopic fractionations occurring during the oxidations of NO_x into nitrate or other higher N oxides (such as peroxyacyl nitrate) resulting in significant uncertainties. These uncertainties mainly originate from two factors: first, there are strong spatial and temporal variations in NO_x oxidation pathways such as the amount of nitrate formed via NO_2 + OH in the daytime versus that by NO_3/N_2O_5 reactions in the nighttime. Second, the isotopic fractionation factors of these reactions (and others) are still uncertain but exist in most, if not all, atmospheric nitrogen reactions. The fractionation processes include: 1) the kinetic isotope effect (KIE), which occurs during unidirectional reactions due to the differences in the rate constants between isotopes (Bigeleisen and Wolfsberg, 1957); 2) the equilibrium isotope effect (EIE), the isotopic exchange between co-existing molecules (Walters and Michalski, 2015); and 3) photochemistry-induced isotopic fractionation effect (PHIFE), i.e., the isotopic fractionation during molecular photolysis (Miller and Yung, 2000). Although previous studies have investigated the EIE between NO and NO_2, KIE during the NO_x photochemical cycle, and EIE between some NO_y molecules (Begun and Melton, 1956; Li et al., 2020; Walters et al., 2016; Walters and Michalski, 2015), many fractionation factors of the atmospheric nitrogen chemistry are still unknown. In addition, the importance of each isotopic fractionation process to the overall isotopic fractionation between NO_x emission and nitrate aerosols is still unclear, and the oxidation pathway of NO_x display strong temporal and spatial variations (Alexander et al., 2009), makes it even more difficult to quantify this isotopic fractionation. Therefore, if the $\delta^{15}N$ of atmospheric nitrate is to be used as a proxy for NO_x $\delta^{15}N$

(and NO_x source constraint), a better quantification of the isotopic fractionation between emitted NO_x and the product nitrate aerosols is urgently needed.

In this work, we analyzed the $\delta^{15}N$ of nitrate aerosols collected at Baring Head, New Zealand, a "clean atmosphere" research site. The observed seasonal variations in $\delta^{15}N$ values of aerosol nitrate were used to test two hypotheses. The first hypothesis is that seasonal $\delta^{15}N$ variations are due to changes in regional NO_x sources that generated the nitrate. The second hypothesis is that the variations are due to isotopic fractionation between NO and NO_2 that are a function of NO_x mixing ratios and the isotopic fractionation during the oxidation from NO_2 to nitrate.

6.2 Methods

Size-aggregated ambient aerosol nitrate samples were collected weekly at Baring Head, New Zealand from 30 June 2015 to 11 August 2016 (Figure 1). Baring Head is on the southern tip of New Zealand's North Island overlooking the Cook Strait. It is home to the Baring Head Clean Air Monitoring Station, which has been in operation for more than 40 years measuring greenhouse and other trace gases in air that is representative of the unpolluted mid-latitude Southern Hemisphere. The site, and its lighthouse, are located on an 85 m cliff approximately 200 m from the shoreline and ~15 km to the southeast of the capital city of Wellington, New Zealand. Previous studies have suggested that aerosols at Baring Head are partially derived from anthropogenic emissions from the city of Wellington (Li et al., 2018). The site continuously monitors CO_2 using Cavity laser spectroscopy (Model G2301, Picarro Inc, CA, USA). Measurements of CO and O_3 are also made at Baring

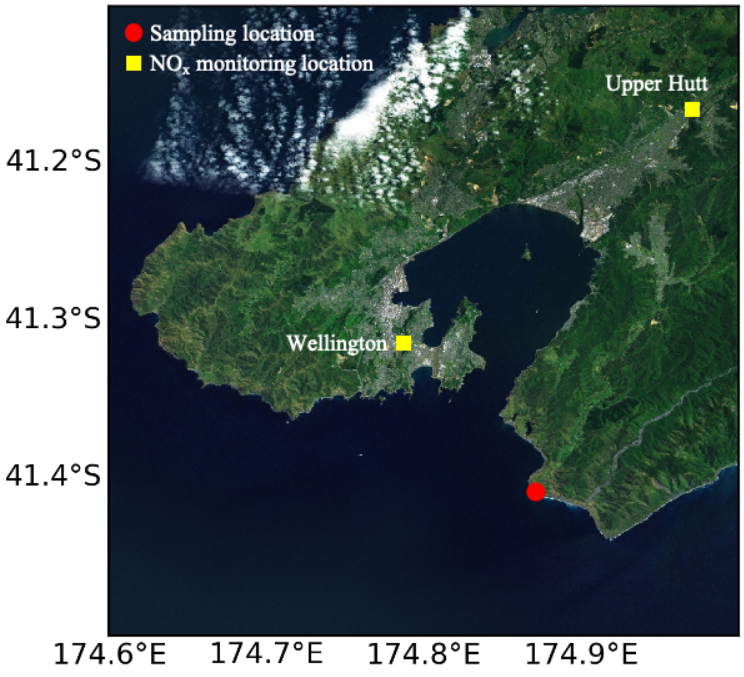

Figure 6.1 Map of the sampling location, nearby cities and the locations of NO_x monitoring sites.

Head. CO has been measured at a frequency of 60-100 times per year since 1998 using gas chromatography on discrete flask samples, and O_3 has been monitored hourly by a standard O_3 monitor (Thermo Electron Corporation Model 49i). There were no NO_x data collected at Baring Head, but Greater Wellington Regional Council measured hourly NO and NO_2 concentrations in two cities near our sampling site, Wellington (15 km to the north-west) and Upper Hutt (35 km to the north), during the sampling period (Figure 1).

Ambient aerosols were collected using a high-volume aerosol sampler (Lear Siegler Australasia, Australia) equipped with size segregating cascade impactor (TE-235, Tisch Environmental Inc., USA) that was set up on a 15-meter tower. The sampler flow rate was set to 1 m^3/min to separately collect coarse (1-16 μm) and fine (0.05-1 μm) aerosols. Cellulous filters were used to minimize sulfate contamination by SO_2 reacting on the substrate (Pszenny et al., 1993) and were replaced every 7 days. After collection, each filter was carefully sealed into Ziploc bags and shipped to Purdue University. Upon arrival, each filter was soaked into 100 mL of 18.2 MΩ cm deionized water and agitated for 30 min to completely dissolve all water-soluble inorganic ions. The solutions were then filtered by 0.2 μm filters to remove any microbes and kept refrigerated until the day of analysis. An aliquot of each sample was used to analyze the anion concentrations by an Ion Chromatography (DX-500, Dionex Corp., Sunnyvale, CA, USA) at Purdue Stable Isotope (PSI) Lab. The ion concentration analysis was previously reported by Li et al. (2018). Another aliquot of each sample was then mixed with 5% HNO_3 solutions then used to measure the cation concentration using an ICP-OES at Purdue Rare Isotope Measurement Lab (PRIME). The standard errors for both anion and cation analysis were ±5%.

The nitrate $\delta^{15}N$ values were analyzed using the bacteria method, which utilizes *Pseudomonas aureofaciens* to completely convert nitrate into N_2O (Casciotti et al., 2002). The denitrifying bacteria were first grown in solutions containing tryptic soy broth, KNO_3, NH_4Cl. After a week, the bacteria were concentrated and rinsed using a nitrate free rinse solution, which is identical to the growth solutions except the rinse solution does not contain KNO_3. The bacteria solutions were then purged with He for 2 hours to remove any N_2O blank in the solution. This solution was then split into 1 mL aliquots in 12 mL headspace vials, and the headspace was flushed with He to keep the solution anoxic. Then sample solutions containing ~500 nmol of nitrate were then injected into each vial to react overnight. Subsequently, 0.5 mL of 5% NaOH was injected into each vial to terminate the reaction and remove any CO_2 in the headspace. The N_2O produced

in the headspace was then cryogenically trapped and purified by gas chromatography (Plot Q column) before being directed into an Isotope Ratio Mass Spectrometer (Delta V) to analyze N and O isotopologues at 44, 45 and 46 atomic mass unit. The results were reported in delta notations:

$$\delta^{15}N\ (‰) = ((^{15}N/^{14}N)_{sample}/(^{15}N/^{14}N)_{reference}-1) *1000‰; \quad \text{Eq. 1}$$

in which the reference material for $\delta^{15}N$ is atmospheric N_2. The standard error was 0.5‰ for $\delta^{15}N$. The standards used during the isotopic analysis were three internal nitrate standards that were calibrated relative to international standards USGS32, USGS34 and USGS35 (Coplen et al., 2002; Michalski et al., 2002).

6.3 Results

There were strong seasonal variations in nitrate aerosol concentrations at Baring Head (Figure 2A). In terms of size fractions, nitrate is primarily in the coarse aerosols (1-16 μm diameter), ranging from 0.38 to 8.03 nmol/m^3 with an average value of 3.51 nmol/m^3. The fine aerosols (0.05-1 μm) had much lower nitrate concentrations of 0.14-0.97 nmol/m^3 with an average value of 0.44 nmol/m^3 (Figure 2A). The nitrate mass fraction in the coarse aerosols average at 0.87±0.05 for all the samples, showing that the majority of total nitrate is in the coarse aerosol mode. The concentrations of nitrate aerosols display significant seasonal variation with lower concentrations in the winter (June-August) and higher concentrations in the summer (January to March, Figure 2A). The average concentration of nitrate in coarse aerosols was 1.47 nmol/m^3 in the winter and 5.20 nmol/m^3 in the summer while the averages of nitrate in the fine aerosols were 0.26 nmol/m^3 in the winter and 0.57 nmol/m^3 in the summer.

NO_x concentrations at both city monitoring sites showed strong seasonal variations (Figure 2B, C). NO_x concentrations in both cities were higher in the winter and lower in the summer. At Wellington, the lowest monthly average NO concentration (5.6 ppb) was overserved in December, and highest monthly average NO concentration (11.2 ppb) was observed in June during the study period. Similarly, the lowest monthly average NO_2 concentration (4.0 ppb) was overserved in December, and highest monthly average NO_2 concentration (9.1 ppb) was observed in June. Upper Hutt had lower overall NO_x concentration relative to Wellington and displayed similar seasonal variations. The monthly average NO concentration was lowest in December (0.8 ppb) and highest

in June (4.9 ppb); while the monthly average NO_2 concentration was lowest in January (1.0 ppb) and highest in July (4.4 ppb). The *f*(NO) values, where *f*(NO) = [NO]/[NO_x], at both sites were lower in the winter (~0.30 at Upper Hutt and 0.4 at Wellington) compared to the summer (~0.6 at both cities).

The $\delta^{15}N$ values of nitrate in the coarse aerosols display significant seasonal variations over the sampling period (Figure 3A). Due to the low concentration of nitrate in the fine aerosols, their $\delta^{15}N$ values were not able to be analyzed. In the coarse particles, the $\delta^{15}N$ values (n=34) range from -12‰ to +6‰, averaging at -4‰, and show significant seasonal variations. In the winter, $\delta^{15}N$ values are higher, ranging from -5‰ to +6‰ with an average of 0‰, while in the summer the $\delta^{15}N$ values ranged from -12‰ to -4‰, averaging at -8‰.

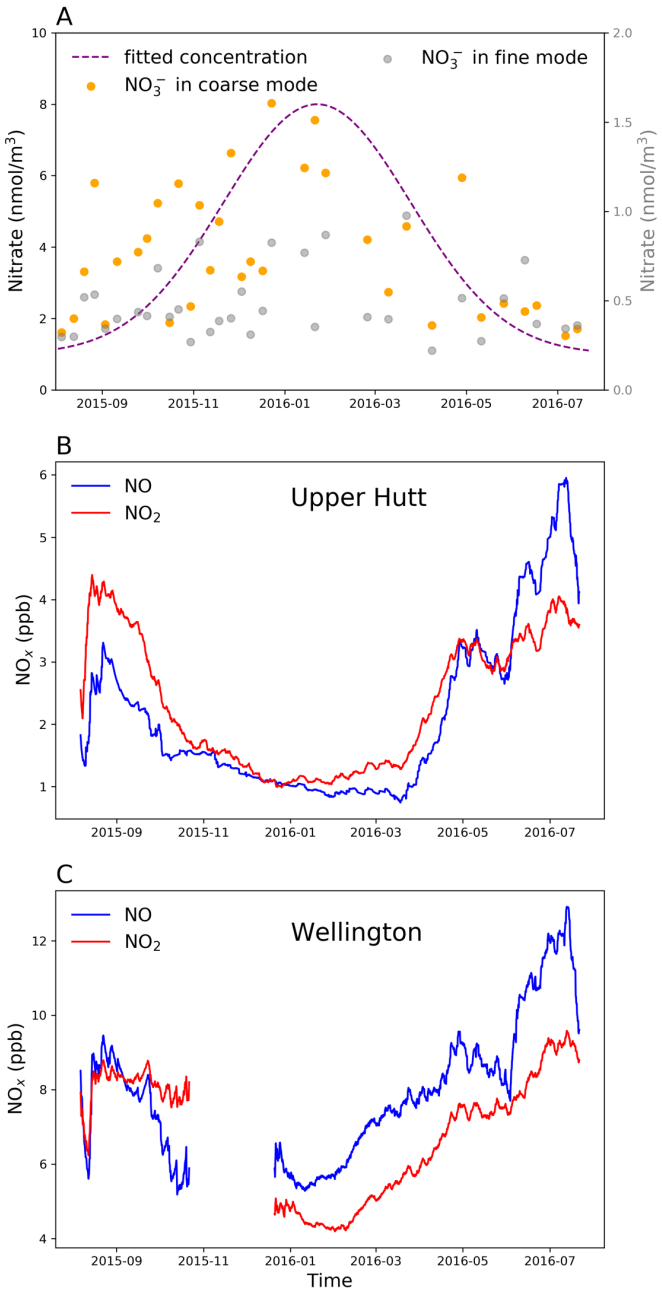

Figure 6.2 **A**. Nitrate concentrations in fine and coarse aerosols and fitted nitrate concentrations in coarse aerosols (see section 4.2); **B, C**: running averages of hourly measured NO and NO_2 concentrations at Upper Hutt and Wellington

6.4 Discussion

6.4.1 Origins of NO_x and nitrate

To interpret the observed nitrate aerosol $\delta^{15}N$ values we need to assess how NO_3^- is partitioned between gas and solid phase, since there are nitrogen isotope fractionations associated with phase equilibrium. As most nitrate was found in the coarse aerosols, we hypothesize that the nitrate aerosols are mainly composed of $HNO_{3(g)}$ entering particle phase and NO_y reacting on sea-salt aerosols. An average of

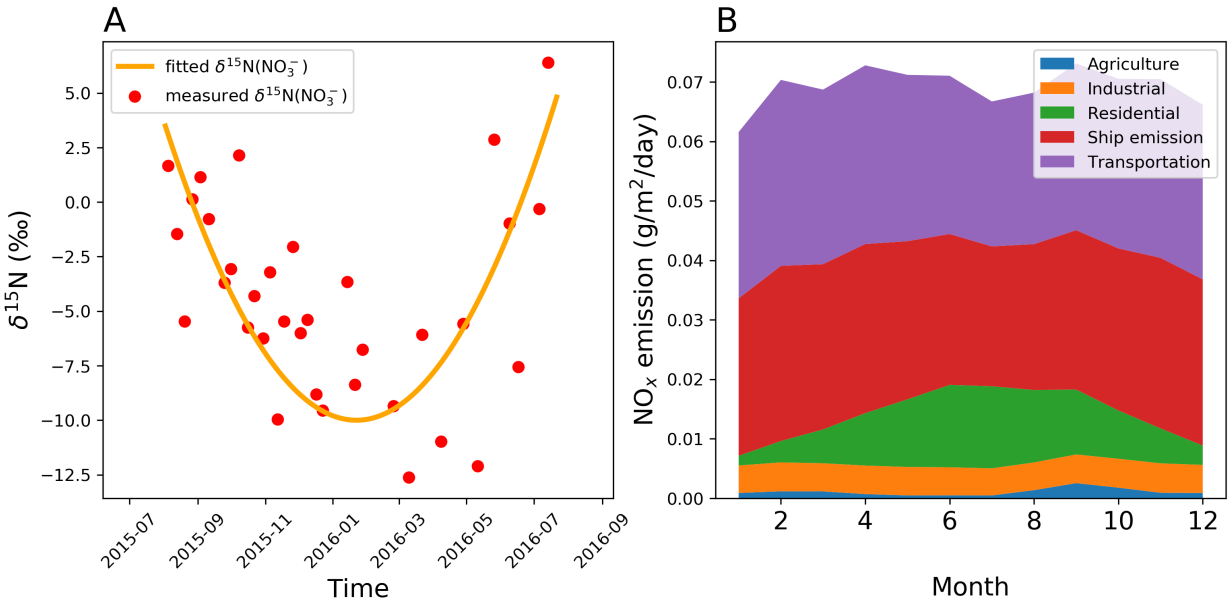

Figure 6.3 Observed $\delta^{15}N(NO_3^-)$ in coarse aerosol samples and fitted $\delta^{15}N$ values (see discussion). B. Monthly NO_x emission inventory of the Greater Wellington region (extracted from EDGAR database).

87% of the total nitrate accumulates in the coarse particle fraction, which is commonly observed in remote marine boundary layers (Baker et al., 2006; Itahashi et al., 2016). This accumulation of nitrate in the coarse particles in coastal areas is often attributed to the high alkalinity of sea salt aerosols. To estimate the mass fraction of sea salt to the total aerosol mass, we assume that all the Na^+ in the aerosols originated from sea salt, and Na^+ mass/aerosol mass ratio was 0.3066 (Millero et al., 2008). Based on observed Na^+ concentrations in the coarse aerosols and their mass, the average sea-salt aerosols mass is estimated to be 9.15 ug/m^3 in the coarse particles, accounting for 99% of the observed coarse aerosols mass. In contrast, the average sea-salt mass in the fine particles is only 0.51 ug/m^3, accounting for 23% of fine aerosol mass with the remainder is attributed to secondary aerosols, such as secondary sulfate derived from atmospheric SO_2 oxidation (Li et al., 2018) and secondary organic aerosols (SOA). Nitrate originating directly from the sea-salt aerosols is negligible in most areas since nitrate in the surface seawater is typically less than 1-2 µM. The concentration of sulfate is 4-5 orders of magnitude higher than nitrate (Rees et al., 1978; Sherlock et al., 2007), yet in the coarse aerosols the nitrate and sulfate concentrations were similar (Li et al., 2018). Therefore, most nitrate in our samples must have originated from atmospheric oxidation of NO_x. $HNO_{3(g)}$ produced by the NO_2+OH reaction, the main $HNO_{3(g)}$

formation pathway (Alexander et al., 2009), can enter the particle phase onto the alkaline, coarse sea-salt aerosols through the acidic displacement reaction:

$$HNO_{3(g)}+NaCl_{(p)} \rightarrow NaNO_{3(p)}+HCl_{(g)}$$

This acidic displacement reaction on sea-salt aerosols is fast, the uptake coefficient of $HNO_{3(g)}$ uptake onto sea-salt aerosols was previously determined to be ~0.2 (De Haan and Finlayson-Pitts, 1997). Using this uptake coefficient, we estimated the lifetime of gas phase HNO_3 (τ) using a pseudo-first order uptake model (Fuchs and Sutugin, 1971):

$$\tau=4/(\gamma*\nu*S_a) \qquad \text{Eq. 2}$$

where γ is the uptake coefficient of the reaction (0.2), ν is the mean molecular velocity of $HNO_{3(g)}$ (316 m/s at room temperature) and S_a is the average surface area of sea salt aerosols. Using the sea salt aerosol mass-surface area ratio of 140 $\mu g/cm^2$ (Andreas, 1998; Guelle et al., 2001), the observed average surface sea-salt concentration of 9.15 ug/m^3, and the average surface area of sea-salt aerosols of $6.54*10^{-6}$ m^2/m^3, leads to an estimated lifetime of gas phase HNO_3 of 2.7 hours. This short lifetime of $HNO_{3(g)}$ suggests most nitrate should exist in the particle phase, especially on the sea salt aerosols since this is a neutralizing reaction for HNO_3. Similarly, the heterogeneous formation of nitrate through N_2O_5 uptake also favors alkaline surfaces (Kane et al., 2001) and Eq. 2 also applies but with γ values that range from 0.005 to 0.03 depending on relative humidity (Evans and Jacob, 2005). This pathway directly removes NO_y to form particle nitrate and becomes increasingly important under cold and dark conditions (e.g., winter). This also suggests that nitrate found in the coarse particles is associated with sea salt aerosols. Therefore, it is reasonable to assume that the observed $\delta^{15}N$ values of nitrate in the coarse aerosols should represent the $\delta^{15}N$ values of total NO_3^- in the Baring Head region and that the possible N isotope effects associated with NO_3^- partitioning between gas and solid phase is negligible.

We tested the hypothesis that the observed seasonal variations of nitrate aerosols $\delta^{15}N$ values were due to seasonal shift in NO_x emission sources by conducting a simple isotope mass balance. The observed nitrate $\delta^{15}N$ values showed an overall seasonal variation of 18‰. If this variation was entirely due to shifts in NO_x emission sources, it would require a significant change in NO_x emissions between summer and winter. We calculated the monthly $\delta^{15}N$ value of each NO_x source in the study region using the Emission Database for Global Atmospheric Research

(EDGAR) NO_x emission inventory (Crippa et al., 2016), literature $\delta^{15}N$ values, and the isotope mass balance:

$$\delta^{15}N(NO_x) = \Sigma\ \delta^{15}N_i * f_i \quad \text{Eq. 3}$$

where $\delta^{15}N_i$ is the estimated $\delta^{15}N$ value of source i and f_i is the mole fraction contribution of NO_x source i to the total NO_x emissions. The mole fractions (f_i) were extracted from the categorized NO_x data from EDGAR gridded emission inventory (Crippa et al., 2016). The monthly average NO_x emission in a 1-degree * 1-degree grid encompassing both Wellington and Baring Head are shown in Figure 3B. The majority of NO_x emissions in this region are on-road vehicles and ocean-going ships (Wellington Harbor), with mole fractions of 0.41 and 0.39, respectively. Residential (0.12) industrial (0.07) and agriculture (0.01) NO_x made up the remainder of the NO_x emission inventory. This EDGAR based NO_x emission inventory data is similar to the emission inventory assembled by the local government (Ministry of the Environment, 2004) which also suggests the majority (96%) of the NO_x emission in the city of Wellington is from a combination of on-road vehicles and ship emissions. Additionally, the seasonal variations of NO_x emissions from all categories in EDGAR are relatively small except for the residential emission that spiked in winter months (25%) relative to summer (4%) due to residential heating. The total EDGAR NO_x emission flux was 40% higher in June ($5.8*10^{-5}$ kg/m^2/day) relative to January ($3.5*10^{-5}$ kg/m^2/day).

Table 6.1 $\delta^{15}N$ values of emission sources

Emission source	$\delta^{15}N$ values ($\pm1\sigma$)	References
Agriculture	-33.0‰ ±12.3‰	Miller et al., 2018
Industrial	+10.0‰ ± 2.0‰	Felix et al., 2012
Residential	-12.8‰ ± 2.4‰	Hastings et al., 2009
Ship emissions	-9.5‰ ± 2.5‰	Walters et al., 2015a, Beyn et al., 2015
On-road vehicles-gasoline	-3.9‰ ± 2.5‰	Walters et al., 2015a, 2015b,
On-road vehicles-diesel	-19.1‰ ± 1.8‰	Walters et al., 2015a, 2015b

The $\delta^{15}N$ values of NO_x from these main sources are obtained from recent published research (Table 1). The $\delta^{15}N$ value of NO_x originating from residential emissions, industrial

emissions, and agriculture emissions are estimated to be -12.8‰ ± 2.4‰, +10.0‰ ± 2.0‰ and -33.0 ± 12.3‰, respectively (Hastings et al., 2009, Felix et al., 2012, Miller et al., 2018). The $\delta^{15}N$ value of NO_x emitted from on-road vehicles varies significantly depending on fuel types, emission control technology, and commute times (Walters et al., 2015a, 2015b). The $\delta^{15}N$ value of NO_x emitted from gasoline powered cars were estimated to be -3.9‰ ± 2.5‰ (1σ) based on the average commute time of ~20 min in the Wellington region (Statistics New Zealand, 2014) and vehicle NO_x $\delta^{15}N$ changes with drive time (Walters et al., 2015a, 2015b), while the $\delta^{15}N$ value of NO_x emitted from diesel cars with selective catalytic reduction technology was estimated to be -19.1‰ ± 1.8‰ (1σ, Walters et al., 2015a). The contributions of gasoline and diesel cars to the total on-road NO_x emissions at Auckland, New Zealand were previously estimated to be 45% and 55%, respectively, due to the relatively higher NO_x emission factor of diesel vehicles comparing to gasoline vehicles (Sridhar et al., 2014). Assuming a similar distribution at Wellington, the overall $\delta^{15}N(NO_x)$ of on-road vehicle emissions is estimated to be -12.3‰ ± 1.5‰. The $\delta^{15}N$ value of NO_x from ship emission has not been directly measured yet, but previous study estimated that ship emitted NO_x is mainly originated from decomposition of atmospheric N_2 (Beyn et al., 2015), the $\delta^{15}N$ of which was estimated to be -9.5‰ ± 2.5‰ (1σ, Walters et al., 2015a).

The calculated $\delta^{15}N(NO_x)$ values do not show seasonal variations similar to the observed $\delta^{15}N(NO_3^-)$ (Figure 4B). Using the above NO_x mole fractions (*f* values), $\delta^{15}N(NO_x)$ values, and Eq. 3, the predicted monthly $\delta^{15}N(NO_x)$ values at Wellington only fluctuate by 0.9‰, ranging from -10.7‰ ± 1.4‰ to -9.8‰ ± 1.4‰ (Figure 4B), which is mainly due to the lack of any significant seasonal variation of the NO_x emission sources. The small $\delta^{15}N(NO_x)$ variations throughout the year is in contrast to the observed $\delta^{15}N$ values of nitrate aerosols which displayed a much stronger seasonal variation of 18‰ (from -12‰ to +6‰). Also, the calculated $\delta^{15}N(NO_x)$ values in the summer are similar to the observed values, but in the winter, the calculated $\delta^{15}N(NO_x)$ values are 7‰ lower than the observed values on average. We hypothesize that the differences between the calculated $\delta^{15}N(NO_x)$ values and the observed $\delta^{15}N(NO_3^-)$ is related to seasonal variations in isotope fractionations that occur during the oxidation of NO_x into nitrate. Such fractionation includes both the EIE between NO and NO_2, and the PHIFE and KIE occurring during oxidation of NO_2 to nitrate via multiple pathways, and the EIE between the NO_x and NO_y molecules. Next,

we first quantify the isotope fractionation between NO and NO_2 and then discuss the isotope fractionation during the oxidation from NO_2 to nitrate.

6.4.2 Quantifying the NO-NO_2 isotopic fractionation

We previously developed a model to quantify the isotope fractionation between NO and NO_2, a combined effect of two different processes (Li et al., 2020). The first process is the EIE between NO and NO_2 molecules, the equilibrium isotopic effect (hereafter refer as EIE), where no change in molecule abundance occurs. The second process is the Leighton cycle isotope effect (hereafter refer as LCIE, Li et al., 2020), the combined KIE and PHIFE occurring during daytime NO_x photochemical cycling. Theoretical and experimental studies (Begun and Melton, 1956; Walters et al., 2016, Li et al., 2020) have suggested that the EIE value should be 1.028±0.004 at room temperature, and the value has been widely applied in many studies (Chang et al., 2018; Fan et al., 2019; Song et al., 2019; Zong et al., 2017). The LCIE is usually overlooked because its effect is generally considered negligible at high NO_x concentrations. Li et al. (2020) shows that the fractionation factor of LCIE is 0.990±0.005, dramatically different from that of the EIE and that LCIE is important when $[NO_x]$<20 ppb, and even dominant when $[NO_x]$<1 ppb. Here, we use this model to quantify the NO-NO_2 isotopic fractionation at our sampling site.

The differences between the $\delta^{15}N$ values of NO_2 and NO_x at Baring Head were calculated using the equation in Li et al. (2020):

$$\delta^{15}N(NO_2) - \delta^{15}N(NO_x) \approx (+28.9‰ - 10‰*A)/(A+1)*f(NO) \qquad \text{Eq. 4}$$

The A factor is an index showing the relative importance of EIE and LCIE, which equals to 0 in the nighttime (when $j(NO_2)$ =0). During the daytime, A is calculated using $j(NO_2)$ value (in s^{-1}), NO concentration ([NO]) and the rate constant of NO-NO_2 isotopic exchange reaction (k_1=8.14*10^{-14} cm^3/s (Sharma et al., 1970)):

$$A = j(NO_2)/k_1*[NO] \qquad \text{Eq. 5}$$

The time series of $j(NO_2)$ values were calculated using the tropospheric radiation (TUV) model (Madronich and Flocke, 1999).

Since the NO_x concentrations at Baring Head were not directly measured, we first estimated the NO_x concentrations at Baring Head using the observed NO_x concentrations at Wellington, the city ~15 km away from our sampling site. The NO_x concentrations at Wellington show clear seasonal variations: wintertime NO_x concentrations are approximately 100% higher than those of summertime. This is likely resulted from a combination of higher NO_x emissions (~65% higher in winter than summer, see discussions above) and lower boundary layer heights in the winter. Since there are no significant NO_x emissions outside the city, the observed NO_x in the Wellington region should have mainly originated from local emissions and Baring Head should follow similar seasonal NO_x concentration trends. Thus, we assume the spatial distribution of NO_x near the city of Wellington follows a Gaussian distribution (Hanna et al., 1982). The distribution of NO_x concentrations ($[NO_x]=[NO]+[NO_2]$) can be expressed as:

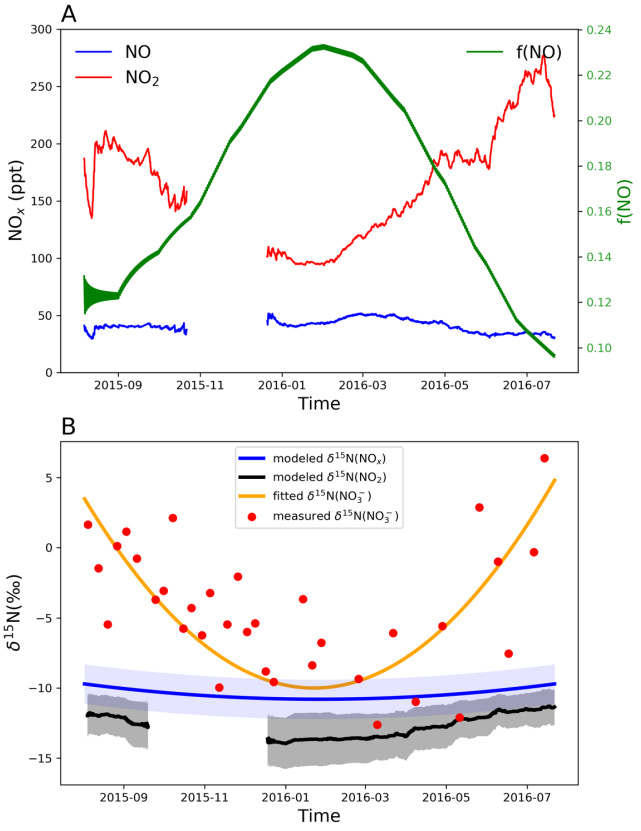

Figure 6.4 **A**. estimated NO_x concentrations and f(NO) values at Baring Head. **B**. Modeled $\delta^{15}N(NO_x)$, running average of modeled $\delta^{15}N(NO_2)$, comparing to observed and fitted $\delta^{15}N(NO_3^-)$. The shaded area around the black and blue lines represents the standard deviations.

$$[NO_x]= [NO_x]_0 * e^{-\frac{d^2}{2\sigma^2}} + [NO_x]_{BG} \quad \text{Eq. 6}$$

Where d is the distance from Wellington and σ is the standard deviation of this Gaussian distribution. Here we suggest the $[NO_x]_{BG}$ can be neglected as NO_x is short-lived and the background NO_x level in the open Southern Ocean is only a few ppt (Monk et al., 1998). While this approach may not accurately predict the temporal NO_x variation in a shorter time scale (hourly or daily) because the meteorological conditions can vary, it should be able to represent the average NO_x concentration at Baring Head over a longer time period (weekly to monthly). To determine

the value of $e^{-\frac{d^2}{2\sigma^2}}$ at Baring Head, we assume CO and NO_x follow similar Gaussian distribution pattern (i.e., same σ value) near the city of Wellington:

$$[CO]= [CO]_0 * e^{-\frac{d^2}{2\sigma^2}} + [CO]_{BG} \quad \text{Eq. 7}$$

Because the lifetime of CO in the atmosphere is long (~2 months through CO+OH oxidation assuming an average OH concentration of $1*10^{-6}$ cm^{-3}, Lawrence et al., 2001), we use the annual average concentrations of CO at the background, clean air monitoring site at Arrival Heights, Antarctica (NIWA database) as the $[CO]_{BG}$ value, then we use the CO concentrations at Wellington ($[CO]_W=[CO]_0+[CO]_{BG}$) and Baring Head ($([CO]_{BH}=[CO]_0 * e^{-\frac{d^2}{2\sigma^2}}+[CO]_{BG}$) to calculate the $e^{-\frac{d^2}{2\sigma^2}}$ value:

$$e^{-\frac{d^2}{2\sigma^2}}=([CO]_{BH}-[CO]_{AH})/([CO]_W-[CO]_{AH}) \quad \text{Eq. 8}$$

Using the previously measured annual average CO concentration in Wellington (220 ± 120 ug/m^3, Mitchell, 2015), Baring Head (46.2±7.8 ug/m^3, NIWA, 2016) and Arrival Heights (44.4±8.2 ug/m^3, NIWA, 2016), the $e^{-\frac{d^2}{2\sigma^2}}$ value at Baring Head is calculated to be 0.0140. As a result, the estimated NO_x mixing ratios at Baring Head range from ~120 ppt in the summer to ~270 ppt in the winter (Figure 4A), with an annual average of ~200 ppt. These estimated NO_x mixing ratios match well with those observed at Cape Grim (~200 ppt in the summer), another "background site" at a similar latitude and located in Tasmania, Australia (Carpenter, 2007). Using the estimated NO_x concentrations at Baring Head, the *f*(NO) values were calculated by assuming photochemical steady state between NO and NO_2 through the following reactions:

$NO_2 \rightarrow NO+O$	$rate=j(NO_2)[NO_2]$
$O+O_2+M \rightarrow O_3+M$	$rate=k_2[O][O_2][M]$
$NO+O_3 \rightarrow NO_2+O_2$	$rate=k_3[NO][O_3]$

Where $j(NO_2)$ is the photolysis rate of NO_2, and k_2 ($6.01*10^{-34}$ cm^6 $molecule^{-2}$ s), k_3 ($1.73*10^{-14}$ cm^3 $molecule^{-1}$ s) are the rate constants of the reactions (Atkinson et al., 2004). At Baring Head, the observed O_3 concentrations range from 20 ppb to 30 ppb, while the HO_2 and RO_2 have very low concentrations (~5 ppt, Carslaw et al., 1999; Sommariva et al., 2004). Therefore, the oxidation of NO to NO_2 at our study site is primarily driven by O_3. Our calculations show that at these

concentrations, the $NO+O_3$ reaction is ~10 times faster than the $NO+HO_2/RO_2$ reactions. Using the above reactions, hourly *f*(NO) values are calculated using the $j(NO_2)$ values estimated by the TUV model (Madronich and Flocke, 1999). The calculated averaged *f*(NO) values range from 0.09 in the winter to 0.24 in the summer (Figure 4A), again agreeing well with the observed *f*(NO) values at Cape Grim (average *f*(NO)=0.17).

The $\delta^{15}N$ values of NO_2 calculated using Eq. 5 are lower than the $\delta^{15}N(NO_x)$ values and displayed a narrow range of variation. Because of the low NO_x concentration, the isotopic fractionation between NO and NO_2 is mainly controlled by the LCIE factor at Baring Head, resulted in negative $\delta^{15}N(NO_2)$-$\delta^{15}N(NO)$ values (Figure 4B). Our calculation showed that the weekly running average (168-hour running average) of calculated $\delta^{15}N(NO_2)$ range from -13.9‰ in the summer to -11.4‰ in the winter (Figure 4B), with an annual average value of -12.8‰, similar to but slightly lower than the modeled $\delta^{15}N(NO_x)$ values. The $\delta^{15}N(NO_2)$ values are still significantly lower than the observed $\delta^{15}N(NO_3^-)$ values with much less seasonal variations. Therefore, we hypothesize that the isotopic fractionation during subsequent NO_2 oxidation into HNO_3 is probably more important in determining the isotopic fractionations between NO_x and NO_3^- at Baring Head.

6.4.3 The isotopic fractionation during NO_2 oxidation to nitrate

The differences between observed $\delta^{15}N(NO_3^-)$ and predicted $\delta^{15}N(NO_2)$ range from 3.7‰ (in summer) to 14.6‰ (in winter) during our study period (Figure 4B). This discrepancy suggests that the modeled $\delta^{15}N(NO_2)$ does not represent the $\delta^{15}N(NO_3^-)$ at Baring Head due to significant isotopic fractionation have occurred during the oxidation of NO_2 to nitrate. This isotopic fractionation (i.e., $\delta^{15}N(NO_3^-)$-$\delta^{15}N(NO_2)$ value) is determined by 1) reaction yield, i.e., the Nitrogen Oxidation Ratio ($NOR=[NO_3^-]/([NO_2]+[NO_3^-])$, and 2) the isotopic fractionation factor of the oxidation process. Therefore, in the following discussion the effect of both NOR and isotopic fractionation factors during NO_2 oxidation are modeled.

Two isotopic fractionation models are applied to estimate the isotopic fractionations between NO_2 and nitrate. The first model assumes the NO_x-nitrate isotopic fractionation is solely controlled by the EIE between NO_2 and nitrate molecules. This fractionation process is expressed as:

$$\delta^{15}N(NO_3^-) = \delta^{15}N(NO_2) + \varepsilon_{obs,E}*(1\text{-}NOR) \quad \text{Eq. 9}$$

where NOR is the NO_2 oxidation ratio and the $\varepsilon_{obs,E}$ is the observed enrichment factor in the EIE model. The second model assumes the isotopic fractionation was solely controlled by the KIE during the oxidation process, and the $\delta^{15}N(NO_3^-)$ can be calculated using the Rayleigh Distillation equation:

$$\delta^{15}N(NO_3^-) = \delta^{15}N(NO_2) - \varepsilon_{obs,K} * \ln(1\text{-}NOR) * (1\text{-}NOR)/NOR \quad \text{Eq. 10}$$

where $\varepsilon_{obs,K}$ is the enrichment factor of the oxidation process in the KIE model.

To directly compare the modeled hourly NO_2 concentrations to the observed weekly nitrate concentration data and apply them in the model, we used fitted lines to represent the nitrate concentration and $\delta^{15}N(NO_3^-)$ values. We applied a Gaussian distribution function to fit the nitrate concentration (Figure 5A). Similarly, we used a quadratic function to fit the weekly observed $\delta^{15}N(NO_3^-)$ values, which displayed a range from -10‰ in the summer to +3‰ in the winter. Using the fitted nitrate concentration values, we calculated the NOR values (Figure 5B). The NOR values show significant seasonal variations during the sampling period, which partially explains the variations of isotopic fractionation between NO_2 and nitrate. Using the modeled hourly NO_2 concentrations and the fitted nitrate concentrations, the annual average of NOR values is estimated to be 0.42±0.25 with a strong seasonality: the monthly average NOR value is highest (0.68) in January and lowest (0.20) in July. These calculated NOR values are lower than typical NOR values observed in the remote boundary layer. In the remote troposphere where NO_x mixing ratios are typically below 100 ppt, the NOR is usually >0.8 (Chatfield, 1994), indicating almost complete oxidation of NO_x into nitrate. In the meantime, our calculated NOR values were slightly higher than typical NOR values in polluted urban environments that usually range between 0.2-0.5 and sometimes can be lower than 0.1 in the winter (Chang et al., 2018; Liu et al., 2020; Luo et al., 2019; Sun et al., 2018). The variations of NOR values play an important role in controlling the isotopic fractionations between NO_2 and nitrate. In both models, increasing NOR tends to decrease the isotopic fractionation between nitrate and NO_2. The high NOR during summer is in line with the lower observed $\delta^{15}N(NO_3^-)$-$\delta^{15}N(NO_2)$ values, suggesting the changes in NOR partially contributed to the variations of isotopic fractionations.

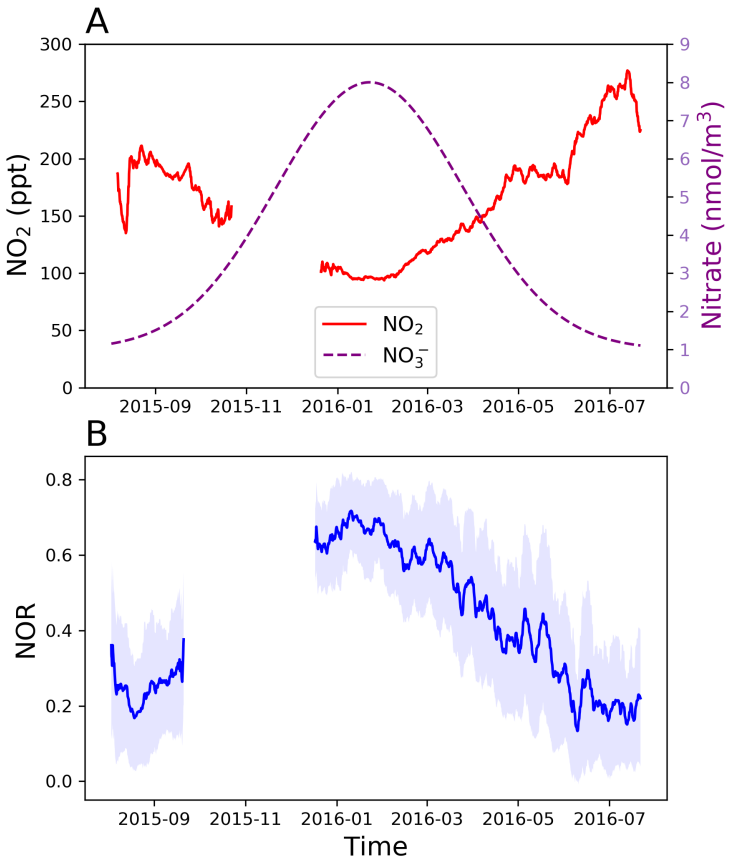

Figure 6.5 **A**. Modeled NO_2 (red line) and nitrate (purple line) concentrations, **B**. calculated NOR values presented in 168-hour running average, shaded area represents the 168-hour running standard deviation.

Using the modeled $\delta^{15}N(NO_2)$, fitted $\delta^{15}N(NO_3^-)$ and NOR values, the ε_{obs} values were calculated for both models. The calculated ε_{obs} values in both models (Figure 6) display clear seasonal variations. In the EIE model, the lowest $\varepsilon_{obs,E}$ is observed in January (+9.5±5.2 ‰) and the highest $\varepsilon_{obs,E}$ is observed in July (+17.0±2.4 ‰). The KIE model also gave similar results with the lowest $\varepsilon_{obs,K}$ (+6.3±3.1 ‰) in February and the highest $\varepsilon_{obs,K}$ in July (+15.8±1.9 ‰). This variation in enrichment factors is unlikely due to the changes in temperature, since the difference of average temperature at Baring Head between January and July is only ~8 °C, which is unlikely to shift the enrichment factor by over 10‰. Instead, the changes in $\varepsilon_{obs,E}$ are attributed to the seasonal variation in the nitrate formation pathways. The two most important nitrate formation pathways in coastal areas are daytime NO_2 oxidation by OH radicals and nighttime N_2O_5 hydrolysis reactions (Alexander et al., 2009; Dentener and Crutzen, 1993; Michalski et al., 2003). The OH oxidation is more important in the summer, while the nighttime N_2O_5 hydrolysis is more important in the winter.

This observed seasonal variation in nitrogen isotopic fractionation factors is in general agreement with previous studies (Freyer, 1991, Walters and Michalski, 2015, Zong et al., 2017) although the detailed fractionation processes are still highly uncertain. The isotopic fractionation during daytime nitrate formation through NO_2+OH is primarily controlled by the kinetic fractionation of the reaction, which has a fractionation factor (ε_{NO2+OH}) of -3‰ (Freyer, 1991); while the isotopic fractionation during nighttime nitrate formation is controlled by the equilibrium fractionation factor between NO_2 and N_2O_5 molecules (Chang et al., 2018; Walters and Michalski,

2015; Zong et al., 2017), which has a fractionation factor ($\varepsilon_{N2O5/NO2}$) of +25.7‰ at room temperature. Our calculated ε_{obs} values (+9.5‰-+17.0‰ in EIE model and +6.3-+15.8‰ in KIE model) are in between ε_{NO2+OH} and $\varepsilon_{N2O5/NO2}$ values, confirming our hypothesis that the variations of ε_{obs} values should be mainly attributed to the variations in the nitrate formation pathways. Assuming the ε_{obs} values represent a combination of both isotopic fractionation factors ($\varepsilon_{obs} = f_{NO2+OH}*\varepsilon_{NO2+OH} + f_{N2O5/NO2}*\varepsilon_{N2O5/NO2}$ in which f values represent the fractional contributions of each oxidation pathway and $f_{NO2+OH} + f_{N2O5/NO2} = 1$), then the lower summertime $\varepsilon_{obs,E}$ and $\varepsilon_{obs,K}$ values comparing to winter indicated an increased contribution of NO_2+OH to the formation of nitrate in the summer time, which is general agreement with GEOS-Chem simulation results (Alexander et al., 2009; Kamezaki et al., 2019). Nevertheless, there are uncertainties in 1) the role of equilibrium isotopic fractionations between NO_2, nitrate, and N_2O_5 with other NO_y molecules, and 2) the contribution of other nitrate pathways and their associated isotopic fractionations, such as NO_3+hydrocarbon and $ClONO_2$/$BrONO_2$ hydrolysis, which are suggested to account for 10-20% nitrate formation in remote marine boundary layer (Savarino et al., 2013). Further study is needed to better quantify the isotopic fractionation of the complex NO_x and NO_y chemistry.

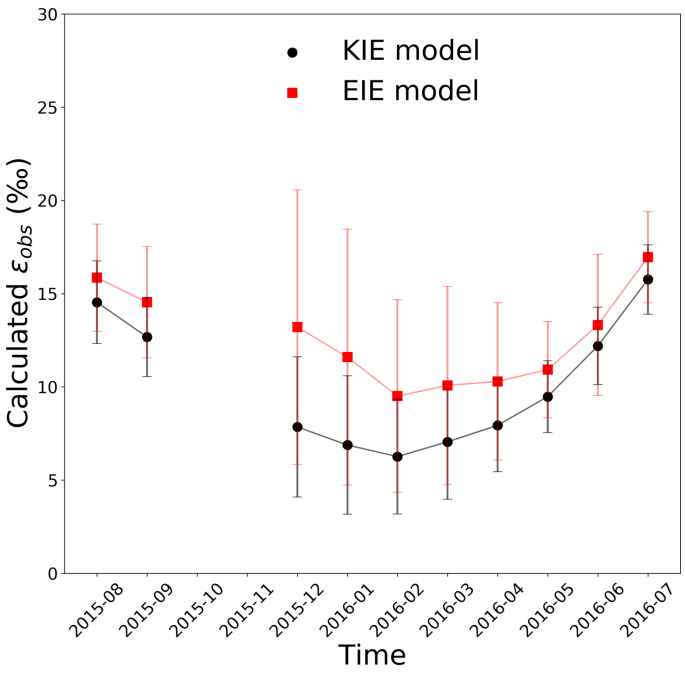

Figure 6.6 Calculated seasonal variations in isotopic fractionation factors (ε_{obs}) between NO_2 and nitrate using KIE (black circles) and EIE (red squares) models. Data is shown in monthly average and error bars represent the standard deviations.

6.5 Conclusions

This work assessed the differences between $\delta^{15}N$ values between the NO_x emissions (calculated) and those in nitrate aerosols collected at a background site at Baring Head, New

Zealand, in order to investigate the isotopic fractionations during the formation of nitrate aerosols. While the $\delta^{15}N(NO_x)$ is relatively constant throughout the year, the measured $\delta^{15}N(NO_3^-)$ is approximately 0-15‰ higher than $\delta^{15}N(NO_x)$ and displays significant seasonal variation. Our study indicates that the fractionation between NO and NO_2 is insignificant at our study site and the differences between $\delta^{15}N(NO_3^-)$ and $\delta^{15}N(NO_x)$ is largely caused by the isotopic fractionation during the oxidation from NO_2 to nitrate. This isotopic fractionation is less significant in the summer than winter, due to the higher nitrogen oxidation ratio and lower isotopic fractionation factor. Further investigation is needed to quantify the isotopic fractionation during the oxidation of NO_2 into HNO_3, including 1) assessing the isotopic fractionation factor of each oxidation pathway, in particular the NO_2 + OH reaction, 2) investigating the temperature dependence of the isotopic fractionation factors, and 3) understanding the relative importance of each fractionation factor to the overall isotopic fractionation between NO_2 and nitrate.

6.6 References

Alexander, B., Hastings, M.G., Allman, D.J., Dachs, J., Thornton, J.A., Kunasek, S.A., 2009. Quantifying atmospheric nitrate formation pathways based on a global model of the oxygen isotopic composition ($\Delta^{17}O$) of atmospheric nitrate. Atmos. Chem. Phys. 9, 5043–5056.

Almaraz, M., Bai, E., Wang, C., Trousdell, J., Conley, S., Faloona, I., Houlton, B.Z., 2018. Agriculture is a major source of NO_x pollution in California. Sci. Adv. 4, eaao3477.

Andreas, E.L., 1998. A new sea spray generation function for wind speeds up to 32 ms− 1. J. Phys. Oceanogr. 28, 2175–2184.

Atkinson, R., Baulch, D.L., Cox, R.A., Crowley, J.N., Hampson, R.F., Hynes, R.G., Jenkin, M.E., Rossi, M.J., Troe, J., 2004. Evaluated kinetic and photochemical data for atmospheric chemistry: Volume I-gas phase reactions of O_x, HO_x, NO_x and SO_x species. Atmos. Chem. Phys. 4, 1461–1738.

Baker, A.R., Jickells, T.D., Biswas, K.F., Weston, K., French, M., 2006. Nutrients in atmospheric aerosol particles along the Atlantic Meridional Transect. Deep Sea Res. Part II Top. Stud. Oceanogr. 53, 1706–1719.

Bauer, S.E., Koch, D., Unger, N., Metzger, S.M., Shindell, D.T., Streets, D.G., 2007. Nitrate aerosols today and in 2030: a global simulation including aerosols and tropospheric ozone. Atmos. Chem. Phys. 7, 5043–5059.

Begun, G.M., Melton, C.E., 1956. Nitrogen isotopic fractionation between NO and NO_2 and mass discrimination in mass analysis of NO_2. J. Chem. Phys. 25, 1292–1293.

Beyn, F., Matthias, V., Aulinger, A., & Dähnke, K. (2015). Do N-isotopes in atmospheric nitrate deposition reflect air pollution levels?. Atmos. Environ., 107, 281-288.

Bigeleisen, J., Wolfsberg, M., 1957. Theoretical and experimental aspects of isotope effects in chemical kinetics. Adv. Chem. Phys., Edited by Prigogine, I and Debye, P., Wiley, pp. 15–76.

Browne, E.C., Cohen, R.C., 2012. Effects of biogenic nitrate chemistry on the NO_x lifetime in remote continental regions. Atmos. Chem. Phys. 12, 11917–11932.

Carpenter, L.J. (2007): Southern Ocean Atmospheric Photochemistry Experiment 2 (SOAPEX-2) Project: In-situ atmospheric chemistry compound measurements at Cape Grim Baseline Air Pollution Station, Tasmania. NCAS British Atmospheric Data Centre, accessed July 2020. https://catalogue.ceda.ac.uk/uuid/9cc7306512fd9659ef19302ea6b1dc45

Carslaw, N., Creasey, D.J., Heard, D.E., Lewis, A.C., McQuaid, J.B., Pilling, M.J., Monks, P.S., Bandy, B.J., Penkett, S.A., 1999. Modeling OH, HO_2, and RO_2 radicals in the marine boundary layer: 1. Model construction and comparison with field measurements. J. Geophys. Res. Atmos. 104, 30241–30255.

Casciotti, K.L., Sigman, D.M., Hastings, M.G., Böhlke, J.K., Hilkert, A., 2002. Measurement of the Oxygen Isotopic Composition of Nitrate in Seawater and Freshwater Using the Denitrifier Method. Anal. Chem. 74(19), 4905-4912.

Chang, Y., Zhang, Y., Tian, C., Zhang, S., Ma, X., Cao, F., Liu, X., Zhang, W., Kuhn, T., Lehmann, M.F., 2018. Nitrogen isotope fractionation during gas-to-particle conversion of NO_x to NO_3^- in the atmosphere–implications for isotope-based NO_x source apportionment. Atmos. Chem. Phys. 18, 11647–11661.

Chatfield, R.B., 1994. Anomalous HNO_3/NO_x ratio of remote tropospheric air: Conversion of nitric acid to formic acid and NO_x? Geophys. Res. Lett. 21, 2705–2708.

Coplen, T.B., Böhlke, J.K., De Bievre, P., Ding, T., Holden, N.E., Hopple, J.A., Krouse, H.R., Lamberty, A., Peiser, H.S., Revesz, K., 2002. Isotope-abundance variations of selected elements (IUPAC Technical Report). Pure Appl. Chem. 74, 1987–2017.

Crippa, M., Janssens-Maenhout, G., Dentener, F., Guizzardi, D., Sindelarova, K., Muntean, M., Van Dingenen, R., Granier, C., 2016. Forty years of improvements in European air quality: regional policy-industry interactions with global impacts. Atmos. Chem. Phys. 16, 3825–3841.

Crippa, M., Oreggioni, G., Guizzardi, D., Muntean, M., Schaaf, E., Lo Vullo, E., Solazzo, E., Monforti-Ferrario, F., Olivier, J.G.J., Vignati, E., 2019. Fossil CO_2 and GHG emissions of all world countries. Luxembg. Publ. Off. Eur. Union.

De Haan, D.O., Finlayson-Pitts, B.J., 1997. Knudsen cell studies of the reaction of gaseous nitric acid with synthetic sea salt at 298 K. J. Phys. Chem. A 101, 9993–9999.

Dentener, F.J., Crutzen, P.J., 1993. Reaction of N_2O_5 on tropospheric aerosols: Impact on the global distributions of NO_x, O_3, and OH. J. Geophys. Res. Atmos. 98, 7149–7163.

Evans, M.J., Jacob, D.J., 2005. Impact of new laboratory studies of N_2O_5 hydrolysis on global model budgets of tropospheric nitrogen oxides, ozone, and OH. Geophys. Res. Lett. 32, L09813.

Fan, M.-Y., Zhang, Y.-L., Lin, Y.-C., Chang, Y.-H., Cao, F., Zhang, W.-Q., Hu, Y.-B., Bao, M.-Y., Liu, X.-Y., Zhai, X.-Y., 2019. Isotope-based source apportionment of nitrogen-containing aerosols: A case study in an industrial city in China. Atmos. Environ. 212, 96–105.

Fan, M., Zhang, Y., Lin, Y., Cao, F., Zhao, Z., Sun, Y., Qiu, Y., Fu, P., Wang, Y., 2020. Changes of Emission Sources to Nitrate Aerosols in Beijing After the Clean Air Actions: Evidence From Dual Isotope Compositions. J. Geophys. Res. Atmos. 125, e2019JD031998.

Felix, J.D., Elliott, E.M., 2014. Isotopic composition of passively collected nitrogen dioxide emissions: Vehicle, soil and livestock source signatures. Atmos. Environ. 92, 359–366.

Felix, J.D., Elliott, E.M., 2013. The agricultural history of human-nitrogen interactions as recorded in ice core $\delta^{15}N\text{-}NO_3^-$. Geophys. Res. Lett. 40, 1642–1646.

Felix, J.D., Elliott, E.M., Shaw, S.L., 2012. Nitrogen isotopic composition of coal-fired power plant NO_x: influence of emission controls and implications for global emission inventories. Environ. Sci. Technol. 46, 3528–3535.

Fibiger, D. L., & Hastings, M. G. (2016). First measurements of the nitrogen isotopic composition of NO_x from biomass burning. Environ. Sci. Technol. 50(21), 11569-11574.

Fiore, A. M., Naik, V., & Leibensperger, E. M. (2015). Air quality and climate connections. Journal of the Air & Waste Management Association, 65(6), 645-685.

Freyer, H.D., 1991. Seasonal variation of $^{15}N/^{14}N$ ratios in atmospheric nitrate species. Tellus B 43, 30–44.

Fuchs, N.A., Sutugin, A.G., 1971. High-dispersed aerosols, Topics in Current Aerosol Research. edited by: Hidy, GM and Brock, JR, vol. 2 Elsevier, pp. 1.

Gobel, A.R., Altieri, K.E., Peters, A.J., Hastings, M.G., Sigman, D.M., 2013. Insights into anthropogenic nitrogen deposition to the North Atlantic investigated using the isotopic composition of aerosol and rainwater nitrate. Geophys. Res. Lett. 40, 5977–5982.

Guelle, W., Schulz, M., Balkanski, Y., Dentener, F., 2001. Influence of the source formulation on modeling the atmospheric global distribution of sea salt aerosol. J. Geophys. Res. Atmos. 106, 27509–27524.

Hanna, S. R., Briggs, G. A., & Hosker Jr, R. P. (1982). Handbook on atmospheric diffusion (No. DOE/TIC-11223). Atmospheric Turbulence and Diffusion Lab, National Oceanic and Atmospheric Administration, Oak Ridge, TN (USA).

Hastings, M.G., Jarvis, J.C., Steig, E.J., 2009. Anthropogenic impacts on nitrogen isotopes of ice-core nitrate. Science (80-.). 324, 1288.

Hastings, M.G., Steig, E.J., Sigman, D.M., 2004. Seasonal variations in N and O isotopes of nitrate in snow at Summit, Greenland: Implications for the study of nitrate in snow and ice cores. J. Geophys. Res. Atmos. 109, D20306.

Itahashi, S., Hayami, H., Uno, I., Pan, X., Uematsu, M., 2016. Importance of coarse-mode nitrate produced via sea salt as atmospheric input to East Asian oceans. Geophys. Res. Lett. 43, 5483–5491.

Kamezaki, K., Hattori, S., Iwamoto, Y., Ishino, S., Furutani, H., Miki, Y., Uematsu, M., Miura, K., Yoshida, N., 2019. Tracing the sources and formation pathways of atmospheric particulate nitrate over the Pacific Ocean using stable isotopes. Atmos. Environ. 209, 152–166.

Kane, S.M., Caloz, F., Leu, M.-T., 2001. Heterogeneous uptake of gaseous N_2O_5 by $(NH_4)_2SO_4$, NH_4HSO_4, and H_2SO_4 aerosols. J. Phys. Chem. A 105, 6465–6470.

Kendall, C., Elliott, E.M., Wankel, S.D., 2007. Tracing anthropogenic inputs of nitrogen to ecosystems. Stable Isot. Ecol. Environ. Sci. 2, 375–449.

Khodayari, A., Olsen, S.C., Wuebbles, D.J., 2014. Evaluation of aviation NO_x-induced radiative forcings for 2005 and 2050. Atmos. Environ. 91, 95–103.

Lawrence, M.G., Jöckel, P., Von Kuhlmann, R., 2001. What does the global mean OH concentration tell us? 1, 37–49.

Li, J., Michalski, G., Davy, P., Harvey, M., Katzman, T., Wilkins, B., 2018. Investigating Source Contributions of Size-Aggregated Aerosols Collected in Southern Ocean and Baring Head, New Zealand using Sulfur Isotopes. Geophys. Res. Lett. 45(8), 3717-3727.

Li, J., Zhang, X., Michalski, G., Orlando, J., Tyndall, G., 2019. Quantifying the nitrogen isotope effects during photochemical equilibrium between NO and NO_2: implications for $\delta^{15}N$ in tropospheric reactive nitrogen. Atmos. Chem. Phys., 20(16), 9805-9819..

Liu, F., Beirle, S., Zhang, Q., 2017. NO_x emission trends over Chinese cities estimated from OMI observations during 2005 to 2015. Atmos. Chem. Phys. 17, 9261.

Liu, J., Ding, P., Zong, Z., Li, J., Tian, C., Chen, W., Chang, M., Salazer, G., Shen, C., Cheng, Z., Chen, Y., Wang, X., Szidat, S. & Zhang, G. (2018). Evidence of rural and suburban sources of urban haze formation in China: A case study from the Pearl River Delta region, J. Geophys. Res. Atmos., 2018, 123, 4712-4726.

Liu, P., Ye, C., Xue, C., Zhang, C., Mu, Y., Sun, X., 2020. Formation mechanisms of atmospheric nitrate and sulfate during the winter haze pollution periods in Beijing: gas-phase, heterogeneous and aqueous-phase chemistry. Atmos. Chem. Phys 20, 4153–4165.

Luo, L., Wu, Y., Xiao, H., Zhang, R., Lin, H., Zhang, X., Kao, S., 2019. Origins of aerosol nitrate in Beijing during late winter through spring. Sci. Total Environ. 653, 776–782.

Madronich, S., Flocke, S., 1999. The role of solar radiation in atmospheric chemistry, in: Environmental Photochemistry. Edited by Boule P., Springer, pp. 1–26.

Michalski, G., Savarino, J., Böhlke, J.K., Thiemens, M., 2002. Determination of the total oxygen isotopic composition of nitrate and the calibration of a $\Delta^{17}O$ nitrate reference material. Anal. Chem. 74, 4989–4993.

Michalski, G., Scott, Z., Kabiling, M., Thiemens, M.H., 2003. First measurements and modeling of $\Delta^{17}O$ in atmospheric nitrate. Geophys. Res. Lett. 30(16), 1870.

Miller, C.E., Yung, Y.L., 2000. Photo-induced isotopic fractionation. J. Geophys. Res. Atmos. 105, 29039–29051.

Millero, F.J., Feistel, R., Wright, D.G., McDougall, T.J., 2008. The composition of Standard Seawater and the definition of the Reference-Composition Salinity Scale. Deep Sea Res. Part I Oceanogr. Res. Pap. 55, 50–72.

Ministry of the Environment, 2004, Emission Inventories for CO, NO_x, SO_2, ozone, benzene and benzo(a)pyrene in New Zealand, Air Quality Technical Report No. 44, Published by Ministry of the Environment, New Zealand.

Mitchell, T., 2015. Air Quality State of the Environment monitoring programme., Published by Greater Wellington Regional Council, New Zealand.

Monks, P. S., Carpenter, L. J., Penkett, S. A., Ayers, G. P., Gillett, R. W., Galbally, I. E., & Meyer, C. M. (1998). Fundamental ozone photochemistry in the remote marine boundary layer: The SOAPEX experiment, measurement and theory. Atmos. Environ., 32(21), 3647-3664.

Morin, S., Savarino, J., Frey, M.M., Domine, F., Jacobi, H., Kaleschke, L., Martins, J.M.F., 2009. Comprehensive isotopic composition of atmospheric nitrate in the Atlantic Ocean boundary layer from 65 S to 79 N. J. Geophys. Res. Atmos. 114, D05303.

Paulot, F., Paynter, D., Ginoux, P., Naik, V., Whitburn, S., Van Damme, M., Clarisse, L., Coheur, P., Horowitz, L.W., 2017. Gas-aerosol partitioning of ammonia in biomass burning plumes: Implications for the interpretation of spaceborne observations of ammonia and the radiative forcing of ammonium nitrate. Geophys. Res. Lett. 44, 8084–8093.

Pszenny, A., Fischer, C., Mendez, A., Zetwo, M., 1993. Direct comparison of cellulose and quartz fiber filters for sampling submicrometer aerosols in the marine boundary layer. Atmos. Environ. Part A. Gen. Top. 27, 281–284.

Rees, C.E., Jenkins, W.J., Monster, J., 1978. The sulphur isotopic composition of ocean water sulphate. Geochim. Cosmochim. Acta 42, 377–381.

Savarino, J., Kaiser, J., Morin, S., Sigman, D.M., Thiemens, M.H., 2007. Nitrogen and oxygen isotopic constraints on the origin of atmospheric nitrate in coastal Antarctica. Atmos. Chem. Phys. Atmos. Chem. Phys. 7, 1925–1945.

Savarino, J., Morin, S., Erbland, J., Grannec, F., Patey, M.D., Vicars, W., Alexander, B., Achterberg, E.P., 2013. Isotopic composition of atmospheric nitrate in a tropical marine boundary layer. Proc. Natl. Acad. Sci. 110, 17668–17673.

Seinfeld, J.H., Pandis, S.N., 2016. Atmospheric chemistry and physics: from air pollution to climate change. John Wiley & Sons.

Sharma, H.D., Jervis, R.E., Wong, K.Y., 1970. Isotopic exchange reactions in nitrogen oxides. J. Phys. Chem. 74, 923–933.

Sherlock, V., Pickmere, S., Currie, K., Hadfield, M., Nodder, S., Boyd, P.W., 2007. Predictive accuracy of temperature-nitrate relationships for the oceanic mixed layer of the New Zealand region. J. Geophys. Res. Ocean. 112, C06010.

Sigman, D.M., Casciotti, K.L., Andreani, M., Barford, C., Galanter, M., Böhlke, J.K., 2001. A bacterial method for the nitrogen isotopic analysis of nitrate in seawater and freshwater. Anal. Chem. 73, 4145–4153.

Silvern, R.F., Jacob, D.J., Mickley, L.J., Sulprizio, M.P., Travis, K.R., Marais, E.A., Cohen, R.C., Laughner, J.L., Choi, S., Joiner, J., 2019. Using satellite observations of tropospheric NO_2 columns to infer long-term trends in US NO_x emissions: the importance of accounting for the free tropospheric NO_2 background. Atmos. Chem. Phys. 19, 8863–8878.

Sommariva, R., Haggerstone, A.-L., Carpenter, L.J., Carslaw, N., Creasey, D.J., Heard, D.E., Lee, J.D., Lewis, A.C., Pilling, M.J., Zádor, J., 2004. OH and HO_2 chemistry in clean marine air during SOAPEX-2. Atmos. Chem. Phys., 4, 839–856.

Song, W., Wang, Y.-L., Yang, W., Sun, X.-C., Tong, Y.-D., Wang, X.-M., Liu, C.-Q., Bai, Z.-P., Liu, X.-Y., 2019. Isotopic evaluation on relative contributions of major NO_x sources to nitrate of PM2. 5 in Beijing. Environ. Pollut. 248, 183–190.

Sridhar, S., Wickham, L., Metcalfe, J., 2014. Future trends in motor vehicle emissions in Auckland. Prepared by Emission Impossible Ltd for Auckland Council. Auckland Council technical report, TR.

Srivastava, R.K., Hall, R.E., Khan, S., Culligan, K., Lani, B.W., 2005. Nitrogen oxides emission control options for coal-fired electric utility boilers. J. Air Waste Manage. Assoc. 55, 1367–1388.

Statistics New Zealand, 2014, New Zealand Household Travel Survey: Travel to work, by main urban area results.

Sun, P., Nie, W., Chi, X., Xie, Y., Huang, X., Xu, Zheng, Qi, X., Xu, Zhengning, Wang, L., Wang, T., 2018. Two years of online measurement of fine particulate nitrate in the western Yangtze River Delta: influences of thermodynamics and N_2O_5 hydrolysis. Atmos. Chem. Phys. 18, 17177–17190.

Walters, W.W., Goodwin, S.R., Michalski, G., 2015a. Nitrogen stable isotope composition ($\delta^{15}N$) of vehicle-emitted NOx. Environ. Sci. Technol. 49, 2278–2285.

Walters, W.W., Michalski, G., 2015. Theoretical calculation of nitrogen isotope equilibrium exchange fractionation factors for various NO_y molecules. Geochim. Cosmochim. Acta 164, 284–297.

Walters, W.W., Simonini, D.S., Michalski, G., 2016. Nitrogen isotope exchange between NO and NO_2 and its implications for $\delta^{15}N$ variations in tropospheric NO_x and atmospheric nitrate. Geophys. Res. Lett. 43, 440–448.

Walters, W.W., Tharp, B.D., Fang, H., Kozak, B.J., Michalski, G., 2015b. Nitrogen isotope composition of thermally produced NO_x from various fossil-fuel combustion sources. Environ. Sci. Technol. 49, 11363–11371.

Zhang, Q., Streets, D.G., He, K., Wang, Y., Richter, A., Burrows, J.P., Uno, I., Jang, C.J., Chen, D., Yao, Z., Lei, Y., 2007. NO $_x$ emission trends for China, 1995–2004: The view from the ground and the view from space. J. Geophys. Res. 112, D22306.

Zhao, Y., Zhou, Y., Qiu, L., Zhang, J., 2017. Quantifying the uncertainties of China's emission inventory for industrial sources: From national to provincial and city scales. Atmos. Environ. 165, 207–221.

Zong, Z., Wang, X., Tian, C., Chen, Y., Fang, Y., Zhang, F., Li, C., Sun, J., Li, J., Zhang, G., 2017. First assessment of NO_x sources at a regional background site in North China using isotopic analysis linked with modeling. Environ. Sci. Technol. 51, 5923–5931.

Zong, Z., Tan, Y., Wang, X., Tian, C., Li, J., Fang, Y., Chen, Y., Cui, S., & Zhang, G.Dual-modelling-based source apportionment of NOx in five Chinese megacities: Providing the isotopic footprint from 2013 to 2014, Environ. Int., 2020, 137, 105592.

CHAPTER 7. CONCLUSIONS AND OUTLOOK

7.1 Studying atmospheric sulfur using stable sulfur isotopes

Chapter 2 and Chapter 3 of this dissertation demonstrate that sulfur isotopic analysis is an excellent tool in identifying sources of sulfate aerosols in the atmosphere. Our study at Baring Head, New Zealand (Chapter 2) showed that, in a clean, Southern Hemisphere coastal environment, marine emission plays an important role in controlling the concentrations of sulfate aerosols. In this environment, sulfate is observed in both coarse (>1 μm in diameter) and fine (<1 μm in diameter) aerosols. The coarse aerosols are primarily composed of sea-salt aerosols and the sulfate in the coarse aerosols is also almost entirely originated from sea-salt sulfate. This is evidenced by 1) the sodium to sulfate ratios in the coarse aerosols are similar to those of sea-salt; and 2) the sulfate in coarse aerosols and sea-salt sulfate display identical $\delta^{34}S$ values. Sulfate in fine aerosols, on the other hand, is originated from atmospheric oxidation of SO_2. The origins of the SO_2 were identified using stable isotopes, showing that on average, 73-77% of the SO_2 is sourced from biogenic emissions by phytoplankton and the rest SO_2 is originated from anthropogenic activities. In the Atacama Desert (Chapter 3), we investigated the sources and interannual variations of atmospheric deposition. Sulfur isotopic analysis was again used to infer the sources of sulfate in the deposition samples. In the coastal region to the west of the Atacama Desert, we suggest that anthropogenic SO_2 emissions is the main source of the atmospheric sulfate. Inside the Atacama Desert, the $\delta^{34}S$ values of atmospheric sulfate generally are similar to local soil gypsum, suggesting local surface soil is the main source of atmospheric sulfate. In the Andes to the east of the Atacama Desert, the atmospheric deposition is mainly wet deposition, and the sulfate is mainly originated from nearby salt lakes and surface soil.

Sulfur isotopes can also be used to infer the formation pathways of atmospheric sulfate when the $\delta^{34}S$ value of SO_2 is known. In Chapter 4, we investigated the sulfur isotopic composition of sulfate aerosols collected during a severe haze episode in Nanjing, China. Significant discrepancy was observed between the sulfur isotopic compositions of sulfate aerosols and SO_2 emissions. We suggest this discrepancy is primarily driven by the isotopic fractionation during the SO_2 oxidation processes, since 1) the observed sulfur oxidation ratio is low (i.e., incomplete SO_2 oxidation) and 2) a negative correlation between the $\delta^{34}S$ values of sulfate and the sulfur oxidation ratio is

observed. A Rayleigh Distillation model was then used to describe the isotopic fractionation process, which yielded a fractionation factor of 5.3±1.8‰. This fraction factor indicated that O_3 oxidation, H_2O_2 oxidation and Transition Metal Ion (TMI) Catalyzed O_2 oxidation were all important during the haze episode, and the combined contribution of O_3 and H_2O_2 pathways was approximately 51±10%, and TMI pathway accounted for the rest. This calculated result is in general agreement with GEOS-Chem model simulations; therefore, we concluded that stable sulfur isotopes have the potential to constrain the formation pathways of sulfate aerosols in future studies.

7.2 Understanding nitrogen isotopic fractionations during tropospheric NO_x chemistry

While the isotopic compositions of different NO_x sources had been extensively studied, there are still many unknowns in the isotopic fractionation during the formation of nitrate aerosols, hindering the use of stable nitrogen isotopes in interpreting the source of NO_x emissions. Therefore, it is important to investigate the isotopic fractionation during the oxidation of NO_x. In Chapter 5, we conducted chamber experiments to measure the isotopic fractionations between NO and NO_2. We find this isotopic fractionation process is controlled by two distinctive processes: equilibrium isotopic fractionation (EIE, i.e., isotopic exchange between NO and NO_2 molecules) and kinetic isotopic fractionation (KIE, i.e., isotopic fractionation during NO_x photochemistry cycle). We first measured the isotopic fractionation factors of both processes using chamber experiments, then derived a mathematical solution to quantify their combined effects at given condition. We found that EIE tend to enrich ^{15}N in NO_2 while KIE tend to enrich ^{15}N in NO. Our measurements show that the EIE factor is +28.9±1.2‰ and the KIE factor is -10±5‰. Also, at high NO_x concentration (>20 ppb), EIE is the main factor determining the NO-NO_2 isotopic fractionation while KIE is the dominant factor when NO_x concentration is lower than 1 ppb. This study provided a useful tool to quantify the overall isotopic fractionations between tropospheric NO and NO_2, which can be used in future field observations and atmospheric chemistry models.

In Chapter 6, we measured the nitrogen isotopic compositions of nitrate aerosols collected at Baring Head, New Zealand to evaluate the isotopic fractionation during atmospheric nitrate formation. The measured the $\delta^{15}N$ values of nitrate aerosols display a clear seasonal variation with winter nitrate $\delta^{15}N$ values approximately 15‰ higher than summer nitrate $\delta^{15}N$ values. This variation, however, cannot be explained by the changes in NO_x emission sources since the $\delta^{15}N$

value of NO_x emission at Baring Head is constant throughout the year. Therefore, we concluded the observed seasonal variation in nitrate $\delta^{15}N$ values reflected variable isotopic fractionation of NO_x chemistry. Then, we quantified the isotopic fractionations between NO and NO_2, finding this isotopic fractionation cannot fully explain the observed $\delta^{15}N$ variations at Baring Head. Thus, we suggested that the isotopic fractionations during the oxidation of NO_2 to nitrate played an important role in regulating the $\delta^{15}N$ values of nitrate aerosols at Baring Head, which is in good agreement with the theoretical calculations. However, a detailed quantification of the isotopic fractionations during NO_2 oxidation is still lacking, mainly because the NO_y chemistry (i.e., the contribution of each NO_2 oxidation pathway) is difficult to constrain. Future research is needed to fully understand the isotopic fractionations between NO_2 and nitrate aerosols.

7.3 Future research outlook

The research projects in this dissertation suggest stable isotopes can be used in atmospheric studies to infer the sources and chemistry of atmospheric pollutants including NO_x, SO_2, nitrate and sulfate. Future research should be conducted to 1) address current unknowns and uncertainties; and 2) extend the applications of these isotopic tools. Specifically, we propose the following four research directions:

1. Improving our understanding in the isotopic fractionation of atmospheric SO_2 oxidation processes. Although the isotopic fractionation factors for the major SO_2 oxidation pathways (gas phase SO_2+OH, aqueous phase SO_2+O_3, aqueous phase SO_2+H_2O_2, and aqueous phase TMI oxidation) have been determined experimentally, there remain questions in 1) whether the isotopic fractionation will remain the same when the SO_2 oxidation occurs on the aerosol/gas surface instead of the aqueous phase? 2) is the isotopic fractionation factor of TMI oxidation dependent on the type of catalyst (i.e., different transition metal ions)? 3) during aqueous phase SO_2 oxidation, what is the isotopic fractionation during the dissolving of SO_2 and how will this fractionation change at different pH? 4) What are the fractionation factors of other oxidation pathways (e.g., SO_2+NO_2, SO_2+HOCl/HOBr), which can be regionally important? 5) Can we use multiple-sulfur isotopic analysis to further infer SO_2 oxidation pathways? Addressing the above questions can provide us a better understanding in the isotopic fractionation processes of atmospheric sulfur.

2.Quantifying the nitrogen isotopic fractionation factors of NO_x and NO_y reactions. Both theoretical calculations and chamber experiments are good approaches in measuring these isotopic

fractionation factors. While previous studies have calculated the equilibrium isotopic fractionations between the NO_y molecules, the kinetic fractionations and photochemistry fractionation factors of most atmospheric reactions have not been determined yet. Similarly, to date, laboratory investigations only measured the isotopic fractionation factors between NO and NO_2, there is no chamber experiments investigating the isotopic effects of NO_y chemistry. Therefore, future theoretical calculations and chamber experiments are needed to fully assess the isotopic fractionation factors of the atmospheric chemistry of reactive nitrogen. In addition, since both troposphere and stratosphere have a wide range of temperature, it is important to investigate the temperature-dependence of the isotopic fractionation factors.

3. Combining atmospheric chemistry models and field observations to further assess the isotopic fractionation of both atmospheric nitrogen and sulfur chemistry. Atmospheric chemistry models are good tool in quantifying the isotopic fractionation during nitrogen and sulfur chemistry and interpret observation data (especially nitrogen and sulfur isotopic compositions of nitrate and sulfate aerosols collected in the field). After we quantify the isotopic fractionations factors of most NO_x and NO_y reactions, we can incorporate them into models. Currently, there are chemistry mechanisms in atmospheric models that can calculate the isotopic fractionations in gas phase NO_x and NO_y chemistry, however, the aerosol chemistry, an important part of nitrogen and sulfur in the atmosphere, has been overlooked. This is because 1) isotopic fractionation factors during such heterogeneous reactions are unknown yet, and 2) computing isotopic fractionations in the aerosol thermodynamic equilibrium package in current atmospheric chemistry models (mainly using ISORROPIA II package) is extremely difficult. Therefore, more work is needed to model the isotopic compositions of nitrogen and sulfur in both gas phase and aerosol phase.

4. Developing novel analytical methods to enable more atmospheric nitrogen and sulfur isotopic analysis (SIMS-sulfur, online LIF N isotopes for NO). Currently, analyzing the nitrogen and sulfur isotopic compositions of nitrate, sulfate, NO_x and SO_2 requires a complex process including field sampling, chemical processing and instrumental analysis using Isotope Ratio Mass Spectrometer. This elongated process resulted in very sparse isotopic measurement (one data point per 3 hours in polluted environment: one data point per week in clean environment) comparing to the concentration measurements of these air pollutant (one data point per 1-10 second). Therefore, developing novel measurement technologies that can measure isotopes online at a higher frequency will greatly advance this research area, and enable meaningful measurements on mobile

platforms such as vehicles, ships, and aircrafts. While this task is difficult in present day, recent development of sub-ppt level NO and SO_2 measurements using state-of-the-art optical spectrometers and mass spectrometers have provided a new perspective for achieving this goal.

APPENDIX A. SUPPLEMENTARY INFORMATION FOR CHAPTER 5

1. Chamber descriptions

The chamber is a 10 m^3 Teflon bag equipped with several standard instruments including temperature and humidity probe, NO_x monitor and O_3 monitor. 128 wall-mounted blacklight tubes surrounded the chamber to mimic tropospheric photochemistry and the photolysis rate of NO_2 ($j(NO_2)$) when all lights are on have been previously determined to be 1.4×10^{-3} s^{-1}, similar to a $j(NO_2)$ coefficient at an 81-degree solar zenith angle. The irradiation spectrum of the blacklights are shown in Figure A.1. The chamber was kept at room temperature and one atmospheric pressure. Before each experiment, the chamber was flushed with zero air at 40 L min^{-1} for at least 12 hours to ensure the background NO_x, O_3 and other trace gases were below detection limit.

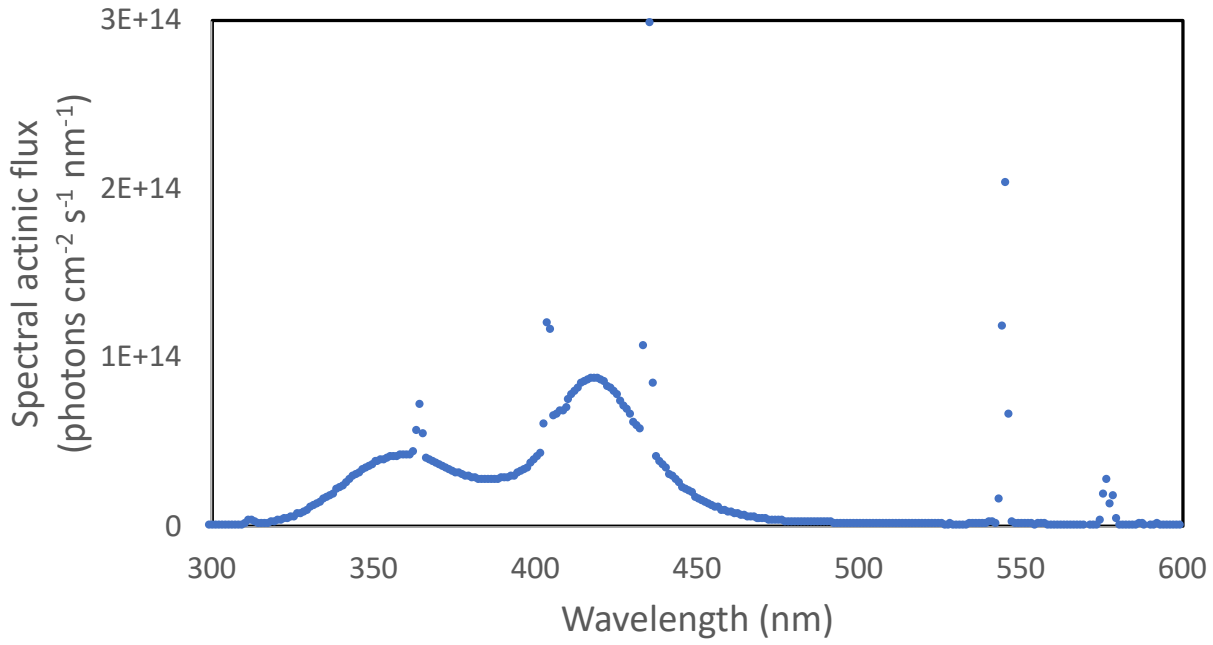

Figure A.5.1 Spectral actinic flux versus wavelengths of the UV light source used in our experiments.

2. Box model assessing the time needed for NO-NO_2 to reach isotopic equilibrium

The time needed to reach NO-NO_2 isotopic equilibrium during light-off experiments were assessed using a 0-D box model. This box model contains only two reactions:

$^{15}NO_2 + {}^{14}NO \rightarrow {}^{15}NO + {}^{14}NO_2$ $k = 8.14000 \times 10^{-14}\ cm^3\ s^{-1}$

$^{15}NO + {}^{14}NO_2 \rightarrow {}^{15}NO_2 + {}^{14}NO$ $k' = 8.37525 \times 10^{-14}\ cm^3\ s^{-1}$

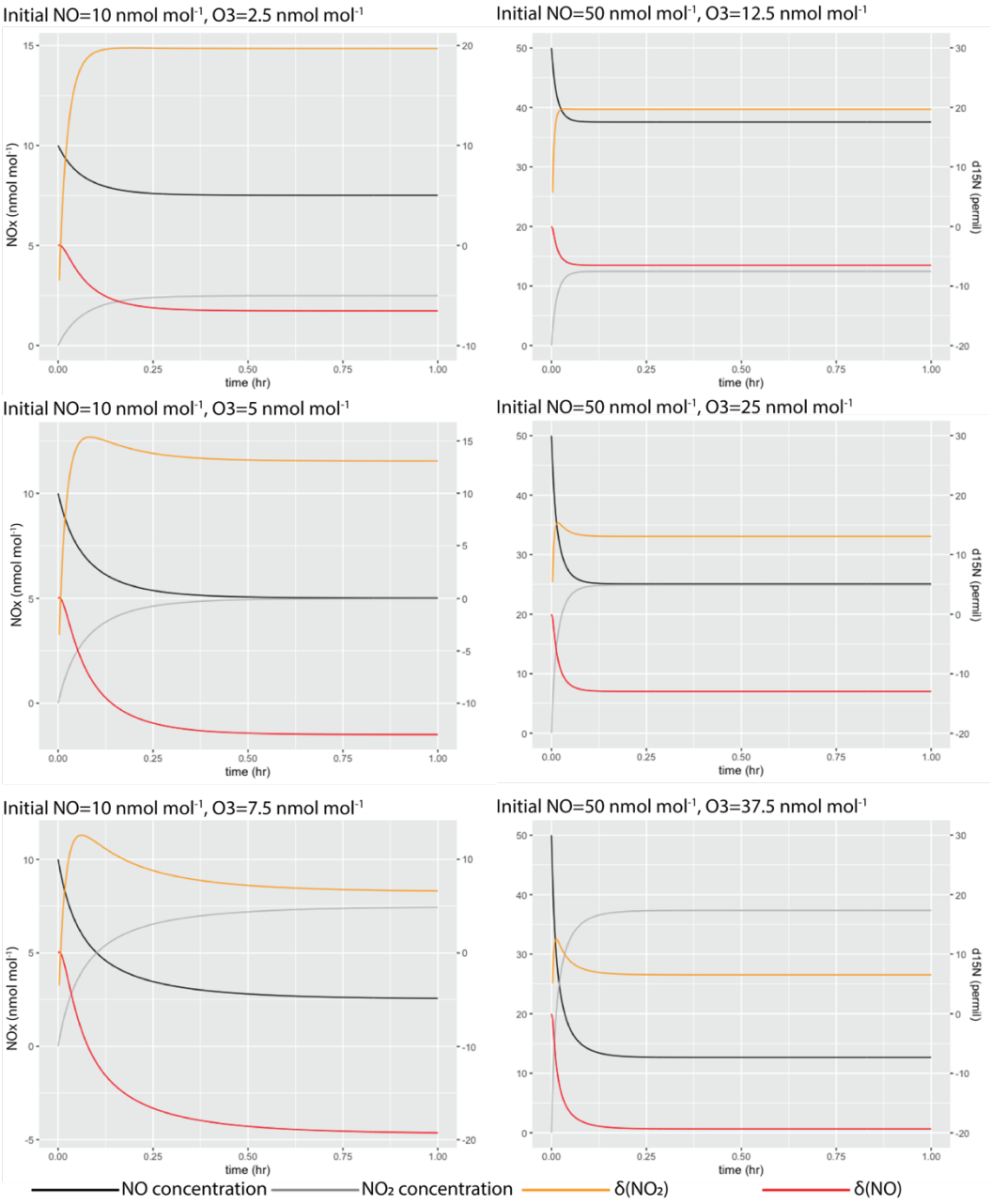

Figure A.5.2 Simulated NO-NO_2 isotopic equilibrium process in the chamber at various NO and O_3 concentrations.

Where k and k' are rate constants of the reactions. The differences in rate constants were calculated by assuming an $\alpha(NO_2\text{-}NO)$ value of 1.0289. Six simulations were conducted at various initial NO (with $\delta^{15}N$=0‰) and O_3 levels that were similar to our experiment. Then the $\delta^{15}N$ values of NO and NO_2 during the simulation were calculated from the model and were shown in Figure A.2,

suggesting that in our experimental condition, all systems should reach isotopic equilibrium within 1 hr.

3. Deriving Equations 5.7 and 5.8

When the system (R1-R6) reaches steady-state, we have:

$$d[^{15}NO_2]/dt=0 \qquad \text{Eq. (1)}$$

Therefore, using R1-R6:

$$k_1\,[^{15}NO_2][^{14}NO]+j(NO_2)\alpha_1[^{15}NO_2]= k_5\alpha_2[^{15}NO][O_3]+ k_1\alpha(NO_2\text{-}NO)\,[^{15}NO][^{14}NO_2] \qquad \text{Eq. (2)}$$

From here we refer $^{14}NO_2$ and ^{14}NO as NO_2 and NO for convenience, rearrange the above equation, we get:

$$\frac{[^{15}NO_2]}{[^{15}NO]} = \frac{k_5\alpha_2[O_3]+k_1\alpha(NO_2-NO)\,[NO_2]}{j_{NO2}\alpha_1+k_1[NO]} \qquad \text{Eq. (3)}$$

Meantime, since the Leighton cycle reaction still holds for the majority isotopes (NO and NO_2), we have:

$$j_{NO2}[NO_2]= k_5[NO][O_3] \qquad \text{Eq. (4)}$$

Thus,

$$\frac{[NO_2]}{[NO]} = \frac{k_5\times[O_3]}{j_{NO2}} \qquad \text{Eq. (5)}$$

From the text, when $j_{NO2}>0$, we defined $A=\tau_{exchange}/\tau_{photo}=j_{NO2}/(k_1\times[NO])$. Using the above equations, we know:

$$\frac{j_{NO2}}{[NO]} = \frac{k_5[O_3]}{[NO_2]} = Ak_1 \qquad \text{Eq. (6)}$$

$$\frac{j_{NO2}}{k_1[NO]} = \frac{k_5[O_3]}{k_1[NO_2]} = A \qquad \text{Eq. (7)}$$

Next, to calculate $\delta(NO_2)$-$\delta(NO)$, we use the definition of delta notation:

$$\delta(NO_2)\text{-}\delta(NO) = R_{NO2}/R_{std}\text{-}\ R_{NO}/R_{std} = (R_{NO2}/R_{NO}\text{-}1)(1+\delta(NO)) \qquad \text{Eq. (8)}$$

$$\frac{R_{NO2}}{R_{NO}} = \frac{[^{15}NO_2][NO]}{[^{15}NO][NO_2]} = \frac{k_5\alpha_2[O_3][NO]+k_1\alpha(NO_2-NO)[NO_2][NO]}{j_{NO2}\alpha_1[NO_2]+k_1[NO][NO_2]} \qquad \text{Eq. (9)}$$

Divide both side by $k_1[NO][NO_2]$:

$$\frac{R_{NO2}}{R_{NO}} = \frac{\frac{k_5\alpha_2[O_3]}{k_1[NO_2]}+\alpha(NO_2-NO)}{\frac{j_{NO2}\alpha_1}{k_1[NO]}+1} \qquad \text{Eq. (10)}$$

Rearrange and substitute $\frac{k_5[O_3]}{k_1[NO_2]}$ and $\frac{j_{NO2}}{k_1[NO]}$ with A:

$$\frac{R_{NO2}}{R_{NO}} = \frac{\alpha_2 A + \alpha(NO_2 - NO)}{\alpha_1 A + 1} \quad \text{Eq. (11)}$$

$$\frac{R_{NO}}{R_{NO2}} = \frac{\alpha_1 A + 1}{\alpha_2 A + \alpha(NO_2 - NO)} \quad \text{Eq. (12)}$$

$$\frac{R_{NO}}{R_{NO2}} - 1 = \frac{(\alpha_1 - \alpha_2)A - (\alpha(NO_2 - NO) - 1)}{\alpha_1 A + \alpha(NO_2 - NO)} \quad \text{Eq. (13)}$$

Thus,

$$\delta(NO_2)\text{-}\delta(NO) = \frac{(\alpha_2 - \alpha_1)A + (\alpha(NO_2 - NO) - 1)}{\alpha_1 A + \alpha(NO_2 - NO)}(1 + \delta(NO_2)) \quad \text{Eq. (14)}$$

Then, using mass balance:

$$\delta(NO_2)\, f(NO_2) + \delta(NO)(1 - f(NO_2)) = \delta(NO_x) \quad \text{Eq. (15)}$$

We can derive Eq. 8:

$$\delta(NO_2)\text{-}\delta(NO_x) = \frac{(\alpha_2 - \alpha_1) \times A + \alpha(NO_2 - NO) - 1)}{\alpha_1 A + \alpha(NO_2 - NO)} (1 + \delta(NO_2))\, (1 - f(NO_2)) \quad \text{Eq. (16)}$$

VITA

Jianghanyang Li

Ph.D. candidate

Department of Earth, Atmospheric and Planetary Sciences

Purdue University, West Lafayette, IN, 47907

Phone: (765)-337-0809 Email: li2502@purdue.edu

Education

University of Sci. and Tech. of China, Hefei	Geochemistry	B.Sc., 2013
University of Alberta, Edmonton	Geochemistry	M.Sc., 2016
Purdue University, West Lafayette	Atmospheric Chemistry	Ph.D., 2021

Appointments

Graduate teaching/research assistant, Purdue University, West Lafayette, IN	2016-2021
Advanced Study Program graduate student visitor, National Center for Atmospheric Research, Boulder, CO	2018

Fellowships, awards and grants

Outstanding Graduate Student Award, Purdue University	2020
College of Science Cagiantas Fellowship, Purdue University	2019
Outstanding Student Presentation Award, American Geophysical Union	2018
Advanced Study Program Graduate Student Fellowship, NCAR	2018
A. H. Ismail Doctoral Research Travel Award, Purdue University	2018
Atmospheric Science Graduate Student Award, Purdue University	2018, 2020
June L. and Tan Sun Chen Research Scholarship, Purdue University	2018
Graduate School Summer Research Grant, Purdue University	2018
Purdue Climate Change Research Center Travel Grant, Purdue University	2017, 2018, 2019
Purdue Graduate Student Government Travel Grant, Purdue University	2017, 2018

Synergistic activities

1. Educational outreach activities: worked as volunteer worker or coordinator for K-12 environmental education programs hosted by Indiana State Museum, Wabash River Enhancement Corporation, Tippecanoe County Government and Purdue University

2. Pedagogies: worked as teaching assistant for 7 different courses, worked with course instructor to redesign class and lab material for a freshman-level course (Dynamic Earth)

3. Undergraduate student mentoring: mentored 8 undergraduate students as research advisor and collaborator on 8 undergraduate research projects, help students acquired 3 research grants

4. Journal reviewer: *Atmospheric Environment, Atmospheric Research*

Public presentations

1. Optimizing the N and O isotopic analysis technique of nitrate using Ti(III) reduction method (*invited*), 2019 AGU Fall Meeting

2. Geochemistry and origins of trace metals in PM_{10} at Arequipa, Peru, 2019 AGU Fall Meeting

3. Quantifying the nitrogen isotopic fractionation of NO_x in atmospheric simulation chamber, 2019 AGU Fall Meeting

4. Seasonal variations in $\delta^{15}N$ of nitrate aerosols at Baring Head, New Zealand: indicator of atmospheric nitrogen chemistry in pristine marine boundary layer, 2018 AGU Fall Meeting

5. Investigating sulfate aerosol formation mechanisms during a severe winter haze-fog event in Nanjing, China using stable sulfur isotopes, 2018 AGU Fall Meeting. *won AGU Outstanding Student Presentation Award*

6. Investigating the isotopic effects during bacterial nitrification and denitrification, Department of Chemistry, Purdue University, 2018

7. Isotopic investigation of inorganic aerosols: indicators of sources and atmospheric chemistry. NCAR Advanced Study Program summer workshop, 2018

8. Stable isotopic investigations of reactive nitrogen: from field observations to chamber experiments to chemistry models. Tropospheric chemistry seminar, NCAR, 2018

9. Using sulfur isotopes to understand the formation mechanism of sulfate aerosols in severe haze episodes. Graduate student EXPO, Purdue University, 2018

10. Geochemical, sulfur isotopic characteristics and source contributions of size-aggregated aerosols collected at Baring Head, New Zealand. 2017 AGU Fall Meeting

11. Sulfur isotopic compositions of size-aggregated sulfate aerosols collected at Baring Head, New Zealand. Invited seminar, Nanjing University of Information & Technology, 2017

PUBLICATIONS

1. **Li, J.,** Zhang, X., Orlando, J., Tyndall, G., & Michalski, G. (2020): Quantifying the nitrogen isotope effects during photochemical equilibrium between NO and NO_2: implications for $\delta^{15}N$ in tropospheric reactive nitrogen, *Atmospheric Chemistry and Physics,* 20(16), 9805–9819

2. **Li, J.,** Zhang, Y. L., Cao, F., Zhang, W., Fan, M., Lee, X., & Michalski, G. (2020): Sulfur isotopes revealed a major role of transition-metal-ion catalyzed SO_2 oxidation in haze episodes. *Environmental Science & Technology,* 2020, 54, 5, 2626-2634

3. **Li, J.,** Davy, P., Harvey, M., Katzman, T., Mitchell, T., & Michalski, G. (2021): Nitrogen isotopic fractionations of atmospheric reactive nitrogen at Baring Head: implications for nitrogen isotopes of aerosol nitrate in pristine environment. *Atmospheric Environment,* 245, 118028

4. **Li, J.,** Wang, F., Michalski, G., & Wilkins, B. (2019): The atmospheric deposition during 2010-2011 across the Atacama Desert, Chile: compositions, sources, and interannual variabilities. *Chemical Geology,* 525 (2019): 435-446.

5. **Li, J.,** Michalski, G. M., Davy, P., Harvey, M., Wilkins, B. P., & Katzman, T. L. (2018): Geochemical, Sulfur Isotopic Characteristics and Source Contributions of Size-Aggregated Aerosols Collected in Baring Head, New Zealand. *Geophysical Research Letter,* 45(8), 3717-3727.

6. **Li, J.,** Zhang, Z., Stern, R. A., Hannah, J. L., Stein, H. J., Yang, G., & Li, L. (2017): Primary multiple sulfur isotopic compositions of pyrite in 2.7 Ga shales from the Joy Lake sequence (Superior Province) show felsic volcanic array-like signature. *Geochimica et Cosmochimica Acta*, 202, 310-340.

7. Fan, M., Zhang, Y., Lin, Y., **Li, J.,** Cheng, H., An, N., Sun, Y., Qiu, Y., Cao, F., Fu, P. (2020): Sulfur oxidation ratios determine stable sulfur isotope in sulfate aerosols in Beijing: implication for formation pathways of sulfate aerosols, *Environmental Science & Technology Letter,* 2020, 7, 883-888

8. Diaz, M., **Li, J.**, Michalski, G., Darrah, T., Adams, B., Wall, D., Hogg, I., Fierer, N., Welch, S., Gardner, C., Lyons, B. (2020), Stable isotopes of nitrate and sulfate in soils from the Transantarctic Mountains, Antarctica: a record of atmospheric deposition and chemical weathering. *Frontiers Earth Science,* 8:341.

9. Yang, C., Smith, A., Li, T., Kinnison, D., **Li, J.**, Dou, X. (2020), Can the Madden-Julian oscillation affect the Antarctic total column ozone? *Geophysical Research Letter,* 47(15), e2020GL088886

10. Qi, Y., Cheng, W., Nan, X., Yang F., **Li, J.,** Li, D., Lundstrom, C., Yu, H., Zhang, G., Huang, F. (2020), Fe stable isotopes in bulk soil and sequential extracted fractions trace iron redox cycling in paddy soils. *Journal of Agricultural and Food Chemistry,* 2020, 68, 31, 8143–8150

11. Abbasi1, A., Salazar, A., Oh, Y., Reinsch, S., Uribe, M., **Li, J.,** Rashid, I., Dukes, J. (2020), Soil responses to manipulated precipitation changes: A synthesis of meta-analyses, *Biogeosciences,* 17, 3859–3873

12. Xia, X., Li, S., Wang, F., Zhang, S., Fang, Y., **Li, J**., Michalski, G., & Zhang, L. (2019). Triple oxygen isotopic evidence for atmospheric nitrate and its application in source identification for river systems in the Qinghai-Tibetan Plateau. *Science of the Total Environment,* 688 (2019): 270-280

13. Li, L., Zheng, Y. F., Cartigny, P., & **Li, J**. (2014). Anomalous nitrogen isotopes in ultrahigh-pressure metamorphic rocks from the Sulu orogenic belt: Effect of abiotic nitrogen reduction during fluid–rock interaction. *Earth and Planetary Science Letters*, 403, 67-78